SIMULATION AND ANALYSIS OF RAREFIED GAS FLOWS IN CHEMICAL VAPOR DEPOSITION PROCESSES

by

Daniel Gene Coronell

B.S. Chemical Engineering, Summa Cum Laude
University of Illinois - Urbana
1988

Submitted to the Department of Chemical Engineering
in Partial Fulfillment of the Requirements
for the Degree of

Doctor of Philosophy

at the
Massachusetts Institute of Technology
September 1993

© Massachusetts Institute of Technology 1993
All Rights Reserved

Signature of Author____________________
Department of Chemical Engineering
July 28, 1993

Certified by____________________
Professor Klavs F. Jensen
Thesis Supervisor

Accepted by____________________
Professor Robert E. Cohen
Chairman, Committee for Graduate Students

MASSACHUSETTS INSTITUTE
OF TECHNOLOGY

SEP 22 1993

LIBRARIES

ARCHIVES

SIMULATION AND ANALYSIS OF RAREFIED GAS FLOWS

IN CHEMICAL VAPOR DEPOSITION PROCESSES

by

DANIEL GENF CORONELL

Submitted to the Department of Chemical Engineering
on July 28, 1993 in partial fulfillment of the
requirements for the degree of Doctor of Philosophy in
Chemical Engineering

ABSTRACT

Simulation models of chemical vapor deposition processes involving rarefied gas flows were developed using the direct simulation Monte Carlo method. Rarefied gas flows in the multi-wafer low pressure CVD reactor operating under ultra-high vacuum CVD conditions were initially investigated. The most distinguishing feature of the UHV-CVD gas flows elucidated by the simulation study was the compressibility of the gas. Under typical operating conditions this resulted in a pressure drop which was comparable to the total operating pressure. Simulations of rarefied gas mixtures in the LPCVD reactor revealed significant separation effects due to pressure diffusion, especially across the wafer stack where the largest pressure gradients occurred.

A heat transfer analysis of the LPCVD reactor was next performed which accounted for thermal radiative heat transfer between the wafers, the reactor tube and the surrounding furnace, as well as conduction in the quartz tube. A Monte Carlo simulation technique was used to model the thermal radiation where the detailed spectral and directional properties of the quartz tube were taken into account. A suppression in the temperature of several wafers at each end of the wafer stack was caused by direct radiative heat loss to the cooled ends of the reactor as well as absorption of the furnace heat flux by the quartz tube. The substantial absorption of infrared radiation by the quartz and subsequent conduction away from the heated interior of the tube resulted in a nonuniform heat flux to the wafers in spite of a uniform heat output provided by the furnace. The computed wafer and quartz temperature profiles were next used as thermal boundary conditions in the DSMC simulations in order to investigate the influence of the thermal variations on the gas dynamics. The nonisothermal gas flow simulations were characterized by substantial density variations near the cooled ends of the reactor and species separation effects due to thermal diffusion for gas mixtures.

A simulation study of rarefied gas transport and film profile evolution over micron-sized features on patterned substrates was next performed. The gas transport in a localized region above the feature was treated with the DSMC method. A new profile evolution technique was developed which predicts step coverage performance as well as the microstructure of the film. The influences of gas phase collisions, surface reactivity, surface diffusion and feature geometry were investigated. The model was extended to a three-dimensional geometry for deposition over a square hole structure.

Thesis Supervisor : Dr. Klavs F. Jensen

Title : Professor of Chemical Engineering

Acknowledgments

I would like to thank IBM for funding provided through generous research grants and an IBM Graduate Fellowship award. Additional funding from ARPA is gratefully acknowledged as well.

I would also like to thank my research advisor, Klavs, for his guidance, counsel and friendship over the past few years. I have benefitted greatly from my association with him and his students.

My graduate student colleagues and research associates are an unforgettable collection of characters. Our lively discussions permeated the technical boundaries of my research efforts, enlightening me on matters from Super Bowls to sushi. I will not soon forget them.

I cannot neglect to mention my appreciation for Dick Martin and the singular influence he has had on my life. His integrity and principled example I shall always strive to emulate.

My heartfelt gratitude for my mother and father, who taught me to believe in myself and to never quit, is not possible to express in words. To them I dedicate this thesis.

Especially important to me has been the love and support of my family, Lori and Jenny. The times and places we have shared and experienced together remind me of what really matters. My life would not be complete without them.

Table of Contents

1. INTRODUCTION & BACKGROUND MATERIAL 10

1.1 Chemical vapor deposition 10

1.1.1 Fundamental concepts of chemical vapor deposition 10

1.1.2 CVD processes 11

1.1.3 Fundamental issues in CVD 19

1.1.4 Modelling and analysis of CVD processes 26

1.2 Rarefied gas dynamics 33

1.2.1 Description and overview 33

1.2.2 Analysis of rarefied gas flows 41

1.3 Thesis objectives 48

1.3.1 Motivation and theme of research 48

1.3.2 Ultra-high vacuum CVD 49

1.3.3 Heat transfer analysis of the LPCVD furnace 49

1.3.4 Nonplanar substrate CVD 50

2. THE DIRECT SIMULATION MONTE CARLO METHOD 51

2.1 General description of the DSMC algorithm 51

2.2 Initialization of a DSMC simulation study 53

2.2.1 Feasibility considerations 53

2.2.2 Generating the cell network 57

2.2.3 Setting the magnitude of the time step 60
2.3 Details of the molecular motion 63
2.3.1 The drift Maxwellian velocity distribution 63
2.3.2 Calculating the influx of molecules at open boundaries 66
2.4 Gas-surface interactions 67
2.4.1 Thermal accomodation coefficients 67
2.4.2 Reactive sticking coefficients 69
2.5 Gas phase collisions 72
2.5.1 Dynamics of binary elastic collisions 72
2.5.2 Molecular models 76
2.5.3 The time counter method 81
2.5.4 Gas phase chemistry in DSMC simulations 83
2.6 Sampling from a prescribed distribution 87
2.6.1 Pseudo-random number generators 87
2.6.2 Inversion of the cumulative probability distribution function 88
2.6.3 The acceptance-rejection method 89
2.6.4 Sampling pairs of values from the normal distribution 91
2.7 Calculation of macroscopic flow field properties 93
2.8 An example problem : heat transfer between two infinite parallel plates 94
2.8.1 Problem description 94
2.8.2 Continuum and free molecular solutions 95
2.8.3 The DSMC solution 98
2.8.4 A comparison between simulation and the exact analytical solutions 101
2.8.5 Computational notes 101
2.9 Speedup of DSMC computations 108

2.9.1 Vectorization of the DSMC algorithm 108
2.9.2 Parallelization of the DSMC algorithm 110
2.9.3 Tricks-of-the-trade 111
2.10 DSMC simulations in CVD process models 112

3. ISOTHERMAL RAREFIED GAS FLOWS IN THE LPCVD REACTOR 114
3.1 Motivation for a rarefied gas dynamics simulation model of the LPCVD reactor 114
3.2 Formulation of a simulation model of the UHV-CVD gas dynamics 115
3.2.1 Model assumptions 115
3.2.2 The DSMC cell network 117
3.2.3 Simulation of internal flows using DSMC 119
3.3 Reference simulation : isothermal flow of a pure component gas 120
3.3.1 Flow field specifications 120
3.3.2 Approach to steady state 122
3.3.3 Density and pressure variations in the LPCVD reactor 122
3.3.4 Macroscopic velocity and molecular motion 128
3.3.5 Residence time distributions in the LPCVD reactor 129
3.3.6 Statistical analysis of the UHV-CVD simulations 134
3.4 The influence of various flow parameters on UHV-CVD gas dynamics 138
3.4.1 Wafer arrangement 141
3.4.2 Outlet diameter 147
3.4.3 Inlet stream velocity 149
3.4.4 Inlet number density 151
3.4.5 Molecular species 153

3.5 Species separation effects in isothermal rarefied gas mixtures 155

3.6 Reactant flux uniformity for silane and disilane flows 160

3.7 Simulation of the transient flow associated with gas switching 164

3.7.1 The transient DSMC algorithm 164

3.7.2 Relevance to UHV-CVD technology 164

3.7.3 Purging of an isothermal N_2/H_2 flow field with pure H_2 166

3.8 Simulation of rarefied interwafer gas transport & deposition in conventional LPCVD 169

3.8.1 The interwafer simulation model 170

3.8.2 The nature of radial growth rate nonuniformity 172

3.8.3 A comparison with the continuum solution 176

3.9 Gas phase chemistry in DSMC simulations of polysilicon LPCVD 184

3.9.1 A new hybrid approach for simulating reactive rarefied gas flows 185

3.9.2 Silane decomposition kinetics 188

3.9.3 Interwafer simulations with silane gas phase chemistry 189

4. HEAT TRANSFER ANALYSIS OF THE LPCVD REACTOR 194

4.1 Motivation for a heat transfer model of the LPCVD reactor 194

4.2 Monte Carlo simulations of thermal radiation heat transfer 195

4.2.1 Photon emission 197

4.2.2 Photon-surface interactions 200

4.3 An example problem : thermal radiation heat transfer between infinite concentric cylinders 202

4.3.1 Problem description 202

4.3.2 Comparison of Monte Carlo results with the exact solution 204

4.4 Development of a Monte Carlo thermal radiation model for the LPCVD

reactor 208

4.4.1 Model description 208

4.4.2 Specification of the material properties 212

4.5 Comparison with experimental data from a commercial scale LPCVD reactor 214

4.6 Thermal analysis of a research scale LPCVD reactor 218

4.6.1 The combined effects of radiation and conduction 219

4.6.2 The influence of the wafer stack properties on the thermal profile 221

4.7 The influence of thermal variations on the UHV-CVD gas dynamics 226

4.7.1 The heating of a cold inlet stream 228

4.7.2 Thermal diffusion effects in nonisothermal gas mixtures 232

5. RAREFIED GAS TRANSPORT & PROFILE EVOLUTION IN NONPLANAR SUBSTRATE CVD 240

5.1 Modelling of nonplanar substrate CVD 240

5.2 Development of a two-dimensional simulation model for deposition over a long narrow trench or circular contact hole 242

5.2.1 Essential features of the model 242

5.2.2 Simulation of gas transport using scaled variables in the DSMC method 244

5.2.3 The modified solid-on-solid approach for the simulation of profile evolution 245

5.2.4 Modelling of reactant surface diffusion 248

5.2.5 The DSMC cell network 250

5.3 Parametric study of the two-dimensional trench problem 250

5.3.1 Nonequilibrium transport effects near the growth surface 250

5.3.2 Step coverage as a performance parameter 252
5.3.3 Effect of the reactive sticking coefficient 256
5.3.4 Effect of the surface mobility on the film microstructure 259
5.3.5 Effect of the Knudsen number 261
5.3.6 Effect of the feature aspect ratio 266
5.3.7 Effect of feature geometry : a comparison with deposition over a circular contact hole 268
5.3.8 A three-dimensional simulation of deposition over a square hole structure 268
5.4 Coupling of the microscale profile simulator with reactor scale simulations of a sputter deposition system 270
5.4.1 The Siemens sputter deposition reactor 272
5.4.2 Free molecular profile simulations 274

6. THESIS SUMMARY & PROSPECTS FOR FUTURE WORK 281
6.1 Rarefied gas flows in the LPCVD reactor 281
6.2 Heat transfer in the LPCVD reactor 282
6.3 Microscale gas flows and profile evolution 283
6.4 Prospects for future work 284
6.4.1 Reactor scale simulations of rarefied gas flows 284
6.4.2 Monte Carlo calculations of thermal radiation heat transfer 285
6.4.3 Feature scale simulations of rarefied gas flows 286

REFERENCES 288

LIST OF PUBLICATIONS 301

Chapter 1 : Introduction & Background Material

1.1 Chemical vapor deposition

1.1.1 Fundamental concepts of chemical vapor deposition

Chemical vapor deposition is one of the principle unit operations in microelectronics processing [Hitchman and Jensen, 1993]. Thin films of metals, semiconductors and insulating materials of high purity, encompassing a wide range of material properties, are routinely deposited by this process. In chemical vapor deposition, or CVD, the desired film constituents are transported in the vapor phase in a molecular precursor form to a reactive surface or substrate. The necessary chemistry is then driven by an external energy source, usually thermal energy, to accomplish the film growth which occurs on the surface.

The stringent demands placed upon the film quality coupled with the complex nature of the underlying physics and chemistry of CVD render the control and analysis of these processes very challenging. The fundamentals of all CVD processes are essentially the same, however, thus providing a framework for understanding the specific intricacies of each process. A number of required steps must take place in the deposition sequence in order to effect the film growth :

a). transport of precursor(s) to the deposition zone,

b). surface adsorption of the precursor(s),

c). transformation of the precursor(s) to film constituent,

d). incorporation of film constituent into crystal lattice (film growth),

e). desorption of reaction by-products,

f). transport of by-products away from the deposition zone.

This sequence of steps is illustrated in Figure 1-1 for a tetrahedrally coordinated precursor (*e.g.* SiH_4) decomposing on a diamond lattice substrate (*e.g.* Si). As shown in the CVD flowsheet in Figure 1-2, however, a number of conditional phenomena may occur which create a labyrynth-like network of sequential and parallel events. The combined efforts of experimentation, theoretical analysis, and numerical simulation have made significant progress towards unraveling these complexities, yet there is still much to be learned about the CVD process.

The usual approach to analysis of chemical vapor deposition has been to ignore or simplify one or more of the steps shown in Figure 1-2. This is often adequate and can provide important insight despite falling short of providing a complete picture. Indeed, some steps are justifiably removed from the scene for certain windows of operating conditions. In the following section, the various types of CVD processes encountered in microelectronics processing will be briefly reviewed and compared in the context of Figure 1-2.

1.1.2 CVD processes

Atmospheric pressure CVD

This category encompasses atmospheric pressure CVD as well as slightly reduced pressure (~ 0.1 atm) processes since the fundamental issues remain the same. Epitaxial films of silicon (Si) and compound semiconductors such as gallium arsenide (GaAs) or indium phosphide (InP) are normally grown under these conditions. Typical growth temperatures range from 1000-1200 K for Si CVD [Jasinski *et al.*, 1987] and 850-1100 K

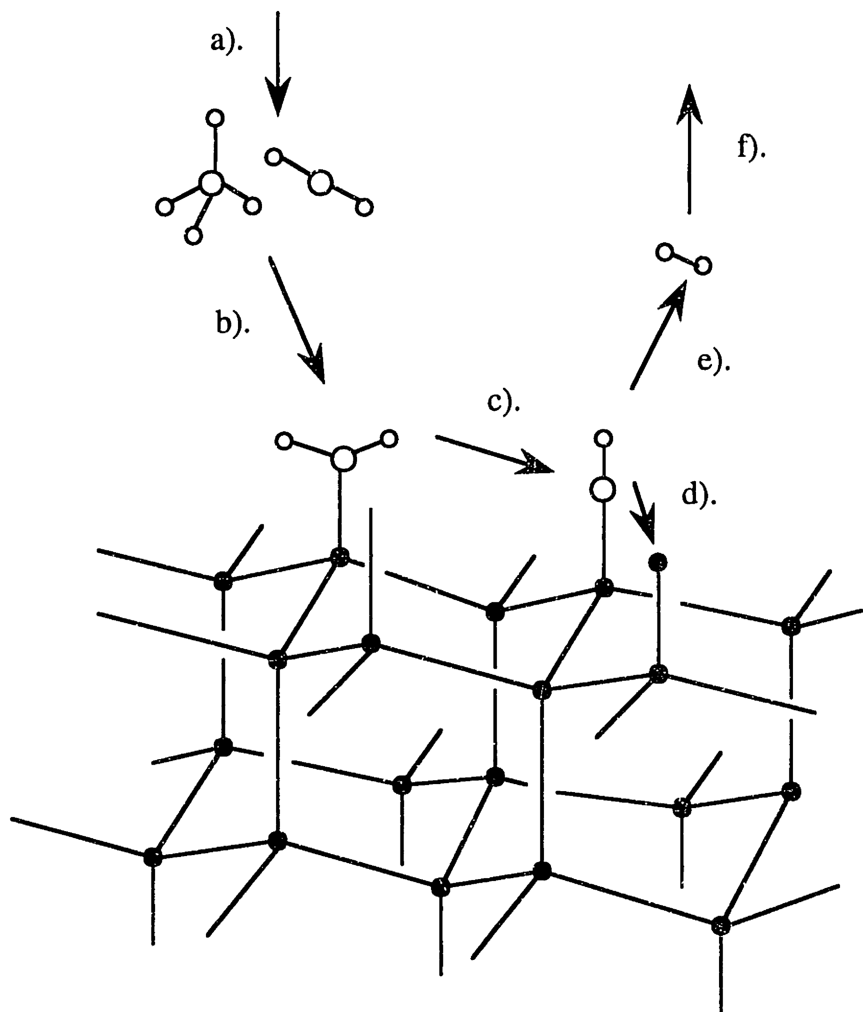

Figure 1-1 : Schematic sequence of steps involved in chemical vapor deposition.

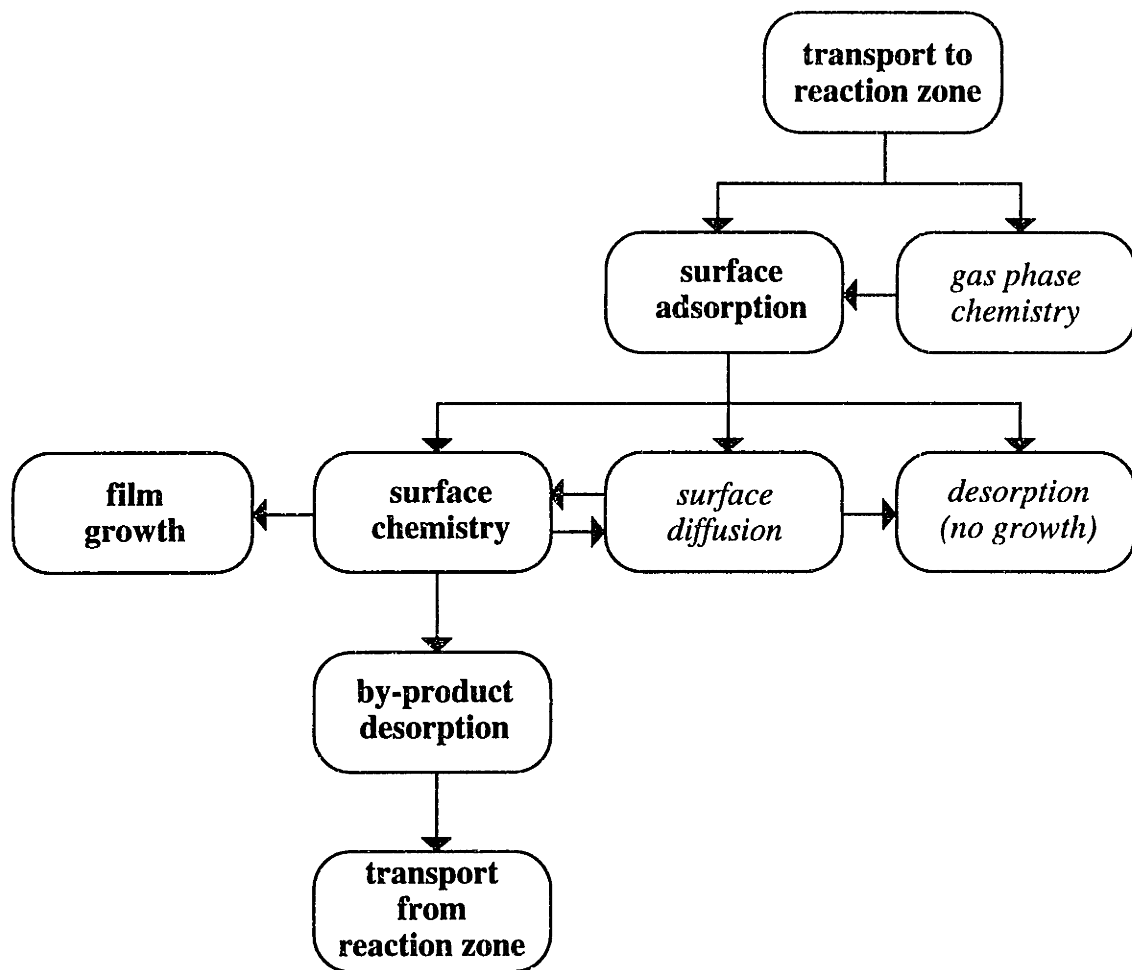

Figure 1-2 : CVD flowsheet - required step in **bold**, conditional step in *italics*.

for compound semiconductors [Kuech, 1987] where the growth rate is limited by the transport of reactants to the growth surface.

The reactor design is of critical importance in transport-limited growth. The desired goal is to achieve highly uniform and reproducible film growth with large throughput and high reactant conversion. As in most engineering feats, the obtainable results are usually a compromise where one or more of these goals are partially sacrificed. The film precursors are introduced into the reactor in dilute concentrations with a carrier gas, typically hydrogen (H_2), in order to avoid gas phase nucleation of the reactants. The substrate, containing one or more wafers, is supplied energy by contact resistance heating or external heating , *e.g.* lamps or radio frequency (RF) coils, and the reactor walls are typically cooled. The cooling serves to reduce the introduction of impurities from the walls and to minimize the premature depletion of reactants.

The CVD reactor configurations commonly employed at atmospheric pressure may be loosely categorized as horizontal and vertical flow reactors [Jensen, 1989]. The horizontal flow configurations include the classical tilted substrate horizontal reactor, used in research and for the growth of compound semiconductors, and the so-called pancake reactor employed in Si technology. The vertical flow reactors include the rotating disk reactor used in compound semiconductor growth and the multi-wafer barrel reactor, the workhorse of Si technology. All of these reactor types may simultaneously process several wafers and are schematically depicted in Figure 1-3. It should be noted that variations of these primary reactor configurations exist and optimal performance usually requires careful design of the reactor and substrate geometry, placement of the inlet(s) and selection of reactor materials.

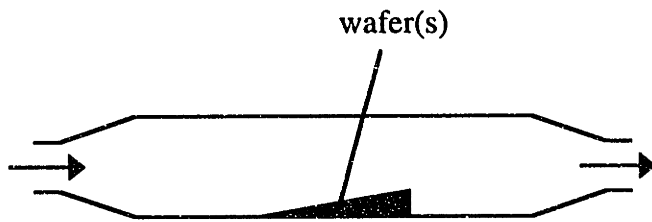

tilted substrate horizontal reactor

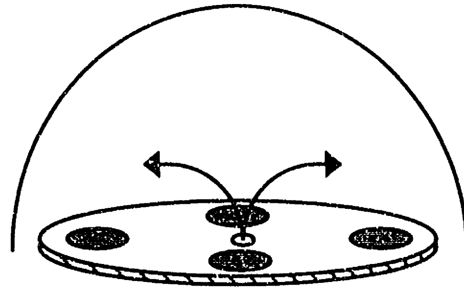

pancake reactor

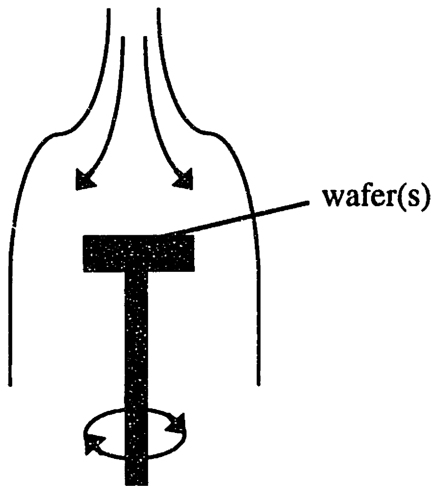

rotating disk vertical reactor

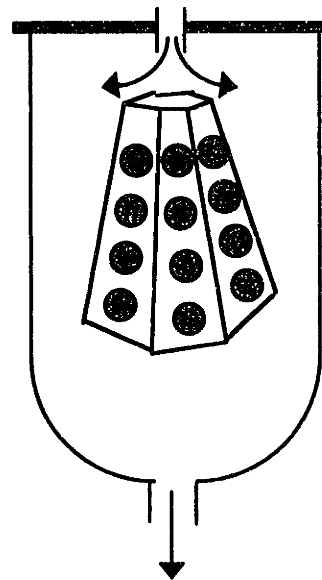

barrel reactor

Figure 1-3 : Atmospheric pressure CVD reactor types.

Low pressure CVD

Low pressure CVD (LPCVD) processes are finding increasing use in both Si and compound semiconductor technologies. The primary stimulus for this movement is the improved uniformity and greater number of wafers which can be processed relative to atmospheric pressure CVD. Traditionally, low pressure CVD is used in Si technology to deposit polycrystalline Si and dielectric films such as silicon dioxide (SiO_2) and silicon nitride (Si_3N_4) [Jensen, 1989]. At operating pressures ranging from 0.1 to a few Torr, the growth rate is usually limited by surface phenomena, *e.g.* adsorption, chemistry, or desorption, as opposed to the gas phase transport as in atmospheric pressure CVD.

The horizontal multiple-wafer LPCVD reactor, illustrated in Figure 1-4, is the predominantly used reactor type for low pressure deposition. The enhanced gas phase diffusion rates obtained at low operating pressures enable several dozen closely spaced wafers to be processed simultaneously with good uniformity. The thermal energy is supplied by thermal radiation from external resistance heaters where several constant temperature zones are used to counter depletion effects which lead to nonuniform growth along the length of the reactor. In contrast to atmospheric pressure CVD, the reactants are not diluted since gas phase nucleation is no longer a concern at these reduced pressures.

Recently, the epitaxial growth of Si has been achieved at very low pressures and temperatures with a technique referred to as ultra-high vacuum CVD, or UHV-CVD [Meyerson, 1986]. This process was pioneered by Meyerson at IBM and employs the multiple-wafer LPCVD reactor at operating pressures in the mTorr range and temperatures as low as 700 K. The lower growth temperature results in the suppression of solid state diffusion and autodoping on the surface, a major issue in conventional Si epitaxy. The benefits of operating at very low pressure include the virtual elimination of gas phase chemistry, thus avoiding nonuniform growth caused by reactive intermediates which has been known to plague conventional LPCVD growth [Meyerson *et al.*, 1986a]. The

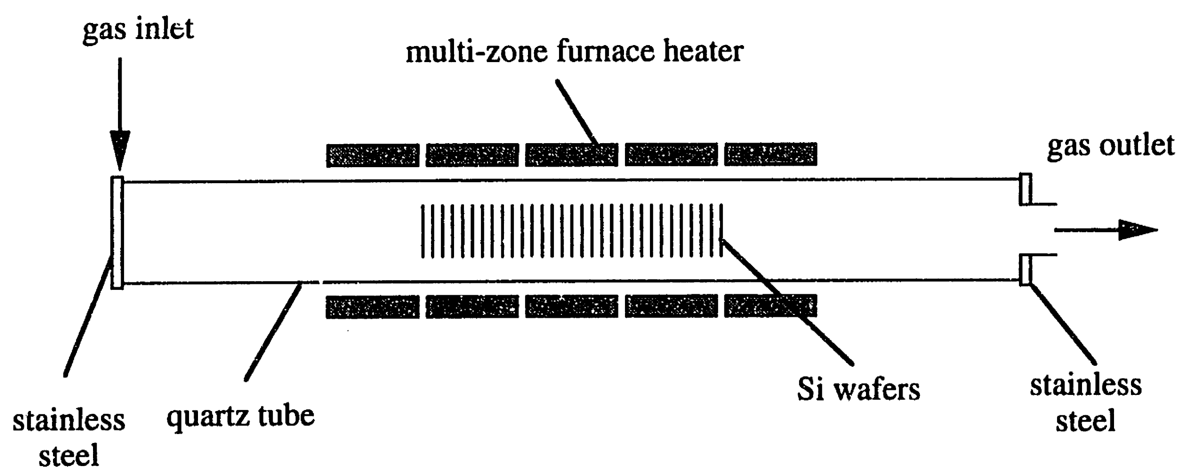

Figure 1-4 : Horizontal multiple-wafer low pressure CVD reactor.

reduced pressure operation also enables the epitaxial growth to occur at temperatures previously yielding polycrystalline Si. Thermodynamic considerations indicate that the substantially reduced partial pressures of both O_2 and H_2O in the UHV-CVD system produce an oxide-free surface which is responsible for this benefit [Meyerson *et al.*, 1986b]. The promise of this new technique is considerable as record breaking speeds for heterojunction bipolar transistors have been achieved, thus redefining the limits of Si technology [Iyer *et al.*, 1989].

Energy-assisted CVD

This category of CVD includes processes which rely upon an additional or alternate energy source in order to drive the necessary chemical reactions leading to film growth. Included in this grouping are plasma-enhanced CVD (PECVD) and laser CVD (LCVD) [Jensen, 1989]. PECVD seeks to eliminate the adverse affects of conventional thermal CVD where the high temperature environment tends to degrade previous processing steps and promote the incorporation of unwanted impurities. The use of lasers, meanwhile, enables more precise control of the chemistry and a spatially well defined deposition area.

Plasma-enhanced CVD relies upon a plasma, or glow discharge, to impart the required gas phase chemistry. The plasma, predominantly comprised of low energy (300 K) neutral and ionic species, induces molecular dissociation and electron-impact ionizations with the relatively few high energy (several eV) electrons which are present. PECVD has also been used to take advantage of the surface modification behavior of the plasma. Despite the widespread interest in the use of plasmas, a detailed understanding of its complex nature is still forthcoming.

Lasers have become increasingly useful in CVD processes. This stems from their ability to project an energy source with precise spatial and energetic control. The laser may serve as a localized thermal source in the pyrolytic decomposition of CVD precursors

where a well-defined growth pattern is achieved. This process is also referred to as laser direct-writing and holds promise, perhaps, in avoiding costly lithographic steps. The laser may also be used to photolyze selected reactant molecules, realizing further control over the CVD process. The usefulness of lasers has been tempered by their inability to attain reasonable growth rates, however, restricting their present use to specialized areas such as circuit repair and customization.

1.1.3 Fundamental issues in CVD

This section will briefly address the primary concerns in the analysis of chemical vapor deposition from a chemical engineering viewpoint. These include gas dynamics, heat and material transport and chemical kinetics issues. A more detailed account may be found in the references listed.

CVD transport phenomena

The controllable delivery of reactants to the growth surface is nontrivial in even the simplest CVD reactor configurations. The stringent requirements of CVD films are compounded by the presence of steep thermal gradients, multicomponent gas mixtures, chemical reactions and complex flow patterns.

One of the primary considerations in CVD reactor analysis is identification of the step which limits the overall film growth rate. This could be any one of the steps outlined in Figure 1-2 and depends on the processing conditions. The most influential operating parameters are the substrate temperature and total system pressure. The nature of their influence is qualitatively illustrated in the Arrhenius plot shown in Figure 1-5. The surface chemistry and the surface desorption controlled regimes are seen to be unaffected by the gas pressure.

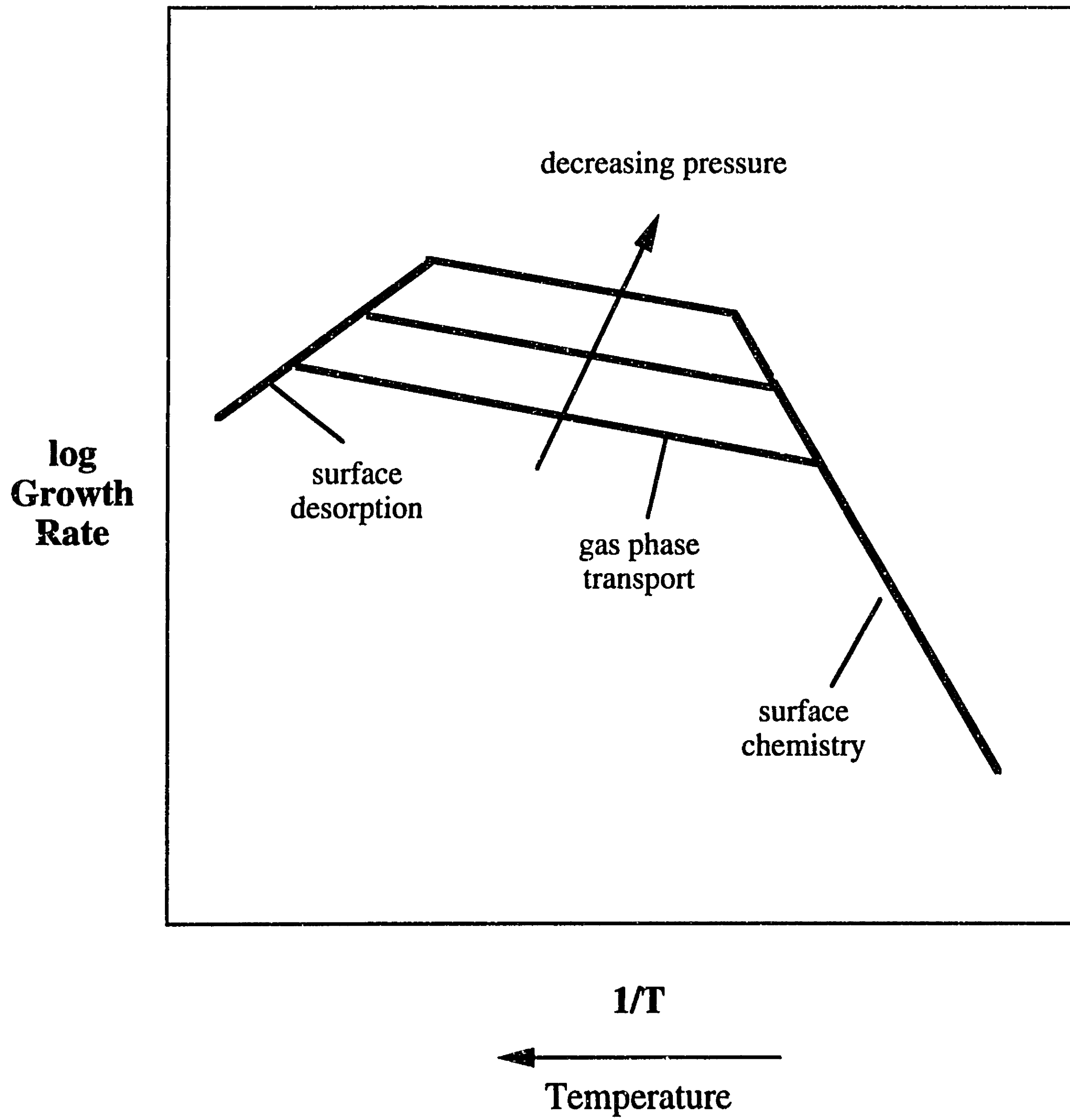

Figure 1-5 : CVD growth regimes as a function of temperature and pressure.

At low temperatures, the growth rate is limited by surface chemistry. In this regime, the details of the gas flow are not a major issue as a uniform flux of reactants to the substrate is readily obtained. Given the strong effect of temperature on the surface chemistry, however, slight temperature variations can lead to unacceptable growth rate nonuniformity. Thermal control in LPCVD reactors is an important issue since surface reactions are rate-controlling under these conditions.

For this reason it is often preferred to operate in the mass transport limited regime where the temperature sensitivity is less pronounced. Reactor design and selection of the appropriate operating conditions are critical when operating in the mass transport limited regime. A reduction in the total pressure serves to increase the film growth rate as the diffusivity of the reactant molecules in the gas phase is inversely proportional to pressure. The complex reactor geometry and sharp temperature gradients inherent in CVD reactors often lead to the formation of recirculation cells. The examples of the types of secondary flows found in CVD reactors, illustrated in Figure 1-6, suggest that careful design of the inlet and regulation of the reactor wall temperature are important considerations. More complex flow phenomena such as periodic behavior, bifurcations, transverse and longitudinal rolls and thermal diffusion have been shown to occur in CVD reactors and are usually the result of strong coupling between the fluid dynamics and heat and mass transfer [Jensen, 1989 and references therein].

Another important consideration in the analysis of CVD fluid dynamics is the particular flow regime which governs the flow. The classification of the various flow regimes is given according to the value of the Knudsen number (Kn), which is defined as the ratio of the mean free path of the molecules in the gas phase (λ) to the characteristic flow dimension (d). As the Knudsen number approaches unity, the local molecular velocity distribution may deviate considerably from the equilibrium or Maxwellian distribution. The Chapman-Enskog theory, which provides the transport coefficients used

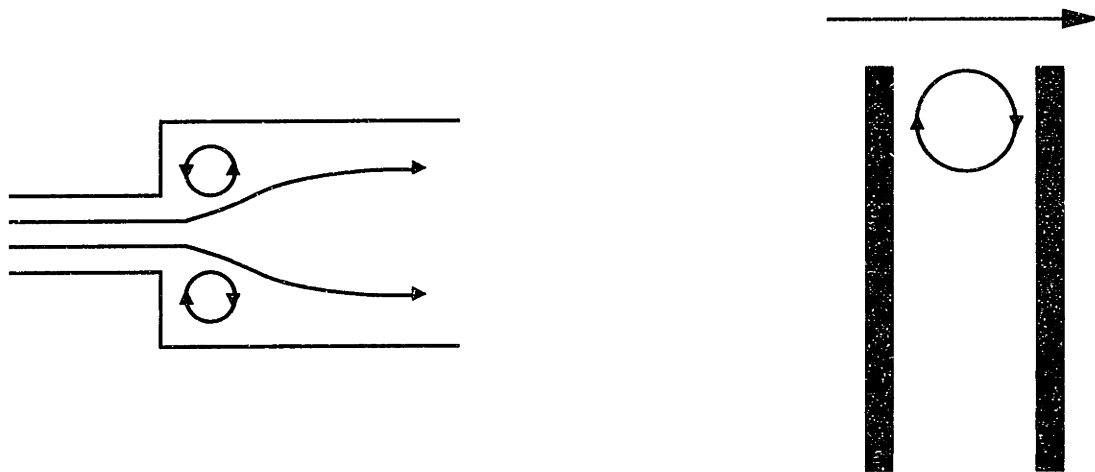
flow separation

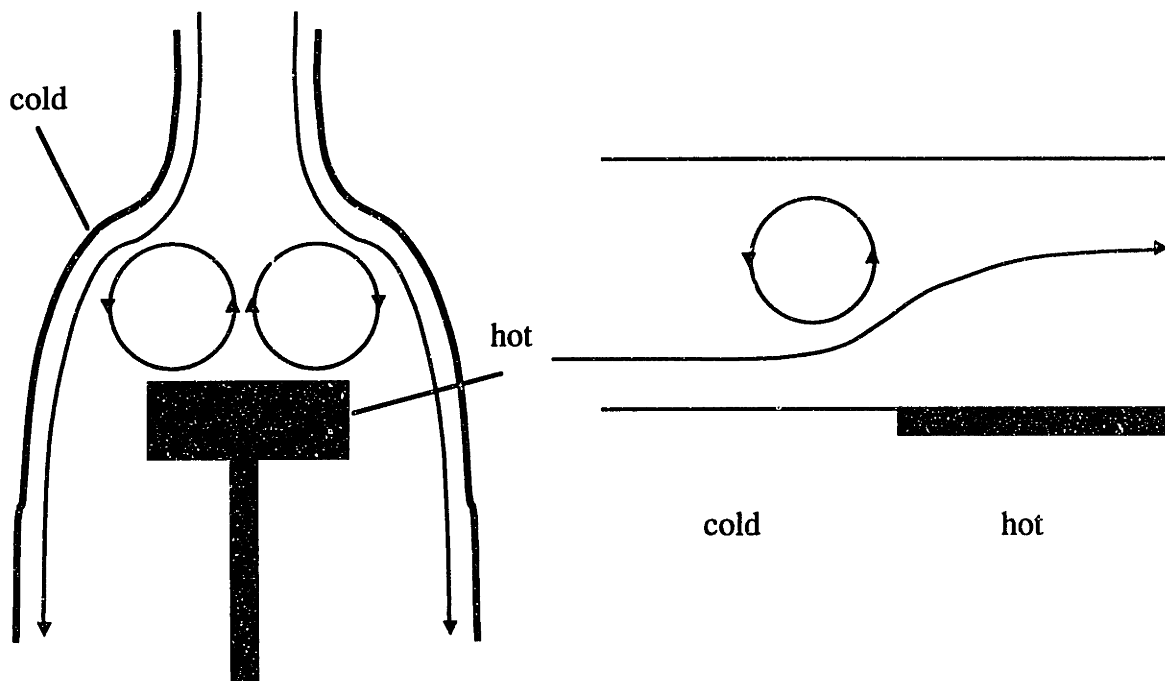

buoyancy driven recirculations

Figure 1-6 : Examples of secondary flows in CVD reactors.

in the continuum description, assumes the gas is slightly perturbed from the Maxwellian distribution. This assumption introduces a significant amount of error (~10%) at around Kn = 0.1 - the conventional demarcation between the continuum and transition regimes [G. Bird, 1988c]. The burgeoning interest in low pressure CVD (large λ) and the need to describe flows in and around microscale features (small d) have necessitated an understanding of transition and free molecular flows. The analysis of rarefied gas flows will be discussed in detail in section 1.2.

CVD chemistry

The abundance of molecular precursors imparts great versatility to the CVD process. In order to exploit this versatility, however, an understanding of the relevant chemistry is required. Although this task is nontrivial, the burden has been eased somewhat by the precedent set in combustion and heterogeneous catalysis research. The pathway to understanding CVD chemistry is the workplace of chemical kinetics and chemical reaction engineering principles.

The information that is most essential to obtaining this understanding is the reaction mechanism. Fortunately, a complete accounting of the mechanism is usually not necessary. It is often sufficient to combine several elementary reactions into one overall reaction step or to include only those reactions which are relevant to the deposition process. Once a plausible reaction mechanism has been formulated, the corresponding rate expressions are derived and the rate constants are obtained from experimental data.

In order to illustrate the approach and level of understanding regarding CVD chemistry, the chemistry of silane (SiH_4) will be presented as a case study. Silane is a commonly used precursor for Si CVD and is employed in both atmospheric pressure and low pressure deposition. The primary advantage of using silane is its low decomposition temperature relative to the chlorosilane predecessors.

It has been well established that the gas phase chemistry of silane is initiated by the unimolecular decomposition of silane to form silylene (SiH_2) and hydrogen [Meyerson *et al.*, 1986a] :

$$SiH_4 \rightarrow SiH_2 + H_2. \qquad (1\text{-}1).$$

The pressure dependence of the unimolecular rate constant varies from zero order at high pressures to first order at low pressures (*e.g.*, UHV-CVD conditions). Silane decomposition in conventional CVD typically lies in the falloff regime where some fractional dependence on the total pressure exists. Kinetic modelling of unimolecular reactions will often require the experimentally obtained rate constants to be adjusted by the RRKM method, a phenomenological model which predicts the pressure sensitive rate constant in the falloff regime where CVD chemistry frequently occurs [Moffat *et al.*, 1991].

The silylene radical is a highly reactive species and will rapidly insert into any collision partner or contribute to Si film growth with a reactive sticking coefficient (P_{rxn}) of unity. Reinsertion into a hydrogen molecule is simply the reverse reaction of (1-1) and proceeds with nearly zero activation energy [Moffat *et al.*, 1991]. The insertion of silylene into silane, however, creates the highly reactive disilane (Si_2H_6) molecule :

$$SiH_2 + SiH_4 \rightarrow Si_2H_6. \qquad (1\text{-}2).$$

The formation of higher silanes can proceed by this route and promote the undesirable onset of gas phase nucleation of Si. In addition, the presence of these highly reactive species can lead to unacceptable growth rate variations [Meyerson *et al.*, 1986a].

The usual approach to prevent gas phase nucleation has been to use dilute mixtures of silane in hydrogen. The overwhelming abundance of hydrogen serves to increase the

likelihood of reinsertion of silylene into hydrogen rather than the formation of higher silanes. An alternative approach is to use low pressure CVD where the gas phase chemistry is suppressed entirely due to the substantially reduced collision frequency of the molecules in the gas phase. The residence time in the reactor has also been shown to be a factor in determining the reaction pathway [Meyerson *et al.*, 1986a]. The presence of dead spots or recirculation cells in the reactor permit the decomposition process to proceed further. This once again underscores the importance of careful consideration in reactor design.

The unimolecular decomposition of silane and the formation of higher silanes do not represent the complete gas phase chemistry. Detailed reaction mechanisms containing 26 reactions and 17 different species have been proposed [Coltrin *et al.*, 1989]. Kinetic models have shown, however, that the reactive intermediates are present in trace quantities. Thus a much smaller subset of reactions is all that is required in order to obtain an adequate description of the gas phase chemistry.

The silicon bearing species which ultimately reaches the surface is often a distribution containing several stable and reactive silicon hydride molecules and radicals [Meyerson *et al.*, 1986a]. The subsequent surface chemistry is still not very well understood due to the difficulty of experimentally probing the reacting surface. Recent studies using secondary ion mass spectrometry (SIMS) and temperature programmed desorption (TPD) have suggested that the adsorbed silicon hydride species undergo successive elimination of atomic hydrogen [Gates *et al.*, 1990b]. The surface decomposition of silane, for example, would then consist of the following series of reactions :

$$SiH_4 + 2_ \rightarrow SiH_3^* + H^*, \quad (1\text{-}3a).$$

$$SiH_3^* + _ \rightarrow SiH_2^* + H^*, \quad (1\text{-}3b).$$

$$SiH_2^* + _ \rightarrow SiH^* + H^*, \quad (1\text{-}3c).$$

$$2\ SiH^* \rightarrow 2\ Si_{film} + H_2, \quad (1\text{-}3d).$$

where * implies an adsorbed species and _ is an available surface site. The rate-limiting step in this reaction series has been shown to be the dissociative chemisorption of silane (1-3a) at temperatures greater than 500 K which are typical of conventional CVD. This mechanism is further complicated by the experimental finding of a parallel competing reaction for adsorbed silylene which becomes important with increasing hydrogen coverage :

$$2\ SiH_2^* \rightarrow 2\ SiH^* + H_2. \quad (1\text{-}4).$$

The silane decomposition route which prevails depends strongly upon the processing conditions. As shown in Figure 1-7, the unimolecular decomposition of silane is the primary decomposition route under atmospheric pressure CVD conditions. As the pressure is lowered, the gas phase collision frequency and residence time in the reactor of silane is proportionately reduced. Thus, in LPCVD and UHV-CVD, silane molecules predominantly reach the surface intact where the reaction sequence in (1-3) takes place. The strong interplay between the processing conditions and the reaction pathways of silane is representative of many CVD systems.

1.1.4 Modelling and analysis of CVD processes

This section will briefly outline the approaches to modelling CVD processes. The complexity of CVD models ranges from simplified descriptions, such as the boundary layer

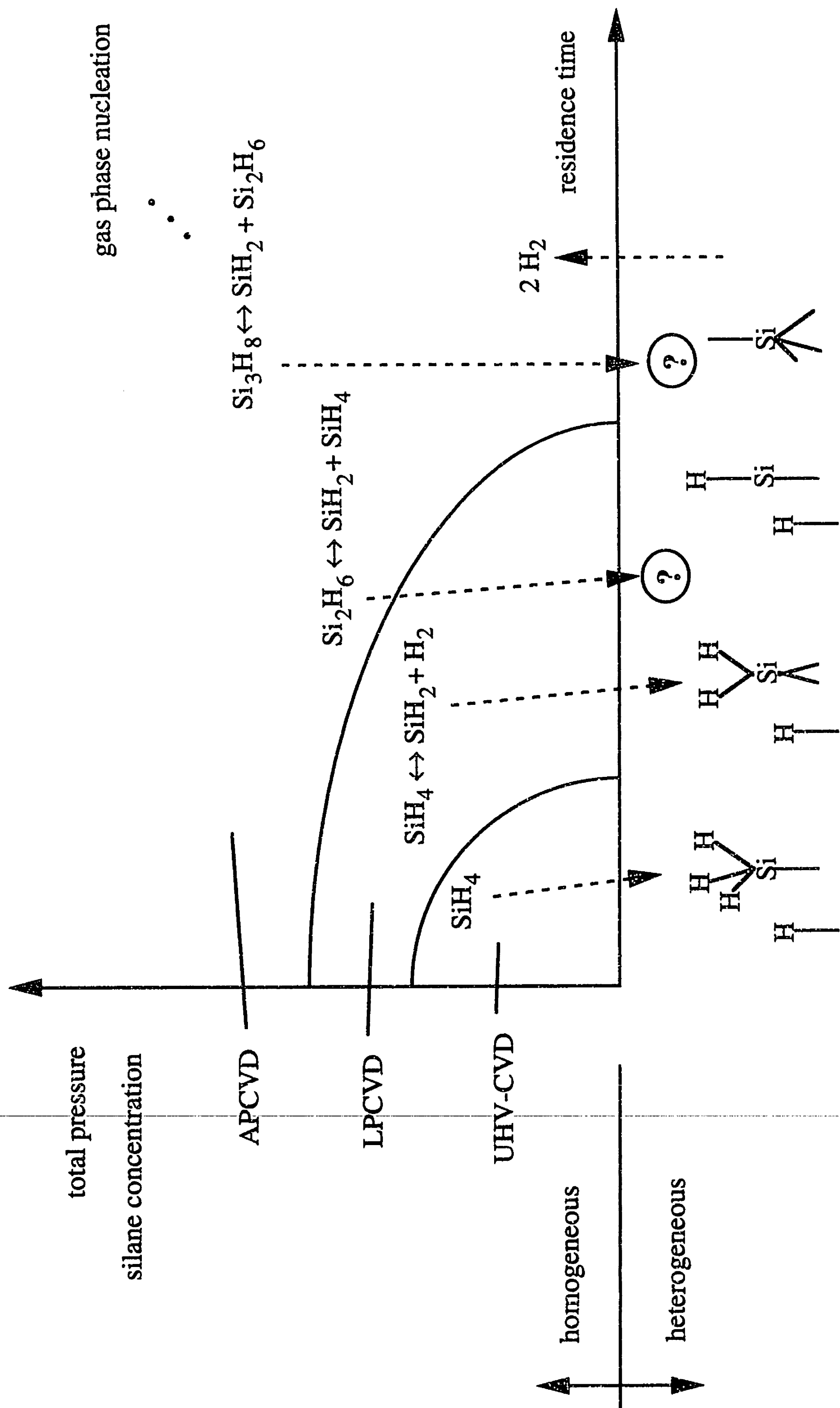

Figure 1-7 : Silane homogeneous & heterogeneous chemistry.

analysis where the physics and chemistry in the bulk of the gas phase are ignored [DeCroon and Giling, 1990], to complex three-dimensional models of the entire reactor where the fluid dynamics, heat transfer and chemistry are all interdependent [Moffat and Jensen, 1988]. The modelling approach used depends upon the level of description sought as well as the computational resources available. In most cases a continuum description of the fluid flow is appropriate. However, when the Knudsen number approaches unity a discrete particle approach must be utilized. The next section will present the governing continuum equations which form the basis of most CVD reactor models.

Fluid dynamics and heat transfer

A continuum level description of the fluid dynamics in CVD reactors usually begins with the ubiquitous Navier-Stokes equations of motion and the continuity equation [R. Bird *et al.*, 1960]. The Navier-Stokes equations are valid for laminar flow of an incompressible Newtonian fluid and may be written in vector form as :

$$\rho \left(\frac{\partial \mathbf{u}}{\partial t} + \mathbf{u} \cdot \nabla \mathbf{u} \right) = -\nabla p + \mu \nabla^2 \mathbf{u} + \rho \mathbf{g}, \qquad (1\text{-}5).$$

where ρ is the fluid density, $\mathbf{u}$ is the velocity vector, p is the pressure, μ is the fluid viscosity and $\mathbf{g}$ is the gravitational vector. The continuity equation is given by :

$$\frac{\partial \rho}{\partial t} + \nabla \cdot (\rho \mathbf{u}) = 0. \qquad (1\text{-}6).$$

The large temperature variations usually present in CVD reactors require the energy equation to be solved also. This may be written for an isobaric fluid, assuming negligible viscous heating, as :

$$\rho C_p\left(\frac{\partial T}{\partial t} + \mathbf{u}\cdot\nabla T\right) = \nabla\cdot(k\,\nabla T), \qquad (1\text{-}7)$$

where C_p is the constant pressure heat capacity, T is the temperature and k is the thermal conductivity [R. Bird *et al.*, 1960]. Also absent in equation (1-7) is the thermal energy associated with the gas phase chemistry. In most cases this may be neglected since the reactants are usually present in very dilute quantities. The Navier-Stokes equations (1-5) and the energy equation (1-7) are coupled through the temperature dependence of the density and viscosity. The temperature dependence of the density is defined through an appropriate equation of state; in most cases the ideal gas equation of state is used :

$$\rho = \frac{PM}{RT}, \qquad (1\text{-}8).$$

where M is the molecular weight of the fluid and R is the universal gas constant. The viscosity temperature dependence is normally provided by experimental data or an appropriate molecular theory [Hirschfelder *et al.*, 1954].

Most CVD flows consist of a small amount of the reactant species (< 5%) with the balance comprised of the carrier gas, usually H_2. This enables the fluid properties in the governing equations to be approximated as those of the carrier gas alone. Furthermore, this allows the solution of the fluid flow and heat transfer problem to be independent of the transport and chemistry of the reactant species. The reactant transport equations will be considered next.

Reactant mass transport

The primary aim of CVD reactor modelling is to achieve controllable transport of reactants to the growth surface. Once the fluid dynamics and heat transfer problems have been solved as outlined above, the problem of mass transport of the reactant species may be addressed. In the event that multiple species contribute to the film growth, separate equations must be formulated and solved for each of the participating species. The reactant transport equation is balanced by convection, diffusion and chemical reaction :

$$\frac{\partial c_r}{\partial t} + \nabla \cdot (c_r \mathbf{u}) = \nabla \cdot c\, D\, \nabla x_r + R_r, \qquad (1\text{-}9).$$

where c_r and x_r are the reactant concentration and mole fraction, respectively, c is the total concentration, D is the diffusivity and R_r represents the reaction terms which may generate or consume the reactant [R. Bird *et al.*, 1960].

Thermal diffusion effects may also be important in CVD flows due to the disparity of molecular weights and the presence of large thermal gradients [R. Bird *et al.*, 1960]. This phenomenon usually results in the repulsion of the heavier species away from high temperature zones. Thermal diffusion is often included in CVD reactor modelling and the diffusion term in equation (1-9) is modified accordingly :

$$\ldots \nabla \cdot c\, D\, (\, \nabla x_r + k_T\, \nabla \ln T\,) \ldots \qquad (1\text{-}10).$$

where k_T is the thermal diffusion ratio.

Rarefied gas dynamics

Rarefied gas dynamics is becoming an increasingly important issue in CVD reactor analysis. The trend towards low pressure operation has underscored the need for alternatives to the conventional continuum-based models in cases where the mean free path approaches the dimensions of the reactor. At the same time, the ever shrinking device feature size has also necessitated the same considerations in microscale flow descriptions where the characteristic flow dimension is on the order of a micron.

In both cases, there have been two distinct approaches to dealing with the issue of rarefied gas flows in CVD processes. The more common of the two has been to cling to the familiar continuum equations with modifications made to the transport properties or boundary conditions. This approach has met limited success and, in general, becomes more inaccurate as the Knudsen number is increased. The second approach has been to employ a discrete particle model where the particulate nature of the gas is recognized. These models typically take the form of Monte Carlo simulations and have the advantage of being able to employ more detailed physics than continuum models. However, the most serious drawback of Monte Carlo simulations has always been the computational inefficiency relative to the efforts required to solve continuum-based model equations. The advancements in rarefied gas analysis have followed the efforts to overcome this inefficiency.

The problem of deposition in a micron-sized trench has been addressed with both of these approaches and thus will be presented in order to compare and discuss the advantages and shortcomings of each. The continuum-based approach to this problem was accomplished by Raupp and Cale [Raupp and Cale, 1989]. In their model, a one-dimensional reaction-diffusion equation is used to describe the transport and deposition of a single reactant species within the trench. The gas is considered to be isothermal and lateral concentration gradients are presumed negligible in the model. The diffusivity of the

reactant species is estimated as the Knudsen diffusivity for a molecule in a finite length tube. A pseudo steady-state approach is used for the reactant transport and the trench walls are locally advanced at discrete intervals.

The advantage of this approach is that a great deal of parameter space may be explored in an effort to understand the relationships between the various parameters. This asset is somewhat tempered, though, by the very same assumptions which make it possible. The formulation of the Knudsen diffusivity and the neglect of lateral variations within the trench do not appear to have been properly justified. In addition, the model does not take into account the likely presence of additional reactive species or possible interactions with other species, *e.g.* multicomponent diffusion, gas phase chemistry. No comparison with experimental results was offered in their study.

The discrete particle approach to this problem was presented by Ikegawa and Kobayashi [Ikegawa and Kobayashi, 1989]. In their model, the direct simulation Monte Carlo (DSMC) method was used to simulate the gas phase motion and interactions of the molecules and a string model [Neureuther *et al.*, 1980] was used to simulate the film growth by advancing the surface in discrete segments based on the local flux. The DSMC routine consisted of specifying the gas composition, density and temperature at a boundary above the trench. Simulated molecules were then allowed to enter across this boundary and move about in the two-dimensional region which defined the trench. Gas phase collisions were included when necessary and a finite sticking probability was assigned to the reactive molecules which impinged upon the trench surface.

The model was shown to give fairly good comparison with experimental results for both sputter deposition and plasma CVD. The biggest drawback, besides the probable long computational time required for this study, appeared to be the use of the string model to simulate the growth of the film. The advancement of the surface in discrete line segments produced an unrealistic film profile at the trench corners. The advancing segments also

appeared to interfere with the normal execution of the DSMC routine as the cell network, which makes up the simulation zone, was distorted with each advancement.

The analysis of rarefied gas dynamics is only now emerging as an important component of CVD reactor engineering. This is in contrast with the aerospace industry where a vast amount of research has been undertaken and numerous computational methods have been developed to study rarefied gas flows for well over three decades. In the same way that the efforts in combustion chemistry and heterogeneous catalysis have paved the way for understanding CVD chemistry, the precedent set in aerospace research may do likewise for rarefied gas flows in CVD. In the spirit of this lesson, an exhaustive survey of the aerospace literature was performed in the initial stages of this research. The next section will give a brief review of the essential findings of this survey.

1.2 Rarefied gas dynamics

1.2.1 Description and overview

Nearly fifty years ago H.S. Tsien alerted the scientific community to a relatively unchartered branch of fluid dynamics, characterized by the molecular mean free path being comparable to or much greater than the characteristic flow field dimension [Tsien, 1946]. This field of study shortly came to be referred to as *rarefied gas dynamics*. The distinguishing feature of rarefied gas analysis is the requirement that the particulate nature of the gas be recognized as a basis for understanding and theoretical development. The kinetic theory of gases, embodied in the Boltzmann equation, has thus served as the foundation for the development of predictive theoretical models for rarefied gas analysis.

For this reason the logical starting point is a discussion of the Boltzmann equation itself. The first section below will discuss the essential details of the Boltzmann equation. This will be followed by a derivation of the continuum-based conservation equations from the Boltzmann equation, making special note of the conditions under which the continuum formulation is valid. The connection to the Navier-Stokes equations (1-5) will also be established through the use of the Chapman-Enskog theory.

The Boltzmann equation and the kinetic theory of gases

The Boltzmann equation is the fundamental equation of the kinetic theory of gases. Therefore, it is instructive to first consider the underlying assumptions of kinetic theory, outlined here for a system of rigid hard spheres. The kinetic theory of gases is based on three primary assumptions :

a). the gas consists of a large number of particles of mass m and diameter d,

b). the size of the particles is negligible compared to the particle separation,

c). the particles interact as perfectly elastic hard spheres, exhibiting no long range interactions.

The consequence of the large number of particles suggested in assumption a) is that the theory is statistical in nature and invokes the concepts of particle probability distributions. Assumption b) leads to the so-called dilute gas approximation which restricts the particle interactions to binary collisions. The system of particles may then be completely described by the single particle distribution function.

The Boltzmann equation is simply the conservation equation of the single particle distribution function, $\mathcal{F}(\mathbf{c},\mathbf{r},t)$, where $\mathbf{c}$ and $\mathbf{r}$ are the phase space variables of velocity and position and t is the time variable. The single particle distribution function is defined by the relation $dN = \mathcal{F}(\mathbf{c},\mathbf{r},t)\, d\mathbf{c}\, d\mathbf{r}$ where dN is the number of particles in the phase space element $d\mathbf{c}d\mathbf{r}$ at time t with velocities ranging from $\mathbf{c}$ to $\mathbf{c} + d\mathbf{c}$ and positions ranging from $\mathbf{r}$ to $\mathbf{r}$ +

dr. The steady-state single particle distribution is then related to the velocity distribution f(**c**), a quantity which will be referred to frequently in later sections, by n(**r**)f(**c**) = $\mathcal{F}$(**c**,**r**) where n is the particle number density.

The stage is now set for the Boltzmann equation which is actually a simplification of the most fundamental equation of nonequilibrium statistical mechanics, the Liouville equation - the 6N Hamiltonian equations of motion of an N-body system [McQuarrie, 1976]. The Boltzmann equation may be written as :

$$\frac{\partial \mathcal{F}}{\partial t} + \mathbf{c}\cdot\frac{\partial \mathcal{F}}{\partial \mathbf{r}} + \mathbf{F}\cdot\frac{\partial \mathcal{F}}{\partial \mathbf{c}} = \int_{-\infty}^{\infty}\int_{0}^{4\pi} (\mathcal{F}^{*}\mathcal{F}_1^{*} - \mathcal{F}\mathcal{F}_1) c_r \sigma d\Omega d\mathbf{c}_1, \qquad (1\text{-}11).$$

where **F** represents any external body forces (*e.g.* gravity), c_r is the relative velocity between molecules of class **c** and $\mathbf{c}_1$ given by ($\mathbf{c}$-$\mathbf{c}_1$), σ is the differential collision cross-section, and dΩ is the differential solid angle.

The first term on the left-hand side of equation (1-11) represents the rate of change of particles of class **c** in the phase space element d**c**d**r**. The second term on the left-hand side is a convection term, representing the net outflow of class **c** particles from the element due to the velocity, **c**. The external force term may be safely neglected for neutral rarefied gases, but represents an important contribution in the description of charged gaseous plasmas [Hess and Graves, 1989]. The single term on the right-hand side is the collision term and represents the rate of increase of particles of class **c** due to intermolecular collisions.

Once the distribution function $\mathcal{F}$ is known, the macroscopic properties of the gas may be readily determined. For a steady-state distribution, $\mathcal{F}$(**c**,**r**) :

$$n \equiv \int_{-\infty}^{\infty} \mathcal{F}(\mathbf{c},\mathbf{r})\, d\mathbf{c}, \qquad (1\text{-}12a).$$

$$T \equiv \frac{m}{3k_B} \int_{-\infty}^{\infty} c'^2\, \mathcal{F}(\mathbf{c},\mathbf{r})\, d\mathbf{c}, \qquad (1\text{-}12b).$$

$$P_{ij} \equiv m \int_{-\infty}^{\infty} c'_i\, c'_j\, \mathcal{F}(\mathbf{c},\mathbf{r})\, d\mathbf{c}, \qquad (1\text{-}12c).$$

where n, T, and P_{ij} are the number density, temperature, and stress tensor component, respectively, and k_B is the Boltzmann constant. The quantity c' represents the peculiar or thermal velocity of the particles which is defined as $c'_i \equiv (c_i - u_i)$ where u_i is the ith component of the macroscopic stream velocity; for a stationary gas, $\mathbf{c}'=\mathbf{c}$. Another important and useful relation given by the kinetic theory of gases is the ideal gas equation of state which relates the gas pressure to the number density and gas temperature :

$$p = k_B n T. \qquad (1\text{-}13).$$

Attempts to solve the Boltzmann equation, a highly nonlinear integral-differential equation, have focussed on simplifications to the collision term as will be discussed in section 1.2.2. The next section will establish the connection between the microscopic description offered by the Boltzmann equation and the continuum-based conservation equations.

The continuum approximation

The average of a property Q associated with a single molecule may be obtained by integrating the product $Qf(\mathbf{c})$ over all of velocity space :

$$\overline{Q} \equiv \int_{-\infty}^{\infty} Qf(\mathbf{c})\, d\mathbf{c}. \qquad (1\text{-}14).$$

The average property $\overline{Q}$, a macroscopic gas property, is referred to as a moment of the velocity distribution, f(**c**) [G. Bird, 1976]. In a similar fashion, a moment of the Boltzmann equation for Q yields the conservation equation for the macroscopic property, $\overline{Q}$, written here without the details of the integration (*c.f.* G. Bird,1976) :

$$\frac{\partial}{\partial t}(n\overline{Q}) + \nabla\cdot(n\overline{\mathbf{c}Q}) - n\mathbf{F}\cdot\overline{\frac{\partial Q}{\partial \mathbf{c}}} = \Delta[Q], \qquad (1\text{-}15).$$

where $\Delta[Q]$ is referred to as the *collision integral.* If Q is either the mass m, the momentum m**c**, or the energy $\frac{1}{2}mc^2$ of a molecule, then the collision integral vanishes [G. Bird, 1976], and one is left with the continuum equations of conservation of mass, momentum, and energy :

$$\frac{\partial \rho}{\partial t} + \nabla\cdot(\rho\mathbf{u}) = 0, \qquad (1\text{-}16).$$

$$\rho\left(\frac{\partial \mathbf{u}}{\partial t} + \mathbf{u}\cdot\nabla\mathbf{u}\right) = -\nabla p + \nabla\cdot\tau + \rho\mathbf{F}, \qquad (1\text{-}17).$$

$$\rho\left(\frac{\partial E}{\partial t} + \mathbf{u}\cdot\nabla E\right) = -p\nabla\cdot\mathbf{u} + \Phi - \nabla\cdot\mathbf{q}, \qquad (1\text{-}18).$$

where the new variables introduced include the macroscopic stream velocity, **u**, the viscous stress tensor, τ, the energy per unit mass, E, the dissipation function, Φ, and the heat flux

vector, $\mathbf{q}$. The dissipation function represents the irreversible degradation of mechanical to thermal energy and is usually important only for high speed flows [R. Bird *et al.*, 1962].

These equations are valid for *any* pure component gas but do not represent a closed set of equations without additional relations among various quantities. These relations are provided by the Chapman-Enskog method which provides a solution of the Boltzmann equation for the case where the velocity distribution function is slightly perturbed from the equilibrium Maxwellian form [Chapman and Cowling, 1970]. The primary assumption underlying the Chapman-Enskog theory is that the velocity distribution may be written in the form of a power series as :

$$f = f_o + Kn\, f_1 + Kn^2\, f_2 + Kn^3\, f_3 + \ldots \qquad (1\text{-}19).$$

where Kn is the Knudsen number, defined as the ratio of the mean free path of the gas molecules (λ) to the scale length over which appreciable gradients in the macroscopic variables occur. This length scale usually coincides with the characteristic flow dimension such as the diameter of a tube for internal gas flows or the nominal size of an object immersed in a flow field for external flows. The quantity f_o is the Maxwellian velocity distribution and is given by :

$$f_o = \sqrt{\frac{m}{2\pi k_B T}}\, \exp\left(\frac{-\, mc'^2}{2k_B T} \right) \qquad (1\text{-}20).$$

The expansion in equation (1-19) may be written in an alternative form as :

$$f = f_o \left\{ 1 + \phi_1(Kn) + \phi_2(Kn^2) + \phi_3(Kn^3) + \ldots \right\}. \qquad (1\text{-}21).$$

The first-order solution, given by the equilibrium Maxwellian distribution f_o, leads to the Euler equations of inviscid flow :

$$\rho\left(\frac{\partial \mathbf{u}}{\partial t} + \mathbf{u}\cdot\nabla\mathbf{u}\right) = -\nabla p + \rho\mathbf{g}. \qquad (1\text{-}22).$$

The second-order solution, given by $f = f_o(1+\phi_1)$, gives a distribution function of the form [Chapman and Cowling, 1970] :

$$f = f_o\left(1 - \frac{\kappa m^2}{\rho(k_B T)^2}\left(\frac{c'^2 m}{5k_B T} - 1\right)\mathbf{c}'\cdot\frac{\partial T}{\partial \mathbf{r}} - \frac{\mu m^2}{\rho(k_B T)^2}\mathbf{c}'\mathbf{c}':\frac{\partial \mathbf{u}}{\partial \mathbf{r}}\right), \qquad (1\text{-}23).$$

where the coefficients of viscosity, μ, and thermal conductivity, κ, are introduced. By substituting this expression for the velocity distribution into the Boltzmann equation and taking the moment of the momentum mc, the Navier-Stokes equations are derived :

$$\rho\left(\frac{\partial \mathbf{u}}{\partial t} + \mathbf{u}\cdot\nabla\mathbf{u}\right) = -\nabla p + \mu\,\nabla^2\mathbf{u} + \rho\mathbf{g}, \qquad (1\text{-}24).$$

as written previously in equation (1-5). The third order solution, $f = f_o(1+\phi_1+\phi_2)$, leads to a complicated set of equations referred to as the Burnett equations. The inclusion of ϕ_2 in the series expansion might be expected to allow the continuum approximation to be utilized at higher Knudsen numbers. However, the Burnett equations have been shown to give diminished agreement with experimental data at the upper Knudsen limits of the Navier-Stokes equations [G. Bird, 1976; McQuarrie, 1976]. This may be due to the breakdown of the validity of the assumed form of the distribution function (equation 1-21) at higher values of the Knudsen number. Nevertheless, the power of the Chapman-Enskog theory

has been shown to be its ability to provide a link between the microscopic and macroscopic approaches as well as to provide analytical expressions for the transport properties.

The validity of the Chapman-Enskog approach hinges on the assumption that the perturbation parameters are much less than unity. For the Navier-Stokes equations to be valid, this then requires that ϕ_1 is much less than unity. The physical implications of this requirement were elegantly illustrated by Bird for the special case where the macroscopic stream velocity is in the x-direction and gradients exist only in the y-direction [G. Bird, 1976]. For a simple gas composed of hard spheres, equation (1-23) may then be rewritten as :

$$f = f_o \left\{ 1 - \frac{15}{16} \sqrt{\pi} \, \frac{v'}{v_m} \left(\frac{c'^2}{v_m^2} - \frac{5}{2} \right) \frac{\lambda}{T} \frac{dT}{dy} - \frac{5}{4} \sqrt{\pi} \, \frac{u'v'}{v_m^2} \, \frac{s\lambda}{u} \, \frac{du}{dy} \right\}, \quad (1\text{-}25).$$

where u' and v' are the x and y components, respectively, of the thermal velocity $\mathbf{c}'$, v_m is the most probable thermal speed ($v_m \equiv \sqrt{2k_BT/m}$), λ is the mean free path, u is the stream velocity, and s is the speed ratio ($s \equiv u/v_m$). Since the thermal velocity components u' and v' are on the order of v_m, it is seen that λ should be small in comparison to the scale length of the temperature gradient and the product $s\lambda$ should be small in comparison to the scale length of the velocity gradient.

In many cases it is appropriate to equate the scale length of the gradients with the characteristic dimension of the flow. The Knudsen number may then be defined as the ratio of the mean free path to the characteristic dimension. If the flow is characterized by sharp gradients in the flow properties, however, then the specification of the scale length will not necessarily coincide with the characteristic dimension of the flow field. The classical example where this applies is the shock wave. In this case the scale length of the gradients, in the vicinity of the shock, is given by the thickness of the shock wave itself. A

continuum description may accurately describe the regions upstream and downstream of the shock wave, yet completely fail to provide an adequate description of the structure of the shock [Nanbu and Watanabe, 1984]. Another example where this may also be the case is the boundary layer region adjacent to the growth surface in CVD reactors where extremely sharp thermal and concentration gradients are present [Fotiadis *et al.*, 1990]. The next section will review the various approaches to analyzing rarefied gas flows.

1.2.2 Analysis of rarefied gas flows

The Chapman-Enskog theory was presented as a means of relating the molecular level description of a gas given by the kinetic theory of gases to the familiar continuum-based descriptions such as the Navier-Stokes equations. The higher-ordered continuum formulation known as the Burnett equations, presumably more accurate than the Navier-Stokes equations for large Knudsen number flows, gives a more difficult set of equations to solve without a corresponding improvement in the description of the gas. In the absence of an adequate continuum description of high Knudsen number flows, rarefied gas analysis has been primarily based upon a molecular level description of the gas. The following sections will briefly review the two main approaches to rarefied gas analysis which may be categorized as theoretical or mathematical models and computer simulation models. In addition, a brief discussion of the use of modified boundary conditions as a means of extending the useful range of the continuum approach to higher Knudsen number flows is included.

Theoretical rarefied gas analysis

The common feature of the various approaches which are labelled as theoretical or mathematical models is that the starting point is the Boltzmann equation. Each then

employs various simplifications which circumvent the usual mathematical intractability of the Boltzmann equation. Most prominent among these is the BGK equation [Bhatnagar, Gross and Crook, 1954] which simplifies the collision term :

$$\frac{\partial \mathcal{F}}{\partial t} + \mathbf{c}\cdot\frac{\partial \mathcal{F}}{\partial \mathbf{r}} + \mathbf{F}\cdot\frac{\partial \mathcal{F}}{\partial \mathbf{c}} = \upsilon\,(\mathcal{F}_0 - \mathcal{F}), \tag{1-26}$$

where $\mathcal{F}_0$ is the equilibrium distribution and υ is generally regarded as a collision frequency but is assumed to be independent of the velocity **c**. The essential feature of the BGK equation is the assumption that the average effect of intermolecular collisions is to change the distribution function by an amount proportional to its departure from equilibrium. Various modifications of the BGK equation have been introduced. Included among these are a velocity dependent collision frequency $\upsilon(\mathbf{c})$, an important consideration for high velocity flows [Cercignani, 1988]. Also, the use of an additional adjustable parameter has been used in the BGK equation which results in the same moment-derived Navier-Stokes equations as the full Boltzmann equation [Cercignani, 1988].

Another approach which has been successful for the specialized problem of determining the structure of a one-dimensional shock wave is the Mott-Smith method [Mott-Smith, 1951]. This method assumes that the distribution function in a shock wave is a weighted combination of the upstream and downstream Maxwellian distributions. The Mott-Smith method has been found to be inadequate for describing weak shock waves but has been surprisingly successful at predicting the thicknesses of strong shock waves [G. Bird, 1976].

An alternative simplification to the Boltzmann equation is to discretize velocity space into a finite number of discrete points [Broadwell, 1964]. A set of n simplified Boltzmann equations may then be written for the n discrete velocities :

$$\frac{\partial N_j}{\partial t} + \mathbf{c}_j \cdot \nabla N_j = G_j - L_j, \qquad j=1,\ldots,n \qquad (1\text{-}27).$$

where N_j is the number of molecules with velocity $\mathbf{c}_j$ and G_j and L_j represent the gain and loss terms due to intermolecular collisions. The Boltzmann equation is then reduced to a set of coupled nonlinear first-order differential equations. The concept of discretizing the independent variables of the Boltzmann equation is taken a step further in the approach referred to as cellular automata which will be discussed in the next section concerning simulation techniques.

A more rigorous approach for solving the Boltzmann equation which essentially involves no simplifications to the collision term is the method first introduced by Nordsieck and Hicks [Nordsieck and Hicks, 1967]. In their method, a Monte Carlo simulation technique is used to solve the integral over the collision term while a finite difference approach is used for the remaining terms in the Boltzmann equation. This method is restricted, due to computational limitations, to one-dimensional steady flows and requires an initial guess of the distribution function over the entire flow field. Furthermore, the discretization of the velocities may result in a systematic buildup of error in the solution and must be kept in check with a correction procedure which ensures that the conservation laws are not violated [G. Bird, 1976].

Simulation of rarefied gas flows

The mathematical difficulty associated with obtaining a solution of the Boltzmann equation has provided the impetus for the development of computer simulation techniques for analyzing rarefied gas flows [G. Bird, 1978]. These differ from the mathematical approaches outlined above in that they are not based on a mathematical equation which

describes the flow, but are derived directly from knowledge of the molecular level interactions of molecules with each other and with solid surfaces.

Molecular dynamics is a powerful simulation technique which is applicable to high density rarefied gas flows where the mean free path, characteristic dimension and molecular size are all of the same order [Allen and Tildesley, 1987]. Clearly this precludes the use of the Boltzmann equation or other concepts of kinetic theory for the analysis of these types of flows as the dilute gas assumption no longer applies. Examples of gas flow systems where molecular dynamics would apply include the study of flow through narrow channels or micropores [Mo and Rosenberger, 1990] and gas-surface interaction studies [Matsumoto and Matsui, 1990]. The molecular dynamics technique calculates the phase space trajectories of an ensemble of molecules whose interactions are governed by a specified intermolecular potential function. The equations of motion for each molecule are integrated over time, with the force exerted on each molecule being given by the sum of the spatial gradients of the intermolecular potential between all other molecules. A molecular dynamics calculation is completely deterministic once the initial positions and velocities are randomly assigned. However, the restriction to high density gas flows and the relatively expensive computational requirements limit the use of molecular dynamics simulations for the study of rarefied gas flows [G. Bird, 1978].

Cellular automaton or lattice gas automaton is an approach to simulating fluid dynamics that is still in its infancy [Hasslacher, 1987]. The fluid is approximated as an ensemble of particles which hop along the sites of a lattice structure. The lattice consists of a hexagonal arrangement of sites such that the fluid particles may move in one of six possible directions. The collision dynamics and boundary conditions are programmed into each site in a manner which allows the computation to completely avoid floating point operations and, instead, rely exclusively on Boolean operations. In addition, the structure of the algorithm is well-suited for exploiting the benefits of multiple processor computers.

This holds great promise for the possibility of analyzing complex flows at a fraction of the computational expense that would be required of other numerical approaches. The current level of detail of cellular automata models, where the fluid is comprised of identical particles moving at the same speed, only gives qualitative agreement with more rigorous and computationally intensive numerical approaches [Hasslacher, 1987].

The test particle Monte Carlo method first introduced by Davis remains a powerful technique for simulating collisionless flows [Davis, 1960]. In this approach a large number of simulated molecules are generated in a serial fashion and followed through successive surface collisions until exiting the flow domain. The test particle method was later extended by Haviland to take into account intermolecular collisions for transition regime flows [Haviland, 1965]. This approach then involves an iterative procedure where an initial guess of the target gas velocity distribution is required and subsequently modified after each cycle of trajectories is generated. The iteration continues until there is no significant difference between the target and incident distributions from cycle to cycle.

The use of the test particle method for the simulation of transition regime flows has been entirely supplanted by the direct simulation Monte Carlo (DSMC) method pioneered by Bird [G. Bird, 1963]. This approach differs from the test particle methods in that the trajectories of several tens of thousands of simulated molecules are followed simultaneously. This in turn circumvents the need to iterate over several runs since the distribution function is implicitly solved for as the steady-state flow field is established. The DSMC method has emerged as the premier technique for simulating transition regime flows and will be reviewed extensively in Chapter 2.

Modified boundary conditions for the continuum equations

The continuum equations (Euler, Navier-Stokes, Burnett, *etc.*) typically employ the no slip boundary conditions which state that the velocity and temperature of the gas at the

wall are equal to the corresponding values of the wall itself. Maxwell was the first to note that those conditions are approximate and that the velocity slip and temperature jump may be significant in some cases [Maxwell, 1879]. Grad later pointed out that the continuum equations are valid at distances from the surface considerably greater than the mean free path [Kogan, 1973].

The convergence of the series given in equation (1-21) is not uniform in space and it has been shown that an error of order Kn may be expected in a thin region (~λ) near the surface known as the Knudsen layer [Kogan, 1973]. An error of order Kn^2 may be expected outside the Knudsen layer in the region where the Navier-Stokes equations apply. If the boundary condition at the wall is not singular (strong adsorption, mirror reflection, *etc.*) the Boltzmann equation can be linearized and the macroscopic gas properties may be determined within the Knudsen layer [Kogan, 1973].

The slip boundary conditions are then set such that the solution of the Navier-Stokes equations within the Knudsen layer asymptotically approaches the solution obtained outside of the Knudsen layer some distance away from the wall. The slip velocity ($\mathbf{u}_s$) and slip temperature (T_s) do not actually correspond to the actual gas properties at the wall as illustrated in Figure 1-8. The fictitious slip boundary conditions are written as :

$$u_s = A\frac{\mu}{n}\sqrt{\frac{2}{mk_BT}}\frac{\partial u_x}{\partial y} + B\frac{2\mu}{nm}\frac{1}{T}\frac{\partial T}{\partial x}, \quad (1\text{-}28).$$

$$\Delta T_s \equiv (T_s - T_w) = C\frac{k}{2k_Bn}\sqrt{\frac{\pi m}{2k_BT}}\frac{\partial T}{\partial y}, \quad (1\text{-}29).$$

where the coefficients A,B, and C depend upon the laws of interaction between the gas molecules and the wall [Kogan, 1973]. The values of the coefficients have been obtained for various types of interactions [Kogan, 1973]. The use of slip boundary conditions may

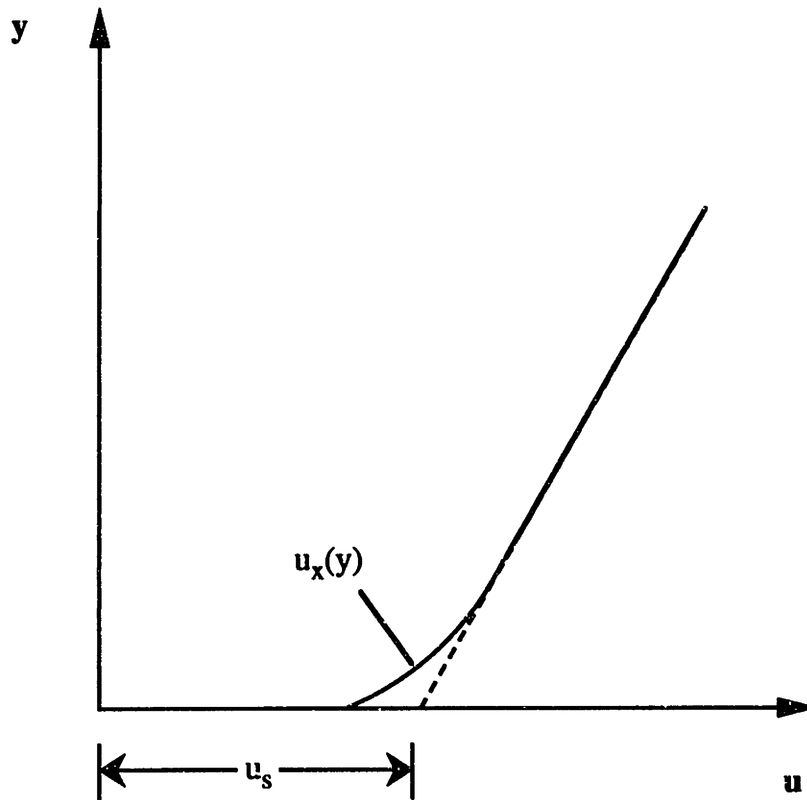

Figure 1-8 : Knudsen layer velocity profile and the hypothetical slip velocity.

seem very appealing to the researcher more familiar with the continuum approach. From a theoretical point of view, however, they can only be regarded as a correctional patch to be used for systems where the Knudsen layer thickness is relatively small compared to the flow field dimensions.

1.3 Thesis objectives

1.3.1 Motivation and theme of research

The encompassing objective of this work has been to develop efficient and accurate models of rarefied gas flows in chemical vapor deposition processes. The progress made in this research has benefitted greatly from the mature study of rarefied gas flows in the aerospace industry. At the same time a number of issues unique to chemical vapor deposition have required a reformulation of established approaches and the development of novel ones.

The direct simulation Monte Carlo method was selected as the tool to study rarefied gas flows in CVD for two reasons. The first reason was its established record for being able to simulate complex flows with quantitative accuracy [Erwin *et al.*, 1989]. The second reason was simply the absence of alternative approaches which offered the computational efficiency of the DSMC method [G. Bird, 1978]. However, the application of the DSMC method to the types of rarefied flows typically encountered in CVD was necessarily preceded by the address of a number of algorithmic and computational issues as will be outlined in later chapters.

1.3.2 Ultra-high vacuum CVD

The promise of the ultra-high vacuum CVD technology mentioned in section 1.1 has provided the primary impetus for the efforts of this research. These efforts have focussed on gaining an understanding of the gas dynamics underlying the UHV-CVD process and how they may affect reactor performance and future potential applications of this infant technology. In particular, determination of the variation of the macroscopic gas properties throughout the reactor and their dependence upon the reactor operating parameters was a primary goal. The properties of interest included the gas density, pressure, temperature, velocity field and, for gas mixtures, the composition. The operating parameters which were investigated were the inlet stream properties (flow rate, composition, density) and the geometry of the wafers (number, spacing, diameter).

1.3.3 Heat transfer analysis of the LPCVD furnace

The film growth rate in an LPCVD furnace is suppressed at the ends of the wafer boat resulting in the sacrificial loss of several wafers at each end. Recent experimental evidence has suggested that this is due to the thermal radiative heat loss to the cooled ends of the reactor and that the heat transfer to the wafers is completely independent of the gas flow [Badgwell *et al.*, 1992a]. This suggests that a heat transfer analysis of the LPCVD furnace may be uncoupled from the gas dynamics problem. The development of a heat transfer model of the LPCVD furnace was pursued for two primary reasons. First, a successful model of the process might provide insight into the experimental observations and suggest ways to improve the performance of the LPCVD furnace. In addition, the thermal profile obtained from a heat transfer model may be used as input to a gas dynamics simulation in order to assess the impact of thermal variations on the gas flow.

1.3.4 Nonplanar substrate CVD

The increasing use of thin film deposition over patterned substrates has spawned a plethora of process models [Jain *et al.*, 1993]. Each of these has involved a number of simplifying assumptions to both the gas transport and the evolution of the film profile. The primary goal in this research effort has been to develop a general purpose simulation model for deposition over arbitrary feature shapes for a wide range of processing conditions. The first specification for the model was that it take into consideration the rarefaction of the gas due to the miniaturization of the flow field dimensions over a device-sized feature. This inevitably required the recognition of the particulate nature of the gas and, accordingly, the direct simulation Monte Carlo method was assigned the task of simulating the gas transport to the nonplanar growth surface. The second requirement was that the simulation of the film growth be able to accurately predict step coverage performance as well as capture the microstructural details of the growing film.

Chapter 2 : The Direct Simulation Monte Carlo Method

2.1 General description of the DSMC algorithm

The direct simulation Monte Carlo (DSMC) technique has emerged as a powerful method for the simulation of rarefied gas flows [G. Bird, 1976]. The DSMC method simulates a real gas flow by simultaneously tracking several thousands of representative molecules as they move through the flow field. The molecular motion and gas phase collisions are uncoupled over a small time step which is some fraction of the mean collision time. The simulated molecules are permitted to exit the flow domain through open boundaries and an appropriate influx of new molecules is computed at each time step. The simulation time corresponds directly to the real flow time in DSMC simulations. A generalized flowchart of the DSMC algorithm is shown in Figure 2-1.

The flow field is sub-divided into a network of cells which serve to facilitate the selection of potential collision partners and the localized sampling of macroscopic flow properties by microscopic averaging. The cells must necessarily be dimensioned such that the change in flow properties across each cell is negligible; some fraction of a mean free path (λ) is usually appropriate.

The gas phase collisions are handled on a probabilistic basis. Within each cell, potential collision partners are randomly selected without regard to their relative positions. A collision is simulated if their collision probability exceeds some random fraction. This

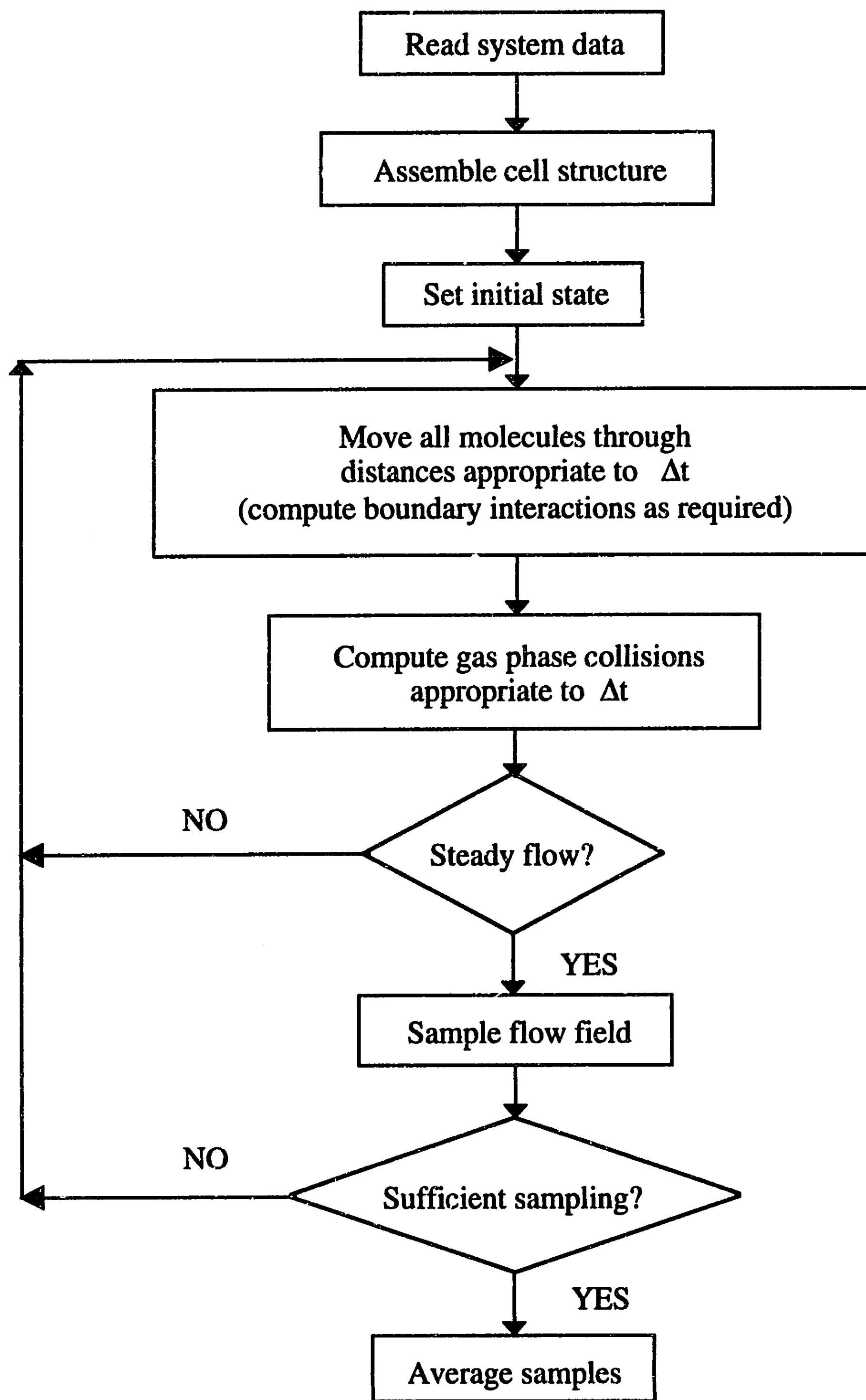

Figure 2-1 : Direct simulation Monte Carlo algorithm flowsheet.

process is repeated until the correct collision rate is obtained in each cell. Only binary collisions are considered as the rarefaction of the gas makes any three-body collisions highly improbable.

For each simulated molecule, the position coordinates (one for 1-D flows, two for 2-D, *etc.*) are stored and updated with each move. The molecules move about in a three-dimensional space, but only those spatial coordinates corresponding to the dimension of the flow are recorded. A molecule is considered to be equally likely to reside at any position in the remaining coordinate(s). All three velocity components must be stored for each molecule, though, to properly simulate the gas phase collisions.

The simulation begins from some specified initial state which may be a vacuum or a distribution of molecules based on a continuum model. The simulation is initially transient but achieves a steady flow after a number of time steps which depends on the initial state. Upon reaching steady flow, the macroscopic flow properties are obtained by time averaging the simulation conditions.

2.2 Initialization of a DSMC simulation study

2.2.1 Feasibility considerations

The dilute gas approximation

The average distance between the centers of two molecules in a gas is given by $\delta \equiv n^{-1/3}$ where n is the number density. Considering a gas comprised of hard spheres of diameter d, the fraction of space occupied by the molecules is of order $(d/\delta)^3$. For sufficiently reduced gas densities this fraction is small enough such that the molecules move freely outside of the influence of the other molecules for the most part and any

intermolecular collisions are essentially limited to binary collisions. This is the dilute gas approximation and is the primary assumption of the DSMC method. The molecular motion may then be uncoupled from the intermolecular collisions over a small time step and be treated as ballistic transport free of long-range attractive forces. It should be noted that the DSMC method has been extended to include ternary interactions by assigning a finite lifetime to a binary collision pair [G. Bird, 1977].

The range of validity of the major approximations discussed to this point are illustrated in Figure 2-2 which has been redrawn from *Molecular Gas Dynamics* [G. Bird, 1976]. In this plot n_0 is the number density at standard conditions and the molecular diameter has been taken to be 3.7 Å. The solid line represents Kn = 0.1 and has been assigned as the demarcation between the continuum approach and the particulate approach. This value was selected since the Navier-Stokes equations will be inappropriate in regions where the local Knudsen number (based on local gradient scales) is greater than about 0.1. Also shown are the limits of the dilute gas assumption, taken here to be $\delta/d = 7$, and the limit for the onset of significant statistical fluctuations where $L/\delta = 100$. Measurements of the density of a gas at this fluctuation limit would include fluctuations with a standard deviation of around three percent [G. Bird, 1976].

Computational feasibility

In principle, the DSMC method may be used to simulate all dilute gases within the range of values of n and L listed in Figure 2-2. In practice, however, it is usually more efficient to utilize the continuum approach for flows where Kn « 0.1 as the number of cells and, thus, the number of simulated molecules becomes prohibitively large. This limit depends upon the available computer hardware (memory and CPU time). The lower Knudsen number limit for the practical application of the DSMC method is being

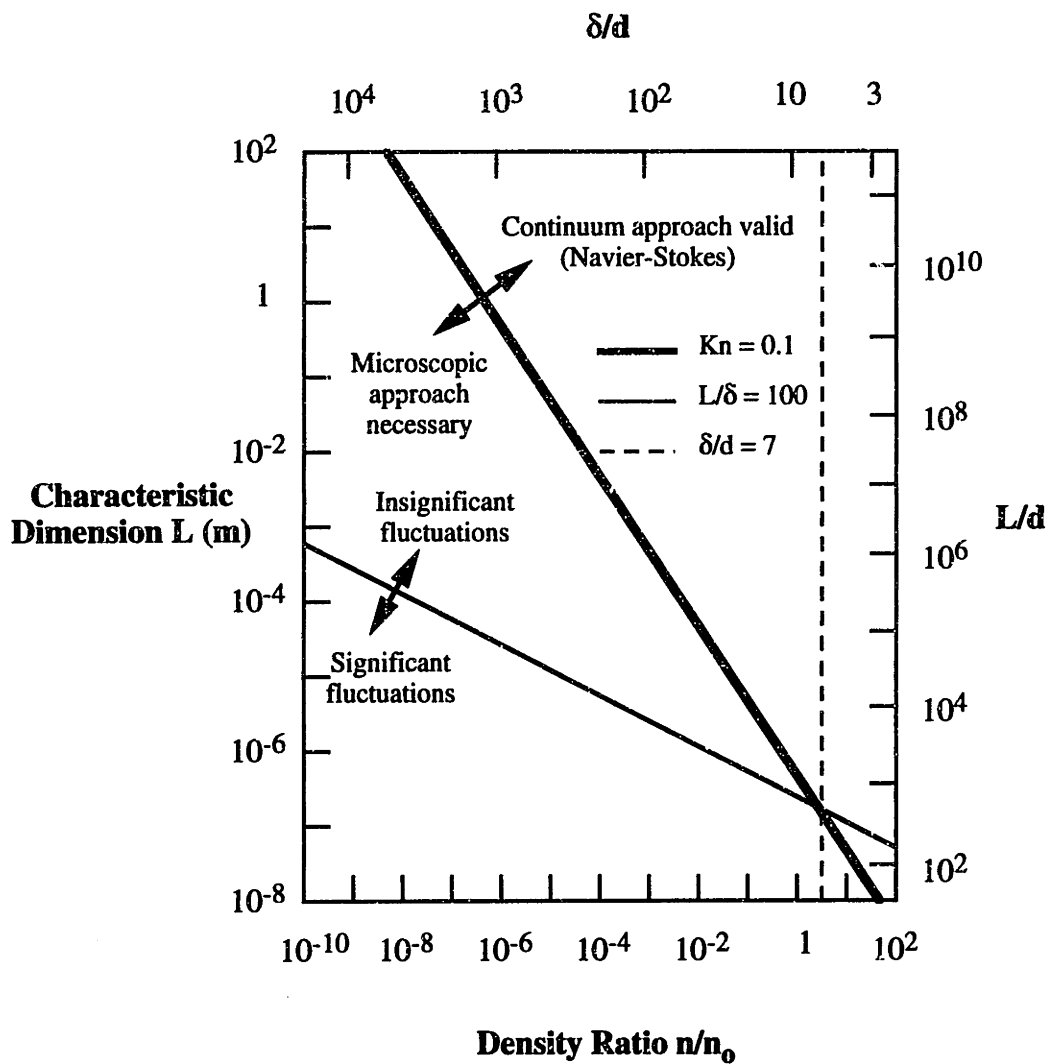

Figure 2-2 : Effective limits of the major approximations in the DSMC method (d = 3.7 Å).

continually pushed further into the continuum regime in direct proportion to the advances in computing power [Dongarra, 1993] and clever programming efforts [G. Bird, 1990b].

As the simulated flow field conditions move towards the fluctuation limit defined above, the sample size required to reduce the uncertainty in the time-averaged results for a steady flow increases. This computing penalty is compounded by the fact that the uncertainty is reduced only as the square root of the sample size [G. Bird, 1976]. This means that in order to reduce the uncertainty by a factor of two it would require four times as many samples to be averaged. Severe fluctuation problems are encountered in DSMC simulations when the number of simulated molecules per cell is reduced to around five or less. This may happen for gas flows involving trace species or in flows involving extreme density variations. Fluctuations may also occur in axisymmetric flow simulations near the axis. This is a problem unrelated to the physics of the gas flow which will be discussed in the next section. The DSMC method is still valid beyond the fluctuation limit but practical limitations associated with the computing environment might prevent its application.

The DSMC method may be used to simulate transient flows as well. In this case, however, the usual time-average sampling of the flow field properties must be replaced with an ensemble-averaging procedure. This involves the averaging of a number of independent simulation runs over the transient period of interest where each run is initiated from a different random number seed. Each sample in time then requires a complete simulation over the entire time period. This contrasts with the time-average sampling for steady flows where the samples are closely spaced in time, permitting a large number of samples to be obtained over a relatively short time period. The enormous amount of computing time required to collect a sufficient number of samples has limited the practical application of the DSMC method to transient flow studies.

2.2.2 Generating the cell network

The success of the DSMC method rests on its ability to simulate real gas flows with computational costs proportional to the number of molecules (N_m) in the simulation. This is in contrast to other particle simulation methods where the computing time increases as N_m^2 [G. Bird, 1978]. This capability originates from the DSMC collision routine where potential collision partners are selected from within a particular cell without regard to their relative positions within the cell. With this approach, it is not necessary to check for possible collisions with *each* surrounding molecule, a requirement which leads to the N_m^2 dependence. The rationale for this approach relies on the assumption that the flow properties are uniform within each cell. Thus, the selected collision pair are equally likely to be found at any location within the cell. This assumption is reasonable as long as the cell dimension is less than a mean free path.

For illustration purposes, consider the mean free path for a multicomponent mixture of hard spheres :

$$\lambda_{mix} = \sum_{i=1}^{n} x_i \left\{ \sum_{j=1}^{n} n_j \, \pi \, d_{ij}^2 \, \frac{\overline{v_{r_{ij}}}}{\overline{v_i}} \right\}^{-1} = \sum_{i=1}^{n} x_i \, \lambda_i, \qquad (2\text{-}1).$$

where x_i, n_i and $\overline{v_i}$ are the mole fraction, number density and average thermal velocity of species i, respectively; d_{ij} and $\overline{v_{r_{ij}}}$ are the collision diameter and relative velocity for species i and j. Using reported hard sphere diameters [G. Bird, 1980], the mean free path for a 50% binary mixture of hydrogen and nitrogen at 300 K and 760 Torr is computed to be $8.1\text{x}10^{-6}$ cm. This is simply the average of the mean free paths for each species, $12.0\text{x}10^{-6}$ cm for hydrogen and $4.2\text{x}10^{-6}$ cm for nitrogen. In a simulation of this gas mixture, the cell dimension would be checked against the *smallest* of the mean free paths of the individual

species. A cell dimension no larger than 1.4×10^{-6} cm would be in accordance with the suggested guideline of the cell size being roughly one third of the mean free path [G. Bird, 1976].

The cell network can be quite irregular with varying size and shape to correspond with the density variations which are present [G. Bird, 1990a]. A typical approach might be to initially specify all cells to be the same dimension. An initial run would then serve to reveal the locations where smaller or larger cell sizes are needed, enabling the cell network to be optimized for the simulation conditions. The network of cells should be kept as simple as possible, however, so that the computational cost associated with the molecular tracking does not become prohibitively expensive.

Examples of 1-D and 2-D cell networks are given in Figure 2-3. The cells are defined in three dimensions with arbitrary depths set for the non-flow directions. The positions of the molecules are not recorded for the non-flow directions as they are equally likely to reside at any position along these directions. In other words, the simulated molecules are representatives of the larger number of real molecules which are uniformly distributed in these directions. Ideally, an average of about 30 molecules per cell is obtained by specifying the ratio of real molecules represented by each simulated molecule. This ratio (γ) may require adjustment after an initial run in order to obtain a sufficient number of molecules per cell since the number density is not known *a priori*.

Axisymmetric simulations

The 2-D axisymmetric cell network illustrated in Figure 2-3 consists of stacks of concentric annular rings. The molecular tracking in axisymmetric flows requires a rotation of coordinates with each move as the molecules are free to move throughout the three-dimensional arrangement of annular rings. This is done in order to map the radial and axial

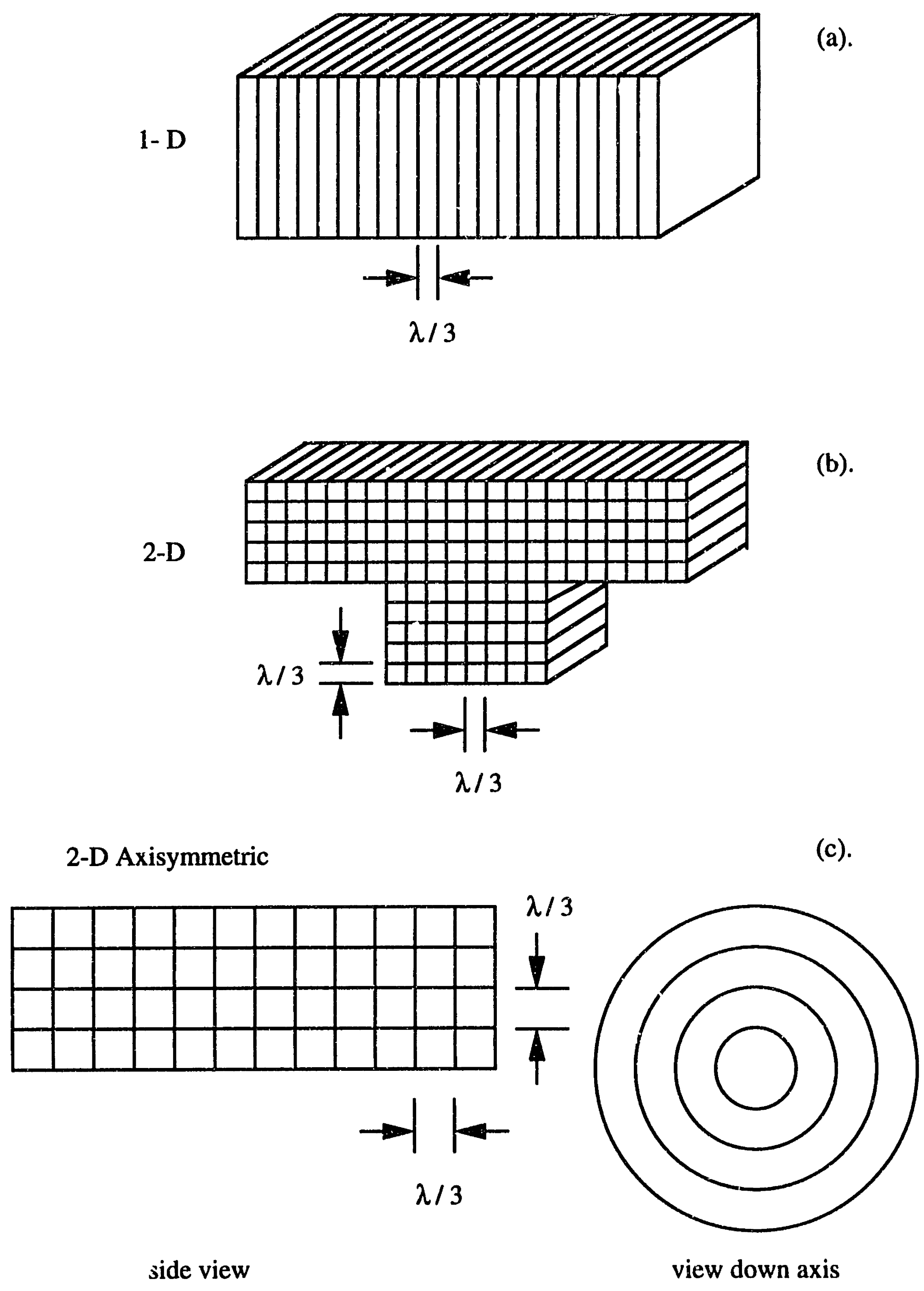

Figure 2-3 : Examples of (a) 1-D, (b) 2-D, and (c) 2-D axisymmetric DSMC cell networks.

positions onto a single plane with the third velocity component always perpendicular to this plane. The assumption of axisymmetry eliminates the need to keep track of the circumferential position of the molecules since each molecule is equally likely to reside at any position along the circumference. Figure 2-4 illustrates the tracking of a molecule in an axisymmetric cell network and the corresponding coordinate transformations.

The statistical sampling difficulties associated with axisymmetric DSMC simulations which were referred to in section 2.2.1 stems from the fact that the cell volume varies with the square of the radius. The cells near the axis thus have fewer molecules from which to sample in order to obtain the flow properties. This leads to an increase in the fluctuations and a corresponding increase in the required sample size for these cells. One approach to dealing with this problem is to reduce the number of real molecules represented by each simulated molecule (γ) for the cells near the axis. The implementation of this idea is usually referred to as using radial weighting factors [G. Bird, 1976]. The real to simulated molecule ratio may vary from cell to cell or any number of regions may be established with each region containing several rows of cells with the same ratio. In either case, as molecules move radially inward or outward they are probabilistically duplicated or removed, respectively, to account for any changes in the local ratio of real to simulated molecules [G. Bird, 1976].

2.2.3 Setting the magnitude of the time step

The essence of the DSMC algorithm is the uncoupling of the molecular motion from the gas phase collisions. This approximation is justified if the time step is much smaller than the average time elapsed between successive gas phase collisions, which defines the mean collision time for the gas molecules. The size of the time step is one of the initial considerations when setting up a simulation. It is desirable to have the time step as large as

molecular trajectory

radial position (y)

velocity component (v or w)

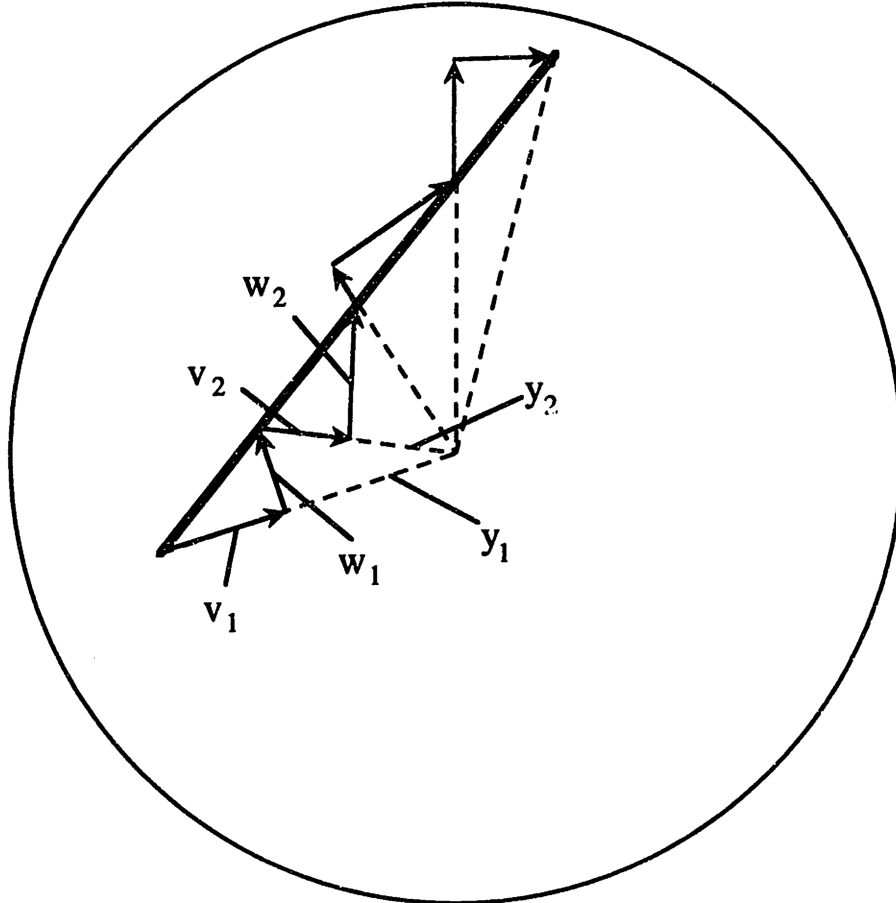

$$y_2 = \sqrt{(y_1 + v_1\Delta t)^2 + (w_1\Delta t)^2}$$

$$v_2 = \frac{v_1(y_1 + v_1\Delta t) + w_1^2\Delta t}{y_2}$$

$$w_2 = \frac{w_1(y_1 + v_1\Delta t) - v_1 w_1\Delta t}{y_2}$$

Figure 2-4 : Coordinate transformation for molecular motion in axisymmetric DSMC simulations.

possible in order to simulate a statistically sufficient amount of the physics of the gas flow. A time step which is less than 20% of the mean collision time has been shown to yield acceptable results [G. Bird, 1976]. Another rule of thumb is to set the time step so that the molecules traverse about 1/3 of the cell per time step, assuming that the cell dimensions have been properly set as outlined above [G. Bird, 1991]. A systematic study of the effect of time step size on the simulation results is a logical first step of any simulation study.

Considering once again a multicomponent mixture of hard spheres, the mean collision time is given by :

$$\tau = \left\{ \sum_{i=1}^{n} x_i \sum_{j=1}^{n} n_j \, \pi \, d_{ij}^2 \, \overline{v_{r_{ij}}} \right\}^{-1} = \left\{ \sum_{i=1}^{n} x_i \, \nu_i \right\}^{-1}, \qquad (2\text{-}2).$$

where ν_i is the mean collision rate for species i. For the same binary mixture as in the previous section, the mixture mean collision time is computed to be 7.8×10^{-11} s; the individual mean collision times are 6.72×10^{-11} s for hydrogen and 8.88×10^{-11} s for nitrogen. Analogous to the cell size considerations, the magnitude of the time step would be checked with the *smallest* mean collision time of the individual species. A time step of 1.3×10^{-11} s would be appropriate for a simulation of this gas mixture.

It is also possible to define a different time step for various regions of the simulation if large density differences exist. This is the usual approach for simulating shock waves and hypersonic flows. If there is a large disparity in the mean collision times between individual species in a mixture, a different time step for the various species might also be feasible although its use in simulations has not been reported in the literature. This situation may arise in CVD flows where hydrogen is used as a carrier gas for a relatively heavy reactant species.

2.3 Details of the molecular motion

2.3.1 The drift Maxwellian velocity distribution

The introduction of a new molecule into the simulation requires the specification of the velocity vector **c** and its three velocity components - u,v,w. In the DSMC method, the velocity components are selected from the Maxwellian velocity distribution with the bulk stream velocity components added as drift terms. The entering gas stream is thus assumed to be in local thermodynamic equilibrium at the specified boundary temperature, T_b. The fraction of molecules with velocity components in the range from (u,v,w) to (u+du,v+dv,w+dw) is then given by f(u,v,w)dudvdw where the drift Maxwellian velocity distribution takes the form :

$$f(u,v,w) = \left(\frac{1}{v_m\sqrt{\pi}}\right)^3 \exp\left\{\frac{-[(u-u_o)^2+(v-v_o)^2+(w-w_o)^2]}{v_m^2}\right\}, \qquad (2\text{-}3).$$

and u_o,v_o,w_o are the velocity components of the macroscopic stream velocity $\mathbf{c_o}$. The quantity v_m is the most probable thermal velocity and is defined for a gas in local thermodynamic equilibrium as :

$$v_m \equiv \sqrt{\frac{2k_BT}{m}} \quad . \qquad (2\text{-}4).$$

Furthermore, the thermal velocity of the molecules, **c'**, is defined as ($\mathbf{c}$-$\mathbf{c_o}$).

A number of informative quantities may now be obtained from this distribution. Consider the distribution of velocities in polar coordinates where the velocity space element

is given by $c'^2 \sin\theta d\theta d\phi dc'$. The fraction of molecules with molecular speeds between c' and c'+dc' is then given by integrating over the limits of θ and ϕ :

$$f(c') = \left(\frac{1}{v_m\sqrt{\pi}}\right)^3 \int_0^{2\pi} \int_0^{\pi} c'^2 \exp\left(\frac{-c'^2}{v_m^2}\right) \sin\theta \, d\theta d\phi dc', \qquad (2\text{-}5).$$

$$= \frac{4c'^2}{v_m^3\sqrt{\pi}} \exp\left(\frac{-c'^2}{v_m^2}\right) dc'.$$

The mean thermal speed is obtained by integration over all possible speeds :

$$\overline{c'} = \frac{4}{v_m^3\sqrt{\pi}} \int_0^{\infty} c'^3 \exp\left(\frac{-c'^2}{v_m^2}\right) dc' = \frac{2}{\sqrt{\pi}} v_m. \qquad (2\text{-}6).$$

The distribution function for a particular thermal velocity component is required for DSMC simulations and is obtained by integration of f(u',v',w') over two of the three velocity components :

$$f(u') = \left(\frac{1}{v_m\sqrt{\pi}}\right)^3 \int_{-\infty}^{\infty} \int_{-\infty}^{\infty} \exp\left(\frac{-[u'^2+v'^2+w'^2]}{v_m^2}\right) dv'dw'du', \qquad (2\text{-}7).$$

$$= \frac{1}{v_m\sqrt{\pi}} \exp\left(\frac{-u'^2}{v_m^2}\right).$$

Since the velocity distribution function is spherically symmetric, the most probable value of a particular thermal velocity component is zero. This symmetry is illustrated in Figure 2-5 along with the distribution of molecular speeds, f(c').

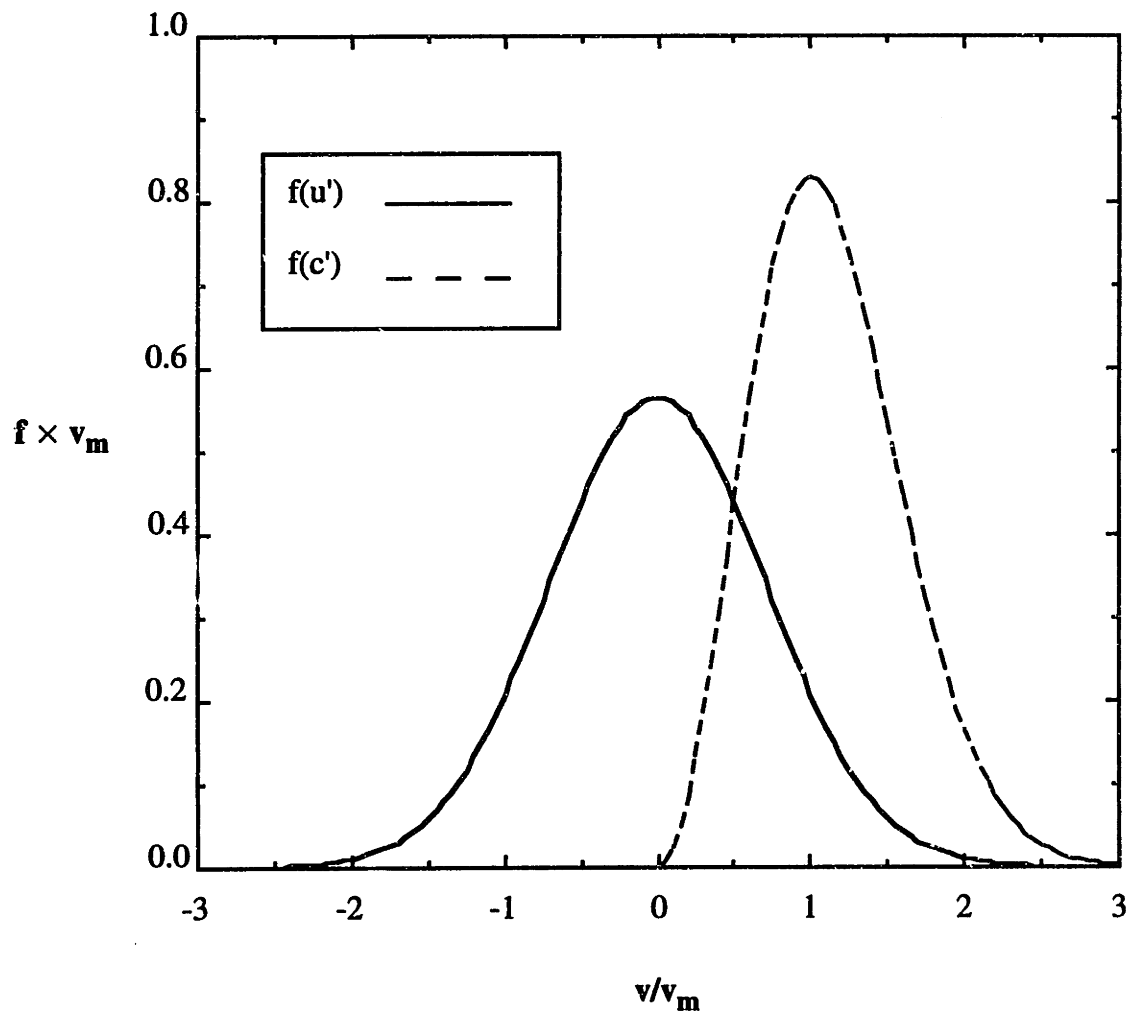

Figure 2-5 : Maxwellian distribution of molecular velocities (u') and speeds (c').

2.3.2 Calculating the influx of molecules at open boundaries

At each time step, a number of new molecules enter the simulation across the open boundaries according to the specified composition, density, temperature and stream velocity of the entering gas. For an entering gas stream in local thermodynamic equilibrium the molecular influx (J) across a surface is readily computed by integration over all velocities directed inward :

$$J = n \int_{-\infty}^{\infty} \int_{-\infty}^{\infty} \int_{0}^{\infty} u \, f(u,v,w) \, du dv dw, \qquad (2\text{-}8).$$

$$= \frac{n\bar{c}}{4} [\exp(-s^2) \pm \sqrt{\pi}\, s \, \{1+\mathrm{erf}(s)\}].$$

where s is the speed ratio and is defined as the ratio of the macroscopic stream velocity to the most probable thermal velocity, v_m, and $\pm$ refers to whether s is directed inward (+) or outward (-). As the speed ratio approaches zero (stagnant gas), equation (2-8) reduces to the familiar result from the kinetic theory of gases, $J = n\bar{c}'/4$.

Molecular influx counters are maintained for the incoming gas and new molecules are generated at each time step until the counters correspond with the flow time. For example, after 200 time steps the influx counters should read :

$$N_{influx} \geq J * A_{cell} * 200 * \delta t / \gamma, \qquad (2\text{-}9).$$

where A_{cell} is the cross-sectional area of the cell, δt is the time step and γ once again is the ratio of real to simulated molecules at the open boundary.

The velocity components parallel to the boundary are assigned according to the single component distribution derived in equation (2-7); the stream velocity component is

simply added to the thermal velocity where appropriate. Special consideration is given to the component normal to the boundary. The velocity distribution for this component, u_n', is given by :

$$f(U) = \frac{1}{\sqrt{\pi}\, v_m} (U+s_n) \exp(-U^2), \qquad (2\text{-}10).$$

where $U \equiv (u_n'/v_m)$ and s_n is the component of the speed ratio normal to the boundary. This distribution is often referred to as a half-range Maxwellian distribution [G. Bird, 1976].

2.4 Gas-surface interactions

2.4.1 Thermal accomodation coefficients

The treatment of gas-surface interactions requires a detailed knowledge of how a particular molecular species interacts with the solid environment. In DSMC simulations, the common approach is to make use of Maxwell's simple diffuse reflection model [G. Bird, 1976]. For a diffuse reflection, the reflection angle of a molecule after it has suffered a surface collision is independent of the incident angle and is directed away from the surface according to the half-range Maxwellian distribution of equation (2-10) with the speed ratio set to zero.

The appropriate temperature for this distribution may range from the temperature of the incident molecule, T_i, to the surface temperature, T_s. The thermal accomodation

coefficient, α_T, is a measure of the extent to which the reflected molecules have adjusted their temperature, T_r, to that of the surface and is defined as :

$$\alpha_T \equiv \frac{T_i - T_r}{T_i - T_s}, \qquad (2\text{-}11).$$

Simple theories such as the Baule model are available for the estimation of thermal accomodation coefficients [Goodman and Wachman, 1976] :

$$\alpha_T = \frac{2\mu}{(1+\mu)^2}, \qquad (2\text{-}12).$$

where μ is the ratio of the mass of the impinging gas atom (M_g) to the mass of the surface constituent (M_s). This model assumes the atoms to be hard spheres and the expression above is averaged over the incident angle and atomic speeds. Furthermore, the model is appropriate only for the cases where $\mu \ll 1$ since the kinetic energy of the surface atoms is assumed to be negligible in comparison to the kinetic energy of the impinging gas.

A somewhat more detailed treatment of the thermal accomodation coefficient, based in part on lattice theory arguments, takes into account the gas temperature dependence and is given by the following semiempirical formula [Goodman and Wachman, 1976] :

$$\alpha(T) = 1 - \exp(-T_0/T) + \alpha(\infty) \tanh\left\{ \frac{\sqrt{M_g T}}{\alpha(\infty)} \frac{a}{\ell} \right\} \exp(-T_0/T), \qquad (2\text{-}13).$$

where a is the Morse binary interaction potential parameter, T_0 and ℓ are empirical parameters which depend on the gas species, and $\alpha(\infty)$ is the "corrected" Baule formula given by :

$$\alpha(\infty) = \frac{2.4\ \mu}{(1+\mu)^2}. \qquad (2\text{-}14).$$

The most questionable assumption involved in this theory is, once again, neglect of the surface kinetic energy.

It is apparent that the current theoretical development prohibits the accurate prediction of thermal accomodation coefficients for more realistic systems involving polyatomic species, lattice vibrations and imperfections, and strongly interacting surfaces. The most reliable approach seems to be to rely on the extensive collection of experimentally measured accomodation coefficients [Goodman and Wachman, 1976]. For a polyatomic species impinging upon a surface with an adsorbed layer, complete thermal accomodation is a fairly good assumption [Wachman, 1991]. This appears to be the case in many CVD systems where molecular precursors and their thermally decomposed fragments are impinging upon a reactive surface.

2.4.2 Reactive sticking coefficients

Simulation of gas flows where one or more species in the gas phase deposits on the surface requires the specification of the reaction probability for each reactive species. The reaction probability, more commonly referred to as the reactive sticking coefficient, is defined as the fraction of the surface flux which permanently adheres to the surface. In the simulation a random fraction is generated and compared to the reactive sticking coefficient with each surface collision. The reactive species is then either removed from the simulation, with the appropriate reaction products being created, or is reflected, depending upon whether the random fraction is less than or greater than the reactive sticking coefficient.

The reactive sticking coefficient is actually a lumped parameter which contains information on both the adsorption process and the surface chemical kinetics according to the relation :

$$P_{rxn} = \frac{1}{\frac{1}{P_{ads}} + \frac{1}{P_{inc}}} \quad , \qquad (2\text{-}15).$$

where P_{rxn} is the reactive sticking coefficient, P_{ads} is the adsorption probability and P_{inc} is the probability that the adsorbate will become incorporated into the surface. For sufficiently fast surface kinetics ($P_{inc} \approx 1$) the reactive sticking coefficient and the adsorption probability are numerically equivalent as suggested by the relation in equation (2-15). It is important to note that the adsorption probability referred to here is often referred to as the sticking coefficient in the literature [Rendulic, 1992].

As with the thermal accomodation coefficient, estimations of reactive sticking coefficients rely primarily on experimental data. To illustrate the influence of various parameters on a typical data set, the technologically important and well-studied interactions between silane (SiH_4) and a crystalline silicon surface will now be considered. The most comprehensive study of this system was performed by Buss and co-workers [Buss *et al.*, 1988]. In their experiments a well controlled molecular beam was directed at a heated silicon surface under a variety of conditions and the reactive sticking coefficient was deduced from *ex-situ* growth rate measurements.

The dependence of the reactive sticking coefficient on the temperature and total SiH_4 flux is shown in Figure 2-6 for the [100] surface of Si. The data suggest two distinct regimes, consistent with the SiH_4 surface decomposition chemistry discussed in section 1.1.3. At low temperatures the rate-controlling step is related to the surface kinetics while the dissociative chemisorption of SiH_4 limits the high temperature kinetics. The transition

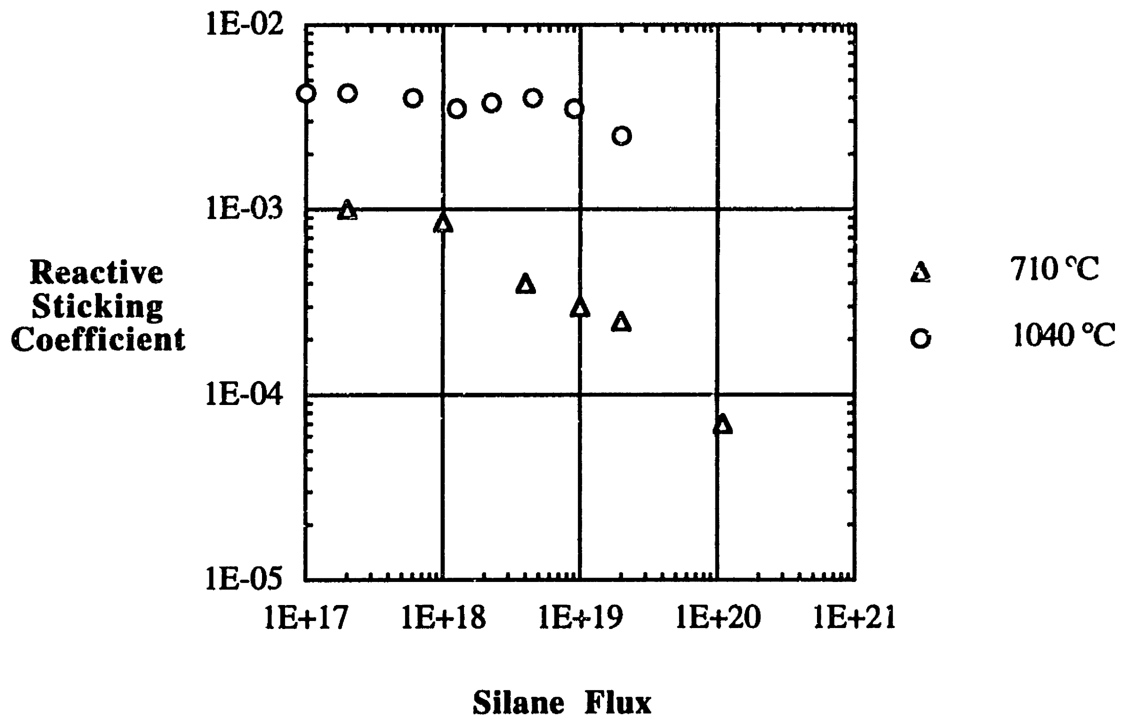

Figure 2-6 : Reactive sticking coefficient of silane on [100] Si vs silane flux at 710 °C and 1040 °C [Buss *et al.*, 1988].

temperature between the two regimes is increased with the total SiH_4 flux. The temperature and flux dependencies are further complicated by the dependence on the crystallographic orientation of the Si surface [Gates *et al.*, 1990a] and the sensitivity of the measurements to the purity of the SiH_4 source gas [Gates and Kulkarni, 1991].

This example served to illustrate the underlying complexities associated with the assignment of the reactive sticking coefficient for DSMC simulations. If sufficient experimental data is available, the dependence of the reactive sticking coefficient on the processing conditions may be implemented in the simulations through the use of appropriate expressions [Kleijn, 1991]. The accuracy of the simulations is then limited by the experimental procedure used to obtain the data.

2.5 Gas phase collisions

2.5.1 Dynamics of binary elastic collisions

The dilute gas assumption of the DSMC method requires the intermolecular collisions to be restricted to binary collisions involving just two molecules. The simplest interaction between two molecules is an elastic collision where there is no interchange of translational and internal energy. This approach is predominantly used in DSMC simulations where a description of the internal state of the molecule is not important.

Consider a typical binary elastic collision where the pre-collision velocity vectors are given by $\mathbf{v}_1$ and $\mathbf{v}_2$ and m_1 and m_2 are their respective masses. The conservation of linear momentum and total energy may be written as :

$$m_1\mathbf{v}_1 + m_2\mathbf{v}_2 = m_1\mathbf{v}_1' + m_2\mathbf{v}_2' = (m_1+m_2)\,\mathbf{V}_m \qquad (2\text{-}16).$$

and

$$m_1 v_1^2 + m_2 v_2^2 = m_1 v_1'^{\,2} + m_2 v_2'^{\,2}, \qquad (2\text{-}17).$$

where **v'** denotes the post-collision velocity vector and $\mathbf{V}_m$ is the velocity of the center of mass of the two molecules which remains unchanged. The pre-collision and post-collision relative velocities of the colliding pair are defined as $\mathbf{v}_r = \mathbf{v}_1 - \mathbf{v}_2$ and $\mathbf{v}_r' = \mathbf{v}_1' - \mathbf{v}_2'$, respectively, and equation (2-16) may be rewritten as :

$$\mathbf{v}_1 = \mathbf{V}_m + \frac{m_2}{m_1+m_2}\mathbf{v}_r \qquad (2\text{-}18a).$$

and

$$\mathbf{v}_2 = \mathbf{V}_m - \frac{m_1}{m_1+m_2}\mathbf{v}_r \,. \qquad (2\text{-}18b).$$

The post-collision velocities may also be expressed in this form :

$$\mathbf{v}_1' = \mathbf{V}_m + \frac{m_2}{m_1+m_2}\mathbf{v}_r' \qquad (2\text{-}19a).$$

and

$$\mathbf{v}_2' = \mathbf{V}_m - \frac{m_1}{m_1+m_2}\mathbf{v}_r'. \qquad (2\text{-}19b).$$

Equation (2-18) shows that the pre-collision velocities are parallel in the frame of reference moving with the center of mass. The same is true of the post-collision velocities as shown in equation (2-19). The collision is therefore planar in the center of mass frame of reference. This is illustrated in Figure 2-7 which shows a series of snapshots of a two body collision at equally spaced time intervals where the center of mass plane is represented by the rectangle.

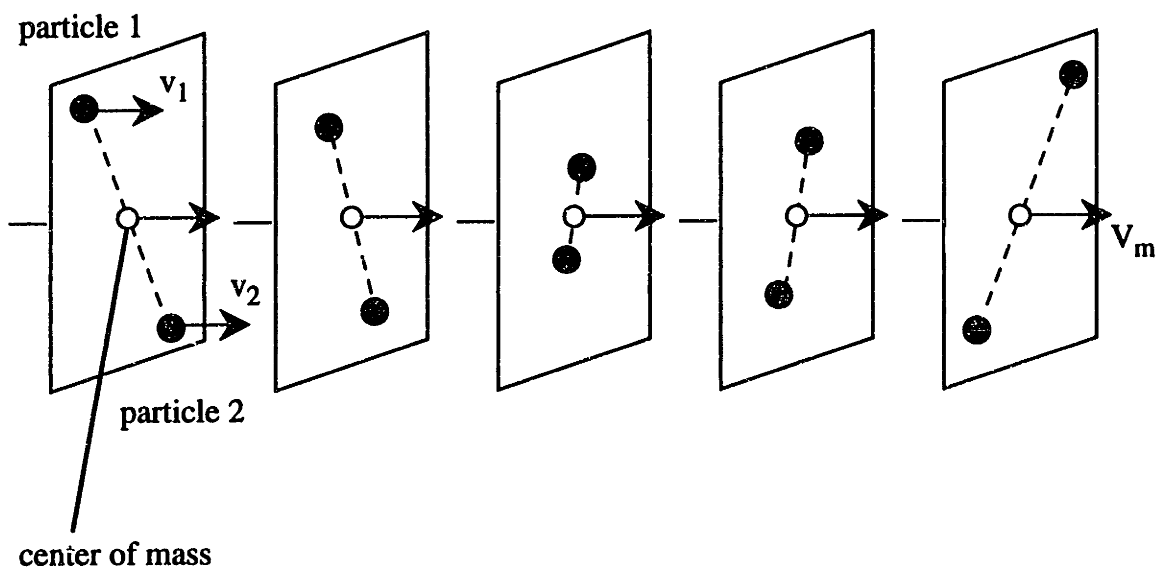

Figure 2-7 : Three-dimensional representation of a two-body collision.

Using the above expressions for the pre- and post-collision velocities, the following relationships are derived :

$$m_1 v_1^2 + m_2 v_2^2 = (m_1+m_2)\, V_m^2 + m_r v_r^2 \qquad (2\text{-}20).$$

and

$$m_1 v_1'^{\,2} + m_2 v_2'^{\,2} = (m_1+m_2)\, V_m^2 + m_r v_r'^{\,2}, \qquad (2\text{-}21).$$

where $m_r = \dfrac{m_1 m_2}{m_1+m_2}$ and is called the reduced mass. A comparison of (2-17) and (2-20) shows that $|\mathbf{v}_r| = |\mathbf{v}_r'|$. The problem is therefore reduced to a determination of the post-collision direction of the relative velocity.

The equations of motion of the collision pair, considered here to be represented by two spherically symmetric point centers of force, are given by :

$$\mathbf{F} = m_1 \frac{d^2\mathbf{r}_1}{dt^2}, \qquad (2\text{-}22).$$

$$-\mathbf{F} = m_2 \frac{d^2\mathbf{r}_2}{dt^2}, \qquad (2\text{-}23).$$

where $\mathbf{r}_1$ and $\mathbf{r}_2$ are the position vectors of the two molecules. These two equations may now be combined, written here in terms of the reduced mass m_r and the relative position vector $\mathbf{r} \equiv (\mathbf{r}_1 - \mathbf{r}_2)$:

$$\mathbf{F} = m_r \frac{d^2\mathbf{r}}{dt^2}. \qquad (2\text{-}24).$$

The motion of molecule 1 relative to molecule 2 is seen to be equivalent to the motion of a molecule of mass m_r relative to a fixed scattering center.

This frame of reference is illustrated in Figure 2-8 where the vector **r** has been replaced by the polar coordinates r and θ. The impact parameter b is defined as the distance of closest approach if no deflection occurs. The variable χ represents the change in direction of the relative velocity vector and is dependent upon the kinetic energy of the collision pair, the potential energy of interaction of the molecules, and the distance of closest approach, b.

2.5.2 Molecular models

The hard sphere model

In a DSMC simulation an appropriate molecular model must be chosen to compute the collision cross-sections between potential collision partners, which in turn sets the intermolecular collision rate. The simplest is the hard sphere model which treats each molecule as a fixed diameter sphere. The molecules do not interact unless they are in actual contact with each other. The collision cross-section is thus set by the diameters of the two molecules, d_1 and d_2 :

$$\sigma_{HS} = \frac{\pi}{4}\{d_1+d_2\}^2. \qquad (2\text{-}25).$$

The important point to note here is the independence of the collision cross-section from the relative velocity v_r and the scattering angle χ. This makes the hard sphere model attractive from a computational standpoint since the collision cross-section may be computed once and for all before the simulation is initiated as opposed to computing it for each potential

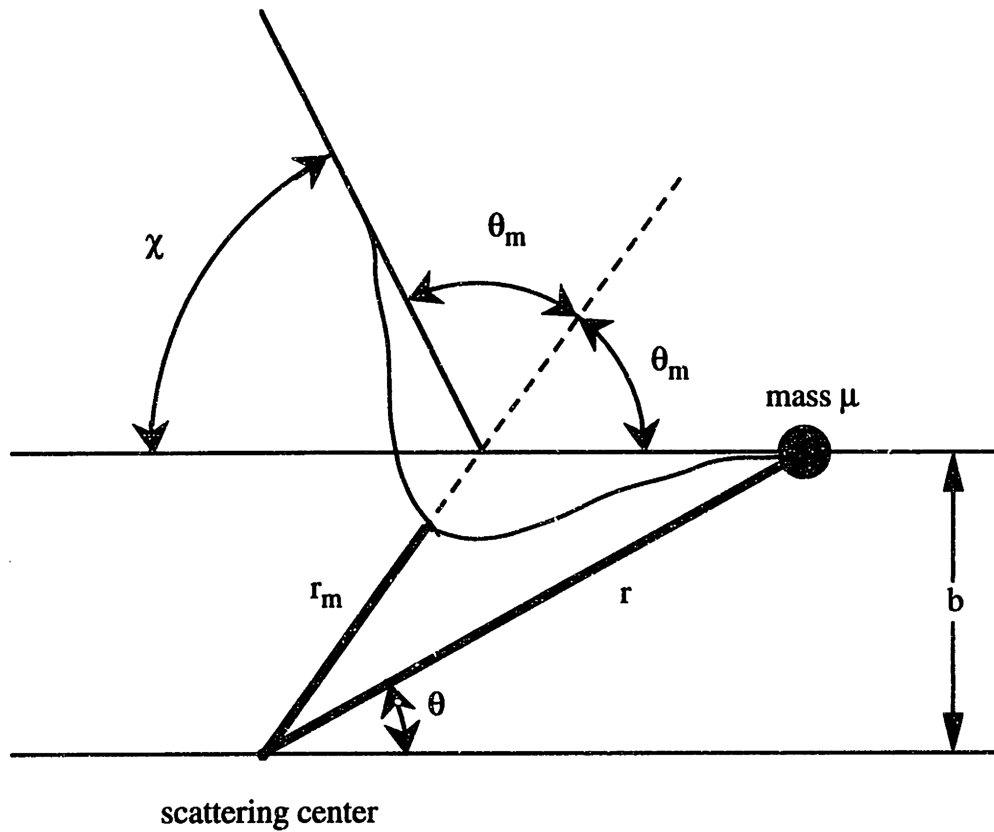

Figure 2-8 : Impact parameters for a binary collision in the center-of-mass frame of reference.

collision partner. The independence from the scattering angle implies that all directions for the post-collision relative velocity $\mathbf{v}_r'$ are equally likely and that scattering of hard sphere molecules is isotropic.

The inverse power law model

A more complex treatment is the inverse power law model which takes into account the temperature (relative velocity) and deflection angle dependence of the collision cross-section [Weston and Schwarz, 1972]. This model completely neglects the attractive component of the intermolecular potential and the repulsive force is defined as :

$$\mathbf{F} = \frac{\kappa}{\mathbf{r}^{\eta}}. \qquad (2\text{-}26).$$

The collision cross-section for inverse power law molecules may be shown to be given by [G. Bird, 1976] :

$$\sigma_{IP} = \pi W_{om}^2 \left\{ \frac{\kappa}{m_r v_r^2} \right\}^{2/(\eta-1)}. \qquad (2\text{-}27).$$

W_{om} is the arbitrarily specified maximum value of the dimensionless impact parameter W_o defined as :

$$W_o \equiv b \left\{ \frac{m_r v_r^2}{\kappa} \right\}^{1/(\eta-1)}, \qquad (2\text{-}28).$$

Specification of this parameter effectively sets the cutoff of the deflection angle χ. For a typical value of $\eta = 9$ and $W_{om} = 1.5$, this corresponds to a deflection angle cutoff of

approximately 1° [G. Bird, 1976]. Although the inverse power law model provides a more realistic treatment of intermolecular collisional phenomena, it suffers from a computational standpoint. This stems from the fact that the determination of the post-collision velocity vector for each collision requires the generation of two random fractions [G. Bird, 1976]. This computational expense was addressed with the development of the variable hard sphere model which is discussed in the next section.

The variable hard sphere model

The variable hard sphere (VHS) molecular model was formulated as a viable alternative to the inverse power law model. The development of the VHS model was based upon the observation that the variation in the collision cross-section was the key component of the molecular model rather than the details of the scattering process [G. Bird, 1980]. The VHS model employs the simple isotropic scattering law of the hard sphere model but accounts for the temperature dependence of the collision cross-section through the use of a single parameter which may be determined from the viscosity temperature dependence :

$$\sigma_{VHS} = \sigma_{ref}\left(\frac{T}{T_{ref}}\right)^{-\omega}, \qquad (2\text{-}29).$$

where σ_{ref} is the collision cross-section at the reference temperature, T_{ref}, and T is the kinetic temperature of the collision partners. The VHS parameter, ω, is related to the temperature exponent of viscosity, s :

$$\eta = \eta_o\left(\frac{T}{T_o}\right)^{s}, \qquad (2\text{-}30).$$

where $s = \omega + 1/2$ and η_o is the viscosity at T_o [G. Bird, 1983]. The VHS parameters and reference diameters for several gases at 273 K are given in Table 2-1.

Gas	**ω**	**d_{ref} (Å)**
H_2	0.17	2.88
He	0.20	2.29
CH_4	0.34	4.67
Ne	0.16	2.72
CO	0.23	4.09
N_2	0.24	4.07
O_2	0.27	3.96
Ar	0.31	4.04
CO_2	0.43	5.41

Table 2-1 : VHS parameters and reference conditions for several gases at 273 K.

The VHS model was originally formulated for the simulation of pure gases. The VHS parameter for gas mixtures may be obtained by computing the gas mixture viscosity from the pure component gas viscosities. The semiempirical Wilke formula is used to compute the mixture viscosity at several temperatures and the temperature exponent is obtained from regression of the data :

$$\mu_{mix} = \sum_{i=1}^{n} \frac{x_i \mu_i}{\sum_{j=1}^{n} x_j \Phi_{ij}}, \tag{2-31a}$$

$$\Phi_{ij} = \frac{1}{\sqrt{8}}\left(1 + \frac{M_i}{M_j}\right)^{-\frac{1}{2}} \left\{ 1 + \left(\frac{\mu_i}{\mu_j}\right)^{\frac{1}{2}} \left(\frac{M_j}{M_i}\right)^{\frac{1}{4}} \right\}^2, \tag{2-31b}$$

where x_i, μ_i, and M_i are the mole fraction, pure component viscosity, and molecular weight, respectively, of species i and Φ_{ij} is a binary interaction parameter [R. Bird *et al.*, 1960].

2.5.3 The time counter method

The time scale of rarefied gas flows is set by the mean collision time which, once again, is the mean time interval between successive collisions by a typical gas molecule. The reciprocal of this quantity is the mean collision rate per molecule. Consider the relative motion of a molecule in some time period Δt less than the mean collision time. The molecule would collide with any other molecule in the cylindrical volume given by $(\sigma v_r \Delta t)$. In the DSMC method the probability of two molecules colliding is then proportional to the product σv_r. From section 2.5.2 it is seen that the overall dependence of the collision probability on the relative velocity of the collision pair depends on the particular molecular model which has been specified :

$$P_{coll} \propto v_r, \qquad \text{(hard sphere)} \tag{2-32a}$$

$$P_{coll} \propto v_r^{\frac{\eta-5}{\eta-1}}, \qquad \text{(inverse power law)} \qquad (2\text{-}32b).$$

$$P_{coll} \propto v_r^{1-2\omega}. \qquad \text{(variable hard sphere)} \qquad (2\text{-}32c).$$

The acceptance-rejection technique of sampling from distributions, discussed in section 2.6, utilizes normalized probability distributions. For the collision probability this is given by :

$$P_{coll} = \frac{\sigma v_r}{(\sigma v_r)_{max}}, \qquad (2\text{-}33).$$

where $(\sigma v_r)_{max}$ is initially set to some arbitrary value at the beginning of the simulation and is updated during the simulation for each cell when it is exceeded.

The correct collision rate in each cell is obtained by use of the time-counter method derived by Bird [G. Bird, 1976]. From kinetic theory, the collision rate per unit time per volume of gas is :

$$N_c = \frac{1}{2} n^2 \overline{\sigma v_r}. \qquad (2\text{-}34).$$

If one considers the period of time Δt_c per collision in a cell volume V_c, rearrangement of equation (2-34) gives the time increment associated with a particular collision :

$$\Delta t_c = \frac{2V_c}{N_m n \sigma v_r}, \qquad (2\text{-}35).$$

where N_m is the number of simulated molecules in the cell volume. In the DSMC method potential collision partners are randomly selected from within the same cell and their corresponding collision probability is compared to some random fraction. Selected collision partners whose collision probabilities exceed the random fraction are subsequently scattered and the time counter is updated using equation (2-35) until the time counters in each cell correspond to the current flow time. A flowsheet of the DSMC collision computation using the time counter scheme is illustrated in Figure 2-9.

2.5.4 Gas phase chemistry in DSMC simulations

The concepts of classical chemical kinetics are readily incorporated into the DSMC method [G. Bird, 1985]. Simulation of bimolecular chemical reactions may be included within the collision routine if an adequate description of the energetics is provided and the appropriate kinetic data is available. The bimolecular reaction rate is given by the product of the collision rate involving collisions with energy in excess of some activation energy and the probability of reaction or steric factor. The steric factor is simply the ratio of the reactive cross-section to the total collision cross-section.

Consider the generic bimolecular reaction written below :

$$A + B \rightarrow C + D \qquad (2\text{-}36).$$

The rate equation for species A, considering the reaction to be irreversible, may be written as :

$$\frac{-dn_A}{dt} = k(T)\, n_A\, n_B, \qquad (2\text{-}37).$$

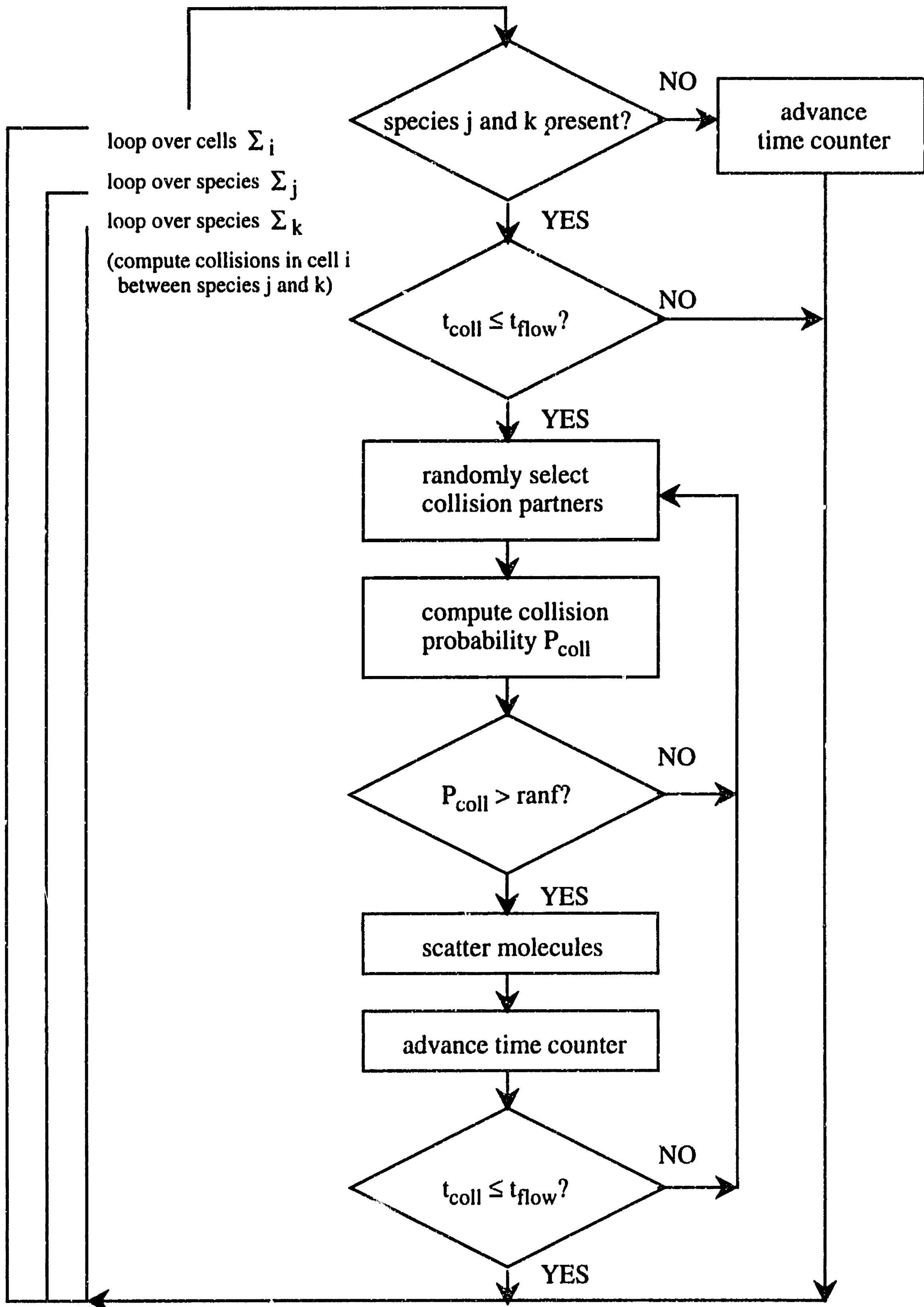

Figure 2-9 : Flowsheet for time-counter method in DSMC simulations.

where n_i is the number density of species i. The temperature dependent macroscopic rate constant, k(T), usually takes the form :

$$k(T) = a\, T^{\,b} \exp(-E_A/k_B T), \qquad (2\text{-}38).$$

where a and b are constants and E_A is the activation energy. The reactive energy of a collision between species A and B is the sum of the relative translational energy associated with the colliding pair and the fraction of internal energy of the two molecules which contributes to the reaction :

$$E_c = E_t + E_{i_A} + E_{i_B}, \qquad (2\text{-}39a).$$

$$E_t = \frac{1}{2} m_r v_r^2. \qquad (2\text{-}39b).$$

A phenomenological description of the internal energy has been the most widely used approach [Borgnakke and Larsen, 1975]. The number of degrees of freedom (ξ) which may contribute energy to the reaction is specified for each participating molecular species where $E_{i_A} = \xi_A k_B T$ for species A and similarly for B. Bird has utilized the following empirical formula in DSMC simulations to compute the number of contributing internal degrees of freedom :

$$\xi = \frac{5-3\zeta}{\zeta-1}, \qquad (2\text{-}40).$$

where ζ is the ratio of the constant pressure and constant volume heat capacities, C_p/C_v [G. Bird, 1976].

Collision theory predicts the reaction rate in (2-37) to be :

$$-\frac{dn_A}{dt} = n_A \upsilon_{AB} \int_{E_A/k_BT}^{\infty} f(E_c/k_BT)\, P_r\, d(E_c/k_BT), \qquad (2\text{-}41).$$

where υ_{AB} is the equilibrium collision rate between A and B, f is the distribution function for E_c and P_r is the steric factor or reaction probability. The full expression for the steric factor for hard sphere molecules was derived by Bird from equations (2-37), (2-38) and (2-41) :

$$P_r = \frac{\Gamma\left[\frac{\xi_A+\xi_B}{2}+2\right]}{(d_A+d_B)^2} \left(\frac{2m_r}{\pi k_B}\right)^{1/2} \frac{a}{\Gamma\left[\frac{\xi_A+\xi_B}{2}+\frac{3}{2}+b\right]} \left[1 - \frac{E_A}{E_c}\right]^{\left(\frac{\xi_A+\xi_B}{2}+1\right)} \left[\frac{E_c-E_A}{k_B}\right]^{b-1/2}, \qquad (2\text{-}42).$$

where Γ is the gamma function. In a DSMC simulation involving a reactive gas mixture, the expression for the steric factor is evaluated for each potentially reactive collision where $E_c > E_A$. If its value exceeds some random fraction, then the simulated molecules are transformed according to the specified chemistry. The associated heat of reaction is added (exothermic) or subtracted (endothermic) from the collisional energy which is distributed between the translational and internal energy of the reaction products.

The most serious drawback to this approach is related to the statistics of the simulation. Gas phase chemical reactions usually proceed at a rate which is orders of magnitude slower than the gas phase collisional rate. This means that a large number of collisions must be sampled before a reactive collision is encountered. The statistical sampling problem is worsened by the presence of species which are present in trace

amounts as is often the case in reactive flows. An alternative approach for simulating gas phase chemistry in DSMC simulations, which circumvents the statistical difficulties mentioned here, is presented in Chapter 3.

2.6 Sampling from a prescribed distribution

The central feature of all Monte Carlo methods is the use of random numbers for the purposes of sampling from probability distributions. The use of probability distributions in the DSMC method is an inextricable result of the probabilistic underpinnings of the kinetic theory of gases. This section will discuss the ways in which the necessary statistical averaging may be accomplished for the various kinds of probability distributions encountered in DSMC simulations.

2.6.1 Pseudo-random number generators

The generation of random numbers on a computer is not an entirely random process. The list of random numbers generated has a finite cycle and always yields the same result from the same initial seed value. Thus, the name pseudo-random number generator is often applied to the built-in functions or portable computer codes which perform this task.

The adequacy of a pseudo-random number generator is dependent upon the particular application for which it is being used. The large number of random number calls in a typical DSMC simulation, or any other Monte Carlo technique, demands certain qualities in the random number generator being utilized. In general, the random number generator should have a long cycle and the numbers should be uncorrelated [Press *et al.*,

1992]. However, there is a definite tradeoff between the randomness of a random number generator and its computational efficiency. Built-in random number generators tend to be on the quick-and-dirty end while portable routines are more reliable yet sluggish. A benchmark test of several different random number generators for an example DSMC simulation is given in section 2.8.

2.6.2 Inversion of the cumulative probability distribution function

Consider the normalized probability distribution, f(x), which is defined such that the probability of x lying between x and x+dx is f(x)dx. If the range of x is from x_i to x_f, then the total probability is unity over the entire range :

$$\int_{x_i}^{x_f} f(x)\, dx = 1. \qquad (2\text{-}43).$$

The cumulative probability distribution, F(x), may now be defined as :

$$F(x) = \int_{x_i}^{x} f(x)\, dx. \qquad (2\text{-}44).$$

As an example, consider the probability distribution used in randomly selecting a radial position, a procedure frequently executed in axisymmetric DSMC simulations. The probability of particular value of r is directly proportional to r as shown here for a distribution between 0 and R :

$$f(r) = \frac{2r}{R^2}, \qquad (2\text{-}45a).$$

$$F(r) = \frac{r^2}{R^2}. \qquad (2\text{-}45b).$$

The probability distributions are shown in Figure 2-10. The cumulative probability distribution varies smoothly from zero to one. If values of F(r) are selected at random, the corresponding values of r will be preferentially weighted to those values which contribute the most to F(r). This offers a convenient method of sampling from the distribution. In order to randomly select a value of r from the range, a random fraction R_f is generated and set equal to F(r) where the corresponding value of r is obtained by inverting the expression for the cumulative distribution :

$$r = R\sqrt{R_f}. \qquad (2\text{-}46).$$

It is not always possible to invert the cumulative probability distribution in order to obtain an explicit expression for the variable of interest. The acceptance-rejection technique is usually employed for these cases.

2.6.3 The acceptance-rejection method

The Maxwellian velocity distribution is utilized in DSMC simulations for generating molecular velocities. The cumulative probability distribution of velocities involves an error function, however, and cannot be inverted, necessitating the use of the acceptance-rejection method [G. Bird, 1976]. In this method, the distribution is first normalized by its maximum value. For the distribution of a particular velocity component as given in equation (2-7) the normalized distribution becomes :

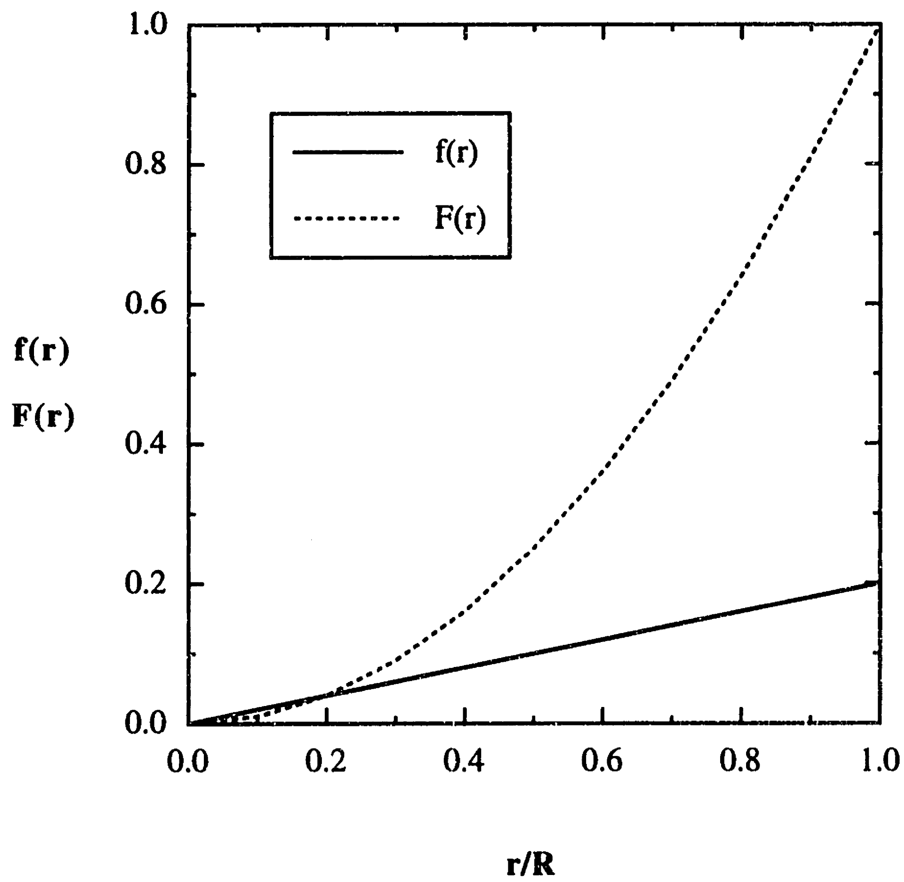

Figure 2-10 : Probability (—) and cumulative probability (---) distribution functions for selecting random radial positions.

$$\hat{f}(u') = \exp\left(- \frac{u'^2}{v_m^2}\right) \qquad (2\text{-}47).$$

A finite range of values of u' must be specified in place of the real limits of $-\infty$ and $+\infty$. If the limits are set to $\pm 3v_m$ then the fraction of values lying outside of this range is 0.000022 [G. Bird, 1976]. A value of the velocity component is then randomly chosen from the given range and the normalized velocity distribution is evaluated at this position :

$$u' = (-3 + 6R_f)\, v_m, \qquad (2\text{-}48).$$

$$\hat{f}(u') = \exp\left\{ - (-3+6R_f)^2 \right\}. \qquad (2\text{-}49).$$

A second random fraction is now generated and compared to $\hat{f}(u')$. The velocity component selection is then accepted or rejected depending on whether the distribution is greater or less than the random fraction.

2.6.4 Sampling pairs of values from the normal distribution

In the DSMC method, it is often required to obtain pairs of values from the distribution of equation (2-7) for molecules entering the open boundary or diffusely reflecting from a solid surface. In this case, there is a direct method for sampling the values from their combined distribution, f(v',w'). In cartesian coordinates, the probability of a molecule having its velocity components between v' and v'+dv', w' and dw' is given by :

$$f(v',w')\ dv'dw' = \frac{1}{v_m{}^2\pi}\exp\left\{-\frac{(v'^2+w'^2)}{v_m{}^2}\right\}\ dv'dw'. \qquad (2\text{-}50).$$

The velocity components may be written in terms of the new variables a and θ where :

$$v' = a\cos(\theta), \qquad (2\text{-}51a).$$

$$w' = a\sin(\theta), \qquad (2\text{-}51b).$$

$$a^2 = v'^{\,2} + w'^{\,2}. \qquad (2\text{-}51c).$$

The transformation Jacobian is readily computed as :

$$\frac{\partial(v',w')}{\partial(a,\theta)} = \begin{vmatrix} \frac{\partial v'}{\partial a} & \frac{\partial v'}{\partial \theta} \\ \frac{\partial w'}{\partial a} & \frac{\partial w'}{\partial \theta} \end{vmatrix} = \begin{vmatrix} \cos(\theta) & -a\sin(\theta) \\ \sin(\theta) & a\cos(\theta) \end{vmatrix} = a, \qquad (2\text{-}52).$$

and the combined distribution then becomes

$$f(v',w')\ dv'dw' = \frac{1}{\pi v_m{}^2}\exp\left(-\frac{a^2}{v_m{}^2}\right) a\ da d\theta, \qquad (2\text{–}53).$$

$$= \frac{1}{2\pi}\exp\left(-\frac{a^2}{v_m{}^2}\right) d\left(\frac{a^2}{v_m{}^2}\right) d\theta.$$

The angle θ is uniformly distributed between 0 and 2π so that :

$$\theta = \xi 2\pi, \qquad (2\text{-}54).$$

where ξ is some random fraction between 0 and 1. The variable (a^2/v_m^2) varies from 0 to ∞ and its cumulative distribution form is given by :

$$F\left(\frac{a^2}{v_m^2}\right) = 1 - \exp\left(-\frac{a^2}{v_m^2}\right) \tag{2-55}$$

Since ξ and $1-\xi$ are equivalent functions where ξ is some random fraction, (2-55) may be inverted to obtain the explicit relation for a :

$$a = v_m \sqrt{-\ln(\xi)}. \tag{2-56}$$

A pair of values for θ and a are sampled directly from (2-54) and (2-56) and the corresponding values for v' and w' are then obtained from the relationship given in (2-51). The remaining velocity component, normal to the entry plane or reflecting surface, is obtained using the acceptance-rejection technique outlined above for the distribution given in equation (2-10).

2.7 Calculation of macroscopic flow field properties

The macroscopic flow field properties are obtained at each cell location by averaging the properties of the resident molecules. The most common properties of interest include the density, velocity, pressure and temperature which are computed according to the following formulae :

$$n = \frac{N_c}{V_c}, \qquad \text{(density)} \qquad (2\text{-}57).$$

$$v_x = \frac{1}{N_c} \sum_{j=1}^{N_c} u, \qquad \text{(x-velocity)} \qquad (2\text{-}58).$$

(similarly for other components)

$$p = \frac{m}{3V_c} \sum_{j=1}^{N_c} (u'^2+v'^2+w'^2), \qquad \text{(pressure)} \qquad (2\text{-}59).$$

$$T = \frac{m}{3k_B N_c} \sum_{j=1}^{N_c} (u'^2+v'^2+w'^2), \qquad \text{(temperature)} \qquad (2\text{-}60).$$

where N_c is the number of molecules in the cell. The quantities defined above are instantaneous values and will fluctuate or change with time. Statistical averaging of the local macroscopic properties is then accomplished by time averaging the instantaneous values for steady flows or ensemble averaging for transient flows, *i.e.* $\bar{A} = (\sum A)/N_s$ where the Σ is over the N_s time-averaged or ensemble samples and A is some macroscopic property. The quantities defined above may be extended to include gas mixtures as well.

2.8 An example problem : Heat transfer between two infinite parallel plates

2.8.1 Problem description

A simple example problem is now presented as a tool for demonstrating the implementation of the guidelines outlined above. The problem of heat transfer between two

infinite parallel plates has been purposefully selected because analytical solutions exist for the two extremes of continuum and free molecular flows. This, in addition, serves as a check of the DSMC technique to ensure that the appropriate limiting behavior is approached.

The problem is schematically depicted in Figure 2-11. Pure argon gas was selected as the intervening medium between the two plates in order to avoid consideration of internal energy when computing the energy flux. The plate spacing (δ) and the upper and lower plate temperatures (T_U and T_L) remained constant at 1 cm, 325 K and 275 K, respectively. The Knudsen number, here defined as the ratio of the mean free path to the plate spacing ($Kn \equiv \lambda/\delta$), was then varied by adjusting the gas density.

2.8.2 Continuum and free molecular solutions

The continuum description of the heat transfer between the plates is given by a simple one-dimensional heat conduction equation, written here for the case where the thermal conductivity does not vary substantially over the imposed temperature gradient :

$$q_{cont} = k\left\{\frac{T_U - T_L}{\delta}\right\}. \qquad (2\text{-}61).$$

The thermal conductivity, k, of pure argon gas is evaluated at the mean temperature $\overline{T}$ where $\overline{T} = (T_U+T_L)/2$.

The free molecular analysis is not as straightforward and requires some preceding discussion. The gas is assumed to diffuse reflectly from the surface with complete thermal accomodation. The flux of molecules diffusely reflected from a surface is equivalent to the flux of molecules from a fictitious equilibrium gas on the reverse side of the surface. At

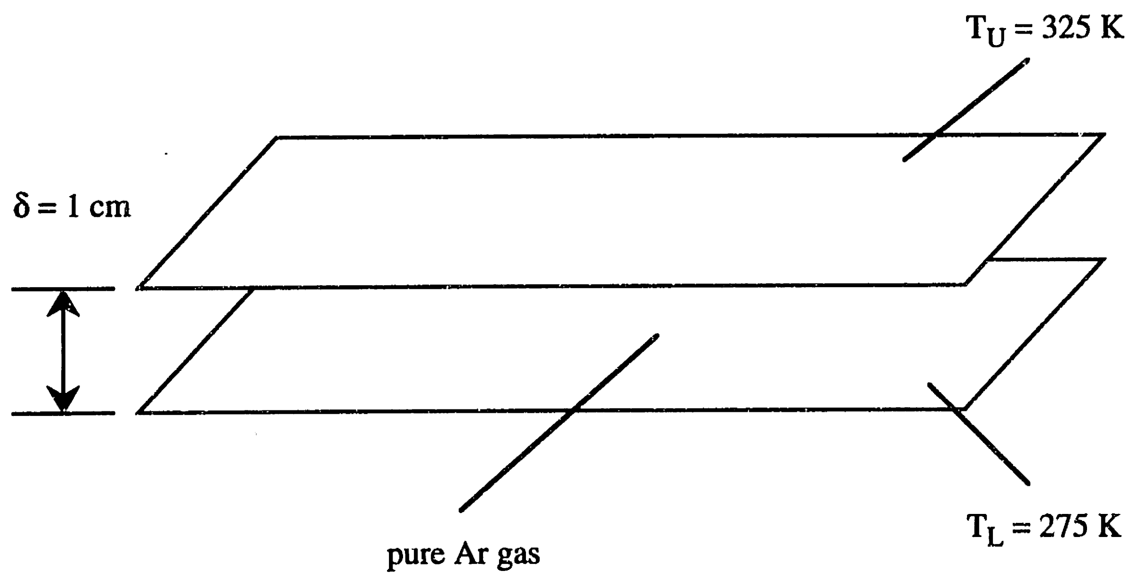

Figure 2-11 : DSMC example problem of one-dimensional heat transfer between two parallel infinite plates.

steady-state, the flux of molecules diffusely reflected from both surfaces must be equal. From equations (2-4), (2-6) and (2-8), this condition may be expressed as :

$$n_U\sqrt{T_U} = n_L\sqrt{T_L}, \qquad (2\text{-}62).$$

where n_U and n_L are the number densities of the diffusely reflected fluxes from the upper and lower surfaces, respectively. The total number density is simply the sum of the two :

$$n = n_U + n_L, \qquad (2\text{-}63).$$

which then allows the upper and lower flux number densities to be written in terms of the two plate temperatures and the total number density as :

$$n_U = \frac{n\sqrt{T_L}}{\sqrt{T_U}+\sqrt{T_L}}, \qquad (2\text{-}64).$$

$$n_L = \frac{n\sqrt{T_U}}{\sqrt{T_U}+\sqrt{T_L}}. \qquad (2\text{-}65).$$

The energy flux for an equilibrium monatomic gas may be obtained in a manner analogous to equation (2-8) which provided the number flux. This is accomplished by taking the moment of the kinetic energy of a gas molecule given by $\frac{m}{2}(u'^2+v'^2+w'^2)$. The resulting expression for a stagnant gas reduces to :

$$q = n\sqrt{\frac{2}{\pi m}}\,(kT)^{3/2}. \qquad (2\text{-}66).$$

The energy fluxes from the upper and lower plates are obtained by substituting the respective temperatures and number densities into the above equation. The net free molecular energy flux is then obtained as the difference between the downward and upward energy fluxes and is given by :

$$q_{FM} = \frac{n\,(2R)^{3/2}}{\sqrt{\pi m}} \sqrt{T_U}\,\sqrt{T_L}\,\left\{\sqrt{T_U} - \sqrt{T_L}\right\}. \qquad (2\text{-}67).$$

The continuum expression for the net energy flux is inversely proportional to the plate separation δ while the free molecular expression is directly proportional to the number density n, which in turn is inversely proportional to the mean free path λ. The ratio of the continuum to free molecular heat fluxes is then directly proportional to the Knudsen number :

$$\frac{q_{cont}}{q_{FM}} \propto \frac{1}{n\delta} \propto \frac{\lambda}{\delta} \equiv Kn. \qquad (2\text{-}68).$$

2.8.3 The DSMC solution

The variable hard sphere molecular model is used in the DSMC simulations with a VHS parameter of 0.31 and a reference temperature and diameter of 273 K and 4.04 Å, respectively [G. Bird, 1980]. The DSMC simulation is initiated by specifying the value of the Knudsen number as defined above, which effectively sets the value of the mean free path. The corresponding number density is then determined from the expression for the mean free path of a VHS gas given by :

$$\lambda_{VHS} = \left(\frac{T}{T_{ref}}\right)^{\omega} \left\{\frac{1}{(2-\omega)^{\omega}\Gamma(2-\omega)\sqrt{2}n\sigma_{ref}}\right\}, \qquad (2\text{-}69).$$

where Γ is the gamma function, ω is the VHS parameter and the mean temperature $\overline{T}$ is used. The number density is conveniently specified such that the 1 cm gap may be discretized into an integer number of cells, each of which is $\lambda/3$ in dimension. The time step is then set so the argon atoms traverse about 1/3 of the cell distance on average in a given time step as suggested in section 2.2.3. For example, in a simulation for a Knudsen number of 0.1 where the mean free path is 0.1 cm, exactly 30 cells are employed across the gap, with a corresponding number density of 1.33×10^{15} cm^{-3} and time step of 0.836 μs.

The cells are initially filled with 30 simulated molecules each from an equilibrium distribution (equation 2-49) at the mean temperature $\overline{T}$. This effectively sets the ratio of real molecules represented by each simulated molecule. For example, at Kn = 0.1 the cell volume is equal to 0.1 cm x 1 cm x 1 cm = 0.1 cm^3. The ratio of real to simulated molecules is then equal to $1.33\times10^{15}/(30/0.1) = 4.43\times10^{12}$.

The simulation is then initiated and the approach to steady-state is monitored. It is important to select the appropriate flow field property to monitor as a measure of whether or not steady-state conditions have been achieved. The gas temperature field is used as this measure. The number density field could have been selected as well, but the small density variations expected are of the same order as the statistical fluctuations in the measurements and would be difficult to monitor. The use of the gas temperature as a monitor of the transient state is perhaps best illustrated by showing a snapshot of the gas temperature when the steady-state flow field has not yet been established. This is shown in Figure 2-12 for the case of Kn = 0.001 after around 9 μs where a linear temperature gradient is expected at steady-state in the continuum regime. It is seen that a large portion of the gas

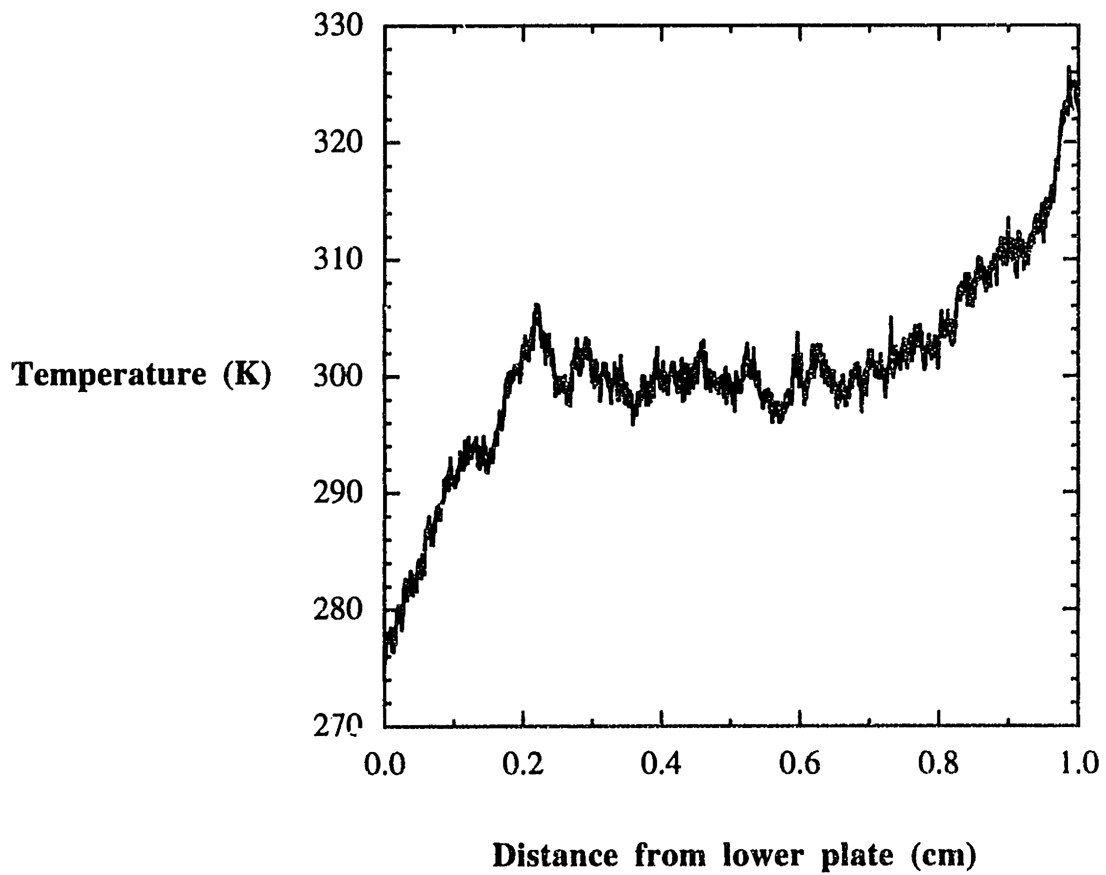

Figure 2-12 : Snapshot of Ar gas temperature prior to reaching steady state conditions for the DSMC example problem.

has not been thermally influenced by the plates and remains at the initial state temperature of 300 K.

2.8.4 A comparison between simulation and the exact analytical solutions

The simulation results for the net rate of heat transfer from the upper plate to the lower plate are plotted as a function of the Knudsen number in Figure 2-13. Also shown are the analytical solutions for the continuum and free molecular flow regimes given by equations (2-61) and (2-67), respectively. The DSMC solutions are bounded by the continuum and free molecular solutions as expected. The deviation from the continuum solution is seen to occur between Kn = 0.01 and Kn = 0.1. This is also reflected in the gas temperature profiles in Figure 2-14 for Kn = 0.01 and Kn = 1.0. At Kn = 0.01 there is no evidence of a temperature jump at the boundary as assumed in the continuum approach and the simulated heat flux agrees with that obtained from the continuum analysis. At Kn = 1.0, however, there is a significant temperature discontinuity at the boundary and the resulting heat flux approaches the free molecular result. The correct limiting behavior illustrated in Figure 2-13 lends support to the credibility of the solutions obtained in the intermediate transition regime which are inaccessible by either analytical approach.

2.8.5 Computational notes

The problem outlined above was selected as a benchmark problem in order to present the computational aspects of performing DSMC simulations. In this section, the CPU time associated with specific tasks within the DSMC algorithm, the use of various random number generators, and running the DSMC simulation on different computer

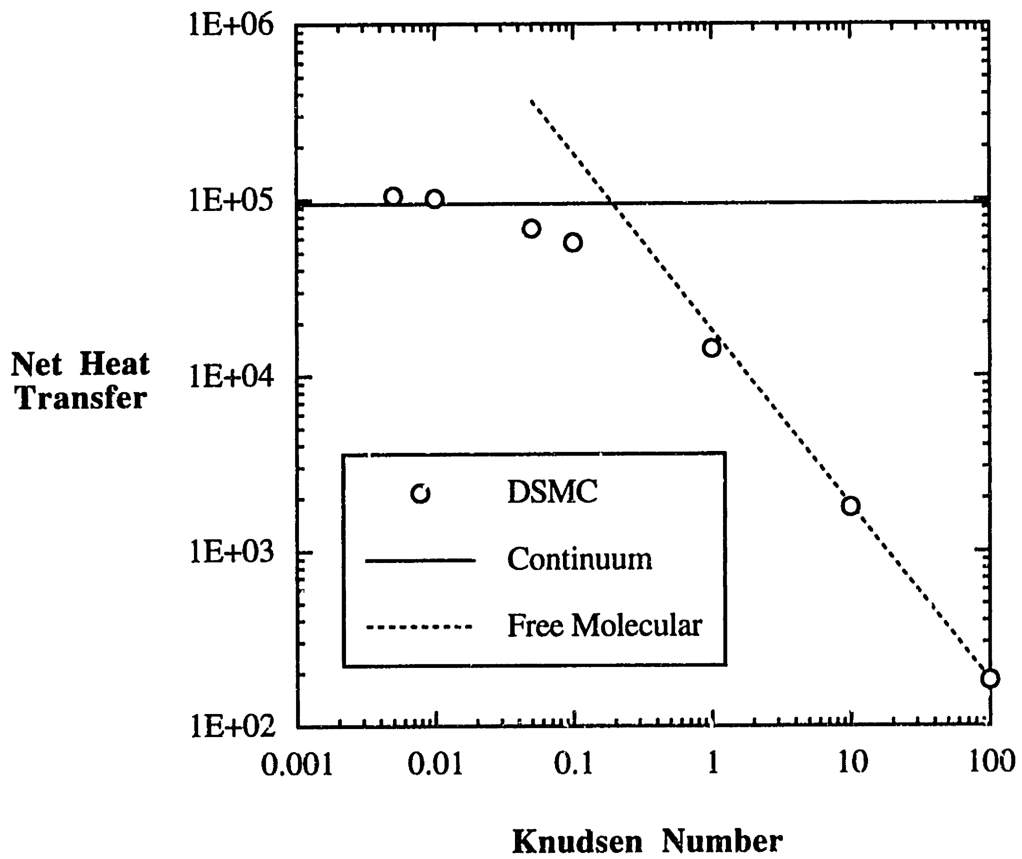

Figure 2-13 : Net heat transfer between infinite parallel plates for DSMC (O), continuum (—), and free molecular (---) solutions.

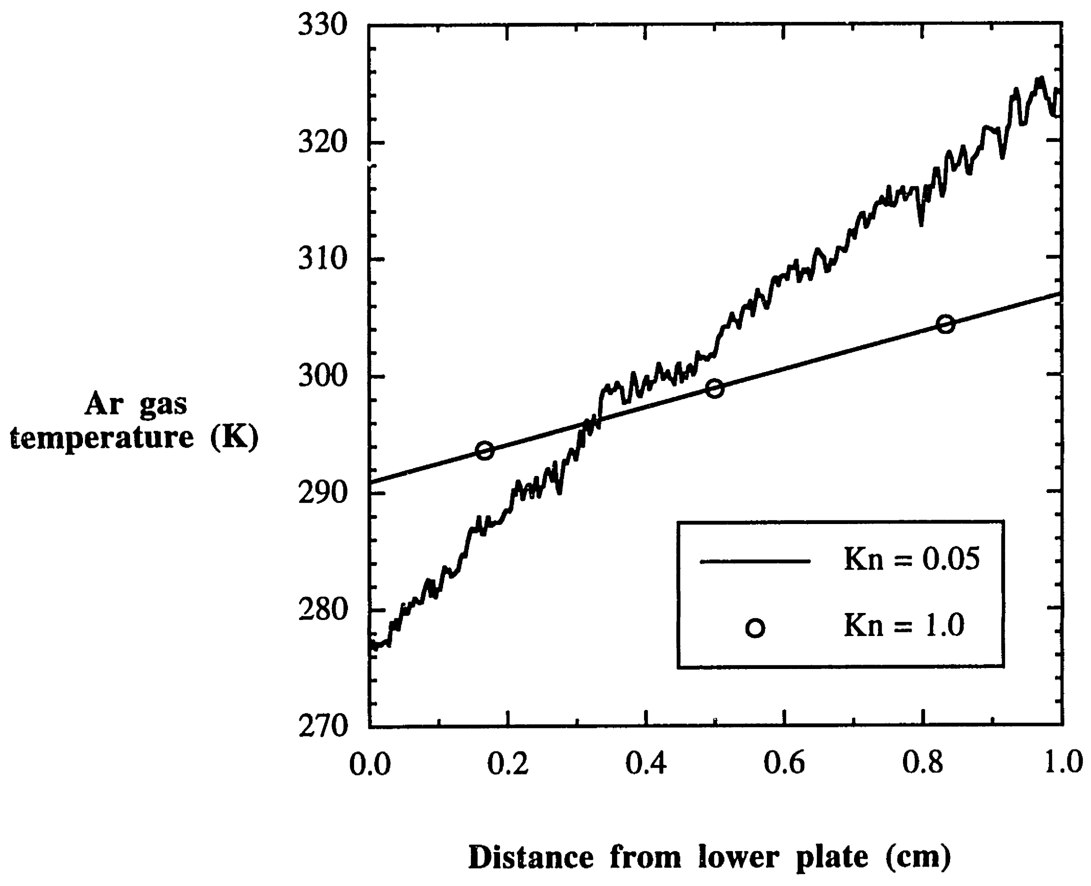

Figure 2-14 : Ar gas temperature profile at Kn = 0.05 (—) and Kn = 1.0 (O) for the DSMC example problem.

workstations will be presented. The simulations will be for a Knudsen number of 0.1 unless otherwise specified with all other conditions the same as presented above.

The primary computational tasks performed in DSMC simulations are the molecular motion, the molecular indexing and the intermolecular collisions of the simulated molecules. The molecular indexing is performed just prior to computing the gas phase collisions and consists of grouping the molecules into an array according to their respective cell locations. The relative amount of CPU time spent performing each task largely depends upon the value of the Knudsen number. The total CPU time increases as the Knudsen number decreases for each of the tasks simply due to the increase in the number of simulated molecules. However, a smaller fraction of molecules will involve gas-surface interactions in the molecular motion routine as the Knudsen number is decreased, so the molecular motion CPU costs escalate more slowly. This is illustrated in Table 2-2 where the percentage of time spent for each of the primary tasks is listed for Knudsen numbers of 0.01, 0.1 and 1.0.

Knudsen Number	**Motion**	**Indexing**	**Collisions**
0.01	39.6 %	8.2 %	52.2 %
0.10	43.4 %	6.9 %	49.7 %
1.00	51.2 %	6.5 %	42.3 %

Table 2-2 : Distribution of total CPU time spent performing various tasks as a function of the Knudsen number for the one-dimensional DSMC example problem.

As mentioned in section 2.6.1 the selection of the random number generator has an impact on the CPU time required in DSMC simulations. This is shown in Table 2-3 where the relative CPU time required for three different random number generators (RNG) are listed. The raw CPU time refers to the amount of time required to generate a large number of random numbers while the DSMC performance refers to the relative time required for steady-state averaging of the problem outlined above. The CPU times are normalized with respect to the performance of the built-in RNG, *ran1*.

RNG	Raw CPU time	DSMC CPU time
ran1	1	1
ran2	0.743	1.005
ran3	1.211	1.078

Table 2-3 : Comparison of CPU costs for various random number generators.

Both *ran1* and *ran2* are simple linear congruential generators and demand less CPU time. The built-in RNG *ran1* is presumably optimized for the particular machine compiler. However, a degree of caution is recommended concerning the use of simple linear congruential generators which may prove to possess an unacceptable amount of sequential correlation. The essence of this type of RNG is seen in the function *ran2*, a quick and dirty random number generator requiring only two lines of Fortran computer code :

```
jran2=mod(jran2*ia+ic,im)
ran2=float(jran2)/float(im)
```

where jran2 is initialized with some integer seed between 0 and im-1. The constants ia, ic and im are moduli which have been optimized to prevent overflow until some predetermined limit has been reached [Press *et al.*, 1992]. The values of the moduli in Table 2-3 were selected for an overflow limit of 2^{31}.

The function *ran3* includes a shuffling procedure which has been proven to break up any sequential correlations which might occur in the functions *ran1* and *ran2*. In addition, it is seen that the additional DSMC CPU time is quite modest. The results of a simple test to illustrate the performance of *ran3* are given in Figure 2-15 where a total of 10^7 random fractions were generated and categorized into discretized bins ranging from 0 to 0.1, 0.1 to 0.2, *etc*. The distribution of random fractions is seen to be quite uniform. The function *ran3* was employed in all of the simulations to follow.

The most efficient platform for DSMC computations is a dedicated computer workstation. Although the memory requirements for relatively small problems would permit the use of personal computers, the computational speed becomes a limiting factor. At the same time the DSMC algorithm is not well-suited for running on supercomputers due to the monetary expense and the difficulty in exploiting the vectorized supercomputer architecture [G. Bird, 1990]. The relative CPU times required for time-averaging the example problem outlined above are listed in Table 2-4 for several different workstations which have been utilized during the course of this research. Also shown are the respective MFLOP ratings for a standard LINPACK benchmark test [Dongarra, 1993].

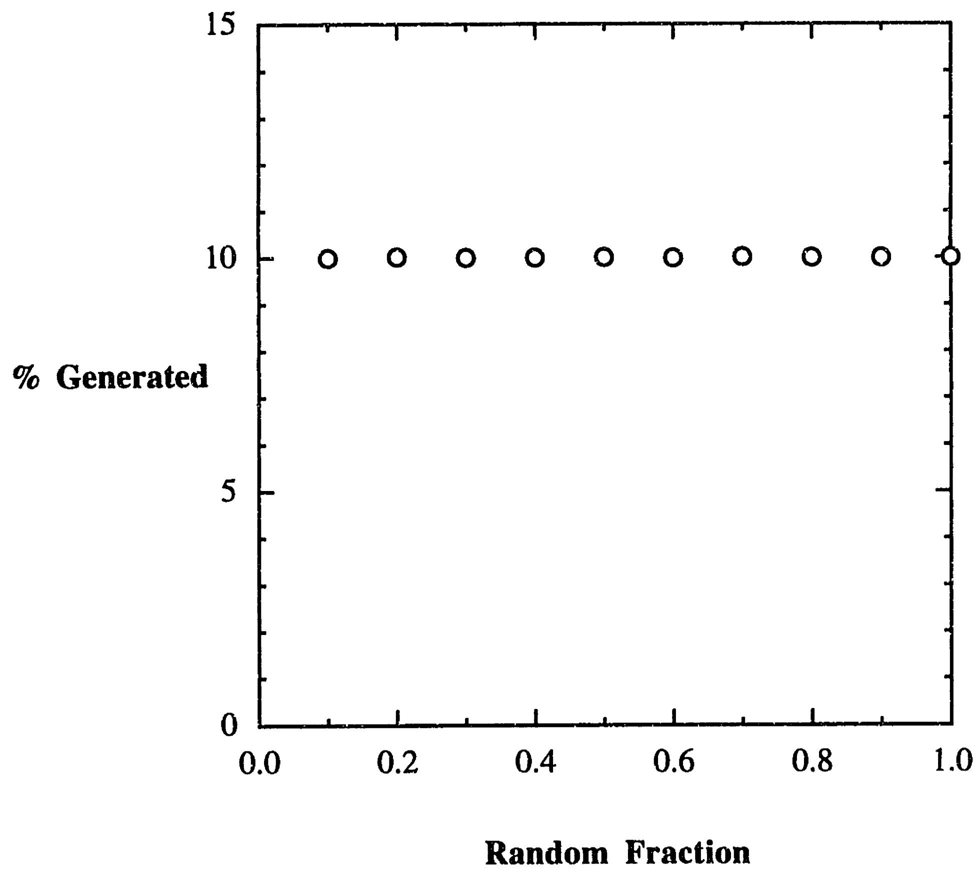

Figure 2-15 : Distribution of 10^7 random numbers generated by RNG *ran3*.

Machine	MFLOP Rating	DSMC CPU time
VAXstation 3100	0.78	29.28
DECstation 5000/200	3.7	2.70
IBM RS6000/350	19	1.27
HP Apollo 735	41	1

Table 2-4 : Comparison of CPU costs for simulation of the one-dimensional DSMC example problem on various workstations.

2.9 Speedup of DSMC computations

The implementation of complex geometries and detailed molecular descriptions, including internal energy modes and chemical reactions, have marked the maturation of the DSMC method. This has necessarily been accompanied by efforts to reduce the lengthy computational times which are associated with Monte Carlo techniques. These efforts have primarily focussed on vectorization and parallelization of the DSMC algorithm, each of which will be briefly discussed below.

2.9.1 Vectorization of the DSMC algorithm

The most timely computational task within the DSMC algorithm is usually the intermolecular collision routine. The normally used time-counter method is not well-suited for vectorization, however, as the number of collisions to be simulated within each cell is

not known *a priori*. This limitation has lead to the development of an alternative approach known as the no time-counter (NTC) method which lends itself to complete vectorization of the innermost loop [G. Bird, 1988b]. This is made possible by the specification of the number of attempted intermolecular collisions beforehand, each of which is accepted according to the probability given in equation (2-33). The expression in equation (2-34) for the collision rate per molecule per unit volume may be rewritten to express this quantity :

$$N_{attempts} = \frac{1}{2} \frac{N_m^2 (\sigma v_r)_{max} \, \delta t}{V_c}, \qquad (2\text{-}70).$$

where N_m is the number of simulated molecules in the cell and $(\sigma v_r)_{max}$ is interactively adjusted as the simulation proceeds.

The innermost loop in the collision routine no longer cycles over the collisions within a particular cell as illustrated in Figure 2-9, but over the cells themselves. This vectorized loop selects potential collision partners from those cells which have not yet reached their specified quota given by equation (2-70), denoted by the setting of a flag as this is accomplished for each cell with the repeated execution of this loop.

The molecular motion of the molecules may likewise be vectorized, with considerably less effort as well. The formula for vectorization is essentially to move all of the molecules simultaneously, appropriately flagging those which have interacted with a boundary for a subsequent loop which handles this task.

The reported values of vector/scalar speedup have ranged from 2.4 [Boyd, 1991] to 6 [Prisco, 1991], where the former demonstrated the ability to execute extremely large simulations using 10^7 molecules and 375,000 cells. This speedup represents a rather modest advantage considering the high costs associated with supercomputing. The

potential speedup associated with running on massively parallel machines is considerably greater, though, as will be discussed below.

2.9.2 Parallelization of the DSMC algorithm

The structure of the DSMC algorithm makes it extremely well-suited to run on multiple processor machines. Each processor may be assigned the task of moving a fraction of the total number of molecules or performing the collisions in one or more particular cells. This is possible since each processor may carry out the events independent of the outcome of events simultaneously occurring in other processors. The theoretical speedup is then given by the number of processors, N_p, although the actual speedup is usually somewhat less. This is due to communication between the host program (assigns task to nodes) and the nodes, internode communication, and the failure to keep all of the nodes busy - a task referred to as load balancing. This discrepancy between the theoretical speedup and the actual speedup represents the major challenge for the programmer.

Results of the implementation of the DSMC algorithm on parallel machines have recently appeared in the literature [Furlani and Lordi, 1990; Wilmoth, 1991]. In each case, the actual speedup increasingly deviated from the theoretical speedup as the number of processors was increased. This results from the fact that the host processor must perform a limited number of tasks and the execution time then becomes limited by the execution of these tasks. Despite this limitation, an order of magnitude speedup has been reported for 16 processors [Wilmoth, 1991] - a promising result considering the lesser speedup achieved with the more expensive vectorized computations on the Cray supercomputer.

2.9.3 Tricks-of-the-trade

In addition to the algorithmic modifications mentioned above, there are a number of other more subtle measures to be taken which may contribute to a more efficient and computationally lean DSMC simulation. Since the demand on CPU time is the primary consideration, it is helpful to substitute division operations with multiplication and to avoid repeated calls to CPU-intensive functions such as SQRT or any of the trigonometric functions (COS, SIN, *etc.*) if at all possible. The alternative is to use a polynomial expansion of the transcendental function as shown here for SQRT and SIN :

$$\mathrm{SQRT}(X) \approx 0.188 + 1.484X - 1.098X^2 + 0.430X^3 + \ldots \qquad (2\text{-}71).$$

$$\mathrm{SIN}(X) \approx X - \frac{X^3}{3!} + \frac{X^5}{5!} - \frac{X^7}{7!} + \ldots \qquad (2\text{-}72).$$

The use of lookup tables for the storage of frequently accessed data is another method of decreasing the computational costs. For example, in the hard sphere and VHS molecular models, the isotropic scattering of each collision pair requires the generation of a random unit vector in spherical coordinates. The selection of one vector involves the generation of two random numbers and calls to the SIN,COS, and SQRT functions [G. Bird, 1976]. The alternative is to generate a large number of vectors outside of the simulation just once. This data file may then be read into any number of simulations and randomly sampled from, reducing the computational costs of simulating the gas phase collisions. For the example problem outlined in section 2.8, typical savings in the collision routine when employing such a lookup table were around 7%.

At least half of the computational costs of performing DSMC simulations are spent during the approach to a steady flow field. One obvious way of reducing the transient period is to initiate the simulation from a state which is as close as possible to what may be expected for steady-state conditions. This initial guess may be provided by a continuum solution of the flow field, if available. If the simulation study involves the investigation of several flow field parameters where repeated runs are required, the use of restart files would be a more practical approach. Restart files are essentially snapshots of the steady-state flow field from a previous run where the molecular positions and velocities are stored. This cuts down considerably on the amount of time spent approaching steady flow conditions.

2.10 DSMC simulations in CVD process models

The success of the DSMC method in aerospace applications has motivated its use in other areas as well. The first application of the DSMC method to analyzing rarefied gas flows in the microelectronics industry was for flow and thin film deposition over micron-sized features [Ikegawa and Kobayashi, 1989; Yuuki *et al.*, 1989]. The continual reduction in feature size coupled with the strict control required over the film properties has elevated the importance of gaining a fundamental understanding of these types of flows. There are no inherent limitations within the DSMC method itself which restricts it from being applied to these microscale gas transport problems. However, the presence of a moving boundary in the DSMC simulation given by the growing film presents new challenges for extending the versatility of the DSMC method.

The work of Nanbu and coworkers represents some of the pioneering efforts in applying the DSMC method to modelling low pressure CVD flows [Igarashi *et al.*, 1990;

Nanbu *et al.*, 1991]. Their studies included simulations of SiH_4/H_2 gas mixtures in a tilted substrate reactor (2-D parallel plate geometry) and around a section of closely spaced wafers (2-D axisymmetric geometry). The heterogeneous decomposition of SiH_4 was modelled by assigning a finite surface reaction probability. The effects of various flow parameters on the growth rate variations were then investigated. The primary deficiency in their simulation studies appears to be the treatment of the downstream boundary condition where the boundary was approximated as a complete vacuum or was treated as an unknown parameter.

More recently, the DSMC method was used to simulate the gas flow associated with a sputter deposition reactor [Kersch *et al.*, 1992]. The simulation model consisted of an axisymmetric reactor with a metal source target at one end and the substrate at the other. The additional complexities involved here were the radially-dependent source target flux, which was specified according to experimental data, and a modified molecular model to account for the large degree of translational nonequilibrium between the source atoms (*e.g.* Ti) and the background gas, in this case argon.

Chapter 3 : Isothermal Rarefied Gas Flows in the LPCVD Reactor

3.1 Motivation for a rarefied gas dynamics simulation model of the LPCVD reactor

A fundamental description of the underlying physics and chemistry of LPCVD processes is essential for the purposes of reactor design and optimization and has been the focus of numerous detailed process models [Kuiper *et al.*, 1982; Jensen and Graves, 1983; Middleman and Yeckel, 1986; Roenigk and Jensen, 1987; Hopfmann *et al.*, 1991; Badgwell *et al.*, 1992b]. The typical modelling approach has been to describe the gas flow in a continuum sense, entirely appropriate for most conventional LPCVD processes. As discussed in Chapter 1, however, a continuum description is no longer valid as the gas becomes rarefied.

With the advent of the UHV-CVD process, where the gas is well into the transition and free molecular flow regimes, a new modelling approach is needed to describe rarefied gas flows in the LPCVD reactor. This also applies to interwafer gas transport in conventional LPCVD when the operating pressures are reduced to a fraction of a Torr. In a broader sense, new tools are needed to analyze the increasingly encountered occurrences of rarefied gas flows in CVD processes. In this Chapter a two-dimensional DSMC gas dynamics model is outlined and results of a systematic investigation of rarefied gas flows in the LPCVD reactor are presented.

3.2 Formulation of a simulation model of the UHV-CVD gas dynamics

3.2.1 Model assumptions

The axisymmetric assumption

An exact model of the multiwafer LPCVD reactor would be fully three-dimensional, owing primarily to the asymmetry of the quartz wafer boat and the gas inlets. The DSMC simulation model is a two-dimensional axisymmetric approximation of the LPCVD reactor. This is accomplished at the expense of neglecting the presence of the quartz wafer boat and assuming a uniform inflow of gas around the perimeter of the reactor tube at the upstream end. The quartz wafer boat is designed to have a minimal influence on the gas flow and deposition by minimizing the amount of surface area comprising the boat. Therefore, its removal from the flow simulations seems to be an appropriate simplification to the model. The approximation of the inlet gas stream is illustrated in Figure 3-1.

Gas-surface interactions

Molecules impinging upon a solid surface may follow one of two possible pathways, reflection or incorporation, depending upon the outcome of a comparison between the reactive sticking coefficient and a random number. Molecules which are reflected are assumed to reflect diffusely with complete thermal accomodation to the surface temperature. This is an appropriate boundary condition for polyatomic species which interact with the surface to some degree [Goodman and Wachman, 1976]. In addition, the wafers are assumed to be infinitely thin in the simulation model, *i.e.* no gas-surface interactions are permitted along the edges of the wafers.

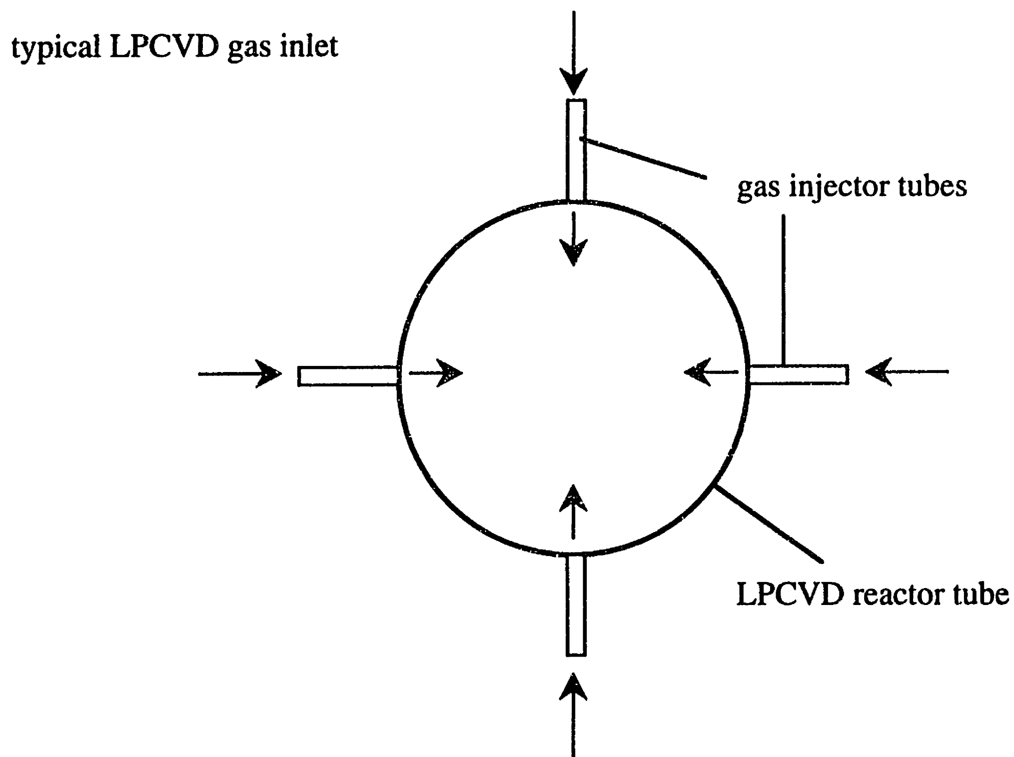

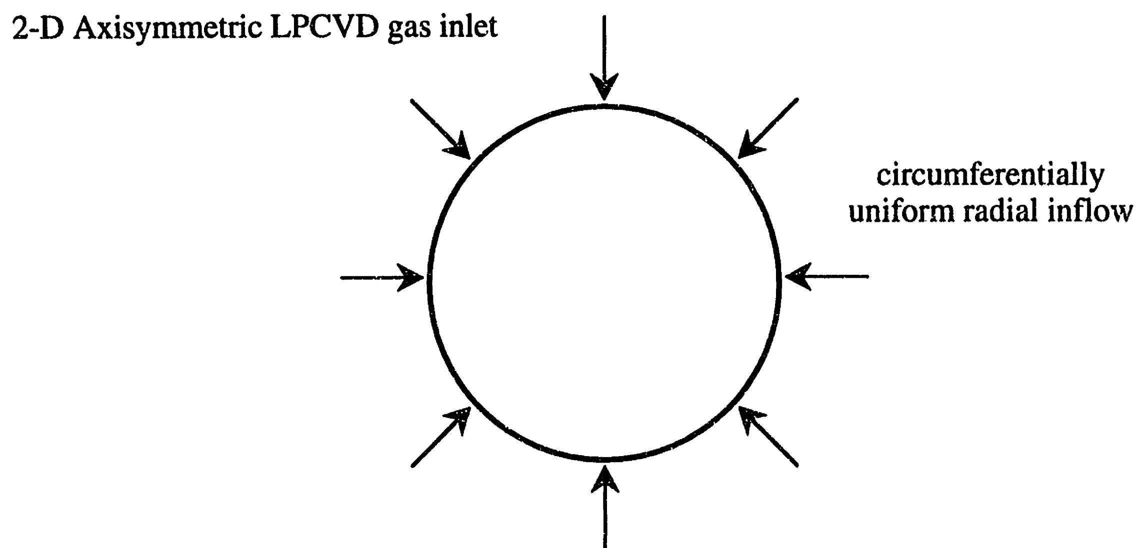

Figure 3-1 : Two-dimensional axisymmetric approximation of the gas inlet for the LPCVD reactor model.

The reactant sources most relevant to UHV-CVD processes are primarily silane (SiH_4) and germane (GeH_4), and to a lesser degree disilane (Si_2H_6). Both silane and germane are characterized by very small reactive sticking coefficients (~10^{-4}). In this case, it is difficult to obtain a statistically sufficient sampling of the surface reactions without the expense of prohibitively lengthy simulation runs. The approach used to circumvent this difficulty is to sample the gas flux to the surface, instead, and compute the growth rate as the product of the surface flux and the reactive sticking coefficient :

$$\text{Growth Rate} = \text{Surface Flux} \times \text{Reactive Sticking Coefficient} \qquad (3\text{-}1).$$

At the same time, it is recognized that the low conversion rates result in a negligible amount of reaction by-products being delivered from the growth surface. Therefore, for silane and germane, the desorption of molecular hydrogen may be completely ignored in the simulation. If a disilane molecule reacts with the surface, the disilane molecule is removed and two hydrogen molecules are formed and desorbed at the point of impact within the time step allotted to the molecular motion. Implicit in both of these approaches is the uncoupling of the surface processes - diffusion and chemistry - from the gas phase transport. The surface kinetics are, instead, implicitly recognized in the assignment of the reactive sticking coefficient as outlined in Chapter 2.

3.2.2 The DSMC cell network

A two-dimensional axisymmetric network of cells for a typical UHV-CVD simulation is shown in Figure 3-2. The location of the wafers is indicated by the darkened lines. The cell size is based on the mean free path for the inlet conditions. All of the cells are dimensioned identically since the density remains the same order of

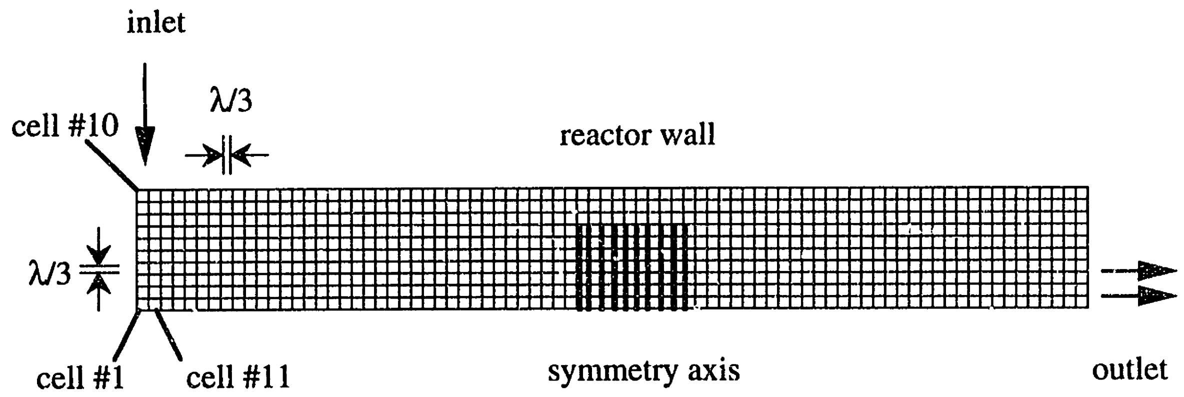

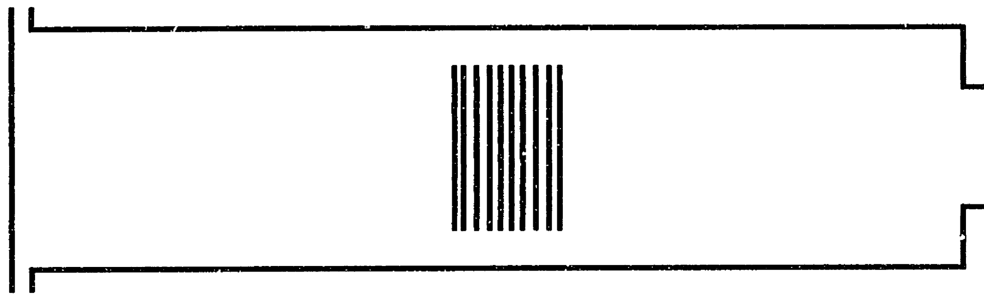

Figure 3-2 : Typical DSMC cell network for UHV-CVD gas flow simulation.

magnitude throughout the reactor. This allows the use of a very efficient algebraic method of determining the cell location, a task which is performed with every move of each simulated molecule. The cell numbering scheme, indicated in Figure 3-2, numbers the cells in a radial sequence from the axis to the reactor wall, proceeding from one axial position to the next downstream position. The current cell location is then easily determined from the coordinates of the molecule, written here in Fortran as :

```
ICZ = INT(Z*CDIMINV) + 1        (3-2a).

ICR = INT(R*CDIMINV) + 1        (3-2b).

NC = (ICZ-1)*NCR + ICR          (3-2c).
```

where Z and R are the axial and radial molecular position coordinates, ICZ and ICR are the axial and radial cell markers, NCR is the total number of cells in the radial direction and the molecule resides in cell number NC. The parameter CDIMINV is simply the inverse of the cell dimension, utilized here in order to substitute division with the computationally less expensive multiplication.

3.2.3 Simulation of internal flows using DSMC

The DSMC algorithm was originally formulated for simulating external gas flows. In this case, it is a straightforward matter to compute the influx of simulated molecules at the open boundaries since the flow field properties may be specified some distance away from the object of interest. The DSMC open boundary conditions are not influenced by the details of the flow for external flows. For internal flows, however, the change in the

flow properties from the inlet stream to the outlet stream is dictated by the flow environment. More importantly, the boundary conditions may not be specified in an *a priori* fashion, necessitating a modification to the conventional DSMC algorithm.

In the UHV-CVD simulations, the inlet gas stream properties - density, composition, stream velocity and temperature - were specified as input to the simulation. The molecular influx from the upstream boundary was then computed according to the approach outlined in section 2.3.2. The influx from the downstream boundary was treated in a dynamic fashion according to the prevailing conditions at the boundary. This involved sampling the properties of the gas in the cells adjacent to the downstream boundary. The prevailing properties, and thus the molecular influx, were then updated at each time step during the transient startup and once every several time steps during steady flow conditions.

3.3 Reference simulation : isothermal flow of a pure component gas

3.3.1 Flow field specifications

The results of a reference base case UHV-CVD flow simulation will be presented in this section. The isolation of this particular simulation will serve to foster the discussion of issues which are relevant to all of the simulations to follow. In addition, it serves as a convenient reference point from which to assess the influence of various flow parameters as they are explored in later sections.

The reactor dimensions and operating conditions are specified to closely match the dimensions of Meyerson's research scale UHV-CVD system at IBM [Meyerson, 1986]. The reactor walls and each of the ten wafers are set at a uniform temperature of

900 K and the entering gas stream is thermally equilibrated. The inlet number density is set to correspond to that of an ideal gas at 10 mTorr of total pressure. In addition, the inlet stream velocity corresponds to the linear velocity of a 48 sccm volumetric flow rate around the annular strip which defines the inlet. The remaining specifications of the simulation are listed in Table 3-1 below.

Inlet Gas Properties	Gas Species	Hydrogen
	Temperature	900 K
	Stream Velocity	12750 cm/s
	Number Density	1.073×10^{14} cm^{-3}
	(Pressure)	(10 mTorr)
Reactor Details	Reactor Length	40 cm
	Reactor Diameter	10 cm
	Inlet Annulus Width	0.5 cm
	Outlet Diameter	2.5 cm
	Number of Wafers	10
	Wafer Diameter	7 cm
	1st Wafer Position	18.5 cm
	Interwafer Spacing	0.5 cm
Simulation Parameters	Cell Dimension	0.5 cm
	Time Step	5.0 μs
	Molecular Model	Variable Hard Sphere
	- VHS Parameter	0.17
	- Reference Temperature	273 K
	- Reference Diameter	2.88 Å

Table 3-1 : Conditions for the reference isothermal UHV-CVD flow simulation.

3.3.2 Approach to steady-state

The specification of the initial flow field will largely determine the amount of simulation time spent in the transient startup period. In the absence of a restart file from a previous run, the simulation may be initiated from a completely evacuated reactor or with an isothermal, constant density stream in place. In either case, the total number of molecules in the reactor is a good measure of whether or not the flow has reached steady-state. This is illustrated in Figure 3-3 where the approach to a steady flow is shown for both cases. It is seen that steady flow is achieved between 15 and 20 ms for both the uniform stream initiation and the initially evacuated reactor, although the computational effort is much less for the initially evacuated case since fewer molecules are tracked during the transient. Subsequent simulations using the restart files from previous runs required only about 20% of the transient time reflected in Figure 3-3.

3.3.3 Density and pressure variations in the LPCVD reactor

The simulated H_2 gas density field in the LPCVD reactor, normalized with respect to the incoming gas density, is shown in Figure 3-4a. The distinguishing feature of the UHV-CVD gas flow is the compressibility of the gas, contrary to the assumption of an incompressible gas commonly used in conventional CVD reactor modelling [Jensen, 1993]. The strongest density variations are seen to occur where the flow is constricted or expanded - primarily at the entrance and exit of the annular flow region, and to a lesser extent at the gas inlet and outlet. This is better illustrated in Figure 3-4b where the radially-averaged density is plotted versus the axial position. The pressure field variations shown in Figure 3-5 correspond with the density variations of Figure 3-4. This is expected for an isothermal low density gas as suggested by the ideal gas equation of

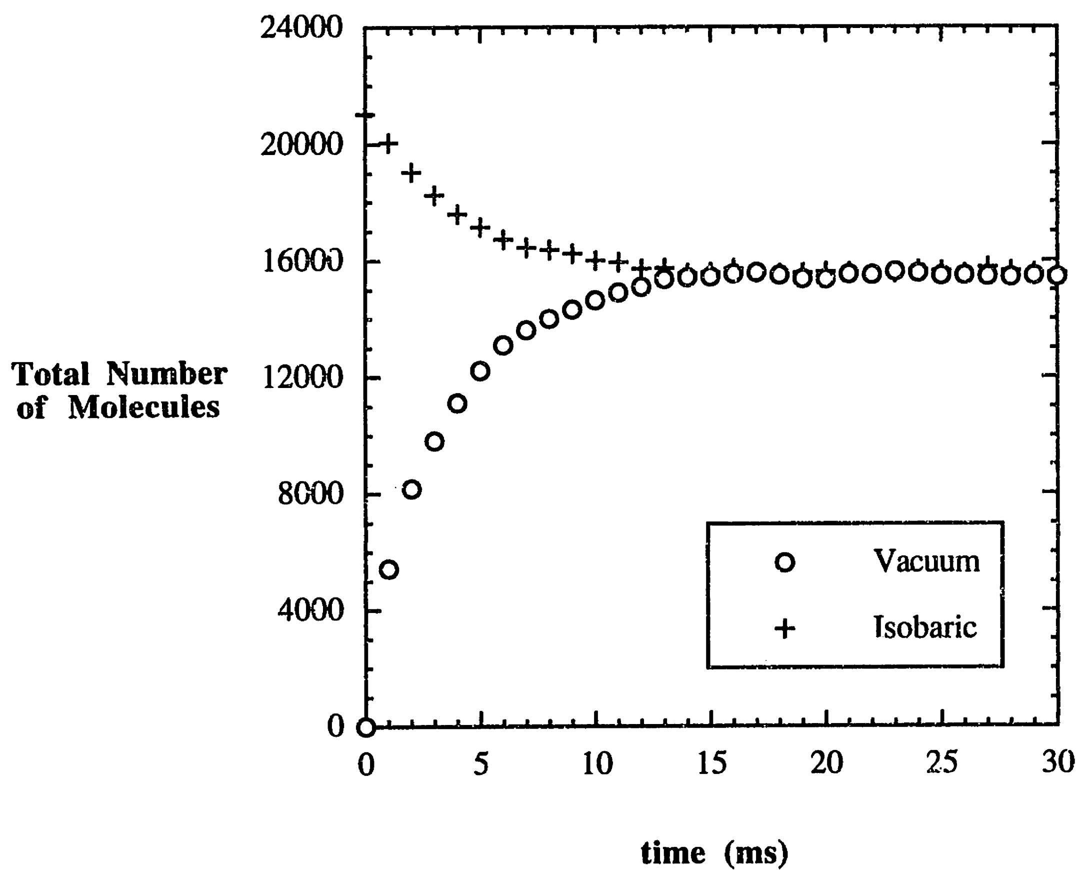

Figure 3-3 : Total number of simulated H_2 molecules vs. flow time for startup from vacuum (O) and isobaric (+) conditions for the reference isothermal simulation.

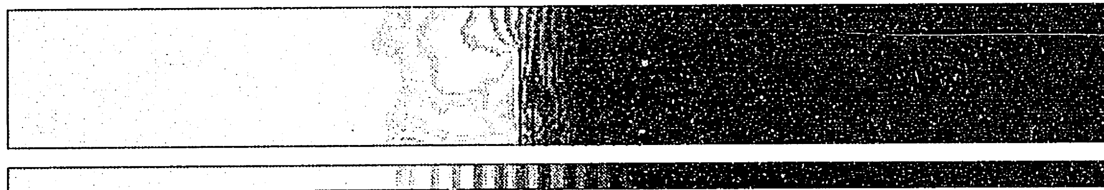

Figure 3-4a : Normalized H_2 density field for the reference isothermal simulation.

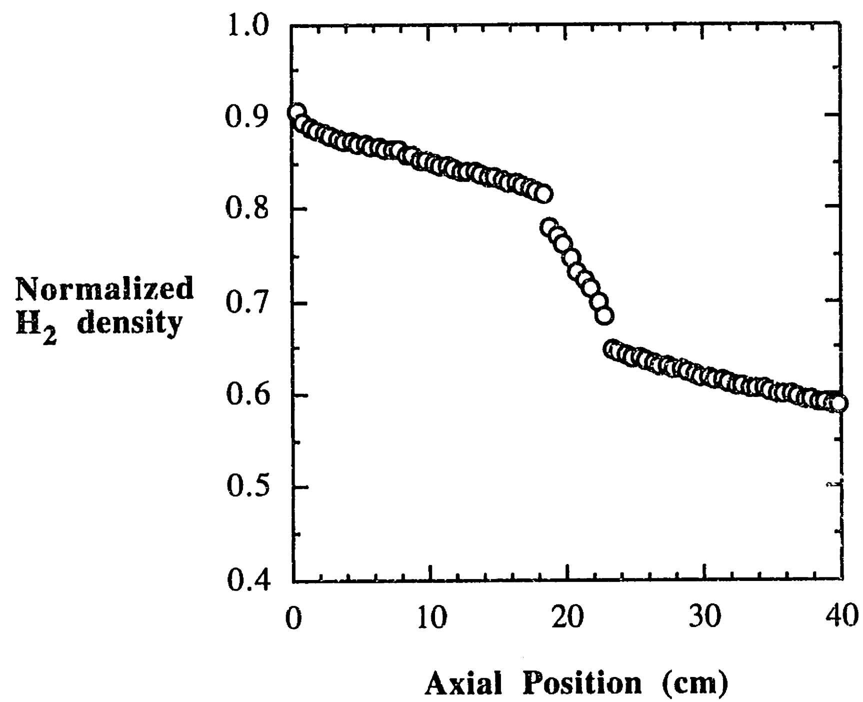

Figure 3-4b : Normalized H_2 density profile for the reference isothermal simulation.

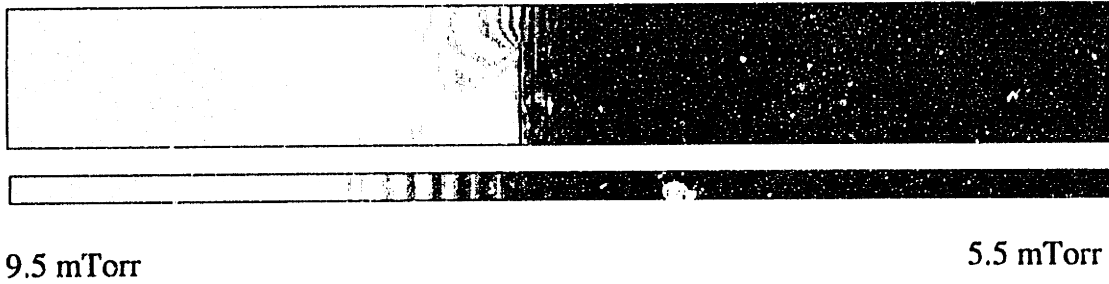

Figure 3-5a : H_2 pressure field for the reference isothermal simulation.

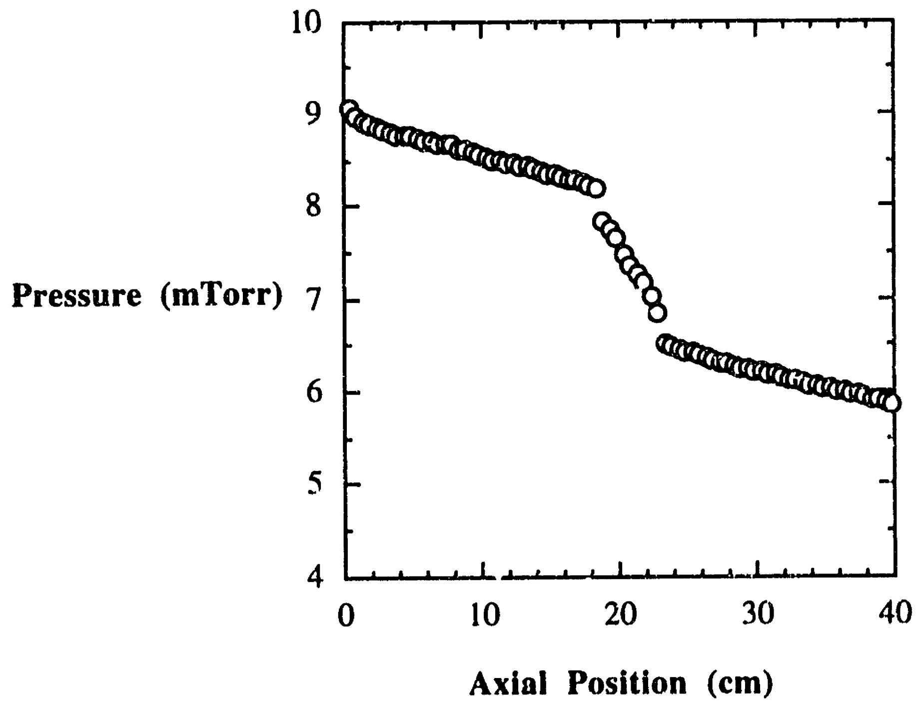

Figure 3-5b : H_2 pressure profile for the reference isothermal simulation.

state as written in equation (1-13). The remainder of the isothermal simulations in this chapter will be characterized in terms of the radially-averaged number density with the understanding that the pressure variations follow accordingly.

The pronounced density variations across the wafer stack have a significant impact on the flux of molecules to the wafers. This is illustrated in Figure 3-6 where the flux to the front side of each of the wafers, normalized with respect to the flux to the first wafer, is plotted versus wafer position. The flux decreases along the wafer stack in direct correspondence to the number density variation. Also plotted in Figure 3-6 are the radial variations in the fluxes, defined as the ratio of the flux at the wafer center to the flux at the wafer edge. The radial uniformity is seen to be greater than 97% across the entire wafer stack.

It is instructive to compare the DSMC results with those obtained from a semi-empirical free molecular analysis frequently employed by vacuum technologists [O'Hanlon, 1989]. This approach computes the overall molecular transmission probability through a vacuum apparatus by approximating the apparatus as a series of elementary geometrical structures. A section of the LPCVD reactor, consisting of an upstream region, several wafers, and a downstream region, may be approximated as an empty tube section, a series of apertures and short empty tube sections, and another empty tube section, respectively. An equation derived by O'Hanlon for this geometry using Haefer's technique for series calculations of overall transmission probabilities is given by :

$$\frac{1}{\alpha_T} = \frac{1}{\alpha_{upstream}} + \frac{1}{\alpha_{downstream}} + \frac{m}{\alpha_{annulus}} + m\frac{A_{tube}}{A_{annulus}} - 2m - 1, \qquad (3\text{-}3).$$

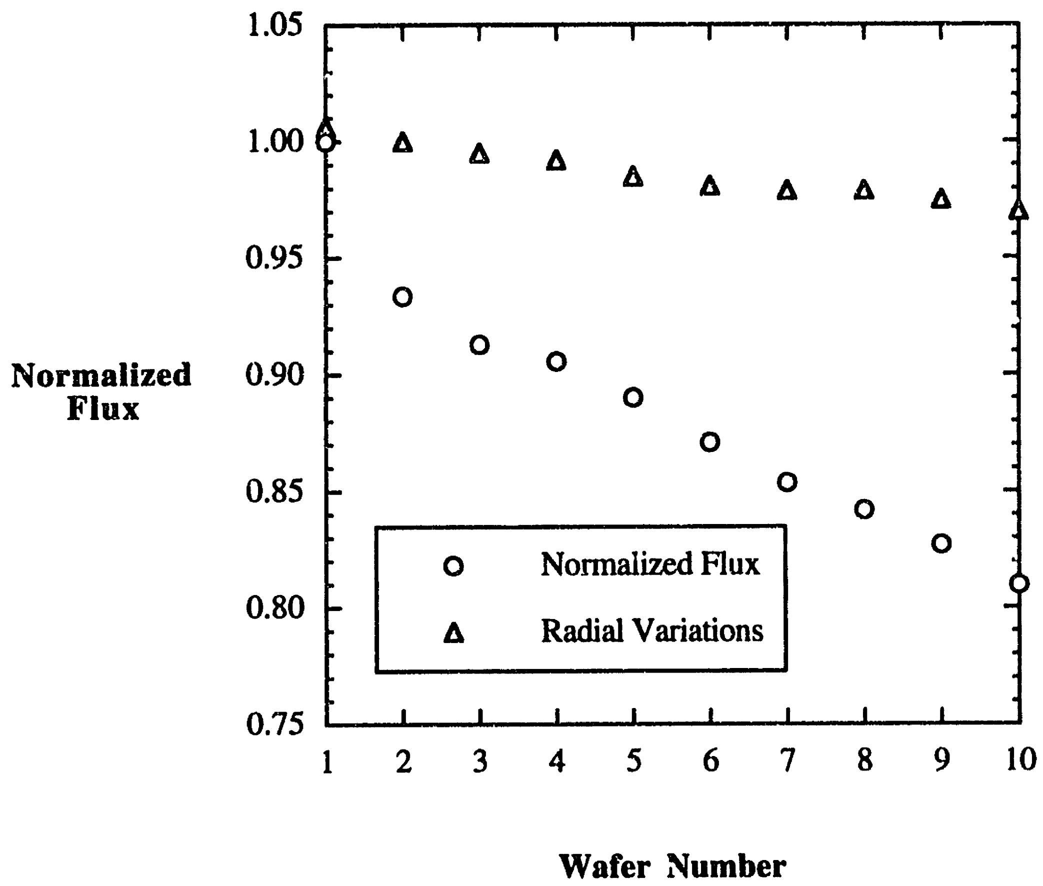

Figure 3-6 : Normalized flux to wafers (O) and radial flux variations (Δ) for the reference isothermal simulation.

where α is the transmission probability, m is the number of wafers, and A is the cross-sectional flow area [O'Hanlon, 1989]. The individual transmission probabilities appearing on the right hand side of equation (3-3) are functions of the tube aspect ratio.

A section of the LPCVD reactor specified in the reference simulation, consisting of the wafer stack and two 10 cm sections upstream and downstream of the wafers, is now considered for comparison of the two approaches. The transmission probability is readily computed in the DSMC simulation. This is accomplished by monitoring the fraction of a large number of molecules crossing the upstream plane which ultimately cross the downstream plane.

The transmission probability determined from the semi-empirical approach of equation (3-3) was 0.0769 while the DSMC simulation gave a transmission probability of 0.13824. The discrepancy between the computed transmission probabilities may be due in part to the fact that the semi-empirical approach is a series calculation which does not consider the coupling between adjacent sections.

3.3.4 Macroscopic velocity and molecular motion

The bulk motion of the gas through the LPCVD reactor is the collective result of the individual motion of the H_2 molecules which comprise the gas. The bulk motion or macroscopic velocity, the quantity which appears in the continuum conservation equations, is roughly 2% of the average thermal velocity for the UHV-CVD reference simulation. In the UHV-CVD simulations the macroscopic velocity is computed in each cell by time-averaging the net velocity of the cell's resident molecules over a number of time steps. The macroscopic velocity vector field for the reference simulation is shown

in Figure 3-7. The H_2 gas is accelerated as it is throttled through the annular flow region, in contrast with the relatively stagnant gas residing in the interwafer regions.

The corresponding streamlines of Figure 3-7 would suggest that the gas moves through the reactor in a uniform fashion, largely bypassing the interior wafer surfaces. For a continuum gas the molecules are essentially confined by intermolecular collisions to an element of gas of the order of a cubic mean free path. The motion of this element of gas through the reactor thus defines the paths of the constituent molecules and is governed by the macroscopic velocity. As the gas becomes rarefied the molecules are no longer confined by intermolecular collisions and, for internal flows, their motion is largely influenced by surface collisions. The deviation of the molecules from the paths of the streamlines would then provide insight into the degree of flow rarefaction and the corresponding importance of gas-surface interactions on the molecular transport.

This information is readily determined from the DSMC simulations since the location of each simulated molecule is monitored at every time step. Some representative molecular trajectories from the reference simulation are shown in Figure 3-8 where a cross-sectional view of the three-dimensional molecular motion in the LPCVD reactor is given. The H_2 molecules are seen to deviate substantially from the streamlines suggested in Figure 3-7. This reflects the fact that it is the thermal velocity rather than the macroscopic velocity which governs the molecular motion, in contrast with continuum gases. The influence of gas-surface interactions on the transport is quite obvious from the trajectory plots as well.

3.3.5 Residence time distributions in the LPCVD reactor

The residence time distribution is an important fundamental property for reactor analysis [Hill, 1977]. In CVD processes where it is desirable to obtain extremely abrupt

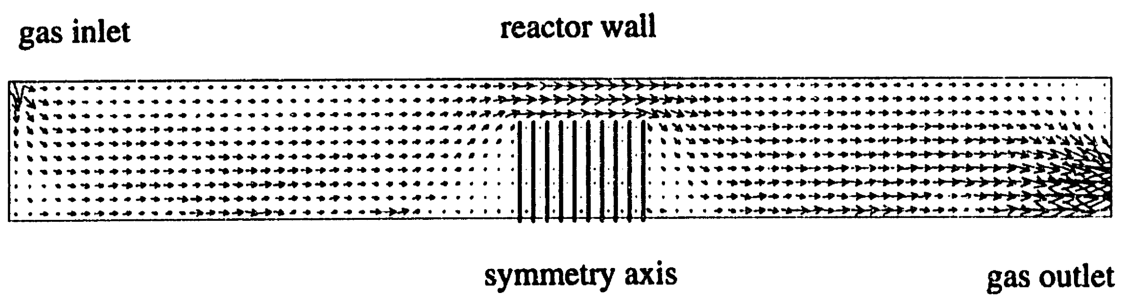

Figure 3-7 : Macroscopic velocity field for the reference isothermal simulation.

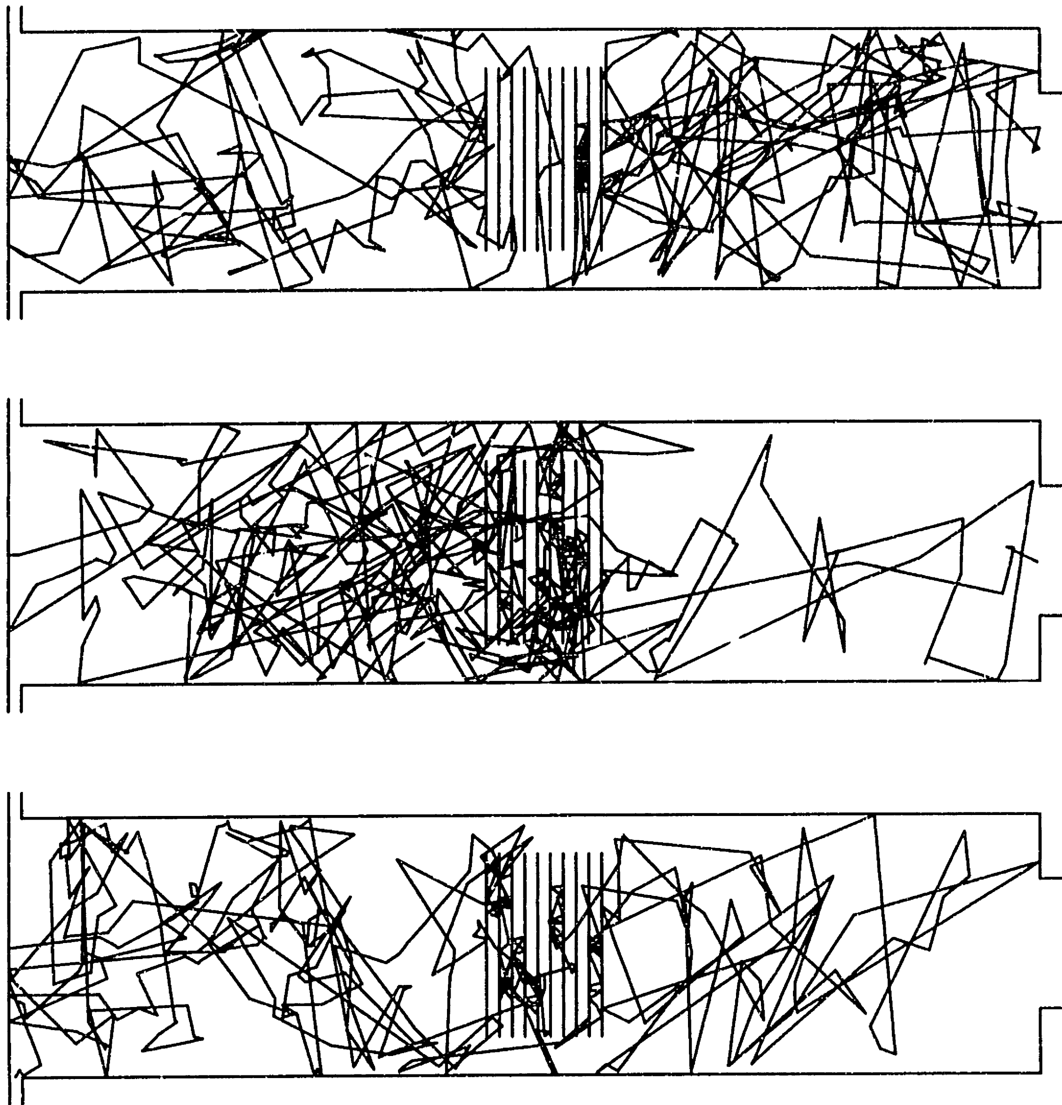

Figure 3-8 : Typical H_2 molecule trajectory plots for the reference isothermal simulation.

growth interfaces, it is of paramount importance to be able to control the residence time of the film growth reactants. The residence time distribution is difficult to measure experimentally, however. This usually involves the introduction of a trace amount of labelled species into the reactor and the subsequent monitoring of the reactor effluent. The residence time distribution is then deduced from the time required to collect the entire portion of the tagged species which was introduced.

The residence time distribution in the LPCVD reactor is readily calculated in the DSMC simulation. It is a simple matter of tagging each of the molecules entering at the inlet with the current flow time and noting the time required to exit downstream. The residence time distribution is then constructed from the individual residence times of a large number of molecules.

The residence time distribution for the reference simulation, normalized with respect to its maximum value, is shown in Figure 3-9. Also shown is the corresponding cumulative residence time distribution. The long tail of the residence time distribution is a result of the molecules which have become trapped in the interwafer regions for a lengthy time period. The average residence time was computed to be 2.20 ms. A H_2 molecule travelling at its average thermal velocity at 900 K would require around 0.13 ms to traverse a distance the length of the reactor. The difference between these two times provides a measure of the deviation of the molecules from a straight line path through the reactor resulting from intermolecular collisions and gas-surface interactions.

The molecular trajectory plots in Figure 3-8 indicated that the motion of the H_2 molecules in the reference UHV-CVD flow was dictated by the thermal velocity rather than the macroscopic velocity. The thermal velocity of a molecule is inversely proportional to the square root of the molecular mass. This suggests that the residence time in the LPCVD reactor for UHV-CVD conditions should depend upon the molecular weight of the species. This indeed was found to be the case as is reflected in the

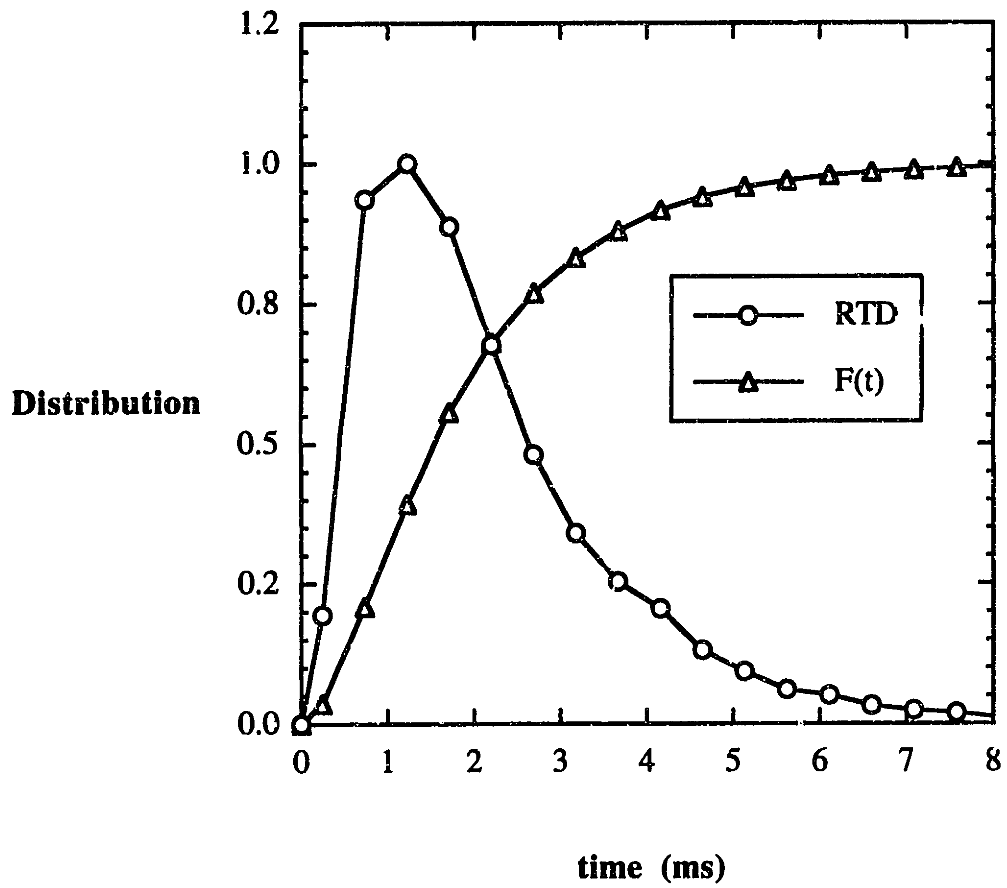

Figure 3-9 : Normalized residence time distribution (O) and cumulative residence time distribution (Δ) for the reference isothermal simulation.

residence time distributions for H_2, N_2 and Ar plotted in Figure 3-10. The simulation conditions were identical for each with the exception of the VHS parameters which are unique to the species. The average residence times for N_2 and Ar were found to be 8.19 and 9.66 ms, respectively. The ratio of the average residence times of the three species, 1 : 3.72 : 4.39, almost corresponds exactly with the ratio of the square root of the molecular weights, 1 : 3.74 : 4.47. This gives clear evidence of the fact that the thermal velocity dictates the motion of the gas in UHV-CVD flows.

3.3.6 Statistical analysis of the UHV-CVD simulations

The principles of statistics may be applied to the DSMC results in order to obtain an estimate of the accuracy of the converged results or, conversely, to determine the number of samples required in order to obtain a specified accuracy. An accuracy of, say 95%, is characterized by a confidence interval which defines the range of values of a particular quantity which has a 95% probability of containing the exact value. Here the exact value refers to that which would be obtained by averaging an infinite number of samples.

The central limit theorem of mathematical statistics states that the distribution of errors tends to a normal or Gaussian distribution as the sample size is increased [Box *et al.*, 1978]. The normal distribution of some arbitrary variable x may be written as :

$$f(x) = \frac{1}{\sigma\sqrt{2\pi}} \exp\left\{ - \left(\frac{x - \overline{x}}{4\sigma} \right)^2 \right\}, \qquad (3\text{-}4).$$

where $\overline{x}$ and σ are the mean and the standard deviation of x, respectively, defined by :

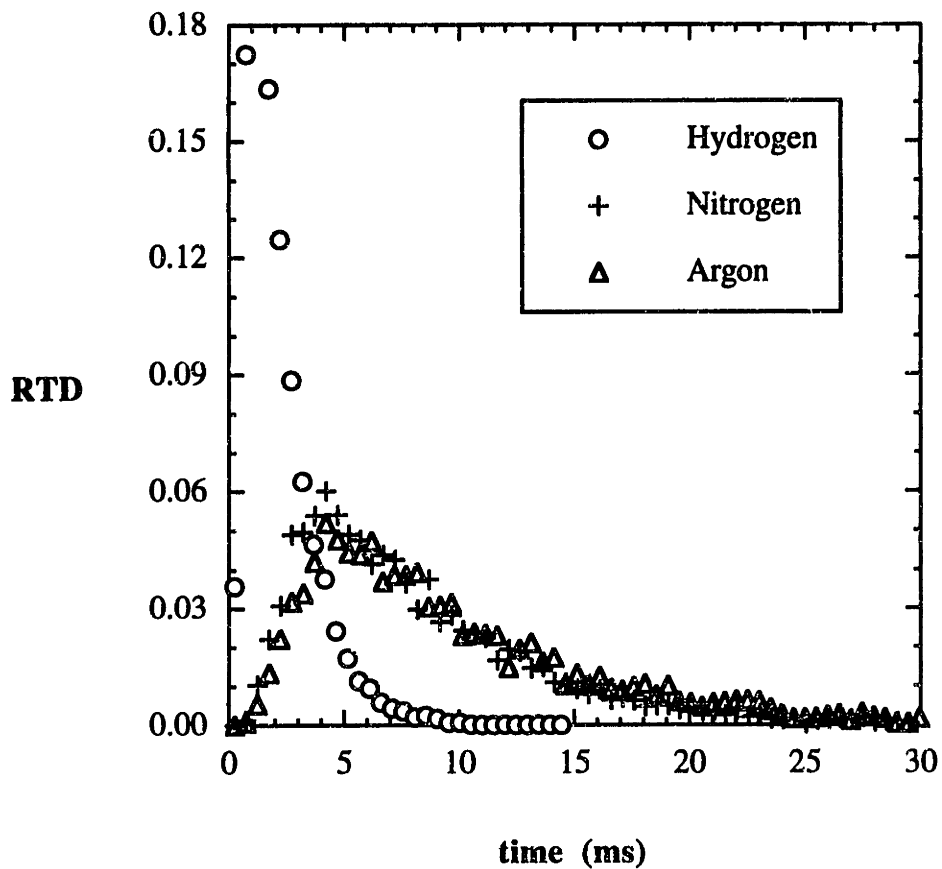

Figure 3-10 : Residence time distributions for H_2 (O), N_2 (+) and Ar (Δ) for the reference isothermal conditions.

$$\overline{x} \equiv \frac{1}{N_s}\sum_{i=1}^{N_s} x_i, \tag{3-5}$$

$$\sigma^2 \equiv \frac{1}{N_s-1}\sum_{i=1}^{N_s} (x_i-\overline{x})^2. \tag{3-6}$$

The quantity N_s corresponds to the number of DSMC time-averaged samples taken. The square of the standard deviation as written above is referred to as the variance. It is convenient to relate the normal distribution to the standardized normal distribution, which is simply a normal distribution with mean 0 and variance 1. The confidence intervals for the standardized normal distribution may be specified in terms of a single dimensionless variable, Z, and are widely available in tabular form [Kreyszig, 1988]. The variable Z is related to the DSMC sample size N_s by :

$$Z \equiv \sqrt{N_s}\frac{k}{\sigma}, \tag{3-7}$$

where $\pm k$ defines the limits of the confidence interval. It is seen that the reduction in the statistical scatter of the data is proportional to $\sqrt{N_s}$, meaning that a 50% reduction in the scatter is obtained by a four-fold increase in the sample size.

The standard deviation of the macroscopic quantities is readily computed in the DSMC simulations. The standard deviation of the number density for the reference simulation, normalized with respect to the local mean number density, is shown in Figure 3-11 at three radial positions for a sample size of 1×10^4 time steps. The standard deviation is seen to increase sharply nearer the axis. This is due to the variation of the cell volumes with radial position for axisymmetric DSMC simulations, leading to a

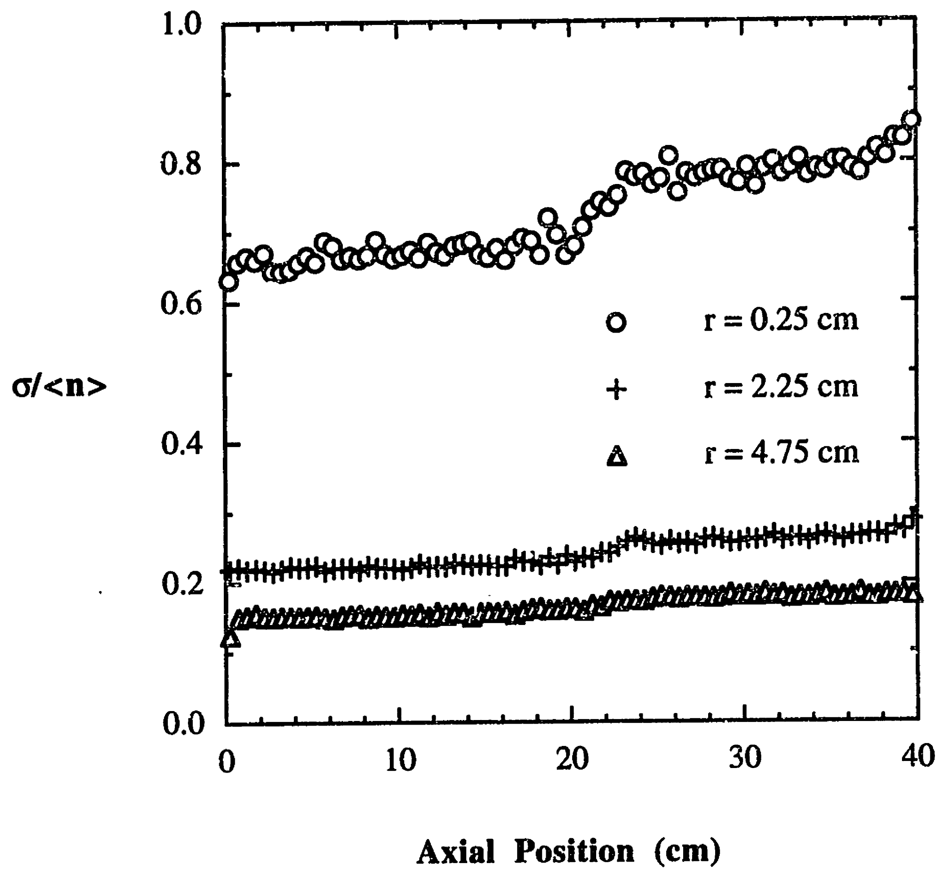

Figure 3-11 : Normalized standard deviation of the number density at r = 0.25 cm (O), r = 2.25 cm (+) and r = 4.75 cm (Δ) for the reference isothermal simulation.

smaller effective sample size nearer the axis. A relatively mild increase in the standard deviation occurs at positions further downstream, resulting from the density variations present in the UHV-CVD flow as seen in Figure 3-4.

An alternative way of illustrating the relationship between the statistical scatter and the sample size is to compute the sample size required within each cell in order to obtain a specified confidence interval. For example, suppose that a 95% certainty is specified that the exact value of the number density is within 1% of the computed mean number density. In other words, the number of samples which must be averaged in order to obtain a 95% confidence interval of $\pm 0.01 \langle n \rangle$ is sought. The required number of samples for each of the cells at the three radial positions used above are given in Figure 3-12. The sample sizes for the cells at r = 2.25 cm (+) and r = 4.75 cm (Δ) are on the order of 10^3 while the sample size at the axis ($\bigcirc$) is on the order of 10^4. The relationship between the statistical scatter and sample size is further illustrated in Figure 3-13 where the number density at the axis is plotted versus axial position for sample sizes of 1×10^4 and 9×10^4. The statistical scatter is reduced by a factor of 3 for a sample size increase of 9x in accordance with equation (3-7). It is evident that the number of time steps to be sampled for axisymmetric DSMC simulations is governed by the standard deviation within the cells at the axis.

3.4 The influence of various flow parameters on UHV-CVD gas dynamics

This section will discuss the results of a systematic study of the effects of various flow parameters on isothermal UHV-CVD gas flows. The first part will focus on the effects of altering the arrangement of wafers. The next section will discuss how varying

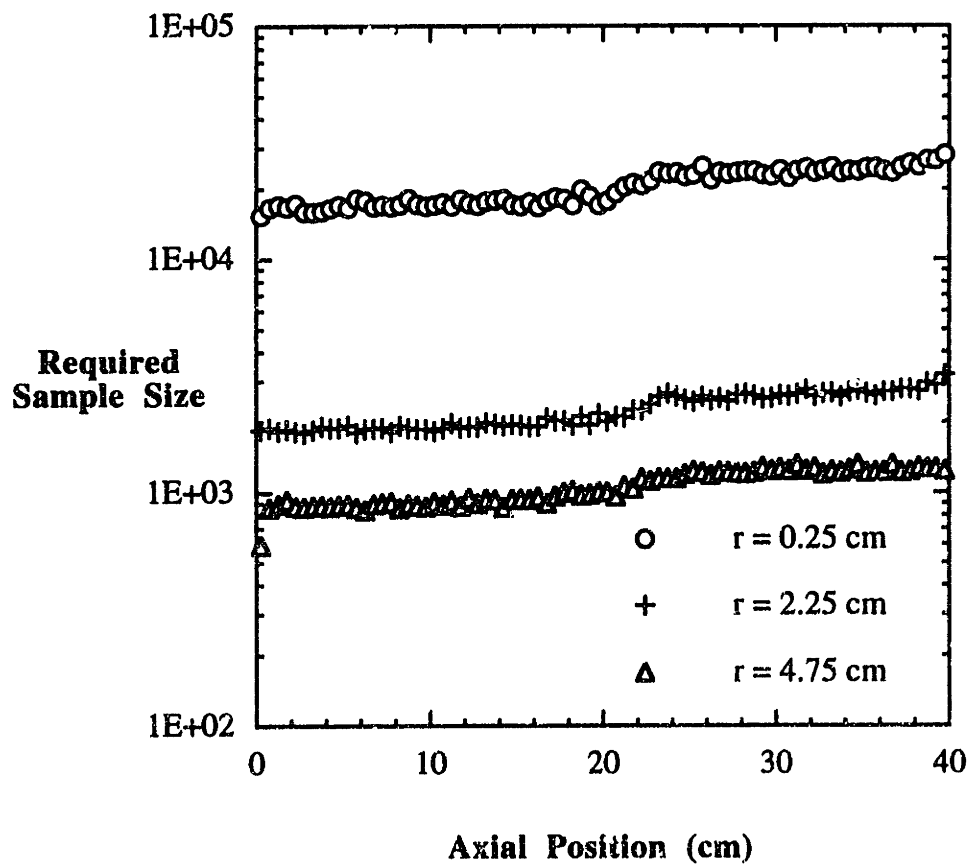

Figure 3-12 : Required sample sizes at r = 0.25 cm (O), r = 2.25 cm (+) and r = 4.75 cm (Δ) for the reference isothermal simulation.

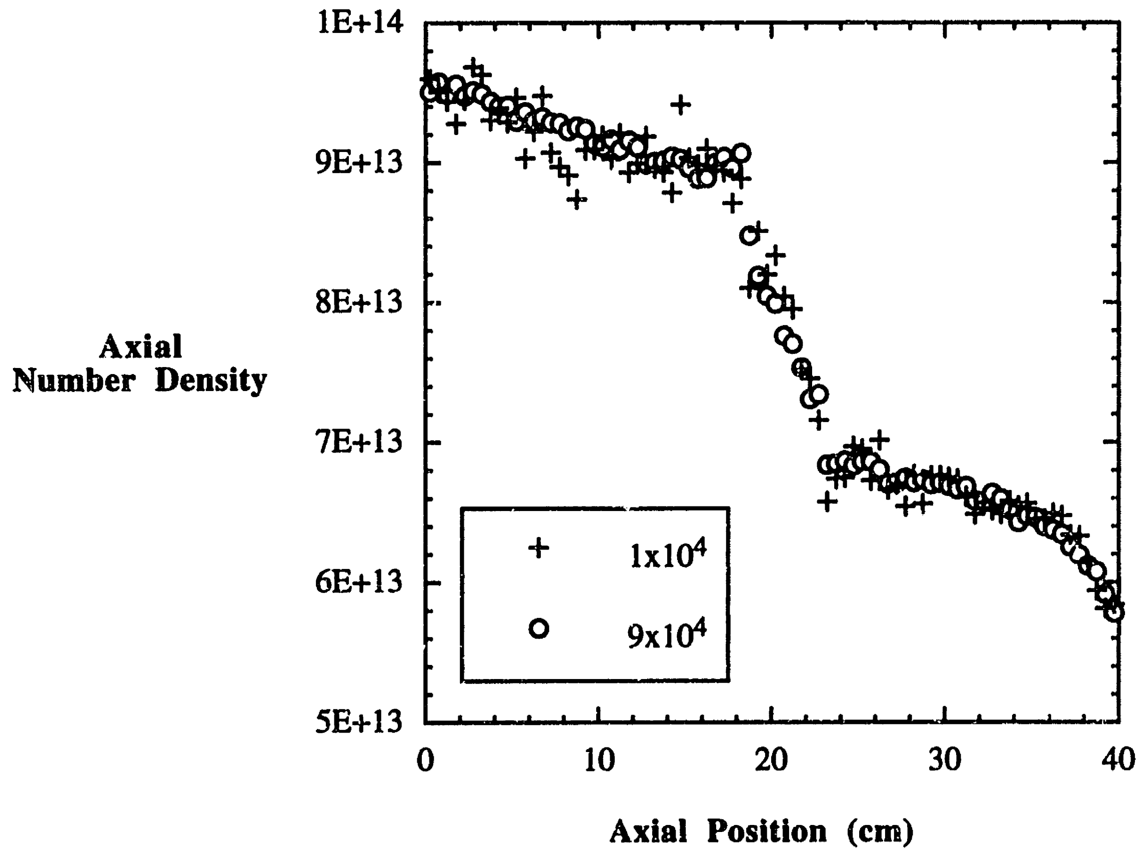

Figure 3-13 : Number density at the axis for the reference isothermal simulation using sample sizes of $1x10^4$ (+) and $9x10^4$ (○).

the outlet diameter affects the gas conditions in the reactor. The last part will present results for a variety of inlet gas stream conditions where the influences of the stream velocity, number density, and molecular species are discussed.

3.4.1 Wafer arrangement

Number of wafers

The realization of commercial scale UHV-CVD systems would require the ability to process a much larger number of wafers than are being considered in this simulation study. With this in mind a number of simulations were performed for the conditions of Table 3-1 where the number of wafers in the wafer stack were varied. The results are summarized in Figure 3-14 where the radially-averaged density, normalized with respect to the inlet gas stream density, is plotted versus axial position for 6, 10, and 14 wafers positioned in the center of the reactor tube. An increase in the wafer load is seen to have an additive effect on the density drop across the wafers. The density gradients for the upstream, annular and downstream regions are identical for each of the three cases.

The compressibility of the gas in UHV-CVD flows is seen to lead to a situation where the density drop becomes comparable to the total density, *i.e.* $\Delta n/n \approx 1$. This results in a significantly reduced surface flux of molecules to the wafers at the end of the wafer stack relative to the front wafers. This issue might be addressed with the strategic placement of gas inlets at intermediate positions along the reactor tube, an approach used in conventional LPCVD to combat the altogether different problem of depletion effects. It will be shown in a later section how restricting the outlet diameter can act like a downstream throttle valve, reducing the density gradients at the expense of increasing the total density throughout the reactor.

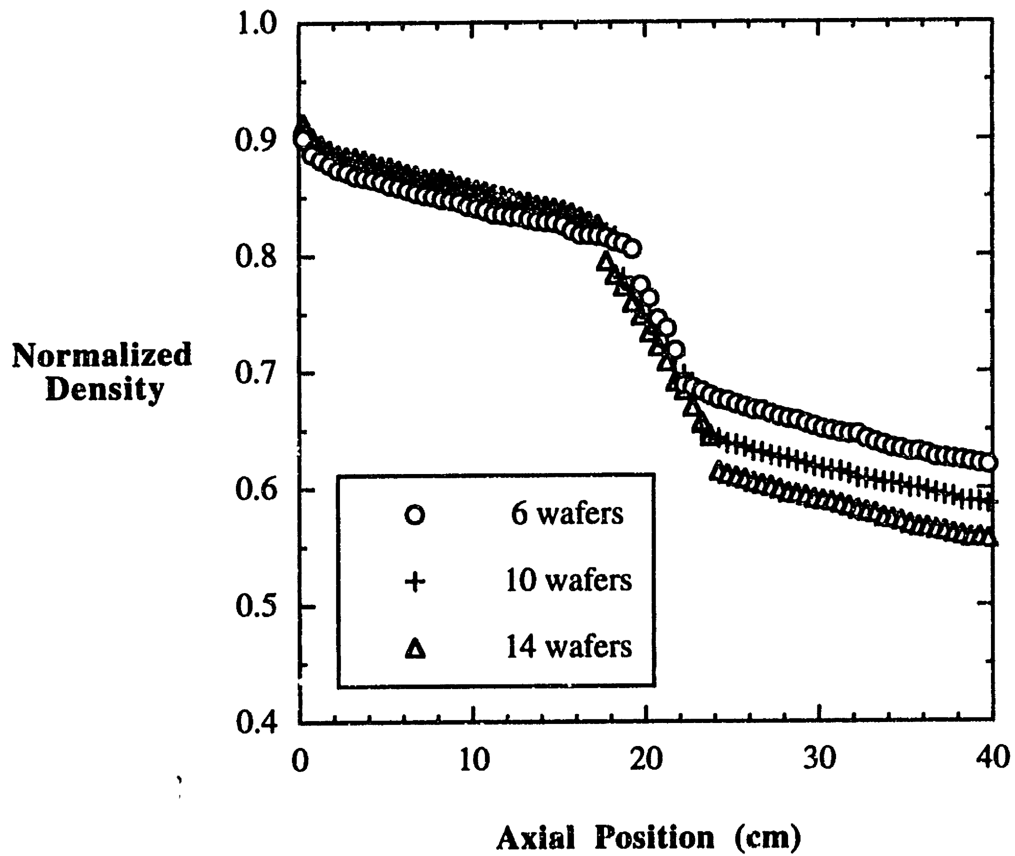

Figure 3-14 : Normalized density profile as a function of the number of wafers for 6 wafers (O), 10 wafers (+), 14 wafers (Δ).

Wafer diameter

The commercial scale-up mentioned in the previous section would also entail the use of larger diameter wafers in addition to an increase in the wafer load. It is not altogether certain whether it is necessary to scale-up the reactor diameter in proportion to the wafers. This question was addressed with a series of simulation runs where the wafer diameter was varied while the reactor diameter and all other conditions remained according to the conditions of Table 3-1. The radially-averaged normalized density is plotted in Figure 3-15 for wafer diameters of 5 and 8 cm. A change in the wafer diameter, for a fixed reactor diameter, is seen to have a very pronounced effect on the density variations in the UHV-CVD flow simulations.

The gas flow is severely choked as the wafer diameter is increased since the cross-sectional flow area in the annular region is reduced. This is illustrated in Figure 3-16 where the relative density variations across the wafer stack are plotted versus the cross-sectional flow area. The density drop across the wafers is seen to escalate in a superlinear fashion as the cross-sectional area is reduced. This reflects the influence of two features which act to increase the density drop as the wafer diameter is increased. The two-dimensional plot of the density field in Figure 3-4a for the reference simulation indicated a density variation across the ends of the wafer stack as the gas was throttled into and out of the annular flow region. This additional density drop increases with wafer diameter as well, contributing to the large effects seen in Figures 3-15 and 3-16.

Interwafer spacing

The radially-averaged density is plotted in Figure 3-17 for wafer spacings of 0.5 and 1.0 cm. The simulation for a 1.0 cm wafer spacing was performed for the reference conditions of Table 3-1 except that every other wafer was removed. The density is consistently lower for the larger interwafer spacing while the profiles are nearly identical

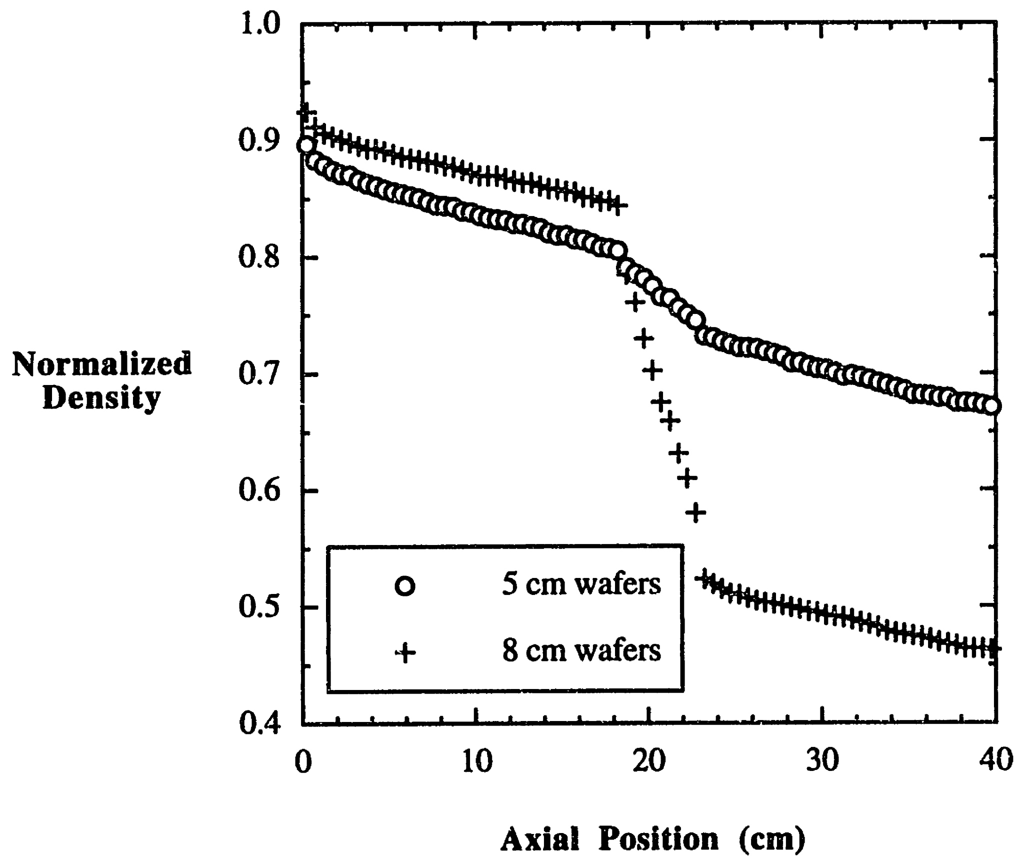

Figure 3-15 : Number density profile as a function of the wafer diameter for 5 cm (O) and 8 cm (+) wafers.

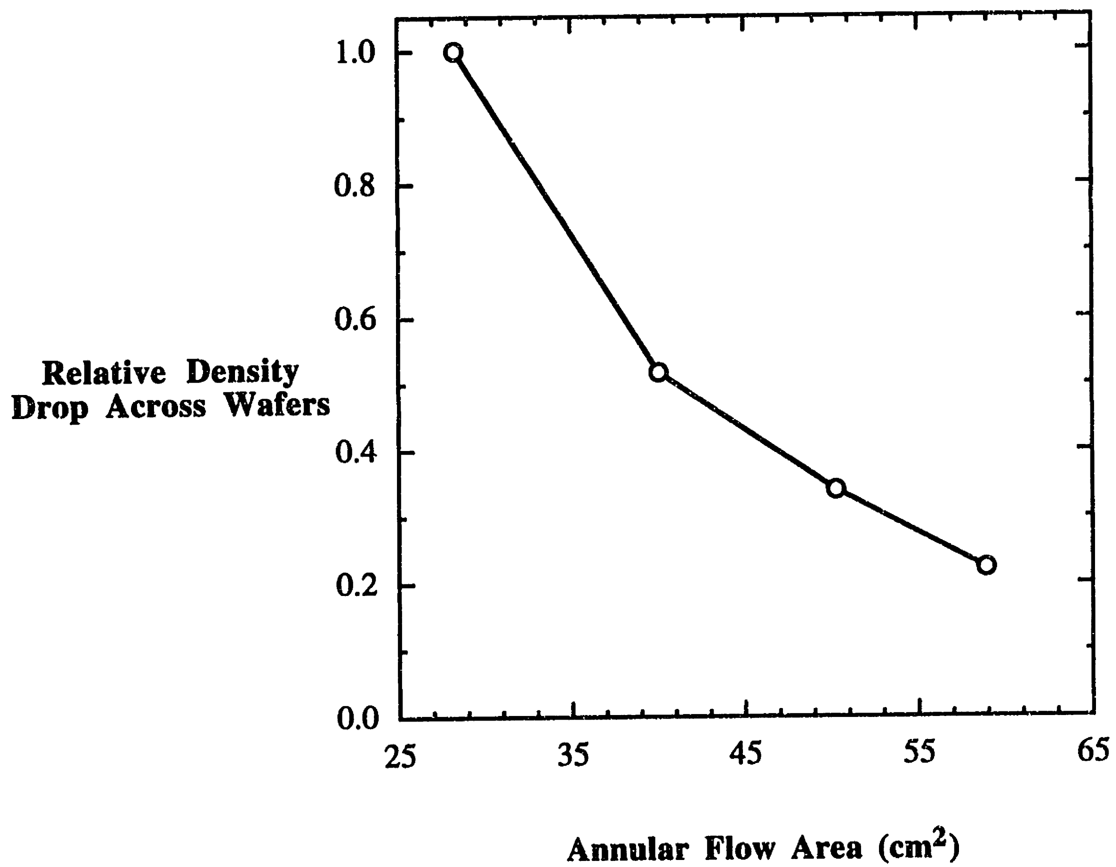

Figure 3-16 : Influence of the annular cross-sectional flow area on the density variation across a stack of 10 wafers.

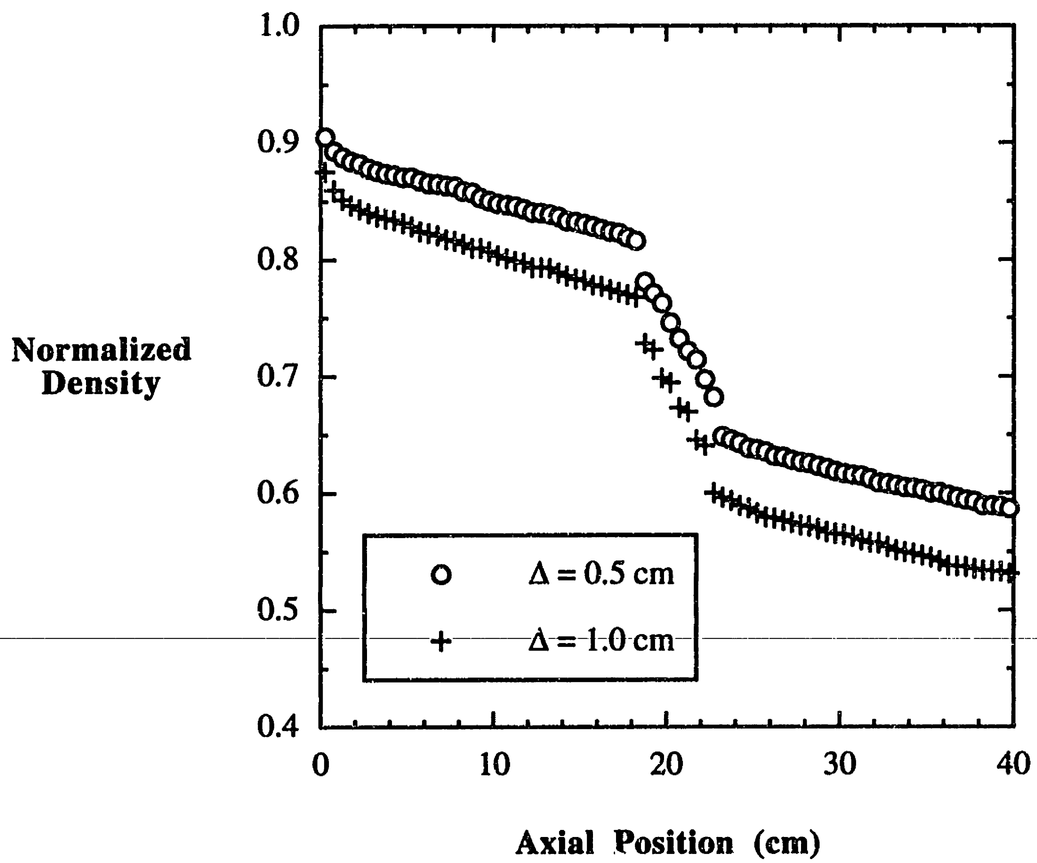

Figure 3-17 : Normalized density profile as a function of wafer spacing for $\Delta = 0.5$ cm (O) and $\Delta = 1.0$ cm (+).

in shape. A small density variation is indicated in the interwafer regions for the 1.0 cm spacing.

The spacing of the wafers apparently serves to dictate the amount of gas backed up in the upstream region. Considering the fate of a typical H_2 molecule entering the annular flow region, the probability of an encounter with a wafer surface is greater for the case of more closely spaced wafers. The interactions with the wafers would then contribute to the molecules being restricted from passing through the annular flow region and would lead to an accumulation in the upstream region as indicated in Figure 3-17.

3.4.2 Outlet diameter

The normalized density profiles for outlet diameters of 3.0, 5.0, and 7.0 cm are shown in Figure 3-18. A decrease in the outlet diameter is seen to have a similar effect to a decrease in the interwafer spacing where the total density is shifted upward throughout the reactor. The outlet diameter may be considered as a downstream throttle valve which controls the overall reactor operating pressure. The trend which has emerged from this parametric study has been that the influence of any geometrical variation in the flow path, whether coming from the wafer arrangement or the outlet diameter, mostly impacts the gas flow upstream of the variation. A slight decrease in the density variations across the wafers with decreasing outlet diameter is indicated in Figure 3-18 as well. This comes at the expense of an increase in the operating pressure, however, perhaps compromising some of the advantages of UHV-CVD discussed in Chapter 1.

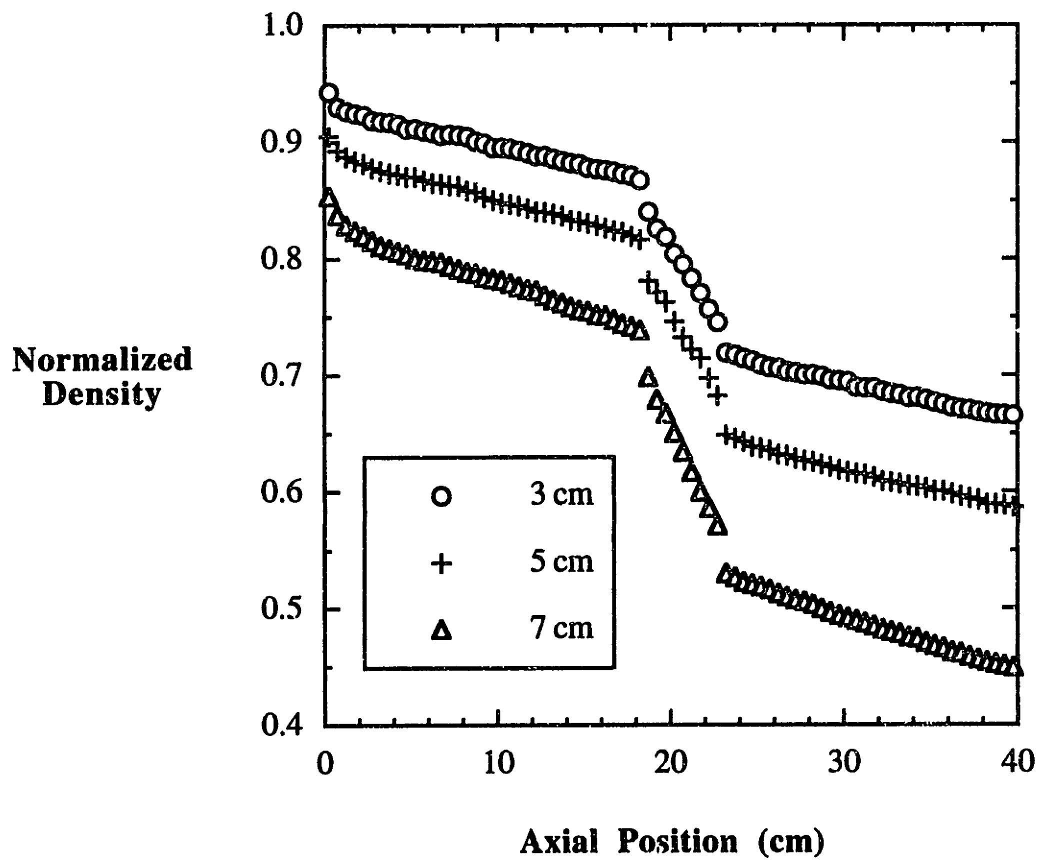

Figure 3-18 : Normalized density profile as a function of outlet diameter for outlet diameters of 3 cm (O), 5 cm (+) and 7 cm (Δ).

3.4.3 Inlet stream velocity

The effects of varying the inlet stream velocity are now examined. It should be emphasized that this is not equivalent to evaluating the effects of changing the inlet mass flow rate which would necessarily include a change in the inlet number density as well. The H_2 mass flow rate, determined by the flux of molecules across the inlet plane, is dictated by the stream velocity, number density, and temperature as shown in equation (2-8), rewritten here for the purposes of this discussion :

$$J = \frac{n\bar{c}}{4} \left[\exp(-s^2) \pm \sqrt{\pi}\, s \, \{1+\mathrm{erf}(s)\} \right], \qquad (3\text{-}8).$$

where the $\pm$ refers to whether the inlet (+) or outlet (-) stream is being considered. As mentioned in section 3.3.1, the inlet stream velocity was selected to provide what was judged to be a reasonable inlet mass flow rate for the reference UHV-CVD simulation. As seen in the above equation the mass flux is a complicated function of the speed ratio s, defined as the ratio of the stream velocity to the most probable thermal velocity, v_m.

The normalized density profiles for speed ratios of 0.023 and 0.070 are shown in Figure 3-19. The total density throughout the reactor is substantially reduced as the inlet stream velocity is increased. Another feature evident in Figure 3-19 is the increase in the density gradients with increasing inlet speed ratio. These trends are better understood by considering the relative number flux across the inlet and outlet planes given by the bracketed expression on the right-hand-side of equation (3-8). These values are given in Table 3-2 for speed ratios of 0.023, 0.047 (reference simulation), and 0.070. As the stream velocity is increased the mass flux at the inlet increases while the back flux of molecules at the outlet decreases. This reduced back flux is primarily responsible for the

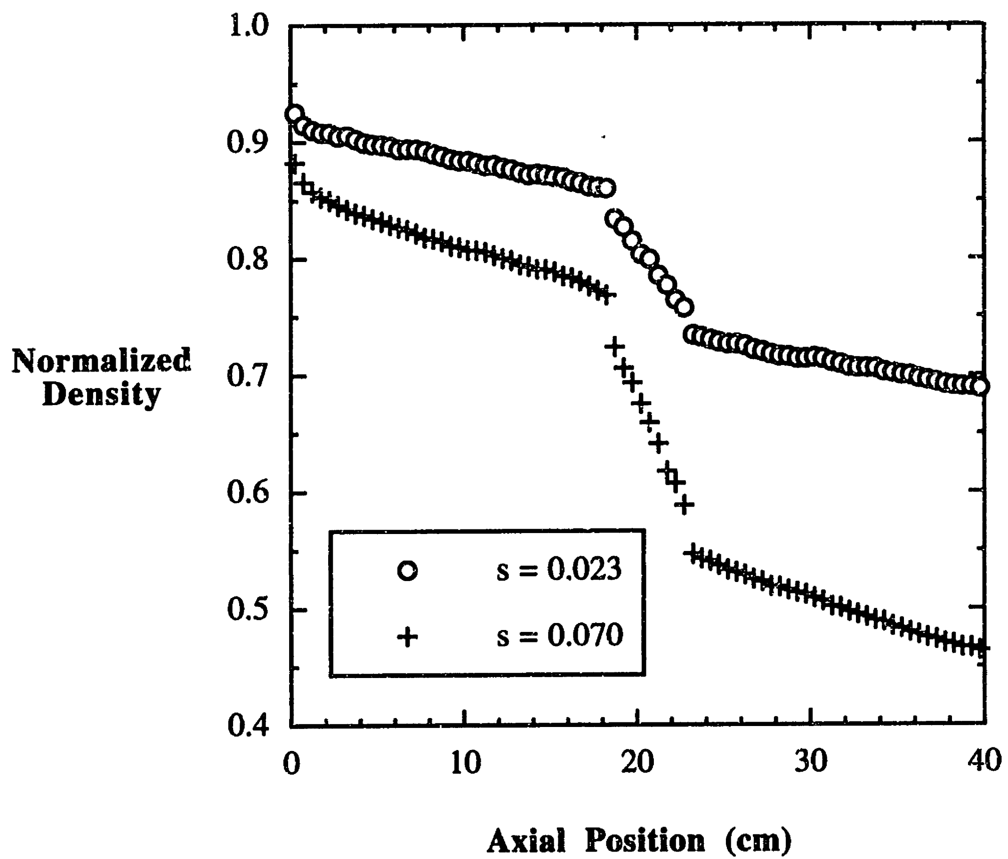

Figure 3-19 : Normalized density profile as a function of speed ratio for speed ratios of 0.023 (O) and 0.070 (+).

reduced total density and increased density gradients throughout the reactor with increasing inlet speed ratio.

Inlet Speed Ratio	Number Flux / ($n\overline{c'}/4$) [inlet : outlet]
0.023	[1.051 : 0.948]
0.047	[1.085 : 0.911]
0.070	[1.203 : 0.787]

Table 3-2 : The effect of speed ratio on the relative mass influxes at the inlet and outlet.

3.4.4 Inlet number density

The trend in UHV-CVD technology has been towards decreasing the operating pressure to the sub-mTorr range [Meyerson, 1992]. This takes the gas dynamics even closer to becoming completely free molecular flow. This section addresses the impact of this trend with a discussion of the simulation results for various inlet number densities or pressures. The remaining conditions of the simulations correspond to the reference simulation conditions of Table 3-1.

The number density profiles for inlet pressures of 1, 5, and 10 mTorr, maintained in dimensional form in this case for the purposes of comparison, are given in Figure 3-20a. The density variations were found to be proportional to the total density in the reactor in each of the cases examined. This is the hallmark characteristic of free molecular internal gas flows where the density or pressure drop across a section of high-

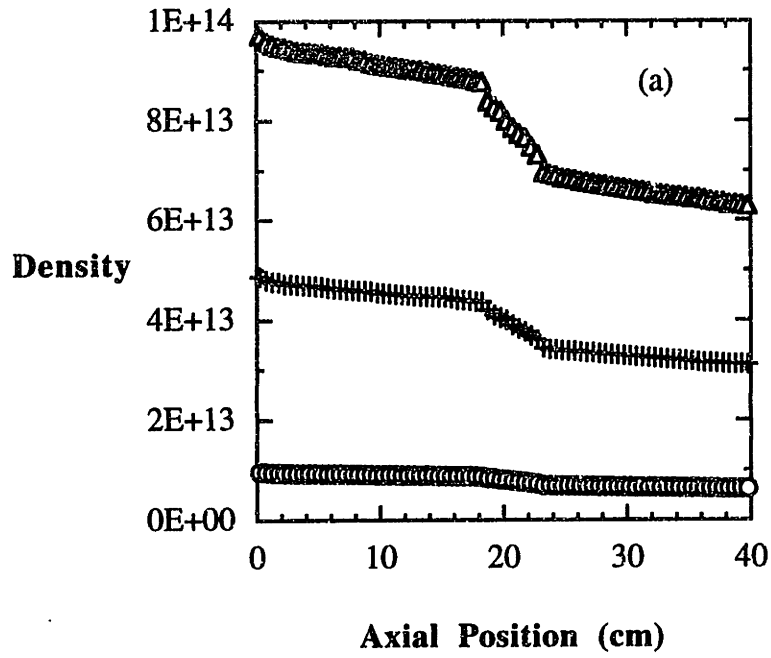

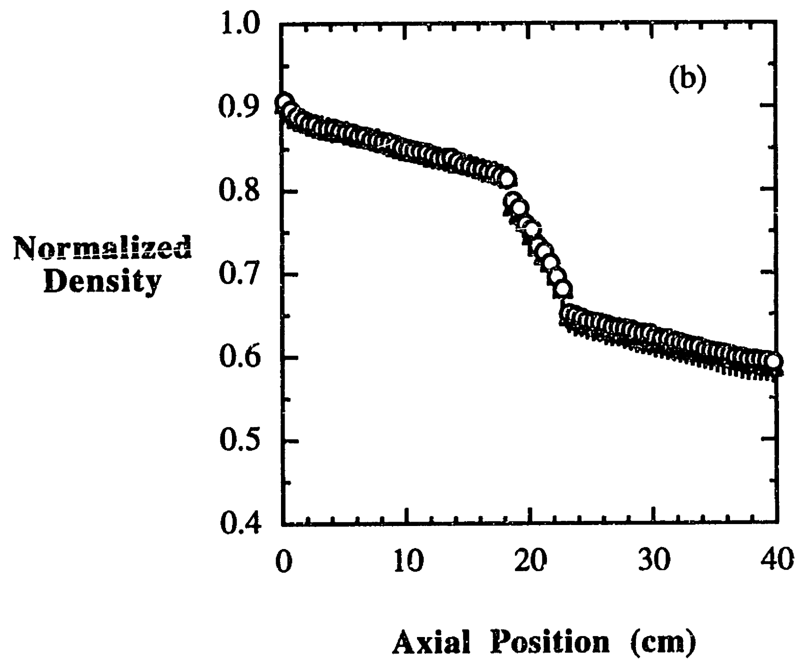

Figure 3-20 : Density (a) and normalized density (b) profiles for inlet pressures of 1 mTorr (O), 5 mTorr (+), and 10 mTorr (Δ).

vacuum equipment is proportional to the upstream conditions [O'Hanlon, 1989]. This feature is further illustrated in Figure 3-20b where the normalized density profiles for inlet pressures of 1 and 10 mTorr virtually overlap each other, *i.e.* $\Delta n/n$ remains constant for each case.

3.4.5 Molecular species

In this section the simulation results for inlet streams of H_2, N_2, and Ar will be presented for the isothermal reference conditions of Table 3-1. The inlet stream velocity was altered for the N_2 and Ar simulations in order to maintain identical speed ratios to the reference H_2 simulation. The respective inlet mass flow rates are then proportional to the mean thermal velocity as indicated by equation (3-8).

The normalized density profiles for the three gases are shown in Figure 3-21. The density drop for the H_2 stream is noticably greater than that of the heavier N_2 and Ar species. The underlying physics which gives rise to this effect is apparently related to the gas phase collision rate since this is where the individual flows primarily differ. Consider the gas phase collision frequency per molecule for an equilibrium gas :

$$\upsilon = \pi d^2 \overline{v_r}, \qquad (3\text{-}9).$$

where πd^2 is the collision cross-section and $\overline{v_r}$ is the mean relative velocity between collision partners, which in turn is inversely proportional to the square root of the molecular mass. The ratio of the mean collision frequencies of $H_2 : N_2 :$ Ar is computed to be 2.27 : 1.21 : 1. This same order is reflected in the density variation profiles in Figure 3-21. The intermolecular collisions act as a diffusional resistance to flow which results in the trend observed for the various gases.

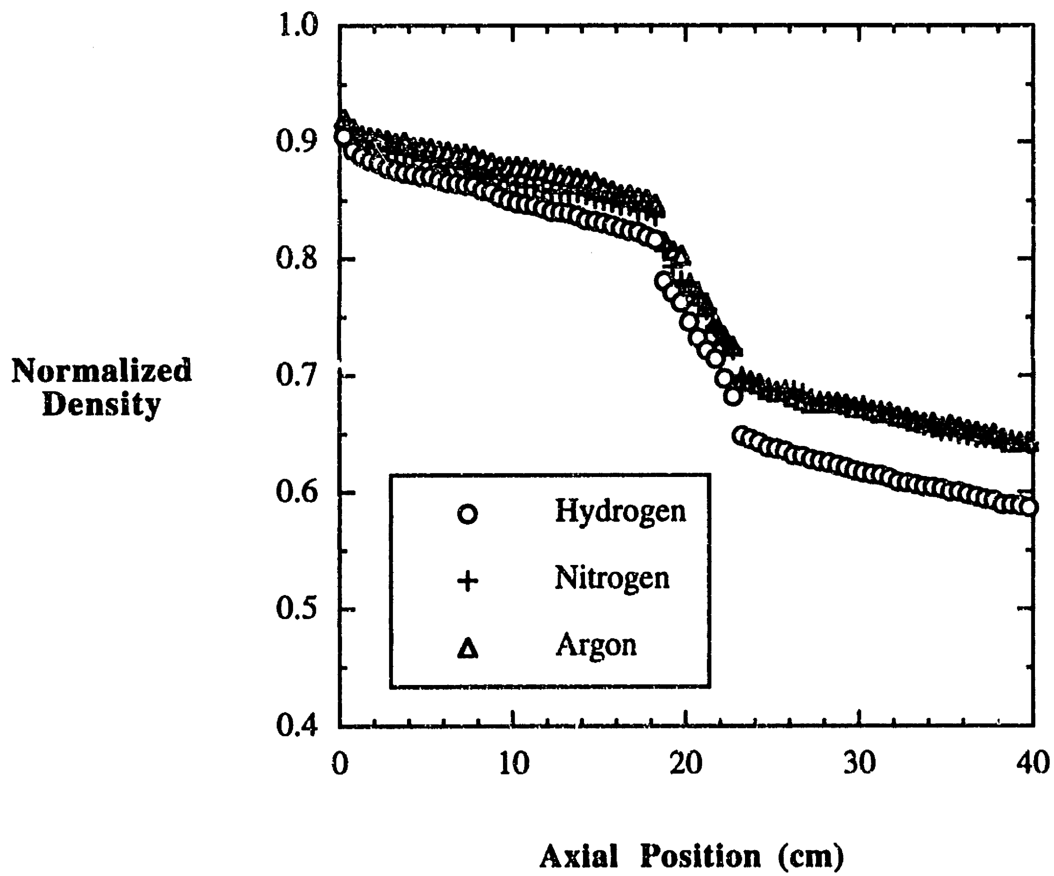

Figure 3-21 : Normalized density profile as a function of molecular species for H_2 (○), N_2 (+), and Ar (Δ).

3.5 Species separation effects in isothermal rarefied gas mixtures

There are many important CVD applications which require the use of gas mixtures. The thin film growth of Si_xGe_{1-x} has been targetted as one of the promising potential applications of the UHV-CVD technique [Meyerson *et al.*, 1988; Greve and Racanelli, 1990]. This necessarily involves the introduction of gas mixtures containing the Si and Ge film constituents, usually the hydrides SiH_4 and GeH_4. In addition, the *in-situ* doping of Si epitaxial films using UHV-CVD requires the addition of dopant precursors to the incoming SiH_4 gas stream [Meyerson *et al.*, 1987; Greve and Racanelli, 1991].

In the flow of rarefied gas mixtures the individual molecular species have a strong tendency to separate owing to the relative diffusive motion of each species [G. Bird, 1984; Nelson and Doo, 1988; G. Bird, 1988a; Chung *et al.*, 1992]. This section will present the results of a simulation study of the isothermal flow of rarefied gas mixtures in the LPCVD reactor. The rarefied gas flow of a N_2/H_2 inlet stream will first be considered since the molecular mass and size disparity should give rise to strong separation effects.

The reactor conditions for the N_2/H_2 gas mixture are identical to those employed in the reference simulation. In this case, however, the inlet stream is comprised of an equimolar mixture of N_2 and H_2. The gas mixture VHS parameter was computed according to the procedure outlined in Chapter 2. The macroscopic flow field properties (pressure, temperature, number density) now consist of individual components which, when weighted by their respective mole fractions, sum up to give the overall macroscopic properties :

$$p_o = \sum_{i=1}^{m} x_i \, p_i, \quad (3\text{-}10).$$

$$T_o = \sum_{i=1}^{m} x_i \, T_i, \quad (3\text{-}11).$$

$$n_o = \sum_{i=1}^{m} x_i \, n_i, \quad (3\text{-}12).$$

where m represents the number of species and x_i is the mole fraction of species i. The overall pressure and number density profiles for the N_2/H_2 simulation are shown in Figures 3-22a and 3-22b, respectively. There appear to be no major differences between the gas mixture flow field and the respective flows for the pure component gases in terms of the overall macroscopic properties.

The simulation does, however, reveal significant separation effects between the N_2 and H_2 species. This is illustrated in Figure 3-23 where the N_2 mole fraction distribution is shown. The N_2 mole fraction builds up to a maximum in a region immediately in front of the wafer stack, is sharply depleted across the wafer stack, and continues to decrease in the downstream region. This separation effect is attributed to pressure diffusion, a phenomenon which acts to drive the heavier species towards regions of higher pressure or density.

The basis for pressure diffusion is usually explained from a continuum standpoint. In an isothermal system there are three mechanical driving forces which act to displace a species in a gas mixture relative to the bulk fluid motion [R. Bird *et al.*, 1962]. These are concentration gradients, pressure gradients, and external forces which preferentially act upon one or more species in the mixture. Diffusion caused by concentration gradients is

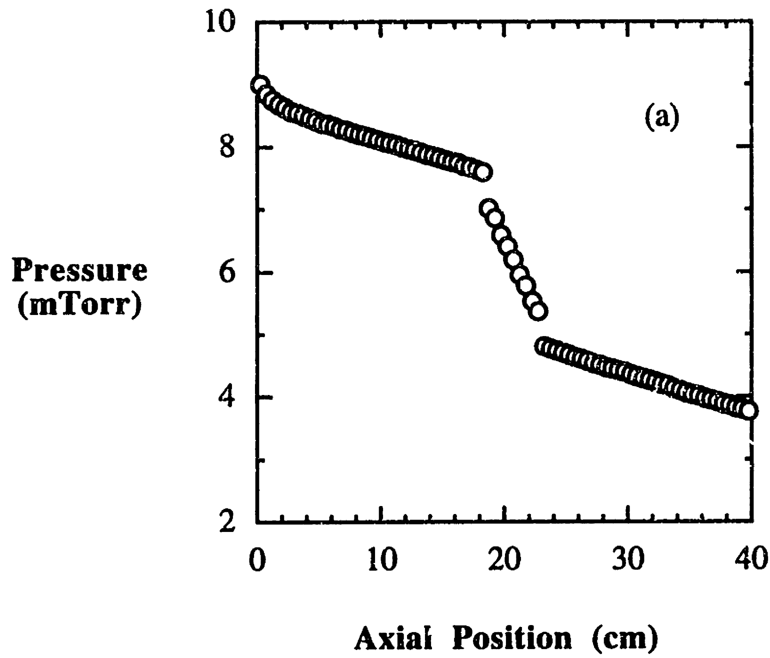

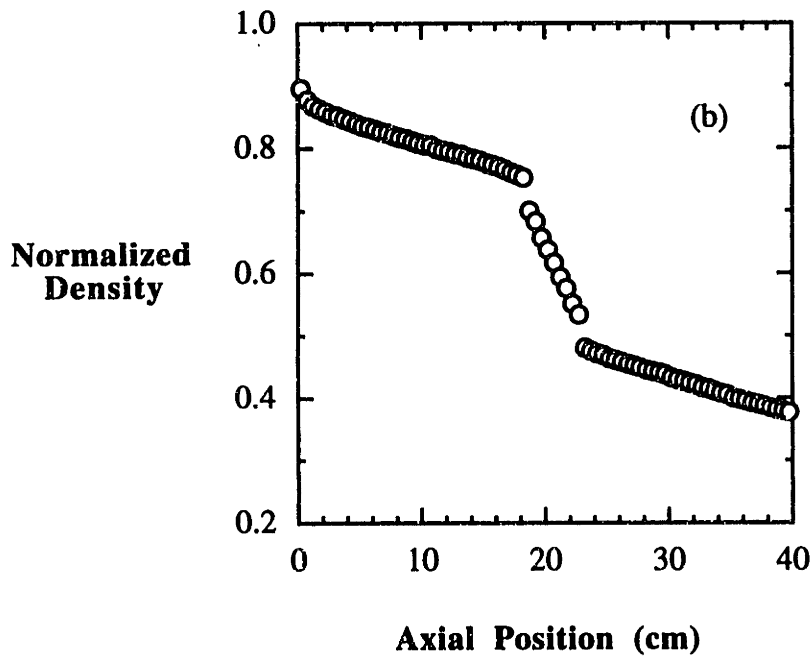

Figure 3-22 : Total pressure (a) and density (b) profiles for a N_2/H_2 gas mixture inlet stream.

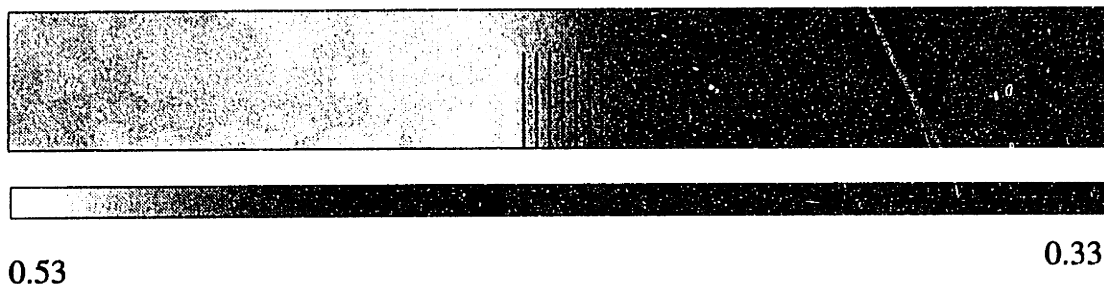

Figure 3-23a : N_2 mole fraction distribution for an equimolar inlet stream of N_2 and H_2 under isothermal (900 K) conditions.

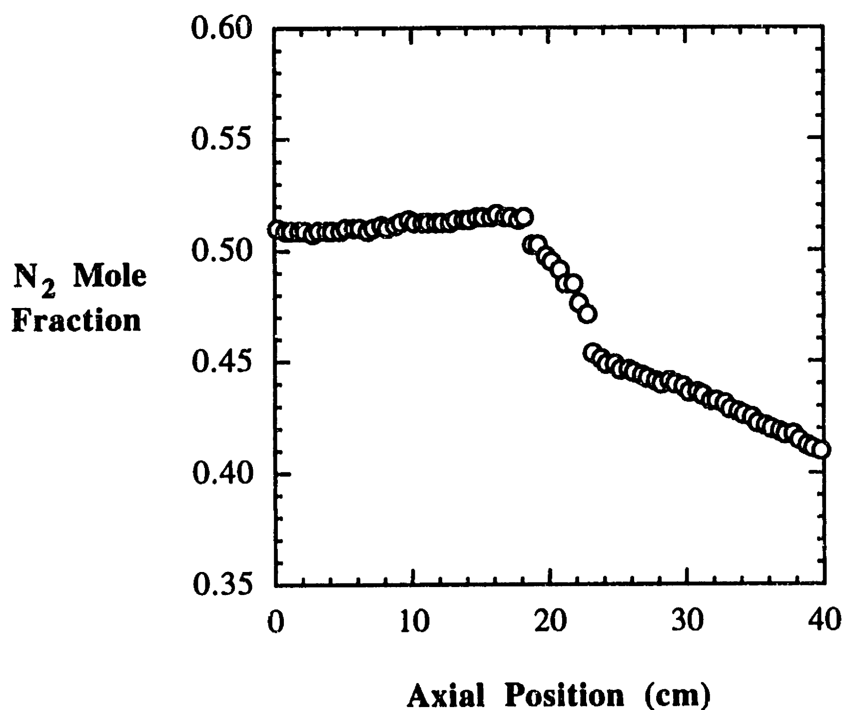

Figure 3-23b : N_2 mole fraction profile for an equimolar inlet stream of N_2 and H_2 under isothermal (900 K) conditions.

the ordinary diffusion which is almost exclusively considered in continuum transport equations. It is the relative motion induced by a pressure gradient which is referred to as pressure diffusion. The pressure diffusion contribution to the overall diffusion velocity, written here for a binary mixture of A and B, is proportional to the difference in the molecular weights and inversely proportional to the to the total pressure [Chapman and Cowling, 1970] :

$$\left(\overline{v_A} - \overline{v_B}\right)_{\text{press. diff.}} = -D_{AB}\left(\frac{M_B - M_A}{\overline{M}}\right)\frac{1}{p}\nabla p, \qquad (3\text{-}13).$$

where D_{AB} is the binary diffusion coefficient and $\overline{M}$ is the mean molecular weight.

In most continuum flows, this term is entirely negligible except in the presence of extreme pressure gradients [R. Bird *et al.*, 1962]. Indeed, this separation effect is exploited in gas mixture separation devices where large pressure gradients are purposefully established such as in gas centrifuges and separation nozzles [Perry and Green, 1984]. It is seen from equation (3-13) that the separation is expected to increase as the total pressure is reduced. Pressure diffusion is important in UHV-CVD flows because $\Delta p/p$ becomes large rather than Δp. It is also seen that a small mean molecular weight enhances the pressure diffusion in addition to the molecular weight disparity. Pressure diffusion effects in high altitude DSMC simulations of gas mixtures were also reported by Bird [G. Bird, 1988a].

Referring back to Figure 3-23, it is seen that the largest separation effects occur as the gas is throttled across the wafer stack. This is consistent with the observation that the largest pressure gradients exist in this region as well as shown in Figure 3-22a. This driving force transforms the annular flow region into a channel which preferentially allows the passage of the lighter species, in this case the H_2 gas. The convection of the

N_2 molecules in the downstream direction is opposed by the pressure diffusion, leading to the N_2 rich region just upstream of the wafers. The gas separation is somewhat reduced in the downstream region as expected since the pressure gradient is also reduced.

A technologically important gas mixture to be considered is that of SiH_4 and GeH_4, commonly used to deposit thin films of Si_xGe_{1-x} [Meyerson *et al.*, 1988; Greve and Racanelli, 1990]. The isothermal gas mixture simulation is now repeated using an inlet gas stream composed of equal parts SiH_4 and GeH_4. The VHS molecular model is once again utilized with the VHS parameter set at 0.20. In addition, the SiH_4 and GeH_4 300 K reference diameters are set at 3.5 Å and 4.0 Å, respectively. All other conditions pertaining to the simulation are identical to the N_2/H_2 simulation.

The radially-averaged GeH_4 mole fraction versus axial position is plotted in Figure 3-24. The degree of separation in this case is seen to be less than was observed for the N_2/H_2 gas mixture. This is expected since the degree of separation is determined by the mass and diameter disparity and the SiH_4 and GeH_4 molecules are more similar in mass and diameter than are N_2 and H_2. In spite of this, the observed separation between the SiH_4 and GeH_4 species may become unacceptably large across a much larger wafer stack where the pressure diffusion acts over longer reactor lengths. Recent experimental measurements have clearly demonstrated the sensitivity of the Si_xGe_{1-x} film composition to the GeH_4 partial pressure in the surrounding gas [Meyerson *et al.*, 1988; Kato *et al.*, 1991; Hiroi and Tatsumi, 1992].

3.6 Reactant flux uniformity for silane and disilane flows

The successful commercialization of UHV-CVD technology depends upon its ability to process a large number of wafers with uniform growth rates on each wafer and

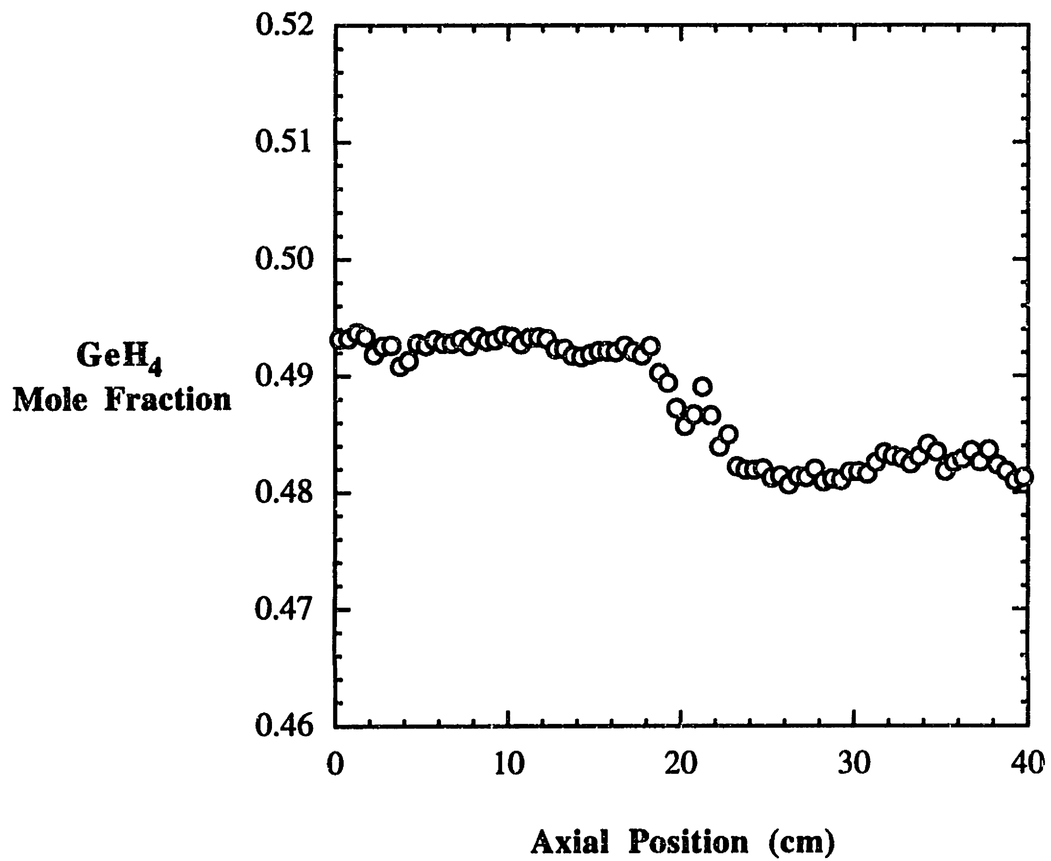

Figure 3-24 : GeH_4 mole fraction profile for an equimolar inlet stream of SiH_4 and GeH_4 under isothermal (900 K) conditions.

from wafer-to-wafer. Accurate modelling of the growth rates under UHV-CVD conditions where the surface kinetics are rate-limiting would require an appropriate surface chemistry model [Greve and Racanelli, 1991; Gates and Kulkarni, 1991; Greve and Racanelli, 1992]. The necessary input to the kinetic model would include the flux of reactants to the surface at several positions along each wafer. This flux distribution may be obtained directly from the DSMC transport model.

In this section the flux uniformity on each wafer and from wafer-to-wafer are computed for the isothermal research scale reactor described in Table 3-1 using pure SiH_4 and Si_2H_6 input streams. The depletion of reactants on the wafer surfaces and along the heated reactor walls is computed using reactive sticking coefficients of $2.5x10^{-4}$ for SiH_4 and 0.05 for Si_2H_6, estimates which represent averages of many reported values.

The flux distributions are given in Figure 3-25 for the two different gases where the average flux to each wafer is normalized with respect to the flux to the first wafer. The flux uniformity is given as the ratio of the flux at the center of the wafer to the flux at the wafer edge. In both cases the largest flux is obtained at the first wafer, consistent with the fact that the gas density is much higher upstream of the wafers. For the case of Si_2H_6, this reduction in the flux is worsened by the depletion due to surface reactions. It is also seen that the radial flux uniformity on each wafer is much better for the less reactive SiH_4 gas, essentially uniform over the entire wafer stack, while the more reactive Si_2H_6 gas results in about a 40% reduction in the flux at the wafer center. This effect is systematically investigated in section 3.8 for conventional LPCVD conditions.

It should be noted that the flux distribution variations shown in Figure 3-25 would not necessarily correspond to the actual growth rate variations, but are expected to have some impact on the growth rate uniformity depending upon the relative time scales involved with respect to the surface chemistry and the gas transport. Another important factor which should also be taken into consideration is the influence of any temperature

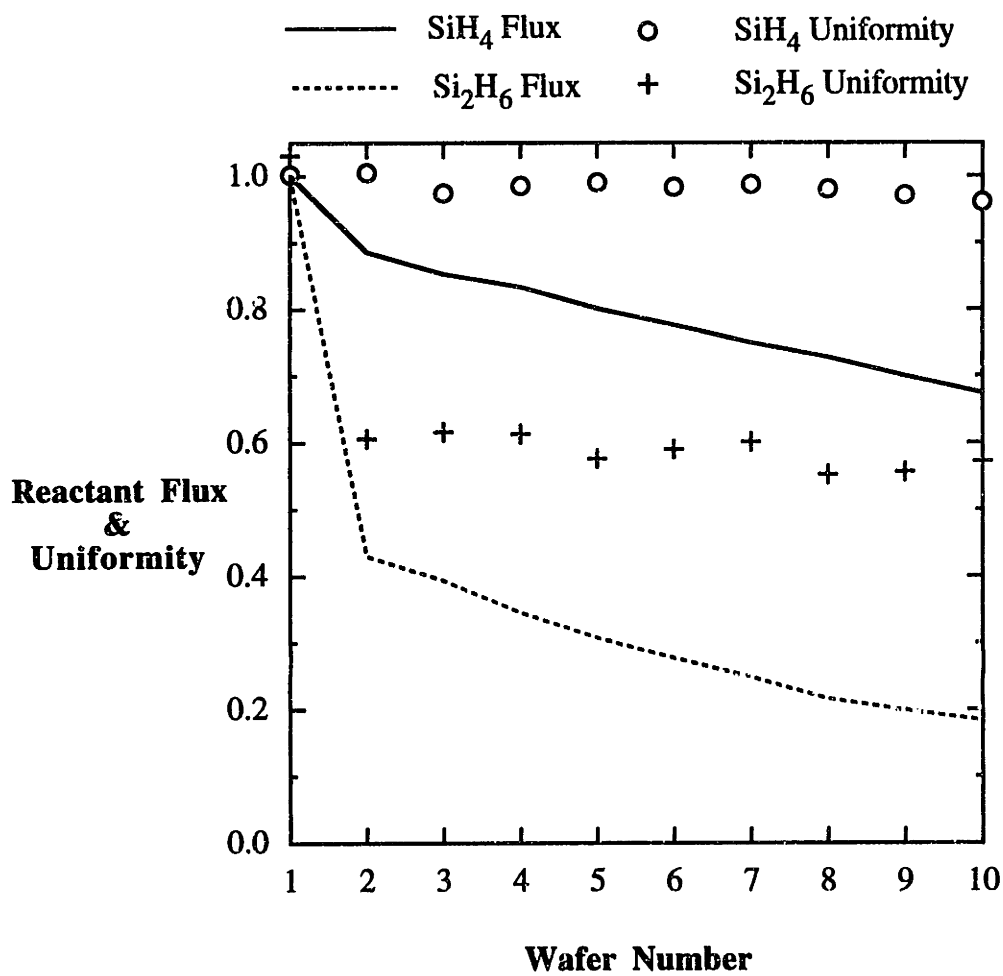

Figure 3-25 : Reactant flux distribution and radial uniformity for isothermal flows of SiH_4 and Si_2H_6.

variations which might exist in the LPCVD reactor. This issue is addressed in detail in Chapter 4.

3.7 Simulation of the transient flow associated with gas switching

3.7.1 The transient DSMC algorithm

The simulation of transient flows using the DSMC simulation is conceptually straightforward. The only difference between transient and steady-state DSMC simulations is that the statistical sampling of the flow properties is now accomplished using ensemble averaging rather than time averaging. This involves repeated initiations from the initial state using different random number seeds. The flow properties are then probed at pre-determined time intervals during each transient cycle. The obvious drawback to ensemble averaging is that only one sample is obtained over the entire transient period of interest, whereas the time averaging used in steady-state calculations accumulates a large number of samples in a relatively short time period. The transient DSMC algorithm flowsheet is given in Figure 3-26.

3.7.2 Relevance to UHV-CVD technology

The successful fabrication of multilayer structures depends upon the ability to achieve abrupt interfaces between adjacent layers. With the reduction in device feature sizes to the sub-micron level and the emergence of nanometer scale quantum device technology, the necessary control now approaches the atomic level. From a CVD processing standpoint, this requires a reactor design which permits the efficient and

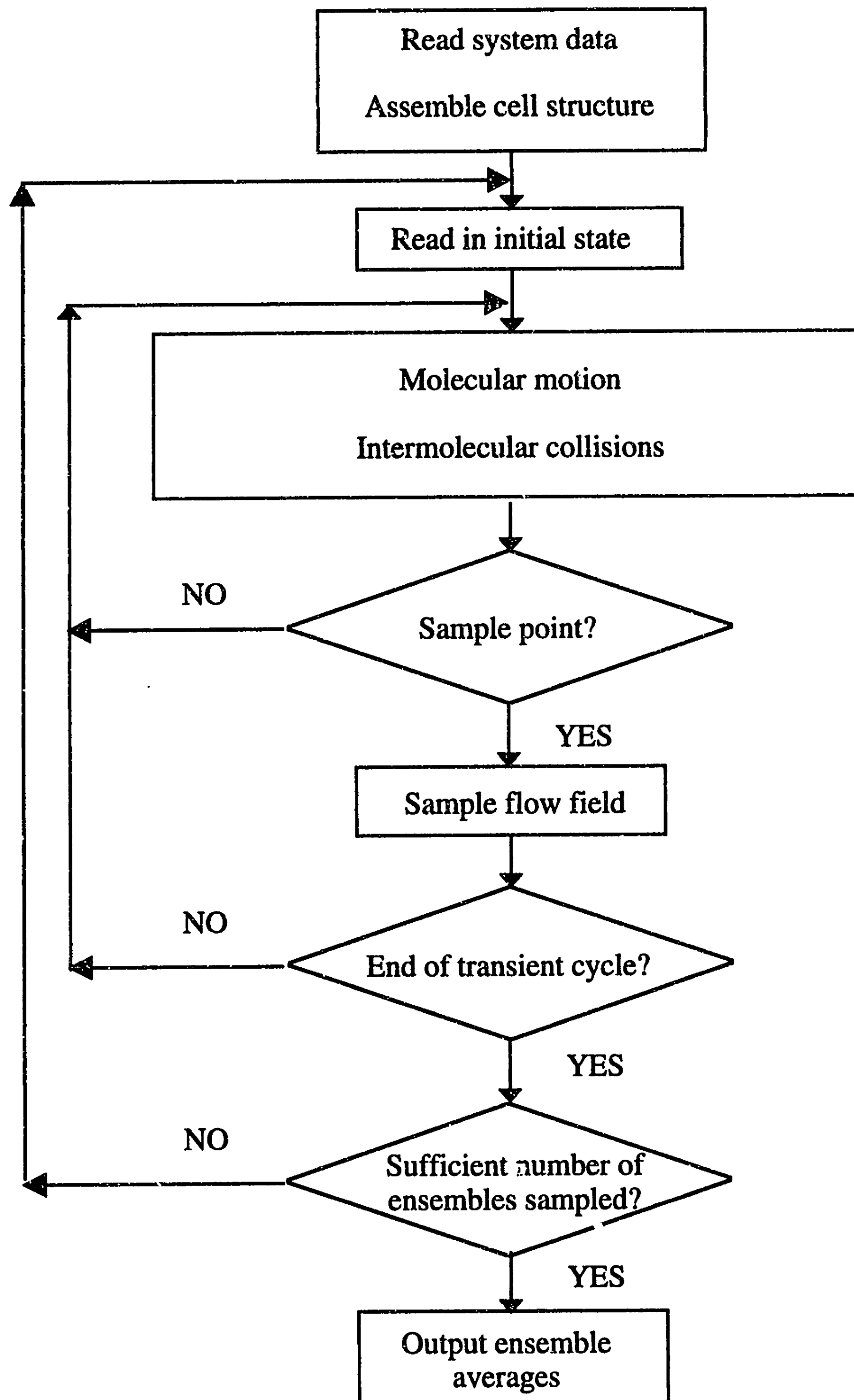

Figure 3-26 : Transient DSMC algorithm flowsheet.

expeditious flushing of reactive gases away from the film growth surface. The efforts in UHV-CVD technology have been primarily related to the fabrication of devices consisting of alternating layers of Si and Si_xGe_{1-x} films [Meyerson *et al.*, 1988; Iyer *et al.*, 1989; Greve and Racanelli, 1990]. With this in mind, a simulation study has been performed which investigates the capability of flushing N_2 from a N_2/H_2 mixture with a pure H_2 gas stream under UHV-CVD conditions.

3.7.3 Purging of an isothermal N_2/H_2 flow field with pure H_2

The steady-state N_2/H_2 flow field obtained in the previous section is used as the initial state for the transient flow simulation. The inlet stream is then abruptly switched to pure H_2 at time = 0. The time scale associated with the complete purging of the N_2 gas is indicated in Figure 3-27 where the total number of both N_2 and H_2 molecules in the reactor are shown as a function of purge time. The relatively lengthy time required to flush the last few remaining N_2 molecules is consistent with the computed residence time distributions which were discussed in section 3.3.5.

The transient distribution of N_2 is shown in Figure 3-28 where the radially-averaged mole fraction versus axial position is plotted. Before the pure H_2 purge, the gas composition corresponds to the steady-state distribution shown in Figure 3-23. After the first few ms the section of the reactor upstream of the wafers is significantly flushed of the N_2 species. This is consistent with the observation that the molecules spend a large fraction of their residence time in the relatively high density upstream region; the effects of the H_2 flush are not immediately felt downstream of the wafers. The remaining few N_2 molecules at the end of the purge cycle indicated in Figure 3-27 corresponded to those responsible for the long tail in the residence time distribution seen in Figure 3-10.

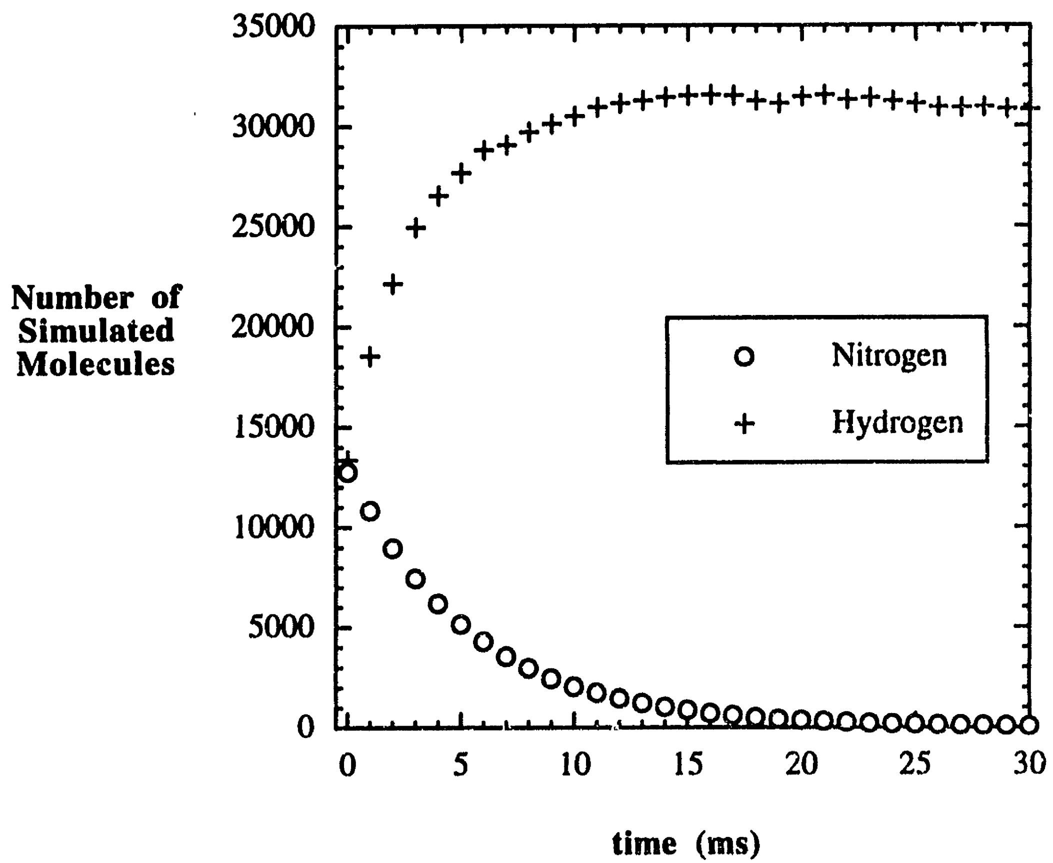

Figure 3-27 : Transient molecular count during H_2 purge of N_2/H_2 gas stream.

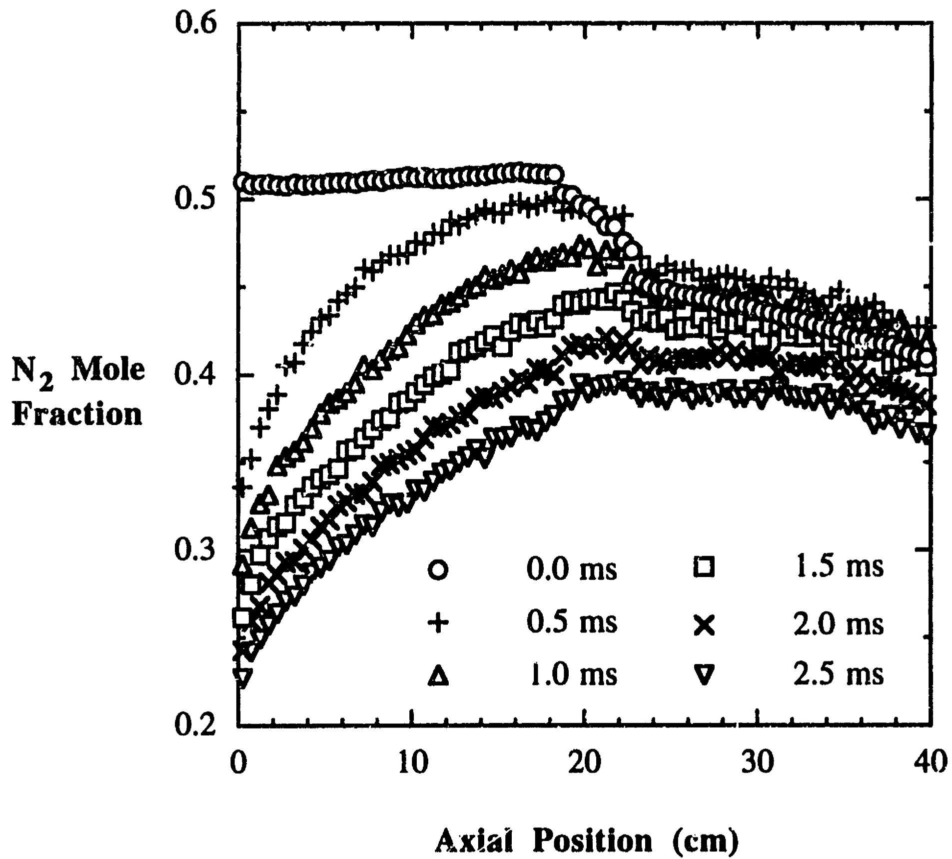

Figure 3-28 : Transient distribution of N_2 during pure H_2 purge of N_2/H_2 gas mixture.

The simulations have shown that under UHV-CVD conditions the research scale reactor may be completely purged in a time scale on the order of 10 ms. For commercial scale reactors where the reactor volume is perhaps an order of magnitude greater, the purge times could be on the order of 100 ms. This may now be compared to typical growth rates of 0.1 μm/hr under typical UHV-CVD conditions [Greve and Racanelli, 1991]. The amount of film which may be grown in this time scale is on the order of 10^{-6} μm. The conclusion to be made is that UHV-CVD may be used to achieve extremely abrupt interfaces.

3.8 Simulation of rarefied interwafer gas transport and deposition in conventional LPCVD

Conventional multiwafer LPCVD processes have been successfully modelled using a continuum formulation [Jensen and Graves, 1981; Yeckel *et al.*, 1989; Badgwell *et al.*, 1992a]. The most widely used approach has been to separate the reaction-transport equations governing the annular flow region from those describing the interwafer region, subsequently matching the solutions at the common boundaries. It has been argued that the reactant species transport in the interwafer region is adequately represented by a gas phase diffusion equation.

The Knudsen number characterizing the interwafer transport may be defined as the ratio of the mean free path to the interwafer spacing. When the total pressure is ~0.2 Torr or less, for a typical LPCVD temperature of around 900 K and interwafer spacing of 0.5 cm, the gas becomes rarefied ($Kn > 0.1$). Under these circumstances a continuum description of the gas transport is unreliable. In particular it is the assignment of the diffusion coefficient which becomes questionable, as outlined in Chapter 1.

This limitation of the continuum approach has served as the primary motivating factor in developing a DSMC simulation model of the interwafer transport and deposition. The objectives of this study are twofold. First, the influence of a number of deposition parameters on the radial growth rate uniformity is investigated. Second, a comparison is made between the DSMC simulation results and a continuum-based analytical solution.

3.8.1 The interwafer simulation model

The interwafer simulation model is schematically depicted in Figure 3-29. The simulation zone consists of the narrow space which defines an interwafer region. The gas transport is assumed to be axisymmetric. Furthermore, a plane of symmetry is imposed between the two wafers, thereby reducing the computational costs by a factor of two.

The gas enters and leaves across the open perimeter boundary where the annular region gas composition, density, and temperature are specified. The source gas consists of a dilute mixture of a single reactant species in H_2 where the reactive sticking probability of the reactant is varied. The physical properties of the reactant molecule, molecular weight and diameter, were specified as those of SiH_4. This system was selected as representative of many CVD systems where a relatively heavy reactant molecule is transported with H_2 as the carrier gas. The wafer surface is assumed to be isothermal and the non-reactive gas-surface interactions are modelled as diffuse reflections with complete thermal accomodation. The simulations utilized the variable hard sphere model where the gas mixture VHS parameter was computed to be 0.21.

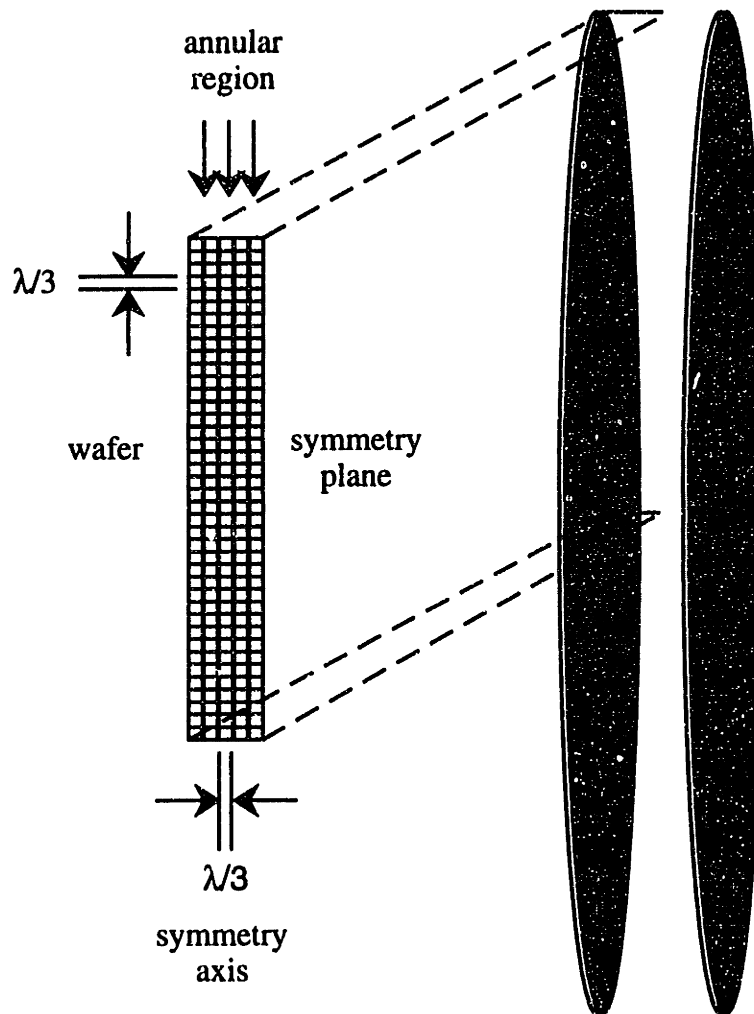

Figure 3-29 : DSMC cell network for LPCVD interwafer simulation model.

3.8.2 The nature of radial growth rate nonuniformity

The film growth process in conventional LPCVD is complicated by the presence of gas phase chemistry. This often leads to a situation where multiple chemical species become major contributors to the overall film growth rate. This may then bring about the onset of radial growth rate nonuniformity where significant growth rate contributions result from highly reactive species. This is especially true for the case when polysilicon films are *in-situ* doped by the addition of PH_3 to the inlet gas stream. It has been suggested that the PH_3 acts to block the adsorption of SiH_4, thereby increasing the importance of the growth channel due to the reactive intermediate SiH_2 formed in the gas phase chemistry [Meyerson and Yu, 1984]. The LPCVD film growth for this system has been modelled as resulting from the additive effects of SiH_4 and SiH_2, where the SiH_2 originates from the gas phase decomposition of SiH_4 [Yeckel and Middleman, 1987]. The simulation results presented below consider the effects of a single highly reactive species on the growth rate uniformity, assuming that the less reactive species contributes to the film growth in a uniform fashion.

The DSMC simulations were performed in order to gain an understanding of the influences of the precursor reactivity and the degree of flow rarefaction on the resulting radial film thickness uniformity. The conditions for the base case simulation are listed below in Table 3-3.

Gas Source Properties	Composition Temperature Number Density (Pressure)	5% Reactant / 95% H_2 900 K 1.073×10^{15} cm^{-3} (0.1 Torr)
Wafer Properties	Temperature Diameter Interwafer Spacing	900 K 5.0 cm 0.5 cm
Simulation Parameters	Cell Dimension Time Step Molecular Model - VHS Parameter	0.05 cm 0.05 μs Variable Hard Sphere 0.21

Table 3-3 : Conditions for the base case interwafer simulation.

The first set of simulations examined the growth rate uniformity as a function of reactive sticking probability for the base case conditions listed above. The reactant flux, normalized with respect to the flux at the wafer edge, is plotted versus the normalized radial wafer position in Figure 3-30 for reactive sticking probabilities of 0.05, 0.1, and 0.3. As the reactive sticking probability is increased the reactant is more efficiently depleted, leading to a suppression in the growth rate near the axis. From a molecular viewpoint, a typical reactant molecule will participate in a number of gas-surface interactions prior to reacting. As the sticking probability is increased the molecule has a greater probability of reacting with the surface before reaching the axis. This effect is further illustrated in Figure 3-31 where the growth rate uniformity, defined as the growth rate at the axis divided by the growth rate at the edge, is plotted as a function of the reactive sticking probability.

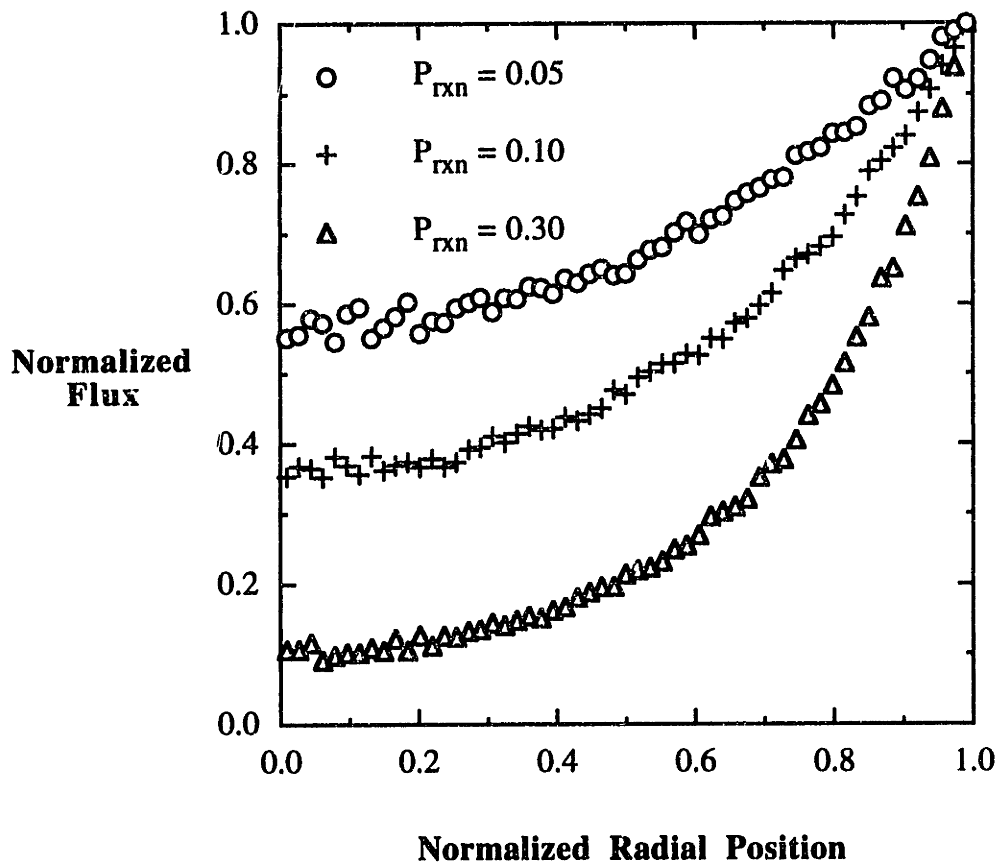

Figure 3-30 : Radial flux distribution as a function of reactive sticking probability for the base case interwafer simulation.

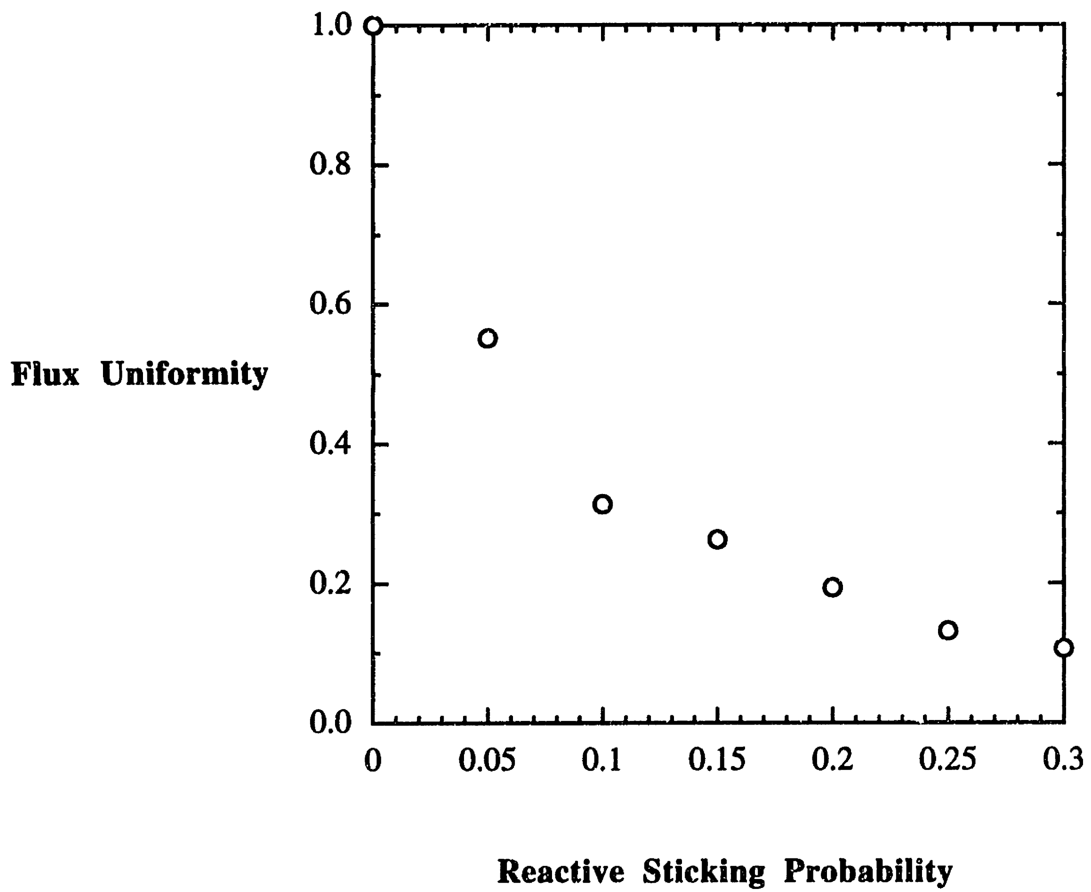

Figure 3-31 : Radial flux uniformity as a function of reactive sticking probability for the base case interwafer simulation.

The next parameter which was investigated was the interwafer spacing. The reactant flux is plotted versus radial wafer position in Figure 3-32 for interwafer spacings of 0.5 and 1.0 cm. The remaining conditions of Table 3-3 apply and the reactive sticking probability is set at 0.3 for both cases. The flux uniformity is greatly improved for the larger interwafer spacing. The larger spacing allows the reactant molecules to diffuse further into the interwafer region before being depleted. This strong dependency of the diffusivity on the "channel" size is characteristic of diffusion under conditions where gas-surface collisions predominate, *i.e.* Knudsen diffusion [Aris, 1975]. Thus, the collisions with the wafers appear to exhibit a strong influence on the interwafer transport under these conditions.

Reactant flux profiles for entering reactant mole fractions of 0.05 and 0.25 are shown in Figure 3-33 where the reactive sticking probability has been set at 0.1 for both simulations. The varying composition would be expected to have an effect upon the transport of the reactant molecules by virtue of the composition dependent gas phase collision rate. This is clearly not the case for conditions in Figure 3-33 as the flux profiles virtually overlap. This once again suggests that the gas transport and the corresponding growth rate profiles are governed by the gas-surfacc interactions for transition regime flows in the interwafer regions.

3.8.3 A comparison with the continuum solution

It is instructive to compare the DSMC simulation results with the analytical solutions given by a continuum-based model which would, in principle, be applicable strictly for $Kn < 0.1$. As discussed in Chapter 1, the transport coefficients predicted by the Chapman-Enskog theory become increasingly unreliable as the Knudsen number approaches unity. The continuum solution derived below requires the specification of the

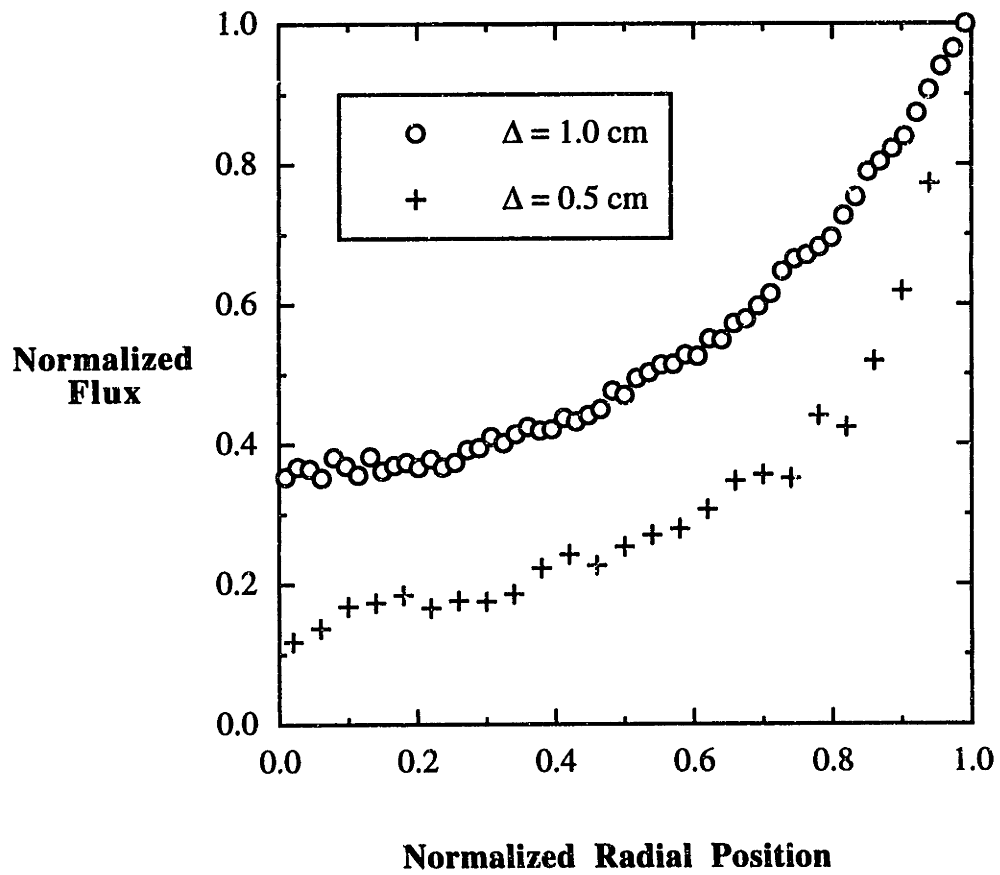

Figure 3-32 : Radial flux distribution as a function of interwafer spacing.

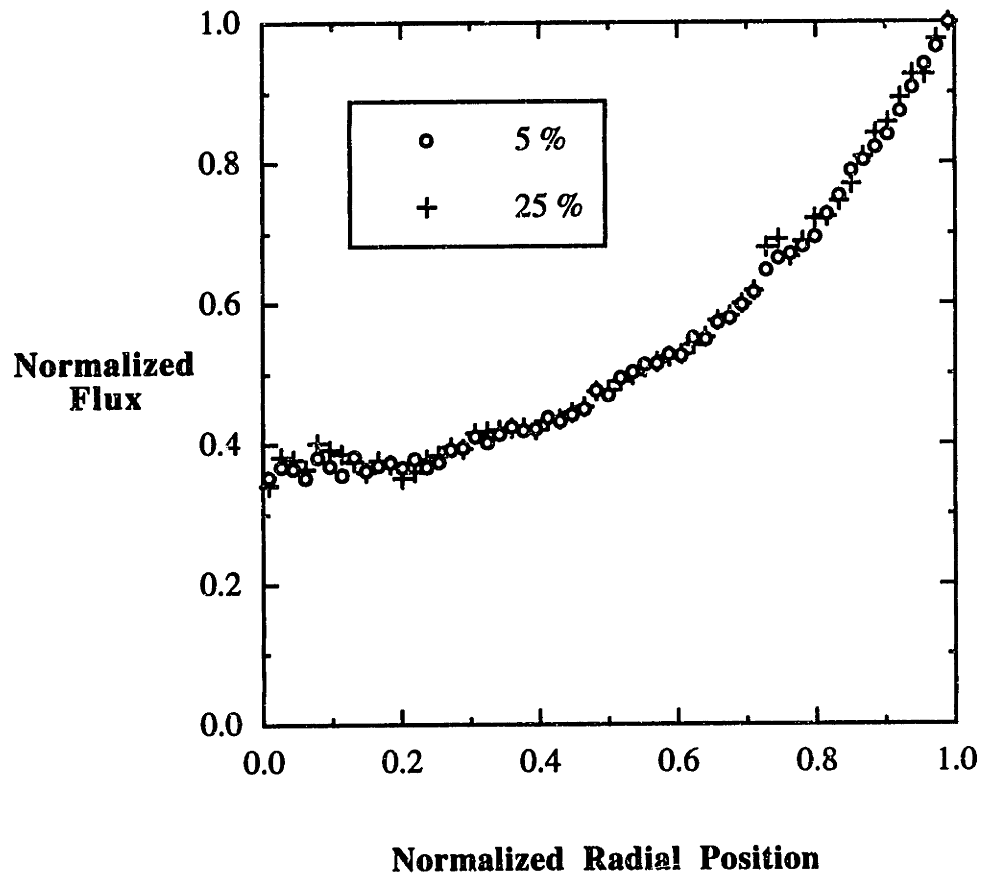

Figure 3-33 : Radial flux distribution as a function of reactant concentration.

reactant gas phase diffusivity in the interwafer region, D_g, as well as the surface reaction rate constant, k_s. In this formulation it is impossible to unambiguously assess whether or not these values have been correctly assigned. For example, an error in the value of the diffusivity may be corrected for by adjusting the value of the reaction rate constant in order to match experimental data.

The DSMC interwafer simulations require essentially the same input as the analytical formula. The important distinction to be made is that the DSMC method does not require any transport coefficients; this information is implicitly contained within the molecular parameters. The reactive sticking probability, P_{rxn}, is related to the first-order surface reaction rate constant, k_s, according to :

$$k_s c = P_{rxn} \times \frac{1}{4} n \overline{c'}, \qquad (3\text{-}14).$$

where $n\overline{c'}/4$ is the impingement rate given by the kinetic theory of gases. By matching the simulated flux profiles with the analytical profiles for a given reactive sticking probability and corresponding reaction rate constant, it is then possible to quantitatively determine the appropriate value of the interwafer reactant diffusivity. This will also provide a measure of how much the transition regime diffusivities deviate from the diffusivities predicted by the Chapman-Enskog theory.

The continuum analysis proceeds under the assumption that the interwafer transport is absent of convective effects, *i.e.* gas phase diffusion acts alone. Furthermore, it is assumed that the source gas is depleted by a first-order reaction on the wafer surface. Multicomponent diffusion effects are neglected as well. The governing transport equation and boundary conditions may be written as follows :

$$D_g \left\{ \frac{1}{r}\frac{\partial}{\partial r}\left(r \frac{\partial c}{\partial r} \right) + \frac{\partial^2 c}{\partial z^2} \right\} = 0, \quad ; \; 0 \le r \le R_w \; , \; 0 \le z \le \Delta \tag{3-15}$$

$$\frac{\partial c}{\partial r}(r{=}0,z) = 0, \tag{3-16}$$

$$c(r{=}R_w,z) = c_o, \tag{3-17}$$

$$\pm D_g \frac{\partial c}{\partial z}(r,z{=}0,\Delta) = k_s c(r,z{=}0,\Delta), \tag{3-18}$$

where c is the reactant concentration, R_W is the wafer radius, and Δ is the interwafer spacing. The analytical solution is conveniently expressed in terms of the dimensionless variables $y \equiv c/c_O$, $\xi \equiv r/R_W$, and $\gamma \equiv z/R_W$:

$$y(\xi,\gamma) = \sum_{i=1}^{\infty} \frac{Io(\lambda_i \xi)\, F_i(A,Ko)}{\lambda_i Io(\lambda_i)} \left\{ \lambda_i \cos\lambda_i \gamma + Ko \sin\lambda_i \gamma \right\}, \tag{3-19}$$

where Io is the modified zero order Bessel function of the first kind. The various other terms appearing in the above expression are related according to :

$$\frac{\tan\lambda_i}{A} = \frac{2\lambda_i Ko}{\lambda_i^2 - Ko^2}, \tag{3-20}$$

$$F_i(A,Ko) = \phi^2 \frac{1 + \left(\frac{\lambda_i^2 + Ko^2}{\lambda_i^2 - Ko^2} \right) \cos(\lambda_i / A)}{\lambda_i^2 + Ko^2 + \phi^2}, \tag{3-21}$$

where $A \equiv R_w/\Delta$, $Ko \equiv k_s R_w/D_g$, and $\phi^2 \equiv 2AKo$. The quantity ϕ is usually referred to as the Thiele modulus in the chemical engineering literature [Levenspiel, 1972]. The reactant flux, normalized with respect to the flux at the wafer edge, is given by :

$$y(\xi,\gamma{=}0) = \sum_{i=1}^{\infty} \frac{Io(\lambda_i\xi)}{Io(\lambda_i)} F_i(A,Ko). \qquad (3\text{-}22).$$

The analytical flux profiles are then uniquely defined once the values of A and Ko have been specified. The solution converges rapidly after about ten terms in the series have been summated.

In transition regime flows, the Bosanquet interpolation formula is commonly used in order to obtain an effective diffusion coefficient, D_{eff}, for a particular geometry [Pollard and Present, 1948]. Implicit in this formula is the idea that the mass transport is impeded by collisions with other molecules as well as collisions with the bounding surface. This formula is conveniently expressed in terms of the reciprocal of the effective diffusion coefficient which represents the overall resistance to mass transport :

$$\frac{1}{D_{eff}} = \frac{1}{D_{gas}} + \frac{1}{D_{Kn}}, \qquad (3\text{-}23).$$

where D_{gas} is the gas phase diffusivity predicted by the Chapman-Enskog theory and D_{Kn} is the Knudsen diffusion coefficient.

The Knudsen diffusivity may be analytically determined for axial diffusion through an infinitely long tube [Kennard, 1938] while semi-empirical expressions have

been derived to address deviations from this ideal case such as finite length tubes [Pollard and Present, 1948] and noncircular cross-sections [Eldridge and Brown, 1976]. However, in the interwafer geometry the notion of a Knudsen diffusivity is a somewhat ill-defined concept as the molecules are not completely confined by the wafers as in the case of axial diffusion through a tube.

In spite of the lack of a parallel to Knudsen diffusion, the general form of the Bosanquet formula may still be used to characterize the interwafer transport. The resistance to flow due to gas-surface interactions is now represented by a new parameter, $\mathcal{R}_{wafer}$:

$$\frac{1}{D_{eff}} = \frac{1}{D_{gas}} + \mathcal{R}_{wafer}. \qquad (3\text{-}24).$$

A number of simulations were performed at various pressures in order to determine the effective diffusivity as a function of the Knudsen number. The entering reactant mole fraction was restricted to 0.05 in order to obtain a useful comparison with the continuum model where multicomponent diffusion effects are not considered. The effective diffusivity is plotted versus the Knudsen number in Figure 3-34. Also shown are the gas phase diffusivity predicted by the Chapman-Enskog theory and the estimated Knudsen diffusivity in a rectangular channel of aspect ratio 10, corresponding to the ratio of the wafer diameter to interwafer spacing [Eldridge and Brown, 1976].

The effective diffusivity is bounded by the Chapman-Enskog diffusivity at low Knudsen numbers where the gas flow is in the continuum regime. As the Knudsen number is increased, collisions with the wafers become predominant and the effective diffusivity approaches the free molecular flow limit where gas phase collisions are absent. The estimated channel Knudsen diffusivity becomes equivalent to the Chapman-

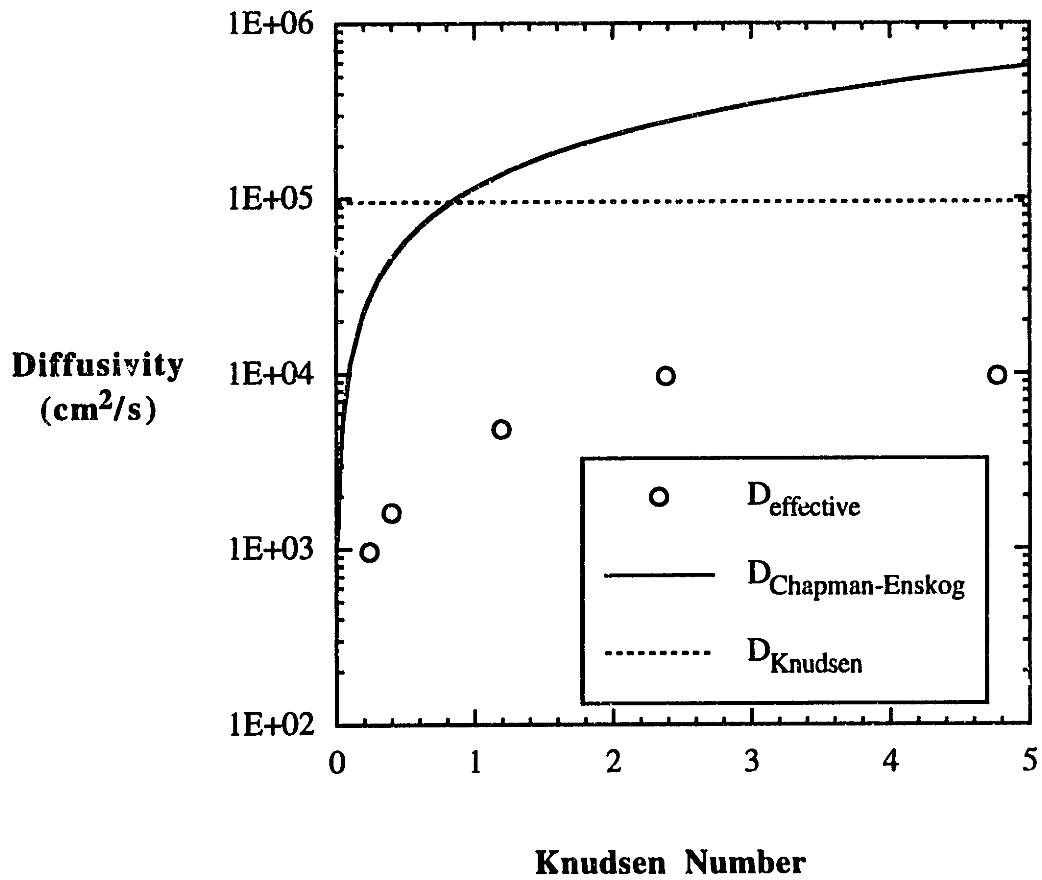

Figure 3-34 : Comparison of DSMC calculated interwafer effective diffusivities (O) with the Chapman-Enskog diffusivities (—) and Knudsen channel diffusivities (---) in the transition regime.

Enskog diffusivity at around Kn = 0.8 (30 mTorr). This suggests that the intermolecular collisions play a major role in the transport at pressures ≥ 30 mTorr. The DSMC results contradict this suggestion, however, as the gas-surface collisions continue to exhibit a strong influence on the transport at around 100 mTorr. By extrapolating the simulation data to higher pressures, it is estimated that the interwafer spacing should be at least ten mean free paths before the gas phase collisions have a significant effect on the transport. It is seen that a continuum description employing conventional Chapman-Enskog diffusivities would be inaccurate for transition regime flows in the interwafer region.

3.9 Gas phase chemistry in DSMC simulations of polysilicon LPCVD

An assumption common to all of the conventional polysilicon LPCVD models to date is that the gas phase decomposition of SiH_4 may be safely ignored. This assumption was challenged by the experimental findings of Scott and Estes where the homogeneous decomposition of SiH_4 was investigated as a function of temperature, total pressure, SiH_4 partial pressure, and reactor residence time [Scott and Estes, 1989]. Their experiments indicated that a measurable onset of SiH_4 gas phase decomposition occurs at pressures around 0.1 Torr for a temperature of 622 °C and a residence time of 0.15 s. These conditions are certainly within the window of operating conditions employed in polysilicon LPCVD processes.

The incorporation of gas phase chemistry into the DSMC algorithm as outlined in section 2.5.4 is conceptually straightforward. This approach has been successfully implemented in simulations of atmospheric chemistry in high altitude hypersonic flows [G. Bird, 1986; Boyd, 1990]. The general idea is to obtain an expression for the steric factor which is consistent with a known macroscopic rate expression for a given reaction.

However, a great deal of uncertainty is associated with the description of the energetics of reactive collisions with regard to the internal energy contribution. In addition, the statistical difficulty associated with the presence of trace species - in this case the reactive intermediates - is compounded by the fact that extremely few intermolecular collisions result in chemical reactions in most cases. The next section outlines a new hybrid approach to simulating reactive rarefied gas flows which circumvents the statistical difficulties associated with gas phase chemistry in DSMC simulations.

3.9.1 A new hybrid approach for simulating reactive rarefied gas flows

The use of a hybrid Monte Carlo-continuum approach for reactive flow simulations was previously demonstrated by DeJong and coworkers [DeJong *et al.*, 1992]. In their simulations the continuum-based Navier-Stokes equations were used to describe the gas transport while the DSMC method was used to compute the gas phase chemistry. In much the same spirit, a new method is presented here which takes the opposite approach. The gas transport is simulated using the DSMC method while a macroscopic kinetic rate expression is solved to simulate the gas phase chemistry. Before describing the details of this approach, it is necessary to briefly mention the use of weighting factors in DSMC simulations.

The use of radial weighting factors to counter the statistical noise near the axis in axisymmetric DSMC simulations was mentioned in Chapter 2. This feature essentially exploits the fact that the number of real molecules represented by each simulated molecule may vary according to the radial position. This allows for a larger sampling to be obtained near the axis where the small cell volumes would otherwise demand prohibitively lengthy simulation runs. In a similar fashion the ratio of real to simulated molecules (γ) may vary according to molecular species. By selectively reducing this ratio

for species which are present in trace amounts, a larger sampling of simulated molecules may be obtained for these species. The gas phase collision routine is slightly modified when using species weighting factors. The post-collision scattering for collisions between species with different weighting factors is always performed for the less prevalent species and is probabilistically performed for the more prevalent species. The end result of this is that energy is not necessarily conserved with each collision but is conserved on average [G. Bird, 1976].

The gas phase chemistry is simulated within each of the cells by integration of the specified rate equations over each molecular motion time step. The chemical transformations are accomplished by adjusting the ratio of real to simulated molecules for each participating species according to the prevailing conditions within each cell. The hybrid approach described here effectively implements weighting factors which vary according to species as well as position.

The statistical advantage gained from this approach is best understood by considering the hypothetical bimolecular reaction between species A and species B :

$$A + B \rightarrow C + D \qquad (3\text{-}25).$$

The rate equation for species A, considering the reaction to be irreversible, may be written as :

$$-\frac{dn_A}{dt} = k(T_{cell})\, n_A n_B, \qquad (3\text{-}26).$$

where n_i is the number density of species i and T_{cell} is the gas temperature within the cell. The temperature dependent macroscopic rate constant usually takes the form :

$$k(T) = a\,T^{b} \exp\left(\frac{-E_A}{k_B T}\right) \qquad (3\text{-}27).$$

where a and b are constants and E_A is the activation energy [Weston and Schwarz, 1972]. Assuming that an average of 10,000 A-B collisions are required before the reaction of (3-25) may occur, in the conventional approach the transformation of the two simulated A and B molecules is sampled on average once every 10,000 collisions. The proposed method outlined above would effectively convert A and B with the same kinetics, yet the statistical noise associated with the infrequent sampling of the conventional approach is avoided since the molecules are fractionally converted at each integration step.

Consider the conversion of A as given by equation (3-26), now in terms of the number of real molecules represented by the simulated molecules in a particular cell. The number of real molecules of A represented in the cell is computed according to :

$$N_A = \sum_{i=1}^{N_A^s} \gamma_{A_i}, \qquad (3\text{-}28).$$

where N_A^s is the number of simulated A molecules in the cell which may have different values of γ according to their previous participation in chemical reactions. In the simulation, equation (3-26) is integrated over some time period $\Delta t = t_f - t_o$ to determine the new value of γ_A for the molecules residing in this cell :

$$-\Delta N_A = N_A(t_o) - N_A(t_f) = \int_{t_o}^{t_f} k(T) N_A N_B \, dt \approx k(\overline{T}) \overline{N_A}\,\overline{N_B}\,\Delta t, \qquad (3\text{-}29).$$

where the average value of the integrand over the time period Δt is used. If Δt corresponds to the molecular motion time step, then the instantaneous value of the integrand is used. γ_A is then modified to reflect the fractional conversion :

$$\gamma_A(t_f) = \overline{\gamma_A}(t_o)\left[1 + \frac{\Delta N_A}{N_A}\right] \quad (3\text{-}30).$$

If A is consumed ($\Delta N_A < 0$), then γ_A is lowered for each simulated molecule in the cell; γ_A is increased otherwise. The balances for the other participating species are similarly computed.

3.9.2 Silane decomposition kinetics

The reaction mechanism to be considered for the simulation of polysilicon LPCVD from SiH_4 is a subset of the complete mechanism [Moffatt and Jensen, 1988]. The mechanism includes the following forward and reverse reactions :

$$SiH_4 \rightleftarrows SiH_2 + H_2 \quad (3\text{-}31).$$

$$Si_2H_6 \rightleftarrows SiH_4 + SiH_2 \quad (3\text{-}32).$$

The forward reaction rate constants (k_1,k_2) were obtained from detailed RRKM calculations and the reverse reaction rate constants (k_{-1},k_{-2}) were deduced from the equilibrium constants [Moffatt *et al.*, 1991]. The unimolecular rate constants for SiH_4 and Si_2H_6 decomposition were found to be well into the low pressure limit, exhibiting a linear dependence on the total pressure :

$$k_{uni} \approx k_o(M) \qquad (3\text{-}33).$$

where k_o is the low pressure bimolecular rate constant and (M) is the total concentration in the gas phase. The kinetic data fo[illegible] SiH_4 chemistry subset is summarized in Table 3-4 where the low pressure values are used and the units are given in (cm^3/s).

Rate Constant	**a**	**b**	**E_A (kcal/mol)**
k_1	1208.161	-2.206	58.17
k_{-1}	1.36×10^{-6}	-2.93	1.02
k_2	3.421×10^{21}	-7.499	54.39
k_{-2}	3.941×10^{7}	-6.528	0.26

Table 3-4 : Kinetic data used in polysilicon LPCVD simulations [Moffat *et al.*, 1991].

3.9.3 Interwafer simulations with silane gas phase chemistry

The interwafer simulations are now performed using the DSMC model outlined in section 3.8.1 with the gas phase chemistry given in equations (3-31) and (3-32). The heterogeneous decomposition of SiH_4, SiH_2, and Si_2H_6 on the Si surface is also included through the use of appropriate reactive sticking coefficients. The composition of the reactive gas entering from the annular flow region was specified according to estimates

provided by continuum calculations [Roenigk, 1987]. The properties of the incoming gas are summarized in Table 3-5.

Species	Inlet Mole Fraction	P_{rxn}
SiH_4	0.848999	$2x10^{-4}$
SiH_2	$1x10^{-6}$	1.0
Si_2H_6	0.001	0.001
H_2	0.15	0

Table 3-5 : Gas properties for the polysilicon LPCVD reactive flow simulations.

The reactive flow simulation is first performed for an annular pressure of 0.1 Torr. The interwafer gas phase concentrations of the highly reactive components SiH_2 and Si_2H_6 are shown in Figure 3-35. For both species the concentration is significantly depleted as the axis is approached, consistent with the results previously shown in Figure 3-30. The SiH_4 and H_2 concentrations were found to be uniform throughout the annular region. Also shown in Figure 3-35 are the relative contributions to the polysilicon film growth made by the SiH_4, SiH_2, and Si_2H_6 species as a function of radial position. It is seen that the radial flux uniformity is inversely proportional to the reactivity of the species.

The reactor operating pressure is now increased to 1.0 Torr. This is done in order to assess the impact on the growth rate uniformity resulting from an enhancement of the gas phase chemistry. The annular region composition is maintained according to the

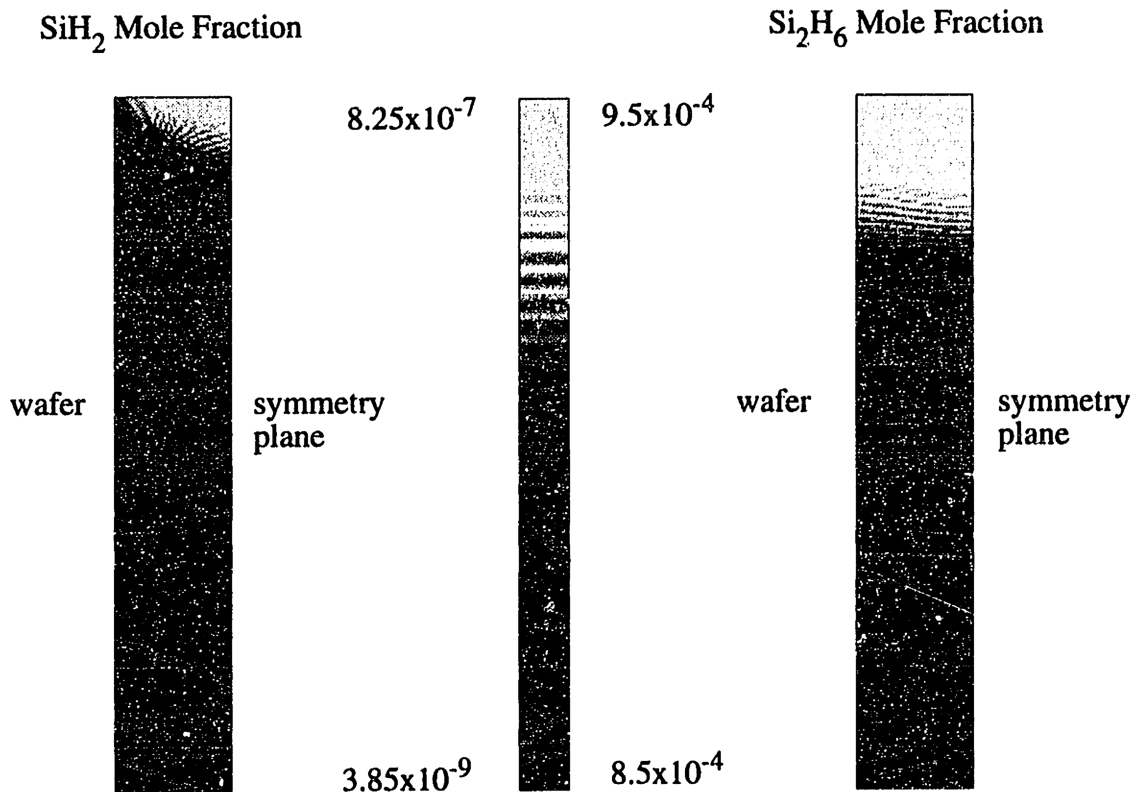

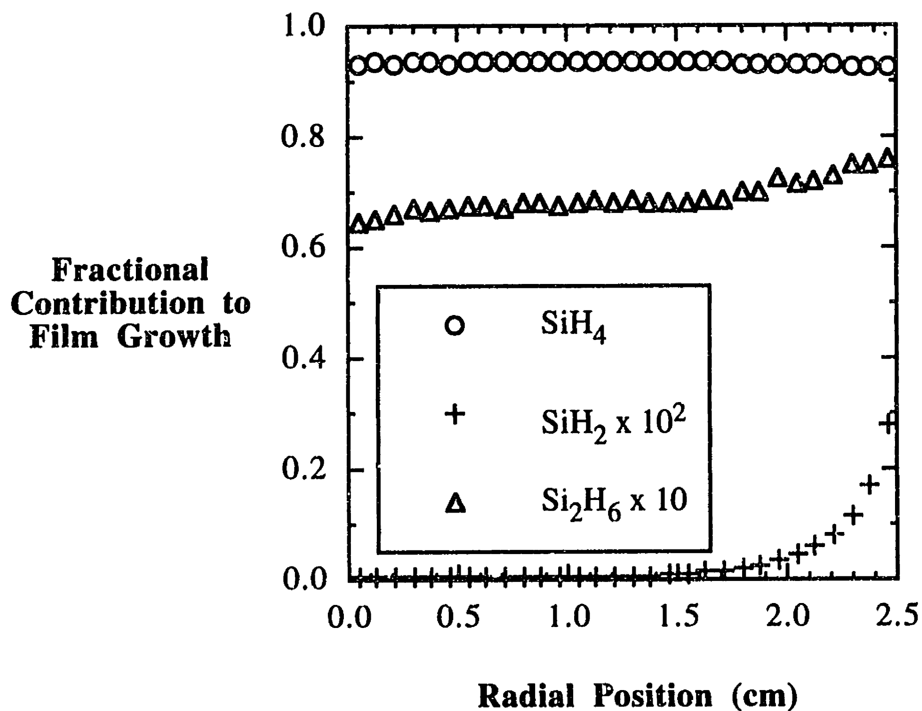

Figure 3-35 : Gas phase distribution and film growth contributions for reactive flow polysilicon LPCVD simulations.

specifications listed in Table 3-5. The total polysilicon film growth rate, normalized with respect to the growth rate at 1.0 Torr, is shown in Figure 3-36a for the two operating pressures. The growth rate is seen to scale with the total operating pressure with no evidence of radial growth rate nonuniformity at the higher pressure. This is consistent with the growth rate contributions due to SiH_2 shown in Figure 3-36b for the two operating pressures. Reactive flow simulations involving higher operating pressures are prohibitively expensive using the DSMC method.

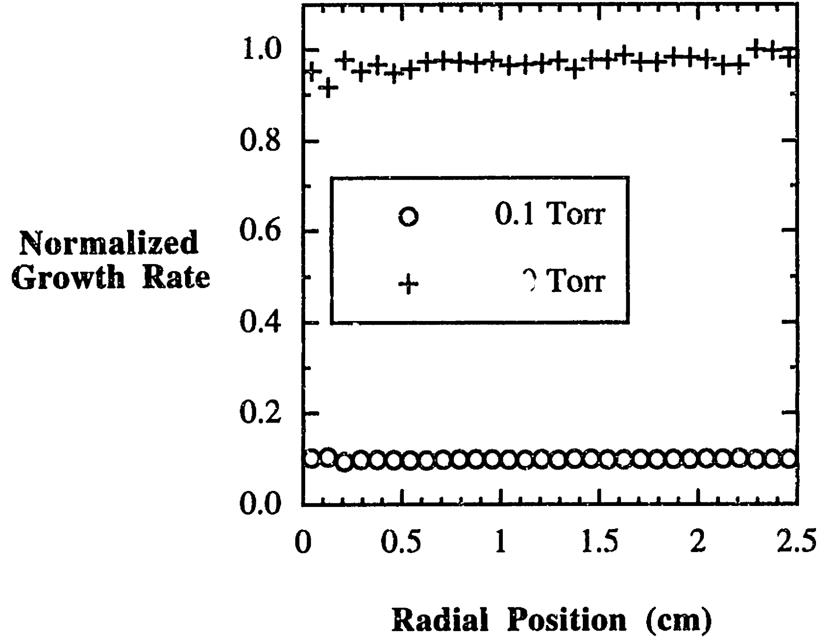

Figure 3-36a : Radial growth rate profiles for polysilicon reactive flow simulations at 0.1 Torr (O) and 1.0 Torr (+).

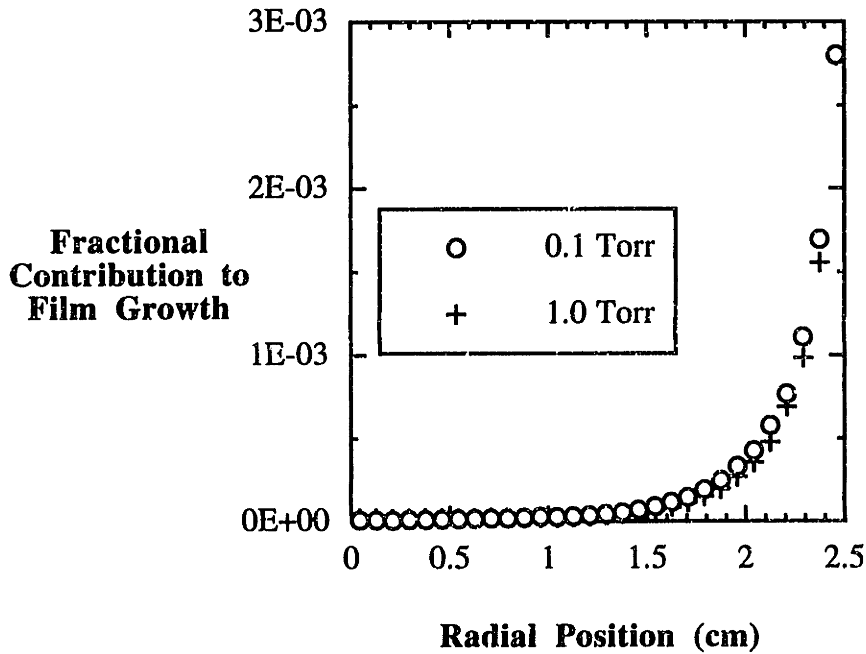

Figure 3-36b : SiH_2 film growth contributions for polysilicon LPCVD simulations at 0.1 Torr (O) and 1.0 Torr (+).

Chapter 4 : Heat Transfer Analysis of the LPCVD Reactor

4.1 Motivation for a heat transfer model of the LPCVD reactor

Most LPCVD reactor models have assumed the reactor to be an isothermal environment [Kuiper *et al.*, 1982; Jensen and Graves, 1983; Middleman and Yeckel, 1986; Roenigk, 1987; Hopfmann *et al.*, 1991]. This assumption is not entirely correct since the ends of the reactor are water cooled in order to protect the O-ring seals. Recent experimental measurements have confirmed that this gives rise to a suppression in the temperature of the end wafers owing to radiative heat losses [Badgwell *et al.*, 1992a]. Since the film growth typically occurs in the surface reaction-limited regime where the temperature is exponentially related to the growth rate, the corresponding growth rate variations result in the sacrificial loss of several wafers at each end of the wafer load.

The model of Badgwell and coworkers was the first to include realistic thermal variations in the LPCVD reactor [Badgwell *et al.*, 1992b]. Their approach was to develop an empirical polynomial expression to describe the radial and axial temperature variations along the wafer stack. The three parameter expression was determined from experimental growth rate uniformity measurements. The use of this expression in the reactor modelling equations was shown to provide an improved description of the axial and radial growth rate variations.

In a followup experiment by Badgwell *et al.*, the wafer temperature variations in a commercial scale LPCVD reactor were determined directly from *in-situ* measurements [Badgwell *et al.*, 1992a]. A number of instrumented wafers, each with several attached thermocouple probes as shown in Figure 4-1, were strategically placed in a boat of 150 wafers. The measured wafer temperature profile was found to be insensitive to both the gas flow rate and composition, thus indicating the negligible contributions of convective and conductive heat transfer, respectively. This suggests that the dominant mode of heat transfer for typical LPCVD conditions is thermal radiation.

Despite the usefulness of the empirical approach for including variations in the wafer temperatures, the thermal profile may be expected to vary with reactor size and wafer configuration [Badgwell *et al.*, 1992a]. This would then require a refitting of the parameters for each different geometry. It is therefore desirable to have a fundamental description of the heat transfer in LPCVD reactors which may be used to simulate the temperature profiles for any set of conditions. The recent work of Houf and coworkers at Sandia National Laboratories represents the pioneering efforts in this respect [Houf *et al.*, 1993]. Their model employed a view factor approach to calculate the radiative heat exchange between the wafers and the surrounding reactor environment.

4.2 Monte Carlo simulations of thermal radiation heat transfer

The use of Monte Carlo techniques to model thermal radiation heat transfer in enclosures is well established [Howell, 1968]. In this approach the thermal radiation is simulated by the generation of a large number of representative photons from each of the participating surfaces. The interactions of the photons with the surfaces of the enclosure are then determined by the specified properties of each surface. The strength of the Monte

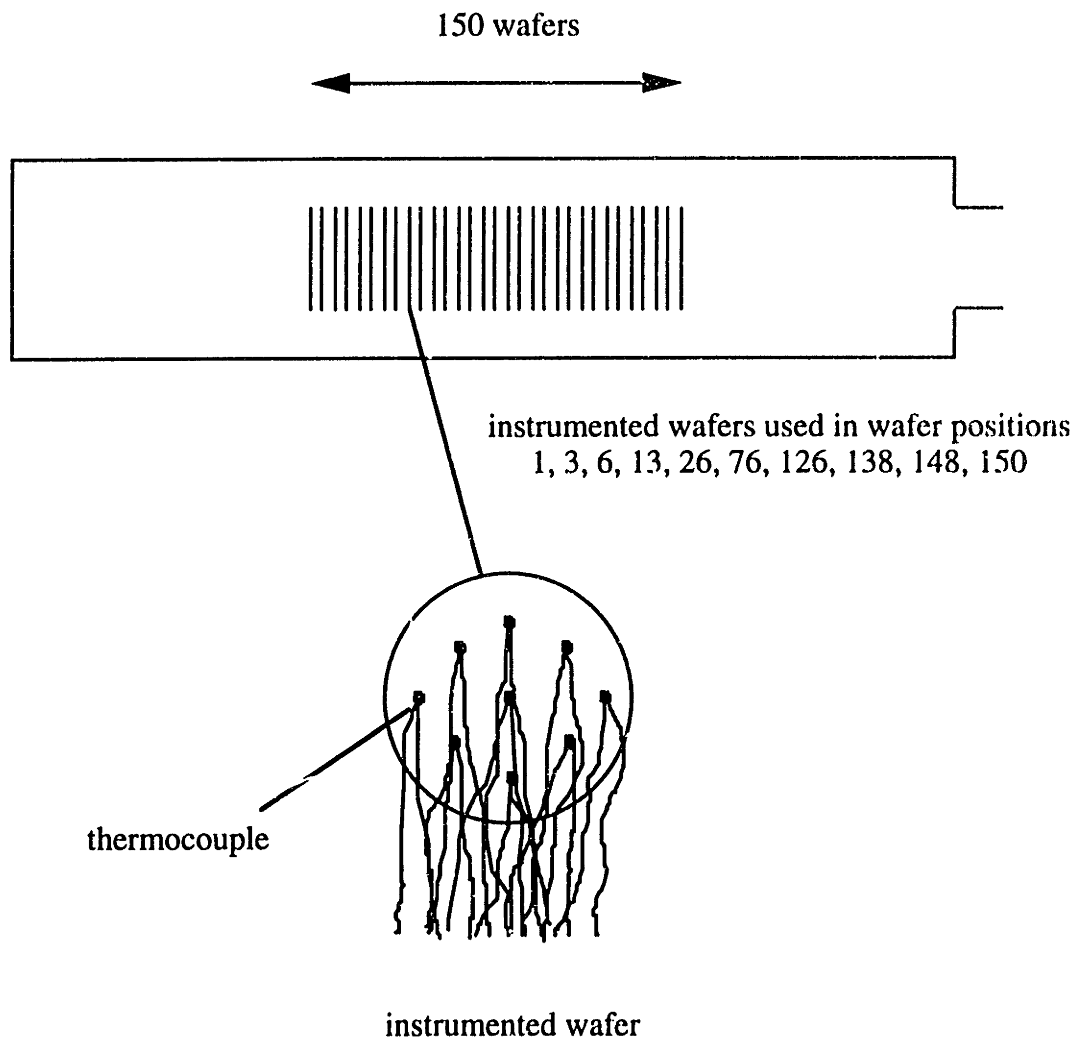

Figure 4-1 : Experimental setup for measuring LPCVD wafer temperatures after Badgwell *et al.*, 1992a.

Carlo approach is its ability to incorporate details which would make other approaches computationally unfeasible such as three-dimensional geometries and participating media [Siegel and Howell, 1992]. An adequate description of the thermal radiation heat transfer in the LPCVD reactor requires such details because of the complex geometry and the presence of non-gray, non-diffuse surfaces. The components of the Monte Carlo approach to modelling radiation heat transfer are outlined below.

4.2.1 Photon emission

The general expression for the radiative power from a surface element is given by :

$$e = \int_0^{\infty} \int_0^{2\pi} \int_0^{\pi/2} \varepsilon(\lambda,\theta,\phi,T)\, i_{b\lambda}(T)\, \sin\theta \cos\theta \, d\theta \, d\phi \, d\lambda, \qquad (4\text{-}1).$$

where ε is the directional spectral emissivity, λ is the wavelength, and θ and ϕ are the cone and circumferential angles, respectively, as shown in Figure 4-2 [Siegel and Howell, 1992]. The quantity $i_{b\lambda}$ is the blackbody spectral intensity of Planck's law given by :

$$i_{b\lambda}(T) = \frac{2C_1}{\lambda^5(e^{C_2/\lambda T}-1)}, \qquad (4\text{-}2).$$

where C_1 and C_2 are universal constants. Through a transformation of coordinates, equation (4-1) may be rewritten as :

$$e = \int_0^1 \int_0^1 \int_0^1 \varepsilon(\lambda,\theta,\phi,T)\, dF_\theta \, dF_\phi \, dF_\lambda. \qquad (4\text{-}3).$$

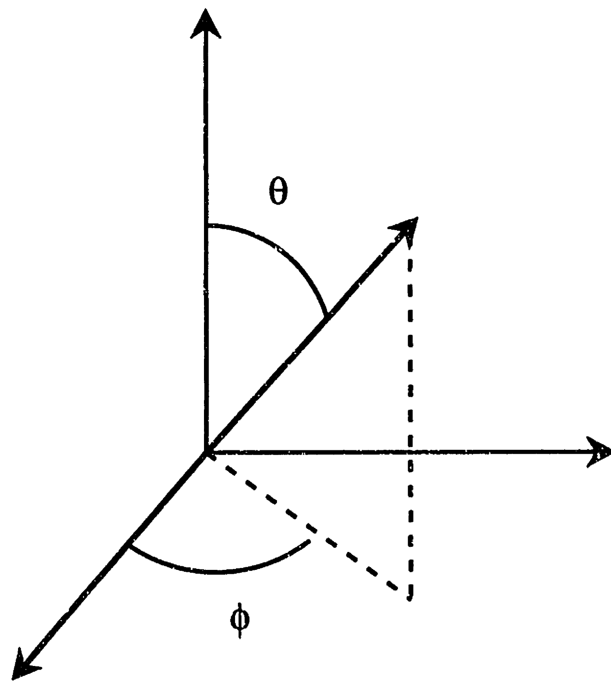

$$0 \leq \theta \leq \pi/2$$

$$0 \leq \phi \leq 2\pi$$

Figure 4-2 : Coordinate system used for Monte Carlo thermal radiation emission .

The variables F_θ, F_ϕ, F_λ represent the cumulative probability distributions for the directional and spectral properties of the emitted photons [Haji-Sheikh and Sparrow, 1969] :

$$F_\theta = \sin^2\theta, \qquad (4\text{-}4).$$

$$F_\phi = \phi/2\pi, \qquad (4\text{-}5).$$

$$F_\lambda = \frac{\left(\pi \int_0^\lambda i_{b\lambda}(T)\, d\lambda\right)}{\sigma T^4}, \qquad (4\text{-}6).$$

where σ is the Stefan-Boltzmann constant. It is well known that the integral in equation (4-6) is a universal function of the product λT alone and, therefore, $F_\lambda \equiv F_{\lambda T}$ [Howell, 1968]. The distributions derived above are completely general or unbiased, meaning they have been derived without reference to any specific properties of the surface. The use of unbiased probability distributions in Monte Carlo algorithms is referred to as direction simulation Monte Carlo [Haji-Sheikh, 1988].

The radiation emitted from the surface element per unit time is approximated as being transported by N representative photons per unit time. The emission angles and wavelengths of the N photons are determined as follows. A set of random numbers are generated for each photon and equated with the probability distributions given above which vary smoothly from zero to one. The corresponding values of θ, ϕ, and the product λT are then determined from equations (4-4), (4-5), and (4-6), respectively. The wavelength of the photon is assigned by division of the chosen value of λT by the temperature, T, of the

surface element from which it was emitted. The energy of the jth photon bundle is then given by :

$$E_j = \frac{\varepsilon(\lambda_j,\theta_j,\phi_j,T)\,\sigma T^4}{N}. \qquad (4\text{-}7).$$

4.2.2 Photon-surface interactions

Once the wavelength and direction of emission have been established for a particular photon, the photon is tracked through the enclosure until a surface is encountered. The possible interactions with the surface, each of which may simultaneously take place to some extent, include :

a). absorption of the photon,

b). reflection of the photon from the surface,

c). transmission of the photon through the solid.

In addition each of the above interactions, in general, will depend upon the photon properties, *i.e.* wavelength (λ) and angle of incidence (θ_i), as well as the properties of the surface - most notably the surface temperature [Siegel and Howell, 1992].

The photon-surface interactions are determined by probability distributions in much the same way as the gas-surface interactions in DSMC gas dynamics simulations are treated as outlined in Chapter 2. A random fraction is generated and compared to the respective probabilities of absorption (α), reflection (ρ), and transmission (τ) of the surface in order to determine the fate of the photon. The probability of absorption is equated with the surface emittance in accordance with Kirchhoff's law and the sum of the probabilities is equal to unity [Siegel and Howell, 1992] :

$$\alpha(\lambda,\theta_i,T) \equiv \varepsilon(\lambda,\theta_i,T), \qquad (4\text{-}8).$$

$$\alpha(\lambda,\theta_i,T) + \rho(\lambda,\theta_i,T) + \tau(\lambda,\theta_i,T) = 1. \qquad (4\text{-}9).$$

The majority of surfaces encountered in engineering applications may be considered to be completely opaque (τ=0). This simplification is no longer valid for sufficiently thin layers (*e.g.* flat plate solar collectors) or for materials possessing a spectral window which does not interact with a certain range of wavelengths (*e.g.* glass). A photon encountering a semi-transparent layer may undergo a number of internal reflections before ultimately being absorbed, reflected, or transmitted. The multiple pass reflectance (R) and transmittance (T) must then be used and are related to the single pass probabilities according to :

$$R = \rho\left\{1 + \frac{(1-\rho)^2\tau^2}{1-\rho^2\tau^2}\right\}, \qquad (4\text{-}10).$$

$$T = \frac{\tau(1-\rho)^2}{1-\rho^2\tau^2}, \qquad (4\text{-}11).$$

$$\tau = \exp(-ad), \qquad (4\text{-}12).$$

where a is the absorption coefficient and d is the thickness of the semi-transparent medium [Siegel and Howell, 1992]. The situation is further complicated when it becomes necessary to account for the refraction of the photon path within the semi-transparent layer. This may occur when the index of refraction deviates considerably from unity in a relatively thick layer.

4.3 An example problem : thermal radiation heat transfer between infinite concentric cylinders

4.3.1 Problem description

An example problem is now considered in order to foster discussion of the salient features of the Monte Carlo thermal radiation technique. The problem of radiation heat transfer between two infinite concentric cylinders, each considered to be opaque gray bodies, was selected for convenience. The gray body assumption eliminates the need to sample from the wavelength distribution (equation 4-6) and the constant energy photons are now given by :

$$E = \frac{\varepsilon_T \sigma T^4}{N}, \qquad (4\text{-}13).$$

where ε_T is the total hemispherical emissivity and N is the number of simulated photons emitted per unit area per time. The problem is schematically illustrated in Figure 4-3. Analytical solutions to this problem are readily obtained for both specularly and diffusely reflecting surfaces, as well, and are written below without derivation [Siegel and Howell, 1992] :

$$Q_{net} = \frac{A_i \sigma (T_i^4 - T_o^4)}{1/\varepsilon_i + (A_i/A_o)(1/\varepsilon_o - 1)}, \qquad \text{(outer cylinder diffuse)} \qquad (4\text{-}14).$$

$$Q_{net} = \frac{A_i \sigma (T_i^4 - T_o^4)}{1/\varepsilon_i + 1/\varepsilon_o - 1}, \qquad \text{(outer cylinder specular)} \qquad (4\text{-}15).$$

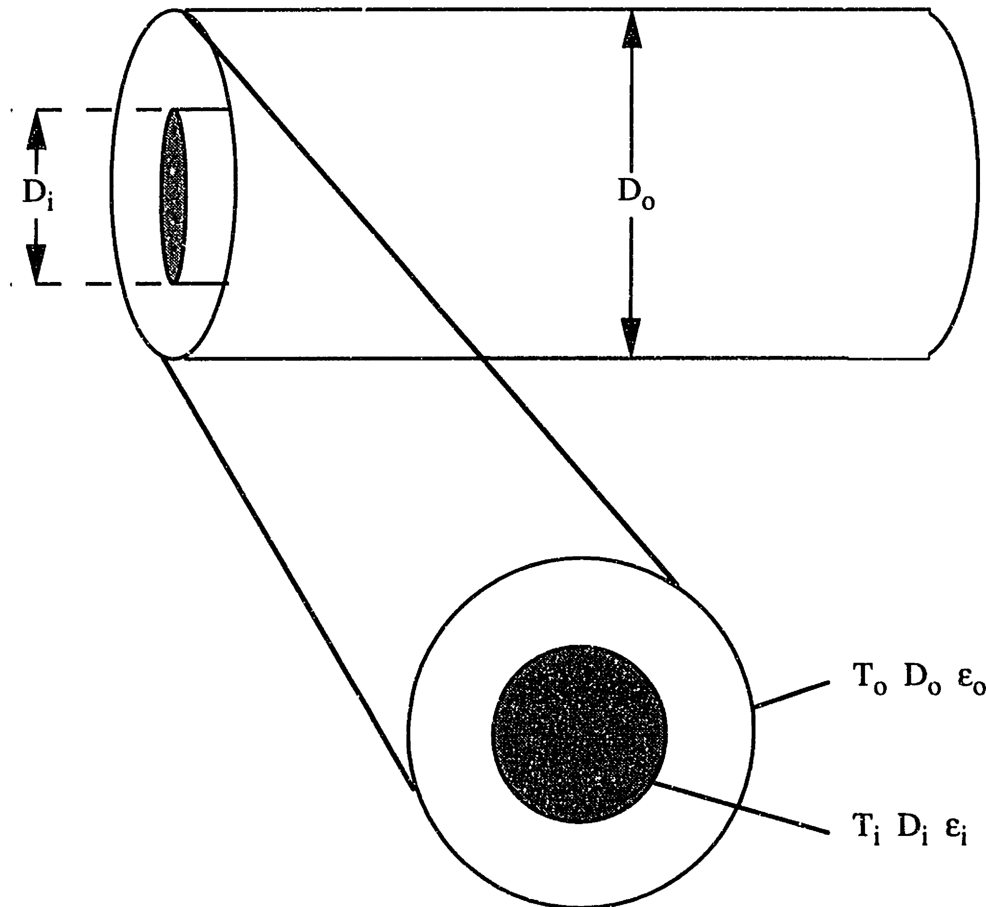

Figure 4-3 : Schematic diagram of example problem of radiation heat transfer between infinite concentric gray cylinders.

where Q_{net} refers to the net rate of heat transfer from the inner to the outer cylinder. The heat transfer is independent of the reflection characteristics of the inner cylinder since all of the photons reflected from the inner cylinder strike the outer cylinder.

4.3.2 Comparison of Monte Carlo results with the exact solution

The input to the simulation includes the diameter (D), temperature (T) and total hemispherical emissivity (ε_T) for each cylinder and the fraction of specularity (β_{spec}) for the outer cylinder which may vary from zero (completely diffuse) to unity (completely specular). The simulation results for various conditions are given in Table 4-1 below where the number of simulated photons generated was 10^6 for the inner cylinder and a proportional amount for the outer cylinder. The quantity Q_{MC}/Q_{exact} is the ratio of the net heat transfer from the inner to the outer cylinder of the Monte Carlo to the exact solutions given above. The Monte Carlo results show excellent agreement with the exact analytical solutions for both diffusely and specularly reflecting outer cylinders.

Inner Cylinder	Diameter	5 cm	7.5 cm	5 cm
	Emissivity	0.75	0.45	0.60
	Temperature	900 K	650 K	750 K
Outer Cylinder	Diameter	20 cm	15 cm	15 cm
	Emissivity	0.25	0.60	0.40
	Temperature	600 K	800 K	500 K
	Reflection	Diffuse	Diffuse	Specular
Simulation Results	$\frac{Q_{MC}}{Q_{exact}}$	1.0004	0.9994	0.9997

Table 4-1 : Comparison of Monte Carlo results with the exact results for thermal radiation heat transfer between infinite concentric cylinders.

The accuracy of the simulation results for the limiting cases of diffusely and specularly reflecting surfaces lends credence to the Monte Carlo solution of the intermediate cases where reflection from the outer cylinder has both diffuse and specular components. This is implemented in the Monte Carlo approach by specifying the fraction of specularity of the photons reflected from each particular surface. With each photon reflection, a random fraction is generated and compared to β_{spec}. If the random fraction is less than β_{spec}, then the reflection is completely specular, otherwise it is computed as completely diffuse. Radiative heat transfer involving these kinds of surfaces is completely unobtainable from the analytical approach.

The net radiative heat transfer is plotted as a function of outer cylinder specularity in Figure 4-4 where the inner and outer cylinder $\{D:\varepsilon_T:T\}$ are specified as $\{5\text{ cm} : 0.75 : 900\text{ K}\}$ and $\{20\text{ cm} : 0.25 : 500\text{ K}\}$, respectively. The normalization is with respect to the heat transfer for a completely diffuse outer cylinder. The Monte Carlo predictions show perfect agreement with the exact solutions of the limiting cases. The intermediate results are compared with a linear interpolation between the diffuse and specular solutions to illustrate the deviation from this tempting simplification.

A final observation to be made with this example problem of Monte Carlo thermal radiation calculations is concerning statistical sampling. In section 3.3.6 it was demonstrated how the statistical scatter is reduced as the square root of the sample size ($\sqrt{N_s}$) in the DSMC gas dynamics simulations. The same principle applies for Monte Carlo thermal radiation calculations as well, except N_s now applies to the number of photons generated. This is illustrated in Figure 4-5 where the ratio Q_{MC}/Q_{exact} is plotted as a function of the number of photons generated from the inner cylinder for several different random number seeds.

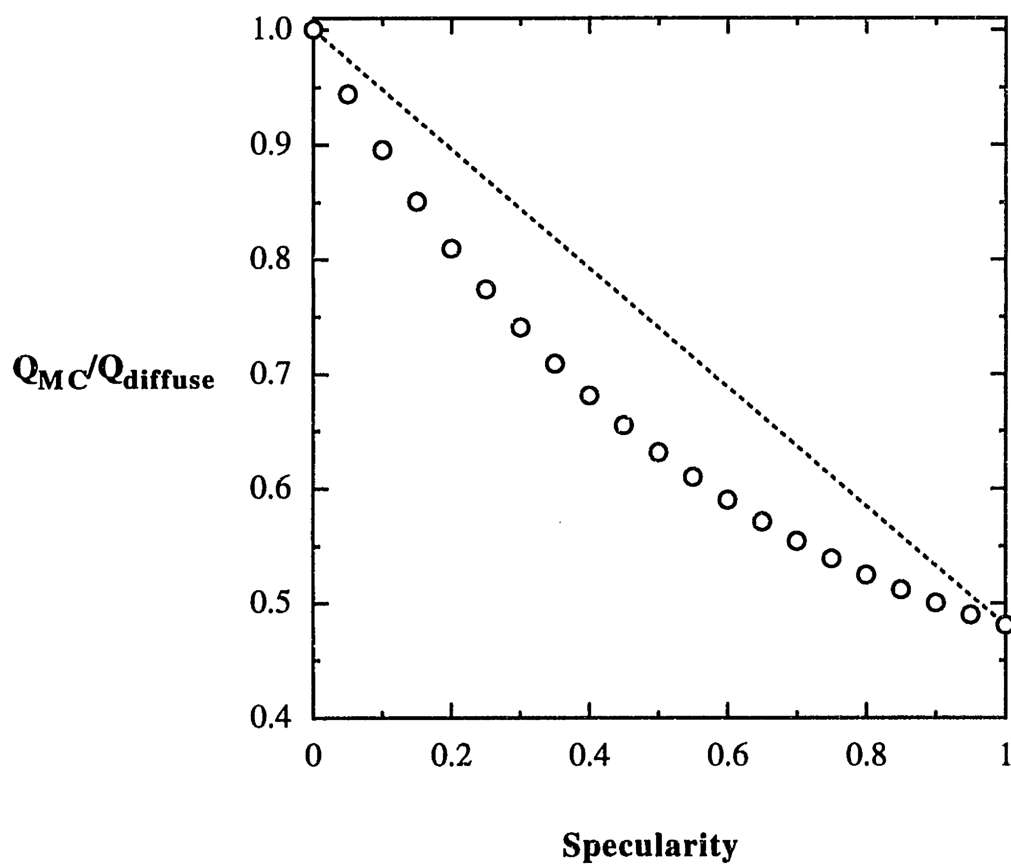

Figure 4-4 : Net radiative heat transfer between concentric infinite cylinders as a function of outer cylinder specularity.

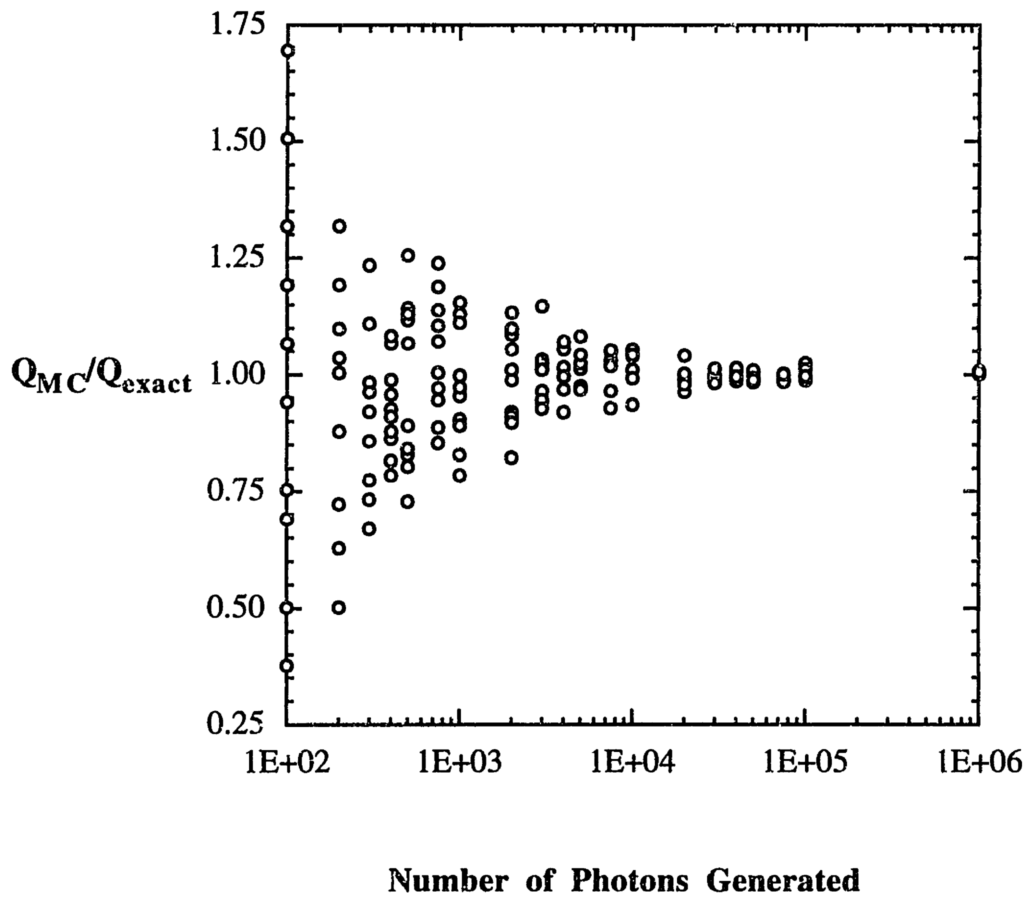

Figure 4-5 : Solution accuracy as a function of sample size for radiative heat transfer between infinite concentric cylinders.

4.4 Development of a Monte Carlo thermal radiation model of the LPCVD reactor

4.4.1 Model description

A two-dimensional axisymmetric LPCVD reactor is assumed for the Monte Carlo thermal radiation model as was utilized in the DSMC gas dynamics simulations. The model is schematically depicted in Figure 4-6. The presence of the quartz wafer boat and gas injector tubes are neglected due to their small surface areas and in order to preserve the axisymmetry. In addition, the relatively cold environment beyond the reactor outlet is approximated as a black body with negligible heat emission. The thermal radiation exchange between the Si wafers, the quartz reactor tube, the stainless steel ends of the reactor, and the alumina heater is considered. The intervening gas medium is assumed to be completely transparent to the thermal radiation. The emittance and reflectance characteristics of the insulating material adjacent to the alumina heater are assigned as those of alumina. The temperatures of the heater and the water-cooled ends of the reactor are specified beforehand and the quartz tube and wafer temperatures are determined in the simulation.

The radiative heat exchange is also coupled with conductive heat transfer in the quartz tube. This was deemed important since the quartz tube is in contact with the water-cooled ends of the reactor tube. The relative importance of radiation and conduction heat transfer in the quartz tube may be measured by considering the appropriate dimensionless group. The conductive heat transfer in the axial direction is approximately given by ($k\Delta T/\Delta z$) where k is the quartz thermal conductivity, ΔT is the temperature difference between the heater and the ends of the reactor, and Δz is the axial distance from the center

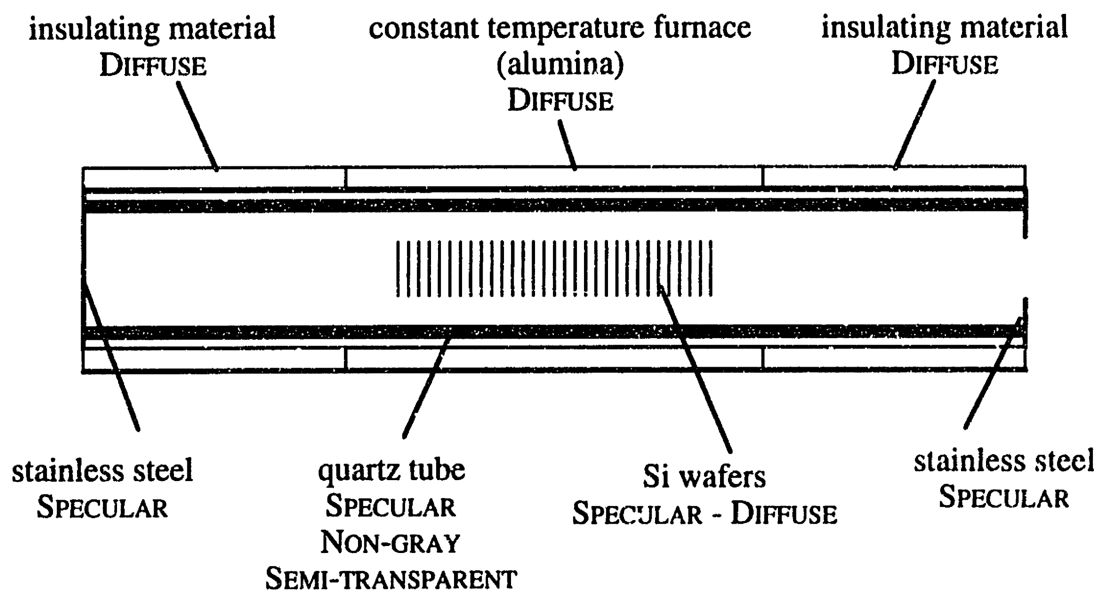

Figure 4-6 : Schematic of the LPCVD thermal radiation heat transfer model.

of the reactor tube to the end. The radiative heat transfer to the quartz tube is approximated as σT^4 where T is the heater temperature. The ratio of conductive to radiative heat transfer is then measured by $(k\Delta T/\Delta z\sigma T^4)$. Considering typical values of the heater and reactor ends to be 900 K and 350 K, respectively, and using the 40 cm research scale reactor described in Chapter 3, this ratio is on the order of 0.1. Although the radiative heat transfer is predominant, the conduction in the quartz tube is appropriately included in the model.

As with the DSMC gas flow simulations, an initial state must be specified and a transient period precedes the convergence to a steady thermal profile. Since only the steady-state conditions are sought, it is advantageous to start with a relatively hot isothermal reactor with the quartz tube and wafer temperatures set to the temperature of the heater. A linear temperature gradient is imposed across the insulating material between the alumina heater and the stainless steel ends. A number of cycles are then iterated until the quartz tube and Si wafer temperatures remain steady, at which time the conditions are averaged over a number of time steps in order to reduce the statistical scatter. A flowsheet of the LPCVD heat transfer algorithm is given in Figure 4-7.

The conductive heat transfer in the quartz tube is computed using a finite difference technique. The quartz tube is discretized into a number of small annular segments which independently emit and absorb radiation and subsequently conduct heat between adjacent segments. Temperature variations within the thickness of the quartz are neglected when performing the energy balance. The temperatures of each of the quartz segments are then governed by the following equation :

$$\rho C_p \frac{\partial T}{\partial t} = q_{rad}(z) + \frac{\partial}{\partial z}\left(k(T)\frac{\partial T}{\partial z}\right) \qquad (4\text{-}16).$$

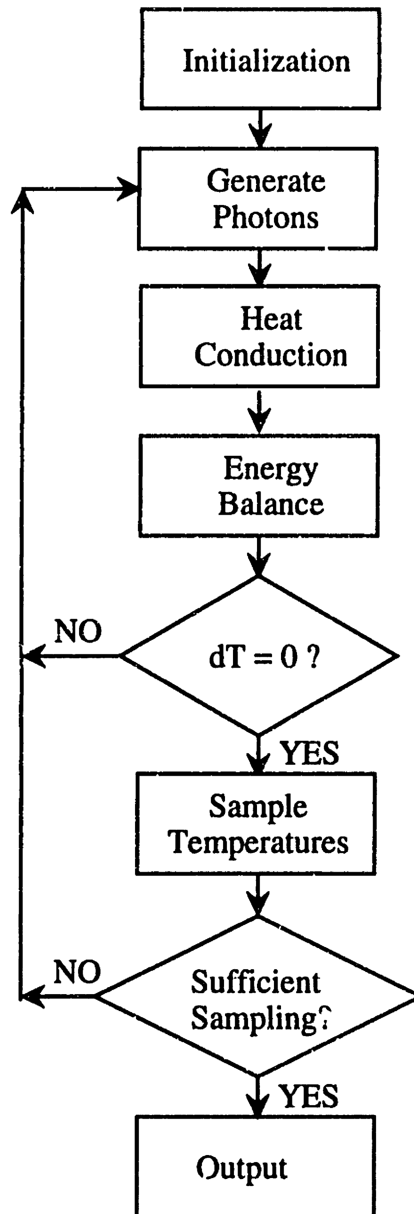

Figure 4-7 : LPCVD heat transfer algorithm flowsheet.

where ρ, C_p, and k are the density, heat capacity, and thermal conductivity, respectively, of quartz. The term $q_{rad}(z)$ is the local radiative heat input rate per unit volume of quartz. The boundary conditions are given by the specified temperatures of the cooled ends of the reactor tube.

The energy balance for each of the wafers is performed at each time step as well. The temperature variations across the thickness of the wafers are similarly neglected. Furthermore, the radial temperature variations are expected to be minimal for all of the wafers with the exception of the end wafers [Badgwell *et al.*, 1992a]. This was supported by the simulations which indicated a relatively uniform flux of radiative heat to the interior wafers. The average temperature of wafer number i is then calculated according to the following energy balance :

$$\rho C_p \frac{\partial T_i}{\partial t} = q_{rad}(i), \qquad (4\text{-}17).$$

where ρ and C_p are the density and heat capacity, respectively, of Si and $q_{rad}(i)$ is the radiative heat input rate to both sides of wafer number i per unit volume of Si.

4.4.2 Specification of the material properties

The emission characteristics of the surfaces participating in the radiative heat exchange, with the exception of the quartz tube, were modelled as opaque gray body materials. The surrounding alumina heater and insulating material are assumed to be diffuse reflectors with a total hemispherical emittance of 0.62 [Siegel and Howell, 1992]. The stainless steel ends of the reactor tube and the Si wafers are assigned total hemispherical emittances of 0.1 and 0.72, respectively [Sala, 1986], but are also assumed

to be specular reflectors due to their highly polished appearance. The material properties are summarized in Table 4-2.

Material	ε_T	Reflector
alumina	0.62	diffuse
stainless steel	0.10	specular
silicon	0.72	specular
quartz	N/A	specular

Table 4-2 : Emittance and reflectance properties of the materials in the LPCVD radiation heat transfer model.

Specification of the radiative properties of the quartz tube requires recognition of the strong spectral and directional dependencies of quartz [Hsieh and Su, 1979; Sala, 1986] and is one of the critical features of the LPCVD heat transfer model. Quartz becomes strongly absorbing for wavelengths beyond 3 μm in the region where ~80% of the radiation from the heater occurs [Siegel and Howell, 1992], is nearly transparent in the region from 3 μm down to around 0.1 μm, and becomes strongly absorbing again at shorter wavelengths. This spectral dependency necessitates sampling from the wavelength distribution (equation 4-6) for each photon emitted in the simulation. In addition, the multiple-pass reflection and transmission probabilities (equations 4-10 and 4-11) must be employed since the quartz tube is semi-transparent.

The corresponding probabilities of absorption (emittance), reflection, and transmission for the quartz as a function of wavelength and cone angle are input to the simulation at discrete values in the form of a lookup table as depicted in Figure 4-8a. Linear interpolation is then used to determine the probabilities for intermediate values. The quartz tube normal ($\theta=0^\circ$) emittance as a function of wavelength is shown in Figure 4-8b.

4.5 Comparison with experimental data from a commercial scale LPCVD reactor

The wafer temperatures predicted by the two-dimensional simulation model are first compared to the experimental measurements of Badgwell *et al.* for a commercial scale BTU/Bruce LPCVD reactor containing 150 wafers [Badgwell *et al.*, 1992a]. The details of the reactor configuration and experimental conditions are given in Table 4-3 below [Elliott, 1993]. The measured and predicted average wafer temperatures are shown in Figure 4-9. Also shown are the model predictions of Houf *et al.* where a view factor approach was used and the results of a simple Monte Carlo simulation where the quartz tube has been removed and a uniform heat flux is provided by the furnace.

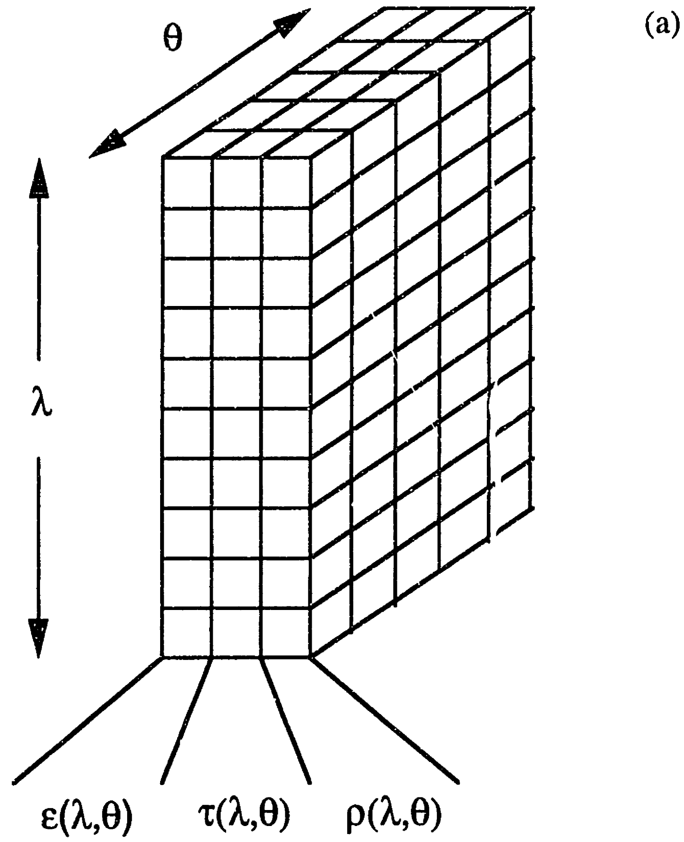

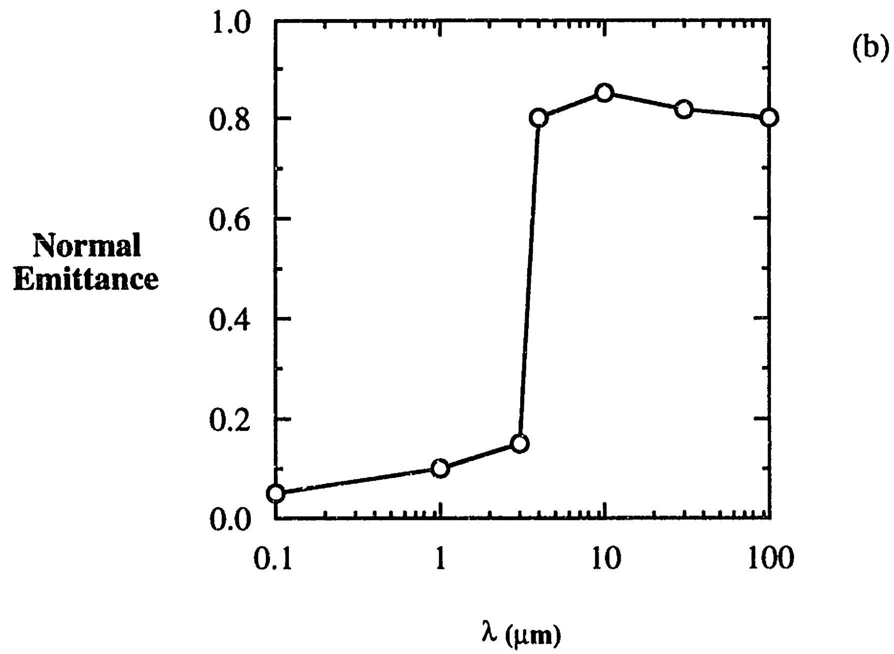

Figure 4-8 : Schematic diagram of quartz material properties lookup table (a) and LPCVD quartz tube spectral emittance (b).

Reactor length	228.5 cm
Quartz tube I.D.	16 cm
Quartz tube thickness	0.5 cm
Furnace I.D.	18 cm
Wafer diameter	15 cm
First wafer position	74.5 cm
Interwafer spacing	0.5 cm
Outlet diameter	10 cm
Furnace position	25 cm
Furnace length	178.5 cm
Furnace temperature	888.15 K
Reactor end temperature	350 K

Table 4-3 : BTU/Bruce commercial scale reactor configuration and conditions for experimental measurements [Badgwell *et al.*, 1992a] and simulation study.

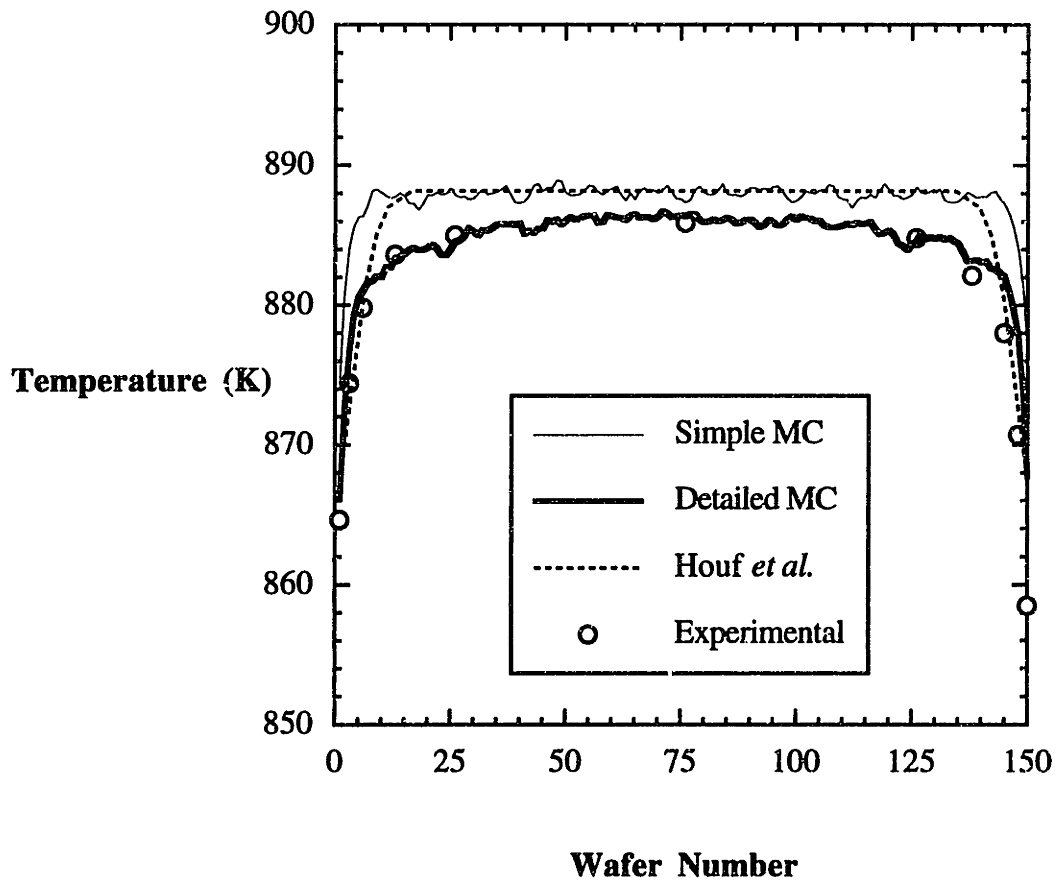

Figure 4-9 : Comparison of detailed Monte Carlo predictions with other models and experimental data (Badgwell *et al.*, 1992a).

Consideration of the semi-transparent quartz tube with its resulting conductive heat losses has a major impact on the temperature of the wafers. The radiative heat loss from the end wafers is still evident in the simple Monte Carlo model but the temperature suppression does not extend much beyond the first couple of wafers on each end. The interior wafers are effectively shielded from the cooled ends of the reactor. The same trend is also observed in the modelling results of Houf *et al.* where the spectral and directional properties of quartz and conductive heat transfer in the quartz tube were also neglected [Houf *et al.*, 1993]. The detailed Monte Carlo simulation results show excellent agreement with the experimental data. This underscores the importance of including the coupled radiation and conduction through the quartz tube along with the detailed material properties of quartz. The relative influence of each of these heat loss mechanisms, direct radiation to the cooled ends of the reactor and conduction through the quartz tube, is detailed in the next section where the heat transfer in a research scale reactor is analyzed.

4.6 Thermal analysis of a research scale LPCVD reactor

A number of heat transfer simulations were next performed for the research scale reactor employed in the rarefied gas flow simulations in Chapter 3. This reactor was used for the purposes of computational efficiency and also as part of an investigation of the influence of the thermal variations on the UHV-CVD gas dynamics to be presented in section 4.7. The details of the reactor are summarized in Table 4-4 below.

Reactor length	40 cm
Quartz tube I.D.	10 cm
Quartz tube thickness	0.5 cm
Furnace I.D.	11 cm
Number of wafers	10
Wafer diameter	7 cm
First wafer position	18 cm
Interwafer spacing	0.5 cm
Outlet diameter	5 cm
Furnace position	5 cm
Furnace length	30 cm
Furnace temperature	900 K
Reactor end temperature	350 K

Table 4-4 : Research scale LPCVD reactor configuration and conditions for the Monte Carlo heat transfer study.

4.6.1 The combined effects of radiation and conduction

The simulated quartz tube temperature profile and the average wafer temperatures for the research scale reactor described in Table 4-4 are shown in Figure 4-10. The quartz tube temperature is seen to drop off sharply outside of the furnace. This creates a strong driving force for the conduction of heat through the quartz tube away from the heated

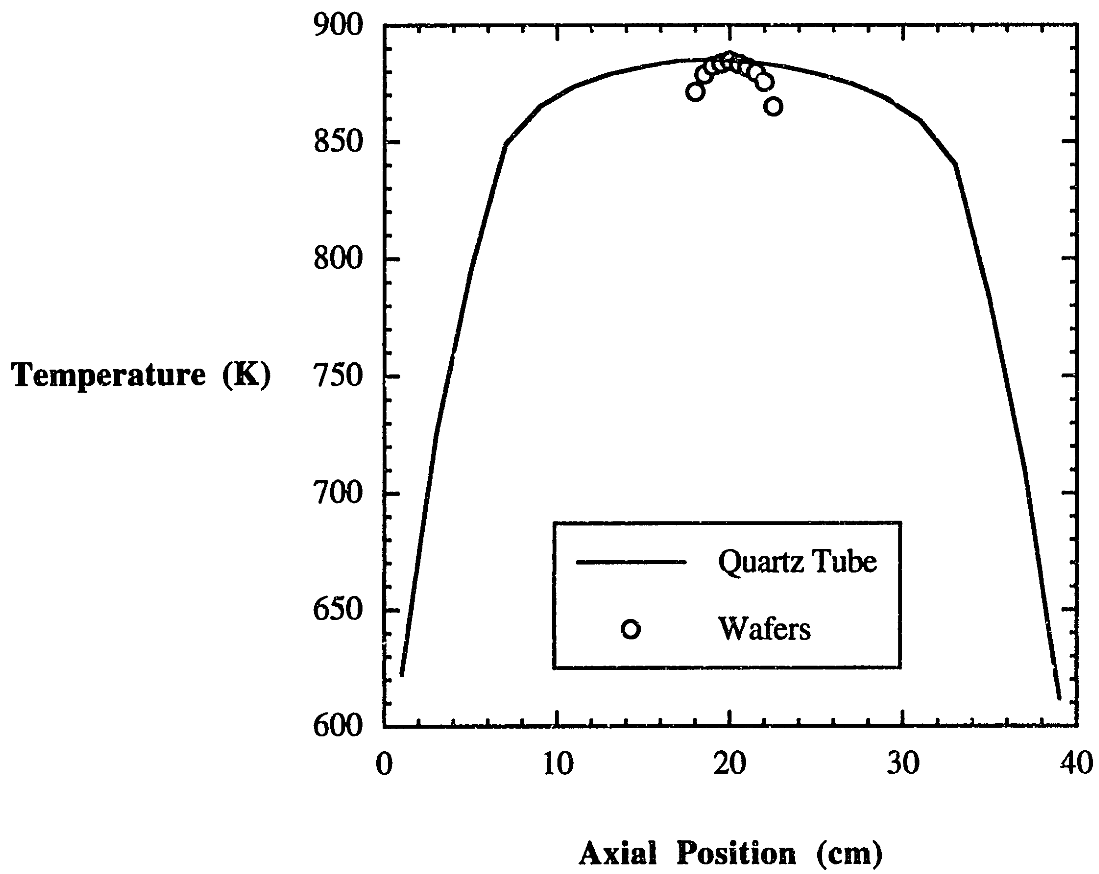

Figure 4-10 : Simulated quartz tube and wafer temperature profile for the research scale reactor.

interior. The radiative and conductive heat participation of the quartz is seen to have two effects. First, the temperature of the wafer load is lower than the furnace temperature as a result of the quartz absorbing a significant amount of the furnace radiation. This feature is captured by the model since the spectral dependent properties of the quartz tube are considered. The second effect is a nonuniform flux of heat to the wafers, in spite of the fact that a uniform heat flux is provided by the furnace. This effect is a direct result of the heat conduction in the quartz tube away from the heated wafer zone. The importance of including both radiation and conduction in the LPCVD heat transfer model is clearly demonstrated by their combined effects in the quartz tube. The end wafers also experience a direct radiative heat loss due to their exposure to the cooled ends of the reactor. The downstream end wafer is slightly cooler than the upstream end wafer because of the additional radiative heat loss to the completely absorbing outlet. The simulation results clearly illustrate how both radiative and conductive heat losses to the cooled ends of the reactor contribute to thermal variations in the wafer load.

4.6.2 The influence of the wafer stack properties on the thermal profile

The effects of varying the configuration of the wafer stack and the reflection characteristics of the wafer surfaces are now considered. The simulation results presented in the previous section considered the wafers to be specular reflectors. This is expected when the optical roughness, defined as the ratio of the root-mean-square roughness height to the wavelength of the radiation, is much less than unity [Siegel and Howell, 1992]. At shorter wavelengths, or for LPCVD films possessing a certain degree of roughness (*i.e.* amorphous Si films), the directional history of the impinging photon is lost and the photon is reflected in a diffuse manner.

The wafer temperature profile for the case of diffusely reflecting wafers is given in Figure 4-11 along with the results for specularly reflecting wafers. It is seen that there is virtually no difference between the two cases. This may be explained by considering the fact that the radiative heat exchange between adjacent wafers is much like that between two parallel plates. When the plates are infinite in length, the heat transfer rates are identical for specular and diffuse reflections [Siegel and Howell, 1992]. The closely spaced wafers behave in much the same way and serve as radiation shields which contain most of the emitted radiation within the wafer stack.

The infinite plate characteristics of the wafers are expected to diminish as the interwafer spacing is increased. This is due to the fact that the wafer surfaces exchange heat more readily with the rest of the reactor environment as the wafer spacing is increased. This is illustrated in Figure 4-12 where the wafer temperature profile for 10 wafers spaced at 0.5 cm is compared to the wafer temperatures for 5 wafers spaced at 1.0 cm. The temperature of the wafers spaced at 1.0 cm is consistently higher since a larger heat flux is received directly from the furnace heater.

The effect of the wafer diameter on the thermal profile for a fixed tube diameter and interwafer spacing is considered next. The wafer temperatures for 7 cm and 8 cm diameter wafers are given in Figure 4-13 where the remaining reactor conditions conform to Table 4-4. In contrast to the interwafer spacing, the diameter of the wafers is seen to have a minimal influence on the wafer temperature profile according to the simulations. In explaining this observation, it is instructional to once again refer to the analogy with heat transfer between infinite plates. The interwafer heat transfer characteristics should approach this idealized case as the aspect ratio, defined as the ratio of the wafer diameter to the wafer spacing, approaches infinity. In Figure 4-12 where the interwafer spacing was doubled and the corresponding aspect ratio was reduced by a factor of two, a relatively large effect on the heat transfer was evidenced. In Figure 4-13, however, reducing the

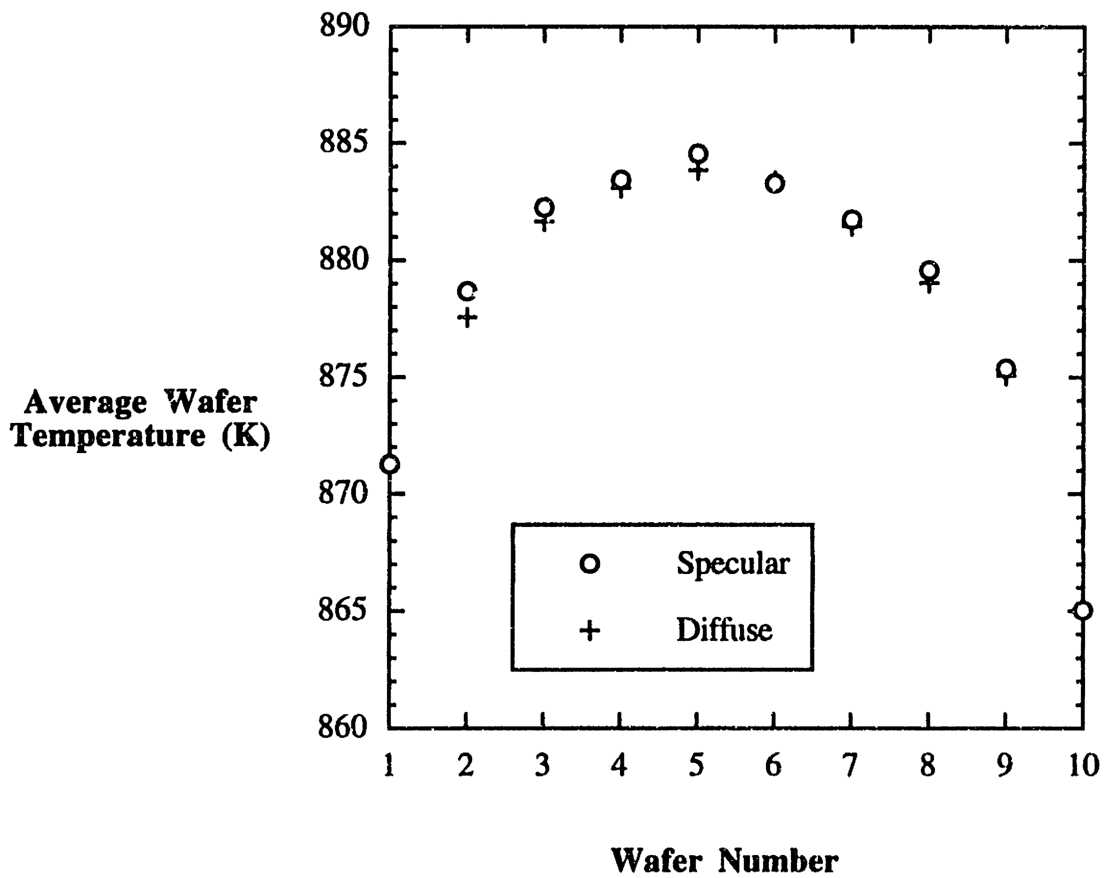

Figure 4-11 : Comparison of wafer temperature profiles for specularly (O) and diffusely (+) reflecting wafers in the research scale reactor.

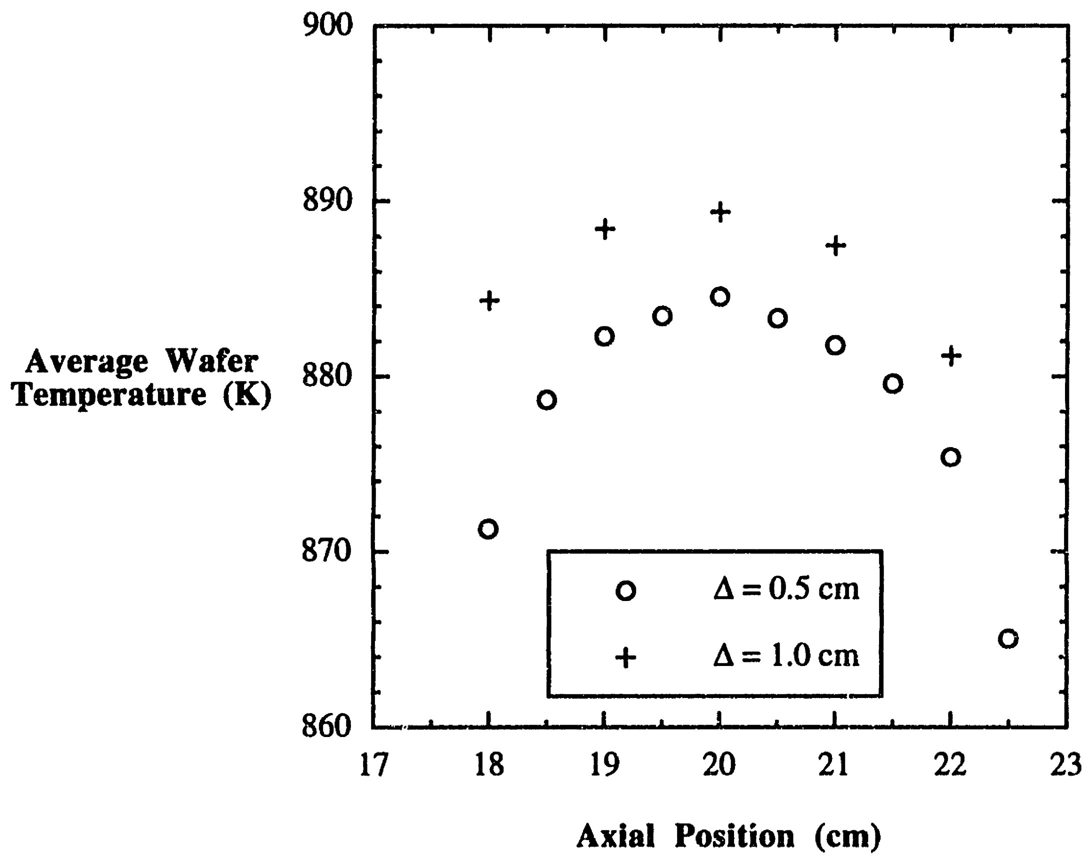

Figure 4-12 : Comparison of wafer temperature profiles for interwafer spacings of 0.5 cm (O) and 1.0 cm (+).

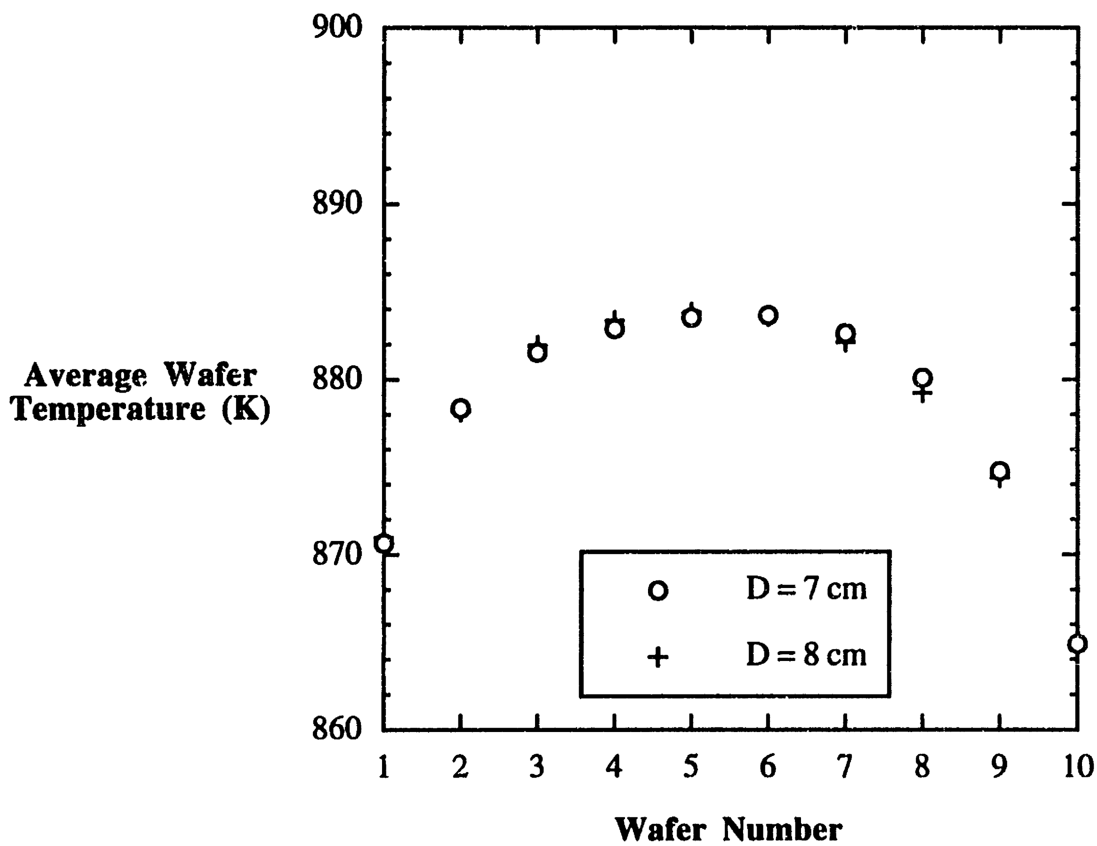

Figure 4-13 : Comparison of wafer temperature profiles for wafer diameters of 7 cm (O) and 8 cm (+).

wafer diameter from 8 to 7 cm represented only a 12.5% reduction in the aspect ratio and, therefore, a minimal influence on the wafer temperature profile was seen.

Finally, the influence of the number of wafers contained in the wafer stack on the resulting wafer temperatures is presented. The simulated wafer temperature profiles for wafer stacks containing 5 and 15 wafers are shown in Figure 4-14. The wafer-to-wafer temperature uniformity is fairly good in the interior of the wafer stack containing 15 wafers. This is not evident in the smaller wafer stack since the influence of the cooled end wafers extends throughout the entire wafer stack. In commercial scale LPCVD reactors where several dozen wafers are typically processed, the temperature variation from wafer to wafer is expected to be minimal across most of the wafer stack according to the simulation results for only 15 wafers. This was confirmed in the preceding section where the results of a heat transfer simulation for a commercial scale LPCVD reactor were presented.

4.7 The influence of the thermal variations on the UHV-CVD gas dynamics

The DSMC gas dynamics model and the Monte Carlo heat transfer model are now combined in order to investigate the influence of thermal variations on UHV-CVD gas flows. This is accomplished by implementing the calculated temperature profiles as thermal boundary conditions in the DSMC simulations. Since the heat transfer was determined to be completely independent of the gas flow for conventional LPCVD conditions of 0.3 Torr pressure (*c.f.* Badgwell *et al.*, 1992a), this procedure is certainly appropriate for the UHV-CVD conditions being considered here (pressure ~ 1 mTorr).

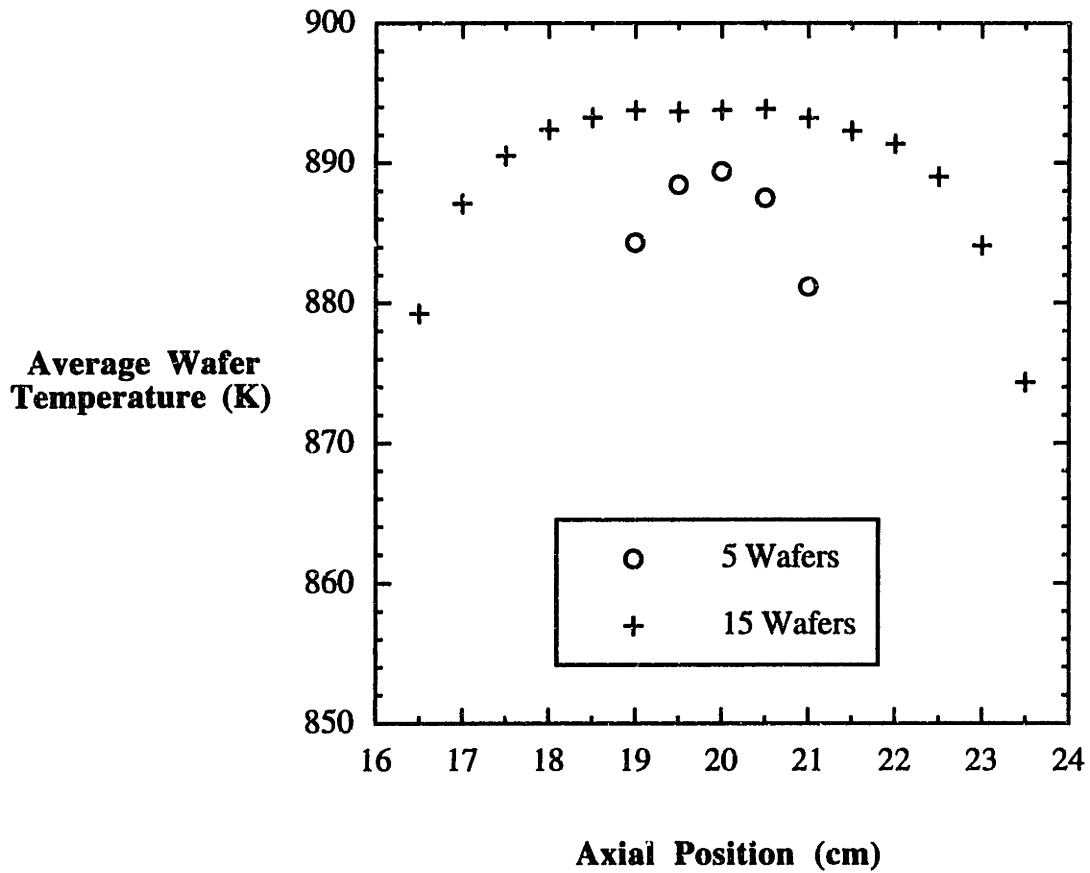

Figure 4-14 : Comparison of wafer temperature profiles for wafer loads of 5 wafers (O) and 15 wafers (+).

4.7.1 The heating of a cold inlet stream

The research scale reactor described in Table 4-3 was used for the gas flow simulations. The inlet stream consisted of pure H_2 at 48 sccm and 10 mTorr, thermally equilibrated at 350 K corresponding to the temperature of the water-cooled stainless steel ends of the reactor. The H_2 gas temperature throughout the reactor is shown in Figure 4-15a. The radially-averaged gas temperature is also given in Figure 4-15b along with the quartz tube temperature. The gas temperature is seen to closely follow the temperature of the quartz tube, although there is evidence of a significant amount of thermal slip at the cooled ends of the reactor.

One of the characteristic features of rarefied gas flows is the compressibility of the gas. This results in the presence of large density variations in the LPCVD reactor for UHV-CVD conditions as was seen in Chapter 3. The density variations due to the gas compressibility are now compared to those induced by the thermal variations. The H_2 number density is shown in Figure 4-16. The density variations across the wafer stack are still pronounced as was previously found in the isothermal flow simulations. The simulation results in Figure 4-16 also reveal that the cooled ends of the reactor give rise to significant local density variations as well. The overall effect of the thermal variations on the gas density is illustrated in Figure 4-17 where the radially-averaged H_2 density is plotted versus axial position for the isothermal and nonisothermal conditions. The upswing in the number density in the relatively cold regions at the ends of the reactor is clearly evident. The influence of the cooled ends of the reactor is seen to extend throughout the reactor as the H_2 number density is consistently higher for the nonisothermal flow.

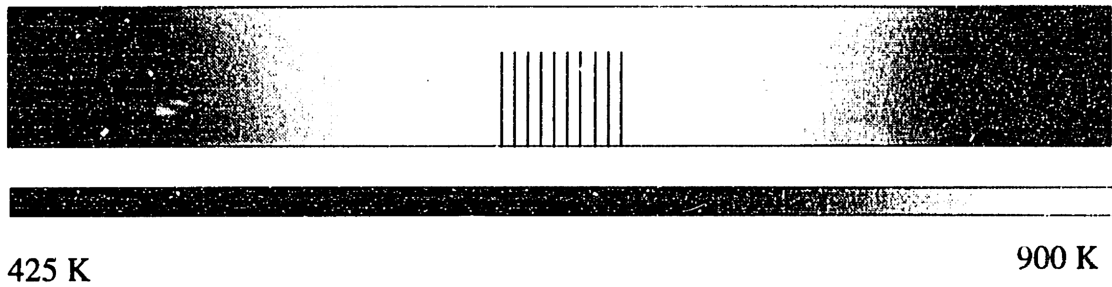

Figure 4-15a : H_2 temperature field for the nonisothermal UHV-CVD simulation.

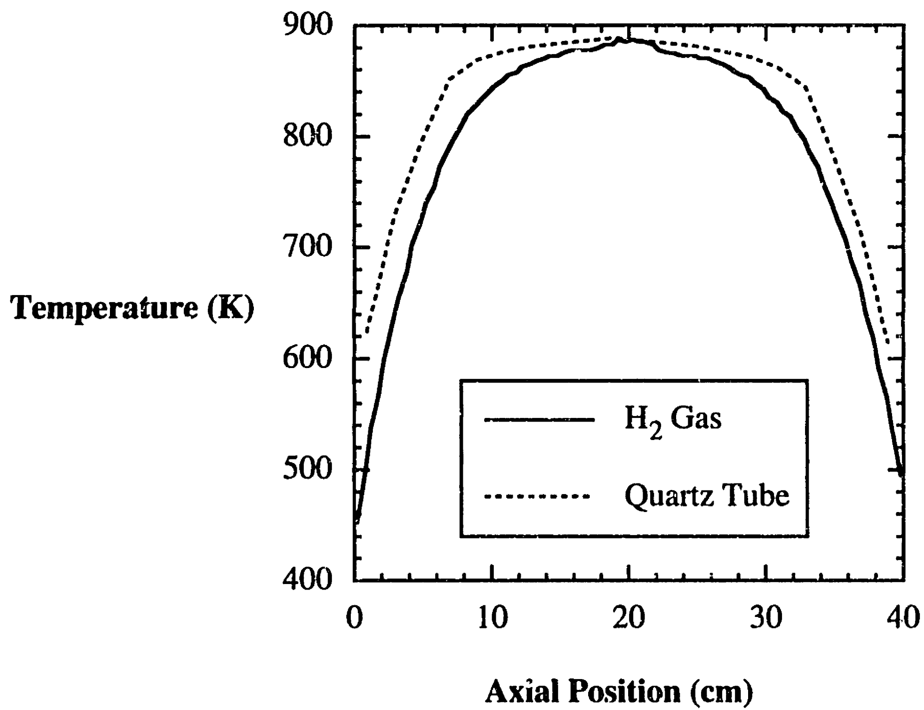

Figure 4-15b : Radially-averaged H_2 temperature and quartz tube temperature for the nonisothermal UHV-CVD simulation.

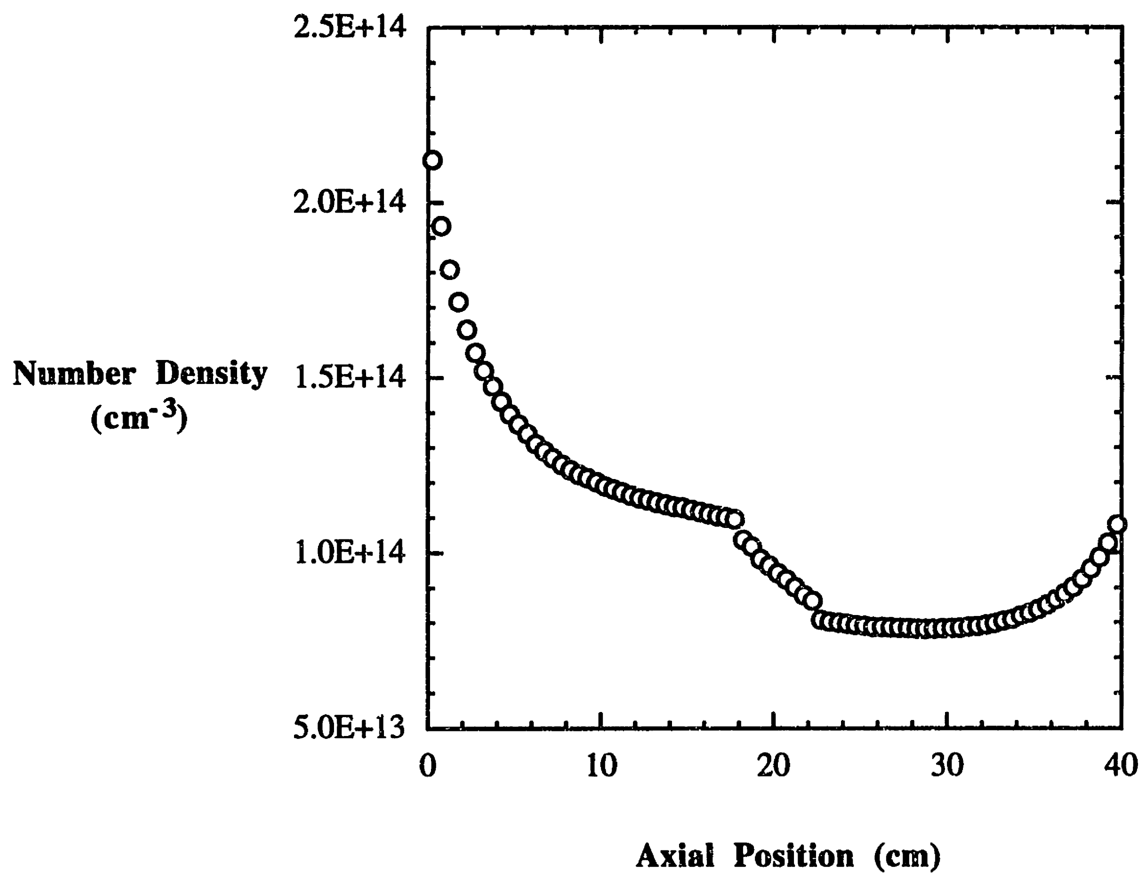

Figure 4-16 : Number density profile for pure H_2 flow under nonisothermal UHV-CVD conditions.

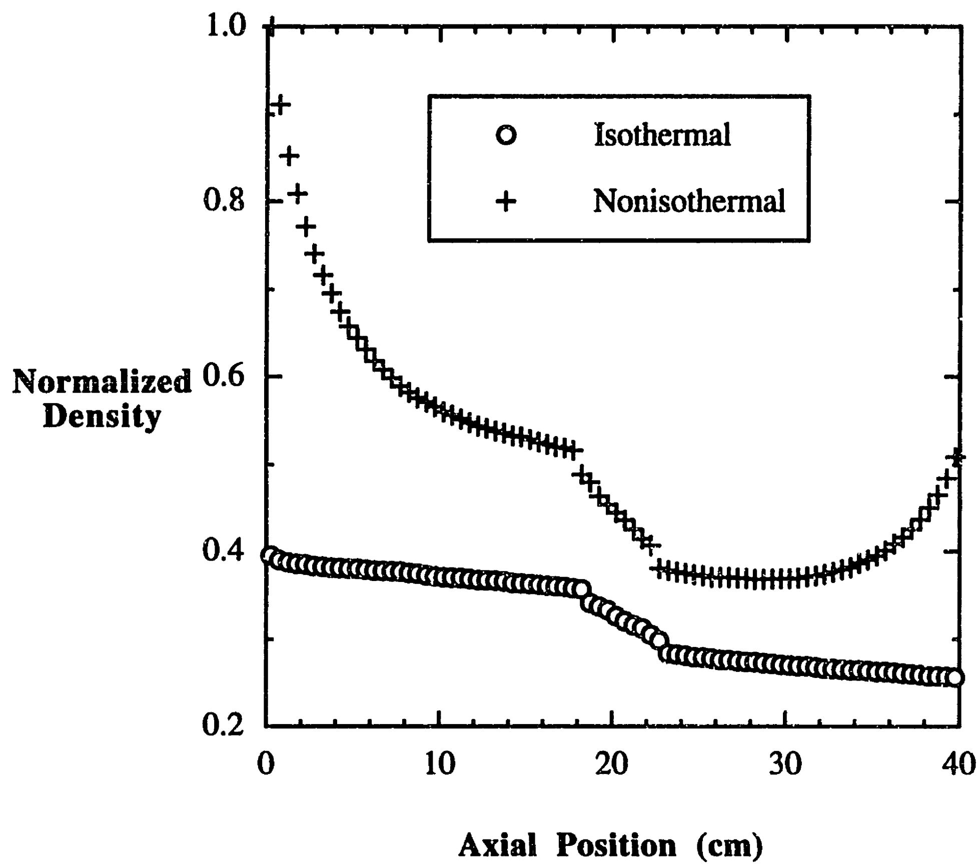

Figure 4-17 : Normalized number density profiles for isothermal (O) and nonisothermal (+) UHV-CVD simulations.

4.7.2 Thermal diffusion effects in nonisothermal gas mixtures

The gas dynamics of isothermal rarefied gas mixtures of N_2 and H_2 was investigated in Chapter 3. In these simulations it was discovered that the differences in the intermolecular collision rates of the individual species in the gas mixture gave rise to strong separation effects. This phenomenon was identified as pressure diffusion as the strongest separation effects were found to occur in the vicinity of the largest pressure gradients. The rarefied gas mixture simulation is now repeated for the nonisothermal LPCVD reactor conditions.

The research scale reactor described in Table 4-3 is used once again with an inlet stream comprised of an equimolar mixture of N_2 and H_2 at 10 mTorr and 48 sccm. The overall gas temperature of the mixture is defined as the sum of the temperatures of the individual species, each weighted with their respective mole fraction. For the N_2/H_2 mixture, the overall temperature (T_o) is given by :

$$T_o = x_{N_2} T_{N_2} + x_{H_2} T_{H_2}, \qquad (4\text{-}18).$$

where x_i is the mole fraction of component i and the individual gas temperatures are defined in equation (2-60). The radially-averaged overall gas temperature is plotted versus axial position in Figure 4-18. The temperature field of the gas mixture is nearly the same as was found for the pure H_2 flow shown in Figure 4-15b. The individual gas temperatures were found to be essentially identical, although translational nonequilibrium among the individual species of a gas mixture is fairly common in high speed rarefied gas flows [G. Bird, 1984].

The overall number density (n_o) of the gas mixture is defined in a manner analogous to the overall temperature :

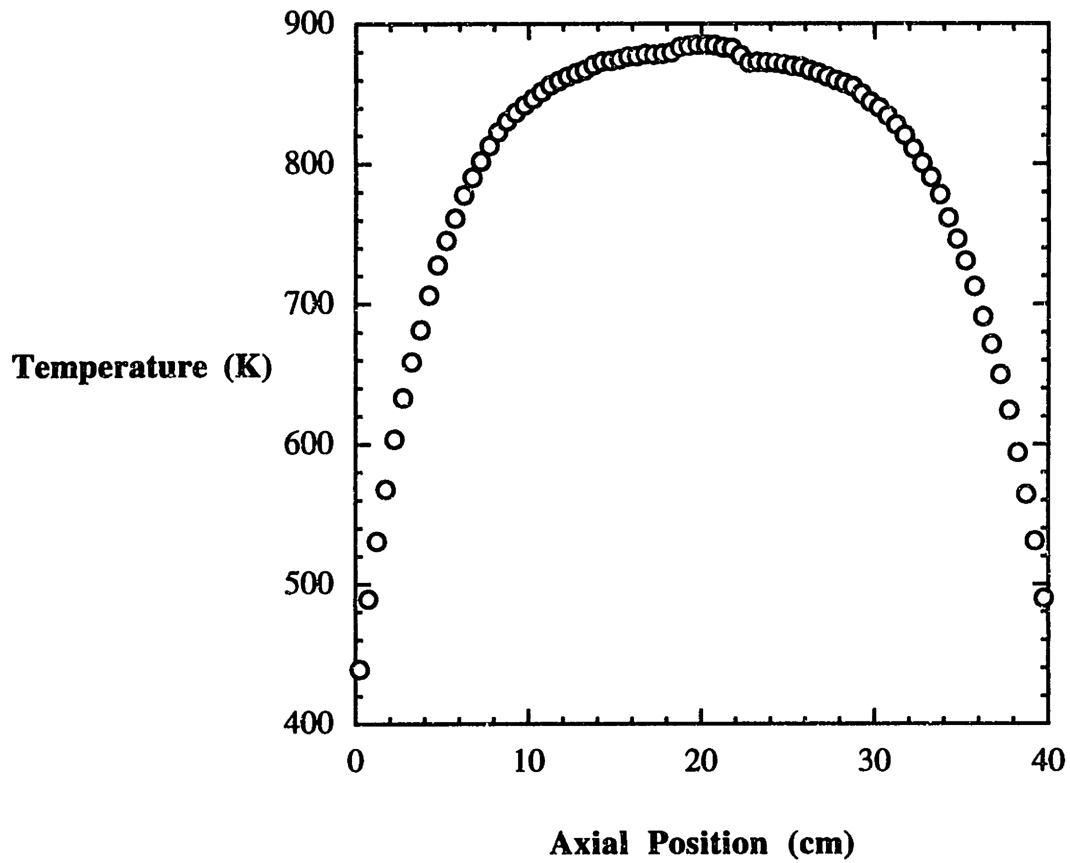

Figure 4-18 : Radially-averaged N_2/H_2 gas mixture temperature for the nonisothermal UHV-CVD simulation.

$$n_o = x_{N_2} n_{N_2} + x_{H_2} n_{H_2} \qquad (4\text{-}19).$$

The radially-averaged overall number density is plotted versus axial position in Figure 4-19 for the nonisothermal flow. Once again, this is seen to closely follow the pure H_2 number density profile shown in Figure 4-17.

The separation effects in the nonisothermal flow are illustrated in Figure 4-20a where the N_2 mole fraction distribution throughout the reactor is shown. The N_2-rich region in front of the wafer stack is evidence that pressure diffusion effects are still present. The simulation results also reveal strong separation effects occurring at the cooled ends of the reactor where the N_2 mole fraction is locally enhanced. This is undoubtedly due to thermal diffusion effects which tend to drive the heavier species towards the cooler regions in the presence of strong temperature gradients [Grew and Ibbs, 1952].

The relative degree of separation of the N_2 and H_2 species due to pressure and thermal diffusion effects is shown in Figure 4-20b where the radially-averaged N_2 mole fraction is plotted versus axial position. The importance of pressure diffusion in low density gas flows was discussed in Chapter 3. The contribution to the overall diffusion velocity due to pressure diffusion for a binary mixture of A and B was given in equation (3-13). This is rewritten again here along with the contribution to the overall diffusion velocity due to thermal diffusion effects :

$$\left(\overline{v_A} - \overline{v_B}\right)_{\text{press. diff.}} = -D_{AB}\left(\frac{M_B - M_A}{\overline{M}}\right)\frac{1}{p}\nabla p, \qquad (4\text{-}20).$$

$$\left(\overline{v_A} - \overline{v_B}\right)_{\text{thermal diff.}} = -D_{AB}\left(\alpha_{AB}\frac{1}{T}\nabla T\right) \qquad (4\text{-}21).$$

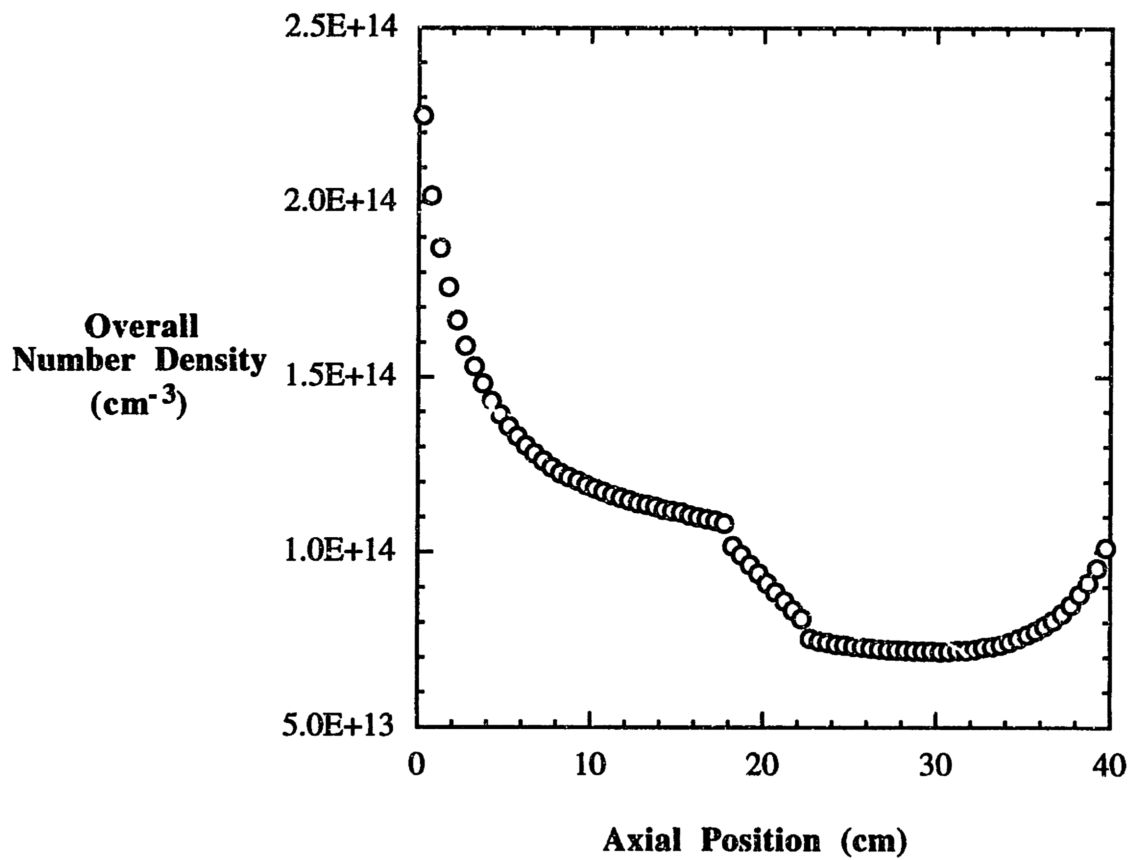

Figure 4-19 : Overall N_2/H_2 gas mixture number density profile for the nonisothermal UHV-CVD simulation.

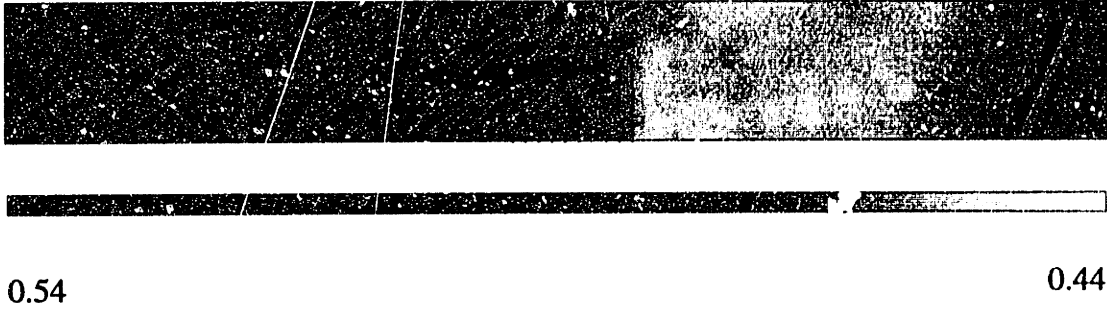

Figure 4-20a : N_2 mole fraction distribution in the nonisothermal UHV-CVD simulation of a N_2/H_2 gas mixture.

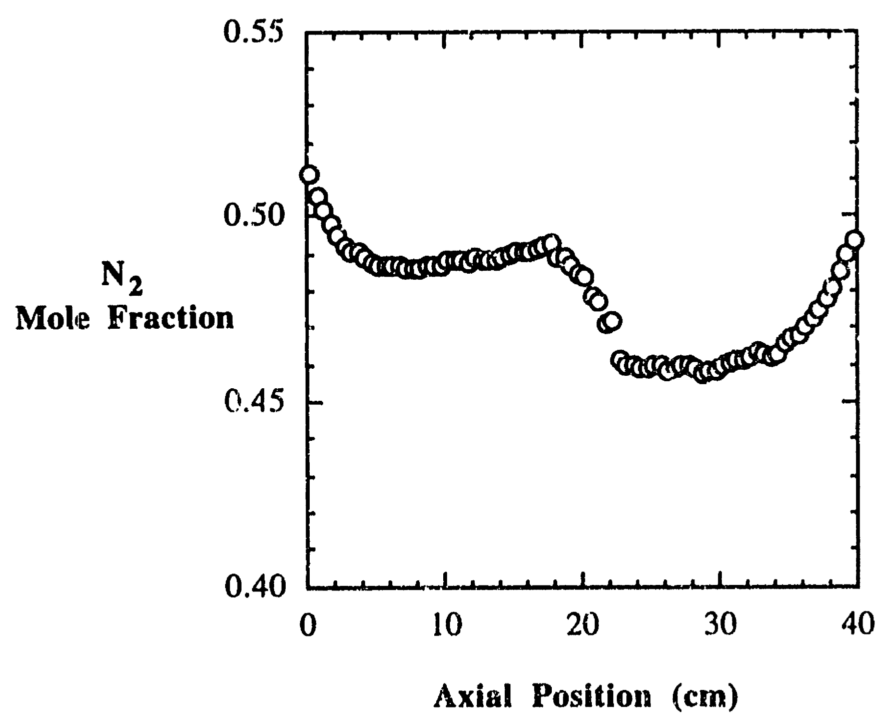

Figure 4-20b : Radially-averaged N_2 mole fraction profile in the nonisothermal UHV-CVD simulation.

where α_{AB} is the composition dependent thermal diffusion factor [R. Bird *et al.*, 1962]. This is in turn related to the more commonly referred to thermal diffusion ratio, k_T, according to :

$$k_T = x_A x_B \alpha_{AB}. \qquad (4\text{-}22).$$

The molecular basis for the observed species separation effects originates from the dependence of the molecular collision rate on the thermal speed of the molecules. The thermal speed in turn depends upon both the temperature and the molecular mass, giving rise to thermal and pressure diffusion, respectively. This suggests that the separation effects should diminish as the flow approaches the free molecular regime ($Kn \rightarrow \infty$) where intermolecular collisions become insignificant. This indeed was found to be the case as shown in Figure 4-21 where the radially-averaged N_2 mole fraction is plotted for inlet pressures of 10 and 1 mTorr. The separation effects are noticeably diminished for the lower pressure run.

The separation effects induced by pressure and temperature gradients in UHV-CVD flows are expected to have an impact on the application of this new technology as discussed in section 3.5. The nonisothermal gas mixture simulation is now repeated using an equimolar inlet stream of SiH_4 and GeH_4 with all other conditions remaining the same as for the N_2/H_2 simulation. The radially-averaged GeH_4 mole fraction is plotted in Figure 4-22 versus axial position. As was seen for the isothermal flow simulation in Chapter 3, the separation effects are less pronounced than was evidenced with the N_2/H_2 mixture. A comparison between Figure 4-22 and the analogous isothermal simulation results in Figure 3-24 shows the additional influence of thermal diffusion near the relatively cold regions at the ends of the reactor, leading to an enhanced localized concentration of GeH_4.

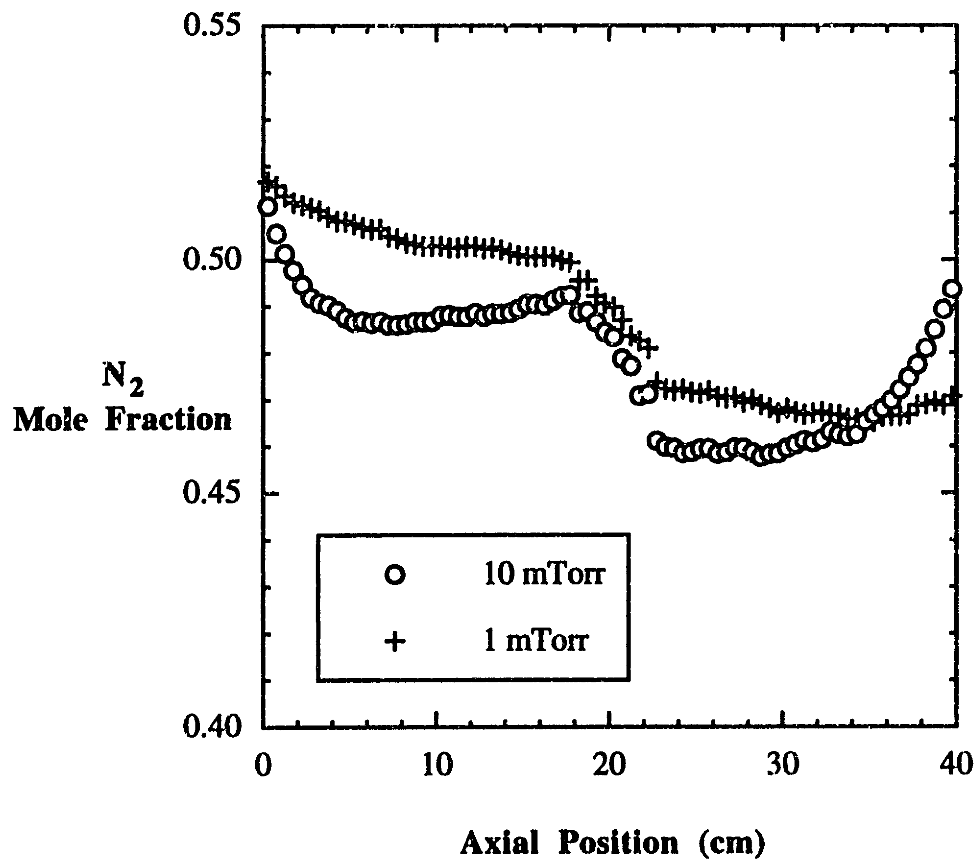

Figure 4-21 : N_2 mole fraction profiles in nonisothermal N_2/H_2 gas mixture simulations for inlet pressures of 10 mTorr (O) and 1 mTorr (+).

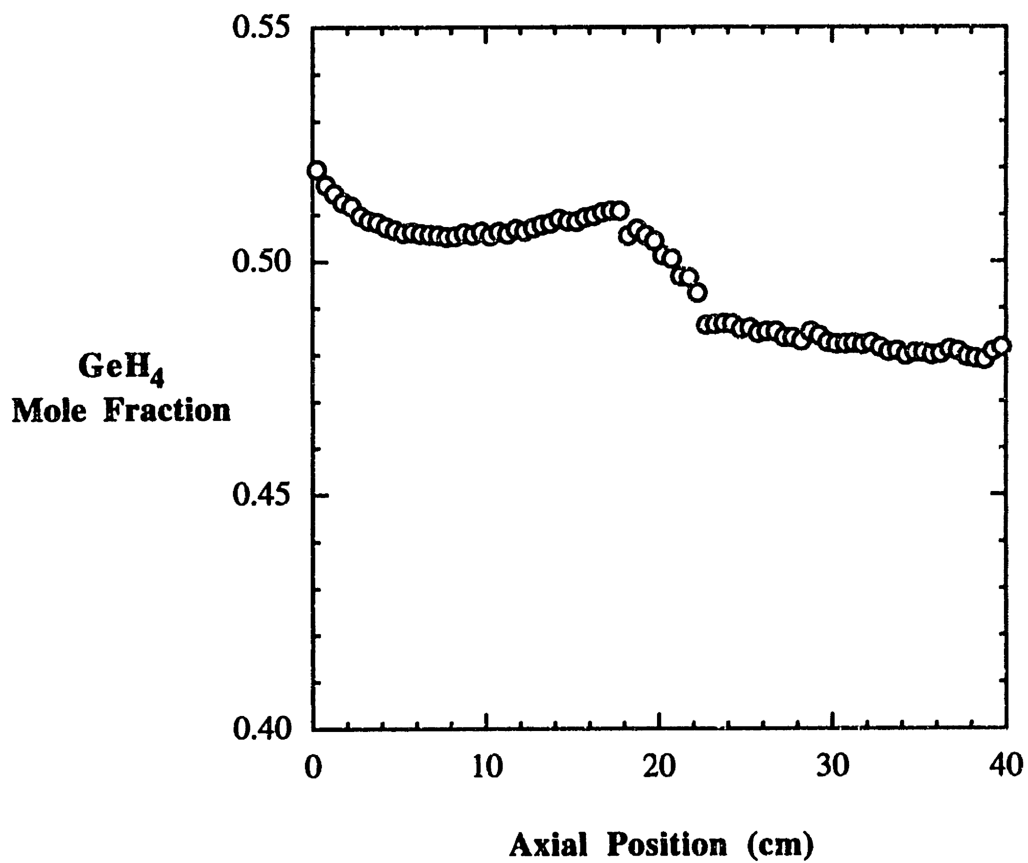

Figure 4-22 : GeH_4 mole fraction profile in the nonisothermal UHV-CVD simulation of a SiH_4/GeH_4 gas mixture.

Chapter 5 : Rarefied Gas Transport and Profile Evolution in Nonplanar Substrate CVD

5.1 : Modelling of nonplanar substrate CVD

Chemical vapor deposition has become the primary technique used to deposit thin films due in part to the precise spatial control of the film growth afforded by the CVD process over a large amount of surface area. At the device feature scale this control is responsible for the superior step coverage achieved when depositing CVD films over topographical features. Examples of such features include narrow trenches or cylindrical contact holes used to establish multilevel electrical connection or isolation.

The continual reduction in the device feature size has challenged this conformal coverage capability, however, as the transport of reactant gases to the bottom recesses of the feature may now be compromised by depletion effects and a host of diffusion barriers. Among these are shadowing effects where the direct flux of reactants to the feature sidewalls and bottom is geometrically blocked. In addition, diffusional resistance due to gas-surface interactions (*i.e.* Knudsen diffusion) and intermolecular collisions might also be expected to inhibit the intra-feature transport of reactants. The frequency of surface collisions within high aspect ratio features may also give rise to depletion effects for highly reactive gases. Each of these effects results in a suppression of the growth rate within structures such as narrow trenches or contact vias. This prevents the void free filling of the feature and ultimately proves detrimental to the performance of the device.

These challenges have necessitated a new level of understanding of the gas transport and deposition over nonplanar substrates. Simulation studies have proven to be an invaluable approach to unravelling the complexities of CVD processes. A number of different approaches have been used to model the filling of trenches and vias. These may be categorized into continuum reaction-diffusion (CRD) models [McConica and Churchill, 1988; Raupp and Cale, 1989; Hasper *et al.*, 1991], ballistic integral equation (BIE) models [Cale and Raupp, 1990a; Cale and Raupp, 1990b] and Monte Carlo simulation models [Ikegawa and Kobayashi, 1989; Cooke and Harris, 1989; Tail *et al.*, 1990; Wulu *et al.*, 1991].

The CRD and BIE approaches are closed form mathematical models and have the distinct advantage of computational efficiency. However, this advantage is somewhat illusory in both cases when a fundamental description of the deposition process is required. In comparison, the various Monte Carlo approaches tend to require lengthier computer runs but may include a more fundamental description of the underlying physics without prohibitively escalating the computational requirements.

The primary weakness of the continuum reaction-diffusion approach is in the assignment of the diffusion coefficient. Since the mean free path is almost always larger than the feature size, the use of Chapman-Enskog diffusivities is completely inappropriate. The situation is further confounded by the lack of reliable methods for effectively estimating the Knudsen diffusivities for free molecular flow in arbitrary geometries. The end result of this shortcoming is usually the introduction of an adjustable parameter into the model to account for the unknown transport coefficient.

The ballistic integral equation approach is analogous to thermal radiation view factor calculations where the line-of-sight fluxes from each of the sources are integrated over the physical domain [Siegel and Howell, 1992]. This is accomplished in a straightforward manner when the primary flux from the source is exclusively considered.

This would be all that is required for determining the reactant flux over patterned substrates when the reactant has a sticking coefficient of unity. When the sticking coefficient is less than unity, however, it is necessary to treat each of the surface elements as potential sources of reactant due to reactant molecules from the primary source being reflected. This is readily incorporated into the integral equation if only a single reflection is assumed and becomes much more complex for multiple reflections. When the sticking coefficient is much less than unity, the reactant molecules would be expected to experience multiple reflections with the surface prior to sticking.

5.2 Development of a two-dimensional simulation model for deposition over a long narrow trench or circular contact hole

5.2.1 Essential features of the model

The CVD process involves a complex mix of interdependent chemistry and physics. Therefore, it is necessary to simplify the picture by including only the essential features of interest. The feature scale simulations outlined below consider the transport and deposition of a single rate-limiting species in a localized region above the feature as depicted in Figure 5-1. The reactant molecules are subject to intermolecular collisions in the gas phase according to the local collision frequency. The possible gas-surface interactions include diffuse reflection as well as incorporation into the film as dictated by the reactive sticking probability. Once adsorbed, the reactants may be further distributed across the growth surface by surface diffusion or may be desorbed from the surface. Thermal gradients are presumed to be negligible and the gas phase decomposition of the

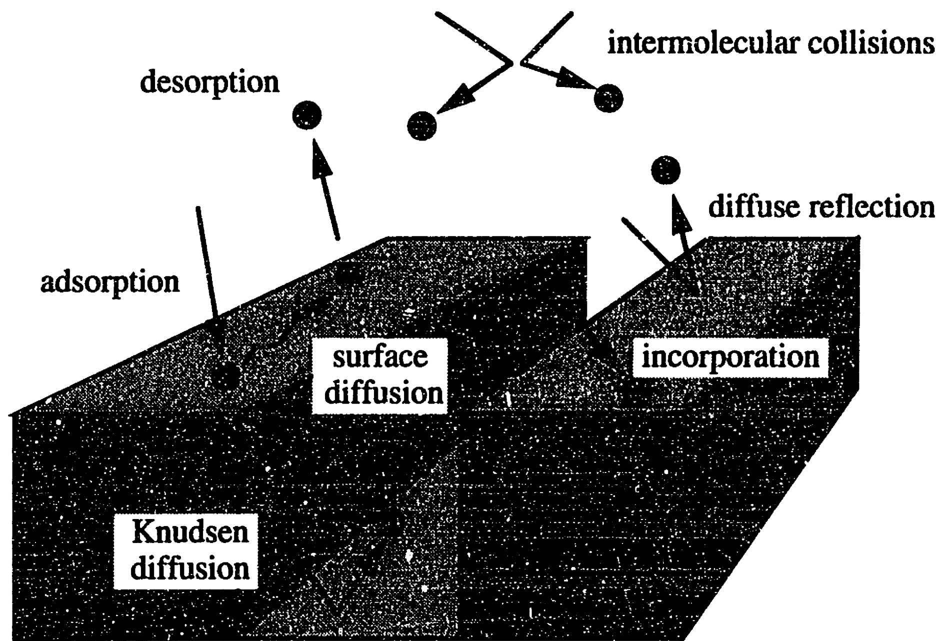

Figure 5-1 : Essential features of the nonplanar CVD simulation model.

precursor is neglected. These assumptions appear to be reasonable at the length scales involved here (~ 1 μm or smaller).

5.2.2 Simulation of gas transport using scaled variables in the DSMC method

A description of the gas flow in and around small features must account for the particular flow regime which governs the flow. The Knudsen number in this case may be defined as the ratio of the mean free path of the molecules (λ) to the characteristic dimension of the flow given by the width of the feature (w). For typical CVD growth temperatures and precursors, λ may range from ~ 0.1 μm at atmospheric pressure to > 100 μm at 1 Torr. Since current feature sizes have decreased to submicron dimensions, this clearly restricts the flow to the transition ($0.1 < Kn \equiv \lambda/w < 10$) and free molecular ($Kn > 10$) flow regimes. Previous simulation studies of microscale transport have either neglected the occurrence of intermolecular collisions, justifiably so for LPCVD processes, or have relied upon simplified phenomenological descriptions [Cooke and Harris, 1989]. Ikegawa and Kobayashi were the first to give detailed consideration to gas phase collisional phenomena with the use of the DSMC method [Ikegawa and Kobayashi, 1989].

The gas transport is described here using a dimensionless form of the DSMC method where the simulation variables of distance and time are appropriately scaled. This is the usual approach employed in molecular dynamics simulations [Allen and Tildesley, 1987]. The dimensionless DSMC method is used in order to render the simulation results as generally applicable as possible given the wide range of conditions (precursors, pressure, feature size, *etc.*) encountered in nonplanar substrate CVD. The gas transport is then completely characterized by the magnitude of the Knudsen number.

The distances are normalized by the mean free path of the reactant molecule in the undisturbed gas away from the growth surface. In addition, this quantity is set to unity for convenience :

$$\text{Length Scale} \equiv \lambda^{\infty} = 1. \qquad (5\text{-}1).$$

Similarly, the most probable velocity of the reactant molecule in the undisturbed gas (v_m^{∞}), the molecular mass (m), and the undisturbed gas temperature (T^{∞}) are regarded as having unit value. The Boltzmann constant and the gas constant are then both equal to 1/2. The time scale is normalized according to :

$$\text{Time Scale} \equiv \frac{\lambda^{\infty}}{v_m^{\infty}} = 1. \qquad (5\text{-}2).$$

The hard sphere molecular model is used to simulate the intermolecular collisions since its implementation in the dimensionless DSMC algorithm is straightforward [G. Bird, 1976].

5.2.3 The modified solid-on-solid approach for the simulation of profile evolution

An accurate description of the emerging film profile is as equally challenging and imperative as the gas transport problem. A number of different approaches have been utilized in previous simulation studies. These include the use of string algorithms [Cale and Raupp, 1990b; Ikegawa and Kobayashi, 1989] where the surface is approximated by a series of jointed line segments, and particle "pile-up" methods [Cooke and Harris, 1989; Tait *et al.*, 1990] where accumulations of adsorbed particles simulate the growing film

profile. String algorithms are conveniently implemented but are unable to capture the microstructural details of the growing film. Moreover, the use of a string algorithm is necessarily accompanied by a compromising distortion of the cell network employed in DSMC simulations [Ikegawa and Kobayashi, 1989]. The pile-up methods used by Cooke and Harris [Cooke and Harris, 1989] and more recently by Tait and co-workers [Tait *et al.*, 1990] demonstrate the ability to capture microstructural details of the growing film as well as to predict the overall step coverage.

The profile simulation routine developed in this work has conceptually borrowed from the solid-on-solid (SOS) approach used to investigate film morphology on planar surfaces [Weeks and Gilmer, 1978]. In the SOS approach, the surface is simulated by a large number of regularly spaced growth sites. Film growth occurs as surface units are perpendicularly stacked onto the growth sites with the restriction that overhangs are not permitted.

In the profile evolution simulations to follow, the DSMC cells in the vicinity of the surface are further discretized into a large number of subcells, typically around 100 (see Figure 5-2). The gas-surface interface is then advanced at the subcell level in much the same fashion as the growth units in the SOS approach are advanced. Overhangs may now occur, though, due to the nonplanarity of the surface. The local flux of reactants into each subcell is monitored and the gas-surface interface is locally advanced after a specified population of adsorbed reactants have been accumulated. This may result from the direct flux of reactants or may occur due to surface diffusion as described in the next section. A separate film growth routine is not included in the simulation algorithm. This is because the film growth is intimately coupled with the reactant transport and the usual steady-state approximation is not required. More importantly, this profile simulation routine is conveniently coupled with the DSMC method and provides microstructural detail of the growing film.

5.2.4 Modelling of reactant surface diffusion

Both simulation studies [Cooke and Harris, 1989; Wulu *et al.*, 1991; Dew *et al.*, 1992] and experimental investigation [Cheng *et al.*, 1991] have provided strong evidence that surface diffusion has a negligible influence on the overall step coverage for CVD deposited films of metals and refractory materials. However, surface diffusion may be expected to maintain a strong influence over the microstructural quality of the films, namely the surface roughness and the morphology (*e.g.* columnar growth).

The mobility of a species adsorbed on the growth surface may be specified in a number of ways. Consider the Einstein relation which defines the surface diffusivity, D_S, as $D_S \equiv \sqrt{x_S/\tau}$ where x_S is the mean diffusion distance along the surface and τ is the mean surface residence time. Increasing the mean diffusion distance or decreasing the mean residence time required to diffuse a given distance is equivalent to increasing the surface diffusivity.

The mobility of adsorbed reactants was simulated by permitting the molecules to shuffle back and forth between interface subcells. Due to the local roughness of the film at the subcell level, the molecules were restricted to moving to adjacent subcells only. The surface mobility was then varied by adjusting the frequency of shuffles (τ) rather than the shuffle distance (x_S). The net flow of adsorbed molecules from one subcell to another was proportional to the difference in populations between them. This ensures that surface diffusion acts to smooth out concentration gradients which exist on the surface. The position of the surface diffusion module with respect to the remaining simulation tasks is shown in Figure 5-3.

5.2.5 The DSMC cell network

The profile simulation model outlined here is capable of simulating infinitely long trenches and cylindrical contact holes, both of which are reduced to two-dimensional simulations due to symmetry considerations. Figure 5-4 shows typical DSMC cell networks used in the two types of simulations. In each case an open boundary is specified several mean free paths above the growth surface where an appropriate influx of molecules is calculated at each time step from a Maxwellian distribution. A symmetry boundary is also placed some distance away from the feature opening, providing a specularly reflecting plane with which the molecules interact. The trench model also includes a symmetry boundary at the midtrench plane.

5.3 Parametric study of the two-dimensional trench problem

This section details the results of a parametric study undertaken to gain insight into the relative influence of various parameters on the step coverage performance. The parameters to be discussed include the reactive sticking coefficient (P_{rxn}), the surface mobility, the Knudsen number, the feature aspect ratio (d/w), and the feature geometry (infinite trench, circular contact hole, finite trench). The results will be presented for an infinitely long trench with an aspect ratio of unity unless otherwise specified.

5.3.1 Nonequilibrium transport effects near the growth surface

Before proceeding with the results of the parametric study, the importance of recognizing the rarefaction of the gas through the use of the DSMC method is illustrated.

As discussed in section 5.1, previous models of CVD over nonplanar substrates have relied upon a continuum description of the gas transport. It was suggested that the use of a Chapman-Enskog diffusivity in the modelling equation is somewhat suspect given the magnitude of the Knudsen number (Kn > 0.1). The primary assumption underlying this theory is that the gas is only slightly removed from equilibrium, *i.e.* the velocity distribution is essentially a Maxwellian distribution [Chapman and Cowling, 1970].

The thermal velocity distribution is readily calculated using the DSMC method. This was accomplished at several positions in the gas phase for a two-dimensional trench simulation with Kn = 0.1 and $P_{rxn} = 0.3$. The velocity distributions immediately adjacent to the growth surface for the perpendicular (v_y) and parallel (v_x) velocity components are shown in Figure 5-5a. Also shown for reference is the equilibrium or Maxwellian distribution. A high degree of nonequilibrium is evidenced for the perpendicular component while the parallel component remains essentially at equilibrium. The nonequilibrium seen in the perpendicular component is undoubtedly due to the influence of the growth surface. This is supported in Figure 5-5b which shows the perpendicular velocity distribution in a nonequilibrium state next to the surface and near equilibrium at several mean free paths away from the surface.

5.3.2 Step coverage as a performance parameter

It is important to specify precisely how the step coverage is defined when characterizing nonplanar CVD films. Two alternative means of defining the step coverage are illustrated in Figure 5-6. These are given as the ratio of film thickness at the feature bottom, or at some position along the sidewall, to the film thickness at the top of the feature some distance away from the feature opening. Figure 5-7 shows the step coverage at the bottom center of the feature and at the lowest position along the sidewall

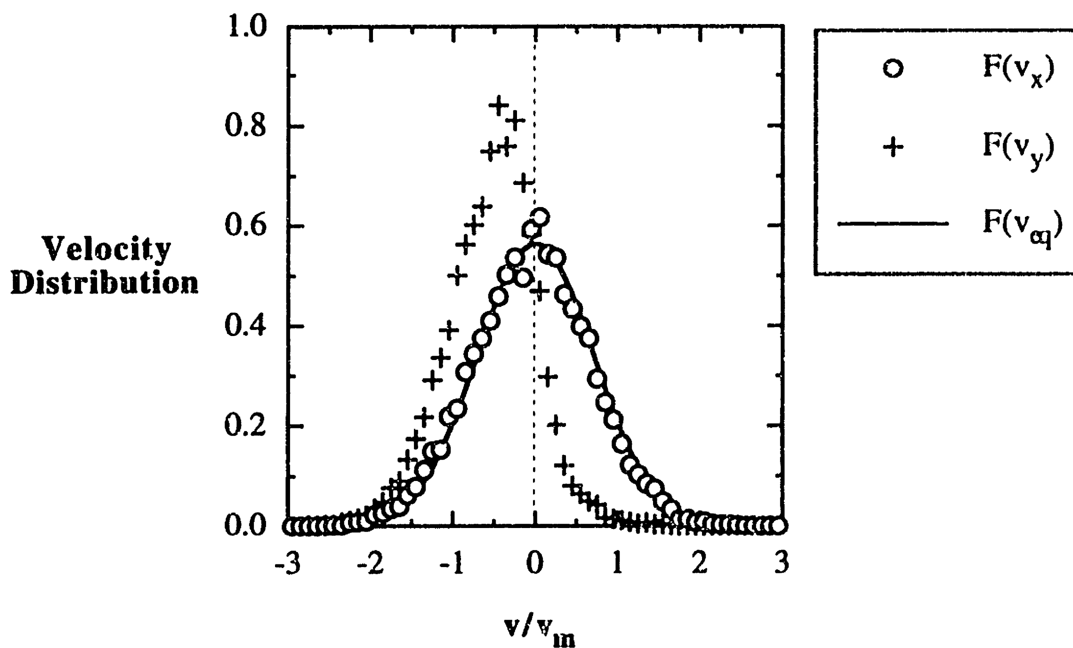

Figure 5-5a : DSMC computed velocity distributions λ/3 above the growth surface for the x-component (O) and y-component (+) and the Maxwellian (—) distribution.

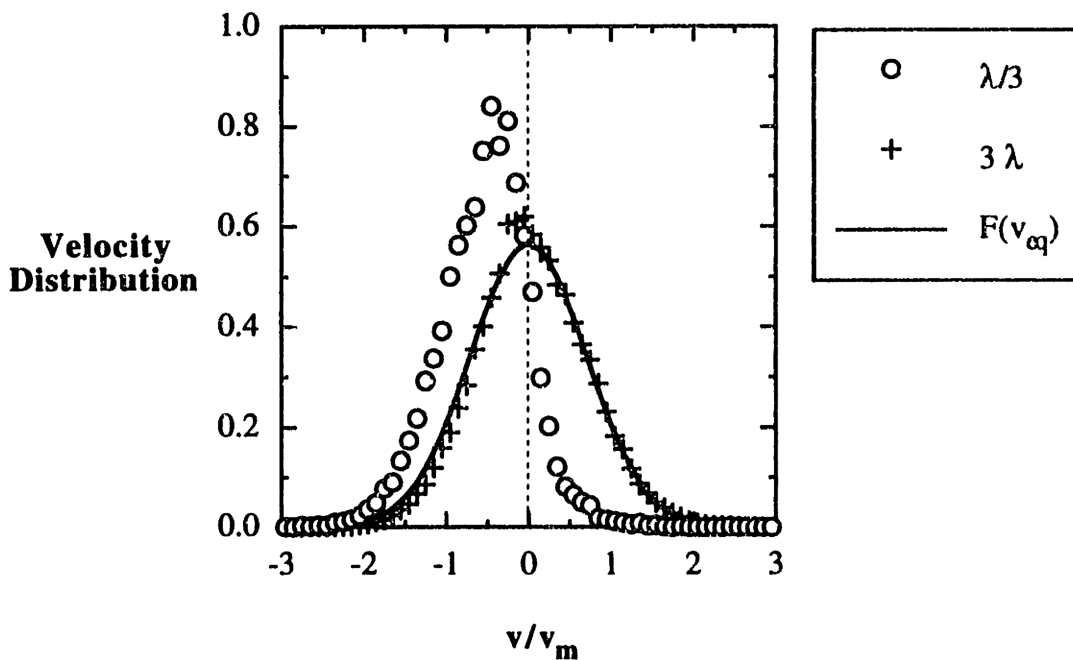

Figure 5-5b : DSMC computed y-component velocity distributions λ/3 (O) and 3 λ (+) above the growth surface and the Maxwellian (—) distribution.

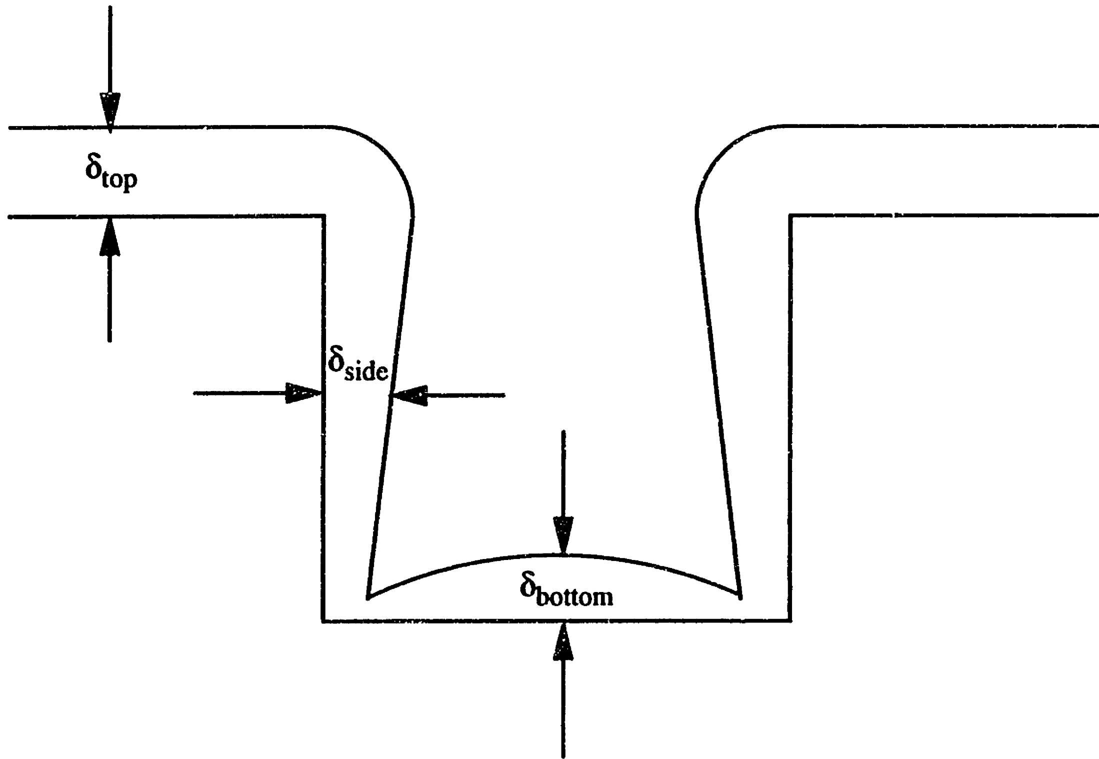

$$\text{Step Coverage} = \frac{\delta_{bottom}}{\delta_{top}} \quad \text{or} \quad \frac{\delta_{side}}{\delta_{top}}$$

Figure 5-6 : Two alternative means of defining the step coverage for deposition over a long narrow trench.

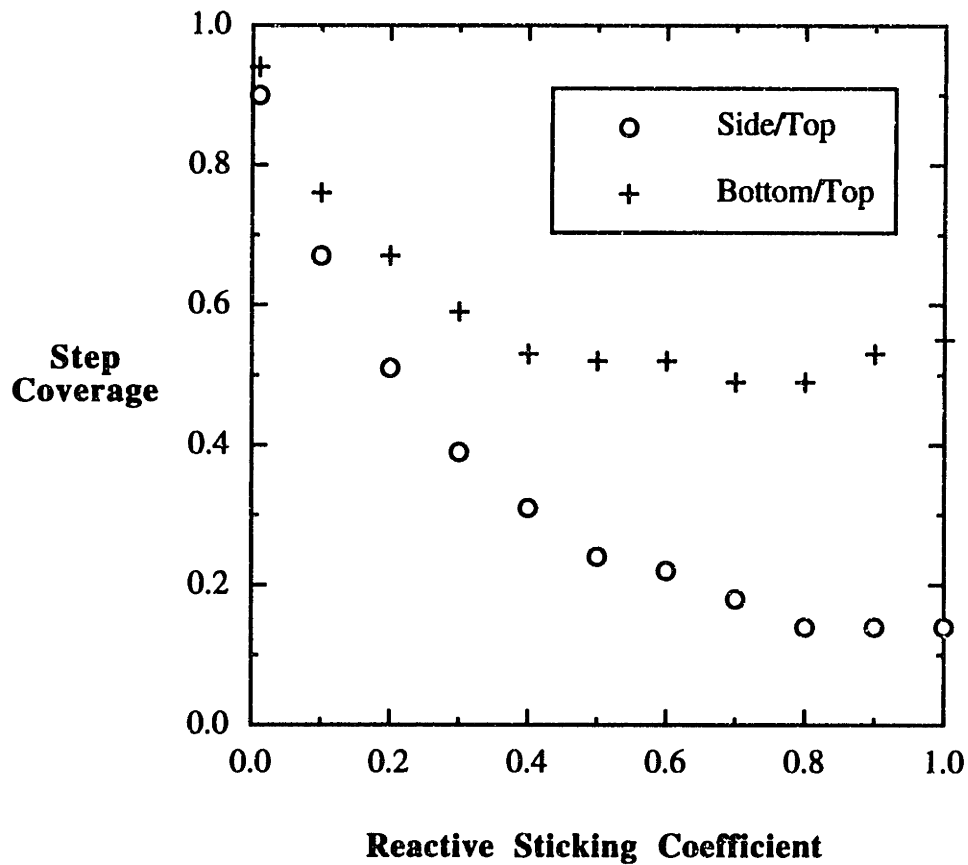

Figure 5-7 : Step coverage at the bottom center (+) and at the lower sidewall (O) as a function of the reactive sticking coefficient for an infinite trench at Kn = 0.25.

as a function of the reactive sticking coefficient for Kn = 0.25. The step coverage is seen to vary considerably between the two alternative positions, particularly as P_{rxn} approaches unity. In the results to follow, the step coverage will be given for the bottom center of the feature.

The measure of the step coverage depends not only on the position from which it is measured but also on the degree of feature closure. This effect is illustrated in Figure 5-8 where the step coverage is given for various film thicknesses for $P_{rxn} = 0.3$ and Kn = 0.25. The step coverage continually decreases during the filling of the feature due to the continually escalating shadowing effects from the growing film. This is further illustrated in Figure 5-9 where the film profile is shown at various stages of growth. The step coverages reported hereafter will be given for a maximum film thickness of 5/6 of the feature width, just prior to complete closure of the feature.

5.3.3 Effect of the reactive sticking coefficient

The reactive sticking coefficient is a difficult quantity to measure experimentally. In addition, there exists no theoretical basis from which their values may be reliably estimated for a given set of conditions. This lack of insight has motivated the use of Monte Carlo simulations as a predictive tool to measure the reactive sticking coefficients by comparison of the simulated profiles with actual SEM micrographs [Ikegawa and Kobayashi, 1989; Yuuki *et al.*, 1989; Watanabe and Komiyama, 1990; Kawahara *et al.*, 1991]. A degree of caution should be exercised when doing so, however, as the presence of several depositing species each with unique sticking coefficients may be a more realistic picture in some cases [Kawahara *et al.*, 1991].

Referring back to Figure 5-7, the step coverage was found to be increasingly independent of the value of the sticking coefficient as P_{rxn} approached unity. At higher

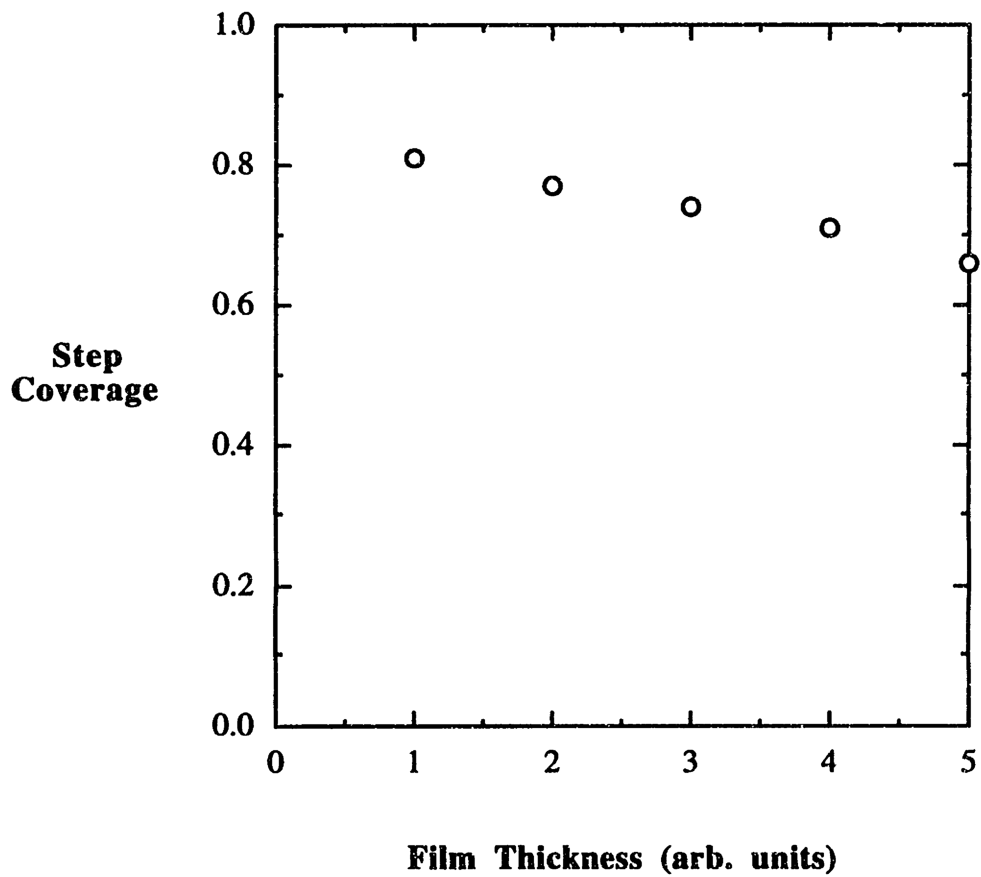

Figure 5-8 : Step coverage as a function of film thickness for an infinite trench at Kn = 0.25 and P_{rxn} = 0.3.

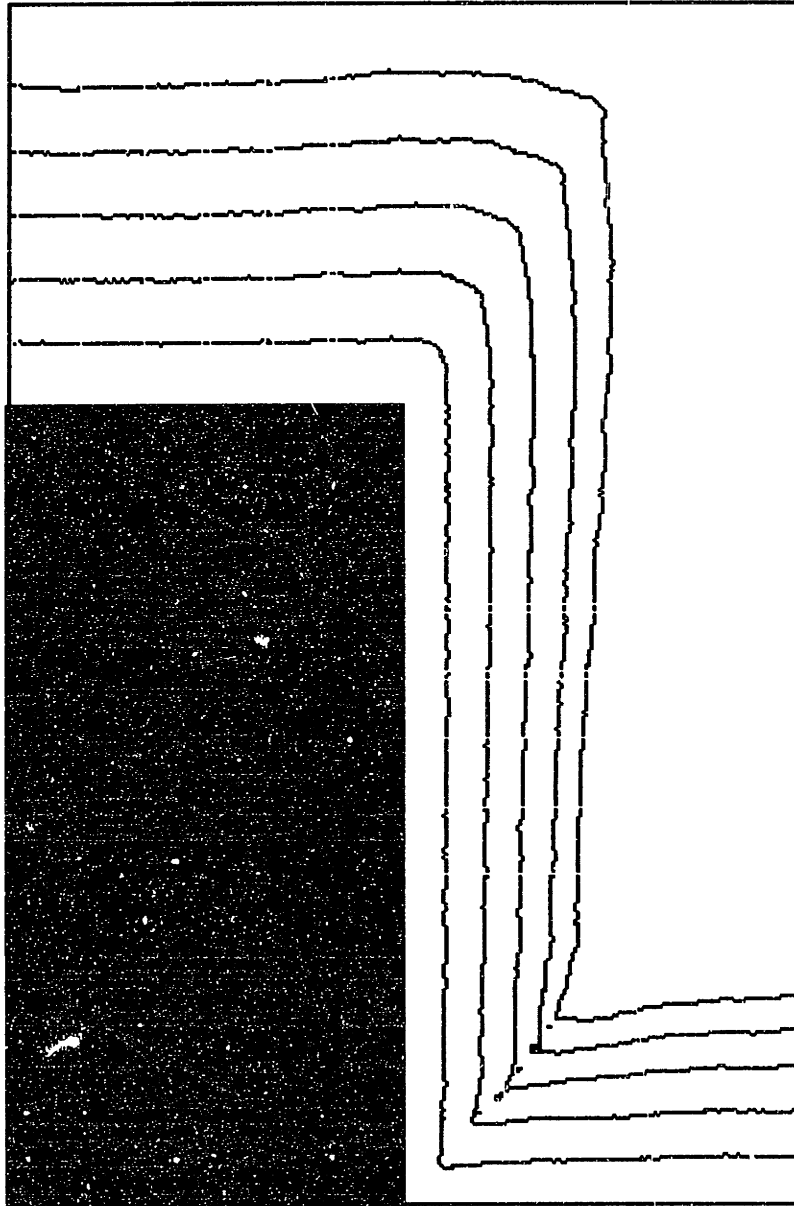

Figure 5-9 : Simulated film profiles at various stages of growth for an infinite trench at Kn = 0.25 and P_{rxn} = 0.3.

values of the sticking coefficient, shadowing effects dictate step coverage as re-emission is essentially negligible. This explains the poorer step coverage obtained along the sidewalls where the direct flux from the source is much less than that received by the feature bottom. As P_{rxn} approaches zero, re-emission dictates the step coverage and the difference between the sidewalls and the bottom is less pronounced. Figure 5-10 illustrates typical profiles obtained for low (0.01) and high (1.0) values of the sticking coefficient at $Kn = 0.1$.

The near independence of the step coverage at higher values of the sticking coefficient may be explained by considering the history of a typical reactant molecule within the feature recess. For $P_{rxn} = 1$, the molecule will likely encounter the top surface and deposit prior to reaching the bottom. The flux of reactant molecules to the bottom of the feature then predominantly consists of those molecules which are directly aimed at the bottom surface from the source. If the sticking coefficient is now reduced to 0.5, the reactant molecules will require, on average, two encounters with the surface before becoming depleted. For sufficiently narrow features, most of the reactant molecules will become depleted prior to reaching the bottom surface, once again restricting the flux to the bottom surface to the direct flux originating from the source. This then leads to identical step coverages for $P_{rxn} = 1.0$ and $P_{rxn} = 0.5$.

5.3.4 Effect of the surface mobility on the film microstructure

The surface mobility was found to have virtually no impact on the step coverage for the range of mobility values explored which varied from zero mobility to several surface shuffles per time step. This is consistent with the results of previous studies and adds to the mounting evidence that re-emission (or, equivalently, P_{rxn}) and shadowing effects ultimately dictate the step coverage.

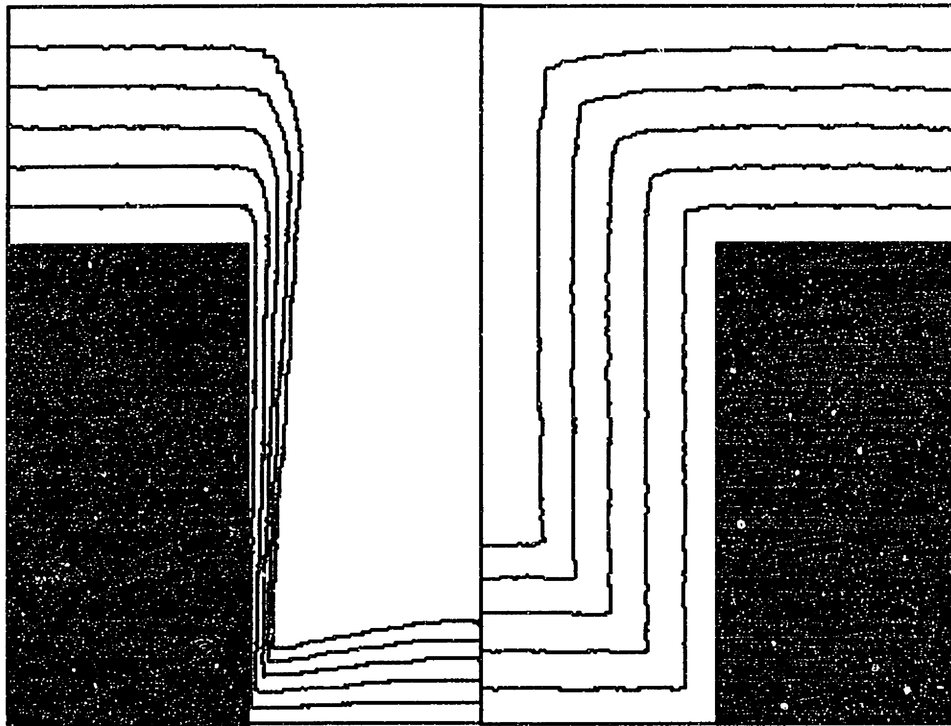

(a) $P_{rxn} = 1.0$ (b) $P_{rxn} = 0.01$

Figure 5-10 : Simulated film profiles for an infinite trench at Kn = 0.25 and (a) $P_{rxn} = 1.0$ and (b) $P_{rxn} = 0.01$.

The microstructure of the deposited films was found to be highly sensitive to the degree of surface mobility, however. This is illustrated in Figure 5-11 where the trench profile is shown for $P_{rxn} = 1.0$ and $Kn = 0.1$ with surface diffusion completely turned off. The highly columnar appearance of the film along the sidewall (a feature common in many CVD films) for the case of zero mobility is not apparent when a sufficient amount of surface mobility is assigned to the adsorbed molecules. This is shown in Figure 5-12 where the simulation conditions are identical except the reactant molecules are now allowed to diffuse along the surface. The microstructural details of the two simulated profiles contrast sharply while a negligible difference is seen between the step coverages.

The appearance of cracks in the corner of the trench was evident at intermediate values of P_{rxn} and became most pronounced at about $P_{rxn} = 0.3$. The development of this feature was found to be sensitive to the surface mobility, also, as shown in Figure 5-13 for the two extremes of adsorbate mobility at $Kn = 0.1$. This feature has been reported in experimental deposition profiles of SiO_2 from SiH_4/O_2 gas mixtures [Tsai, 1986]. The appearance of the crack in the simulated profile suggests that SiO_2 deposition in this system is predominantly due to a highly reactive and relatively immobile species.

5.3.5 Effect of the Knudsen number

The effect of varying the Knudsen number, or equivalently the influence of intermolecular collisions, is discussed next. The Monte Carlo study performed by Cooke and Harris indicated that the step coverage worsened as the Knudsen number was reduced [Cooke and Harris, 1989]. Our results suggested the opposite trend as indicated in Figure 5-14. A slight improvement in the step coverage is seen as the Knudsen number is decreased from 10 to 0.1. This may be anticipated intuitively upon consideration of the fact that intermolecular collisions act to dissipate concentration gradients in the gas

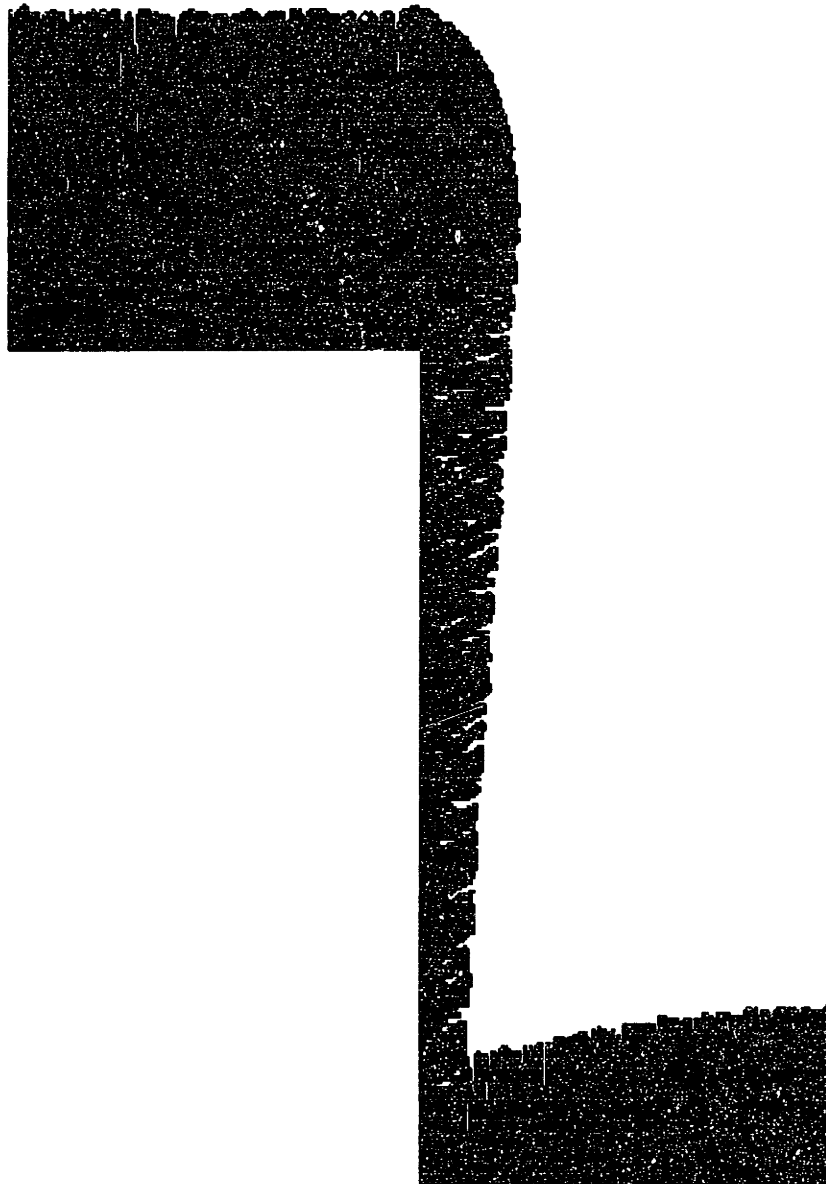

Figure 5-11 : Simulated film profile with no surface diffusion for an infinite trench at Kn = 0.1 and P_{rxn} = 1.0.

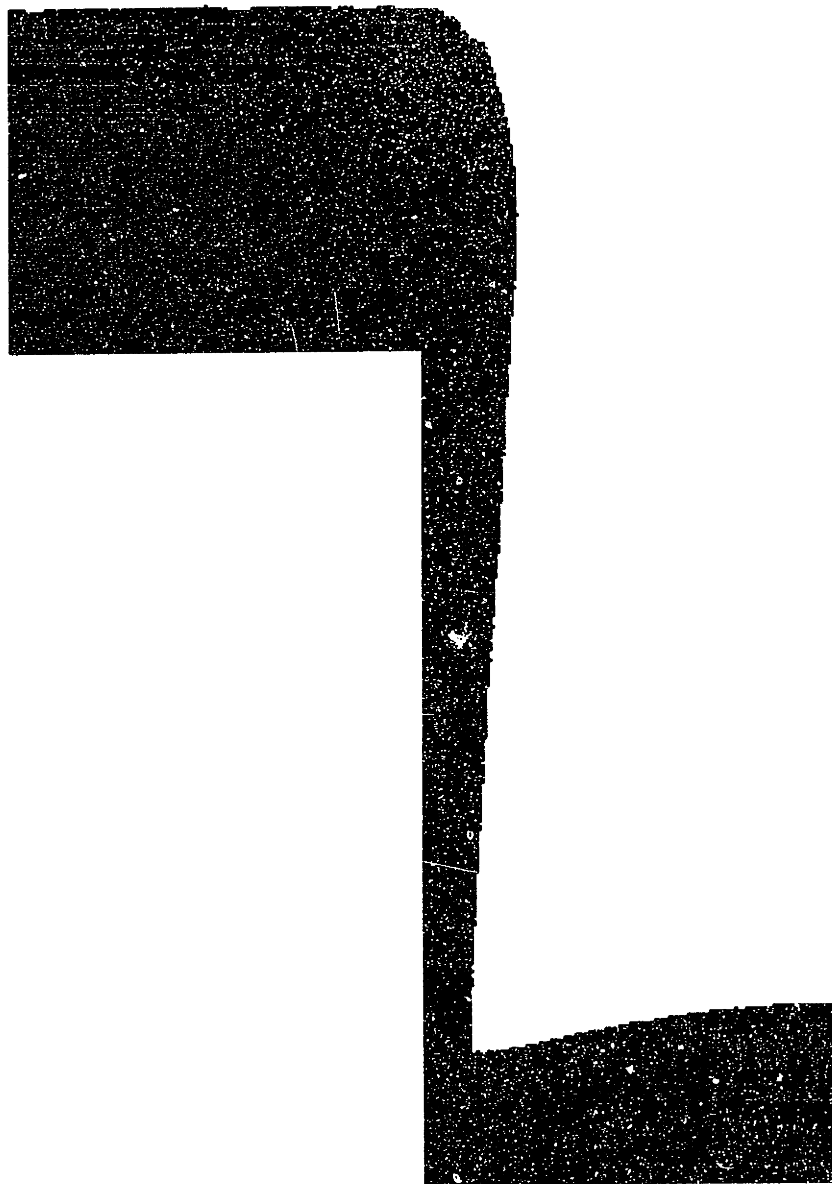

Figure 5-12 : Simulated film profile with surface diffusion for an infinite trench at $Kn = 0.1$ and $P_{rxn} = 1.0$.

(a) No surface mobility (b) High surface mobility

Figure 5-13 : Effect of increasing the surface mobility on the development of a crack in the corner of an infinitely long trench at Kn = 0.1 and $P_{rxn} = 0.3$ for (a) no surface mobility and (b) high surface mobility.

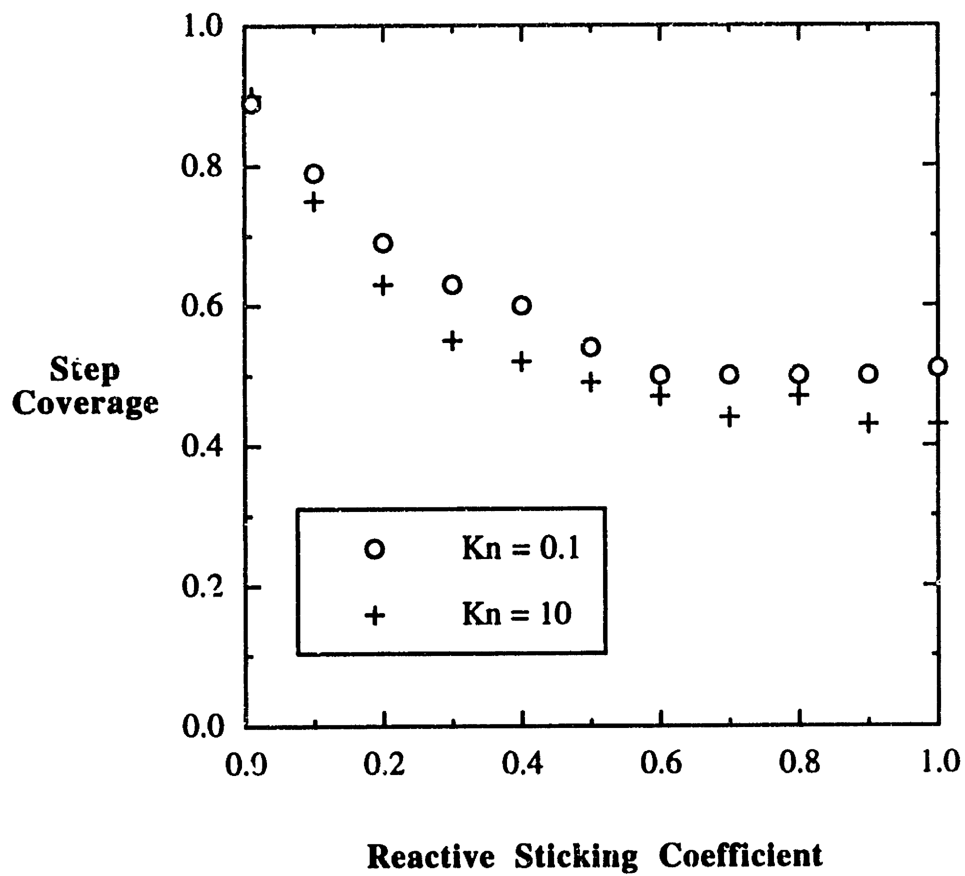

Figure 5-14 : Step coverage for an infinite trench at Kn = 0.1 (O) and Kn = 10 (+).

phase. This would result in the reactants being more uniformly distributed across the feature growth surface.

Despite this effect, a noteworthy observation is that the effect is quite minimal over the range of Knudsen numbers explored, which effectively cover the transition regime. This suggests that the gas phase collisions might be appropriately ignored unless the flow is well into the continuum regime, a tempting assumption given the potential computational savings. The actual picture may be complicated in certain cases where a sufficient decrease in the Knudsen number (increase in pressure) leads to the formation or increased concentration of highly reactive intermediate species which are detrimental to step coverage.

5.3.6 Effect of the feature aspect ratio

The maturation of sub-micron technology depends upon the ability to achieve conformal coverage over increasingly narrower features. The profile simulator should therefore be capable of investigating deposition over a wide range of aspect ratios. The aspect ratio of the feature is readily adjusted in the simulation by prescribing the corresponding feature depth; the feature width is set by the prescribed Knudsen number. As expected, the step coverage varied considerably as the feature aspect ratio was adjusted. This is illustrated in Figure 5-15 where the aspect ratio is doubled by a twofold increase in the trench depth at Kn = 0.25. The maximum step coverage variance between the two cases occurs at higher values of P_{rxn}. Once again, this is due to the fact that shadowing effects become predominant as the sticking coefficient approaches unity and re-emission is negligible. The narrowing of the step coverage difference at lower values of the sticking coefficient is a measure of the extent to which successive re-emission acts to improve the step coverage for the deeper trench.

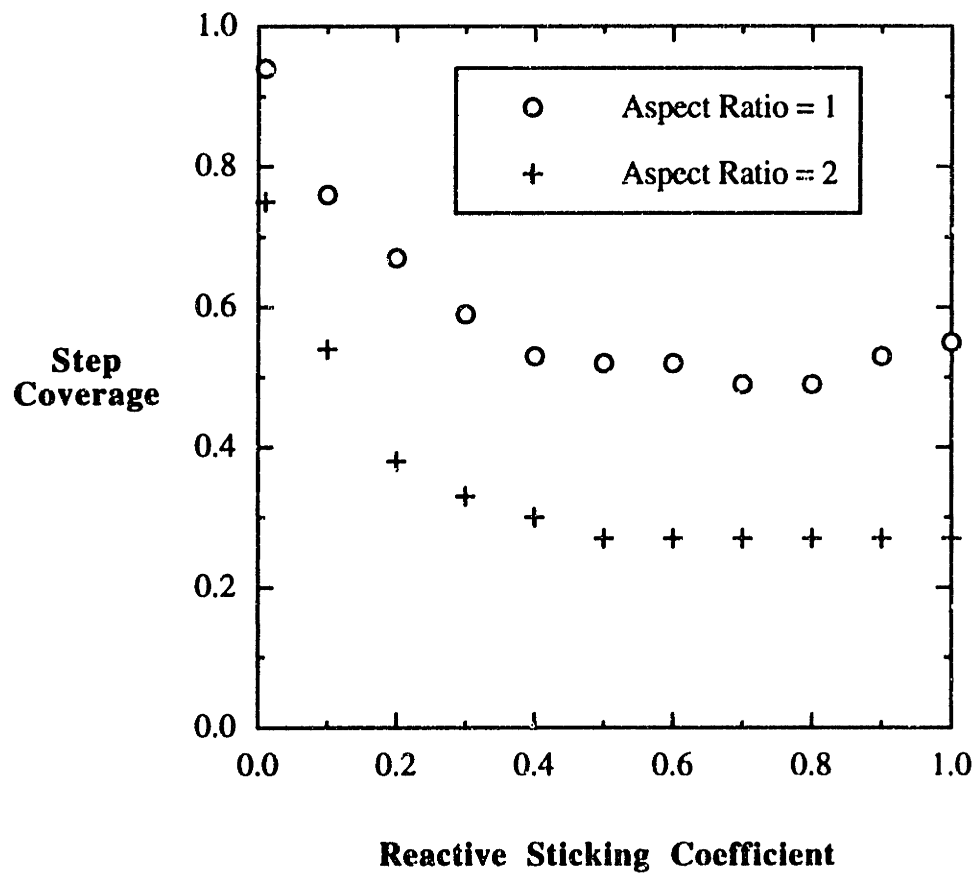

Figure 5-15 : Step coverage for an infinite trench at Kn = 0.25 and an aspect ratio of 1 (O) and 2 (+).

5.3.7 Effect of feature geometry : a comparison with deposition over a circular contact hole

The various parameters discussed above for the long narrow trench exhibit the same trends when applied to the cylindrical contact hole. This is shown in Figure 5-16 where the step coverage is plotted as a function of the reactive sticking coefficient for an infinitely long trench and for a circular contact hole. The Knudsen number is 0.25 in both cases and the characteristic dimension for the contact hole is given by the hole diameter. The primary difference between the two geometrics is the increased influence of shadowing with the contact hole geometry. This trend is easily understood by considering the fact that the infinitely long trench is confined in one dimension while the cylindrical contact hole is effectively confined in two dimensions. The additional shadowing resulting from the completely enclosed feature is further explored in the next section for three-dimensional geometries.

5.3.8 A three-dimensional simulation of deposition over a square hole structure

The two-dimensional geometries considered thus far are idealized representations of actual physical systems encountered in nonplanar CVD processes. In reality the feature is not blessed with the symmetry imposed in most process models. For example, in a finite length trench the two-dimensional description of the deposition may be sufficiently accurate along nearly the entire length of the feature but fall well short of describing the profile near the ends. This complexity does not render the simulation model useless, however, as the DSMC method is easily extended to three-dimensional calculations with a minimal amount of additional programming. In addition, the computational load is only modestly increased since the simulation time is directly

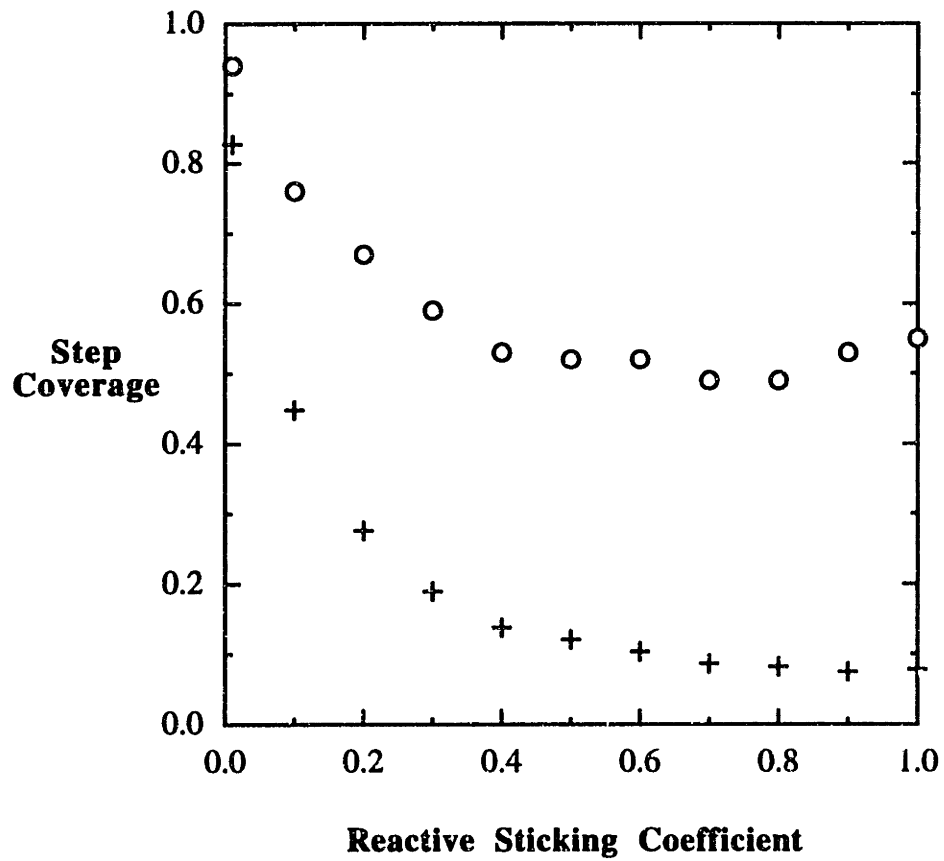

Figure 5-16 : Step coverage for an infinite trench (O) and a circular contact hole (+) at Kn = 0.25.

proportional to the number of molecules and, therefore, scales linearly with the dimensionality of the problem.

A simple three-dimensional structure was considered for the purpose of demonstrating the capability of the simulation model to investigate realistic geometries. The simulated profile over the square hole structure for $P_{rxn} = 0.3$ and $Kn = 0.25$ is shown in Figure 5-17. Also shown is a two-dimensional slice from the central X-Y plane of the three-dimensional profile. A comparison of this profile with that given in Figure 5-9 where the conditions are identical, except the geometry is for an infinitely long trench, clearly illustrates the additional shadowing given by the three-dimensional structure. This is analogous to the effect discussed above when going from the trench geometry to the contact hole geometry.

5.4 Coupling of the microscale profile simulator with reactor scale simulations of a sputter deposition system

The profile simulations presented in the preceding sections have provided insight into how the step coverage performance is impacted by the localized conditions. The local feature scale problem is related to the global reactor scale description through the open boundary condition where the density, temperature, and composition of the entering gas are specified. The simulations thus provide a picture of how changes in the reactor operating conditions might influence the film growth at a microscopic level. Although this is not an entirely novel concept, the strength of the simulation model rests in its ability to simulate nonequilibrium conditions. The DSMC method was recently employed by Kersch and coworkers to simulate a sputter deposition reactor [Kersch *et al.*, 1992]. The reactor configuration and the rarefied gas conditions were found to give

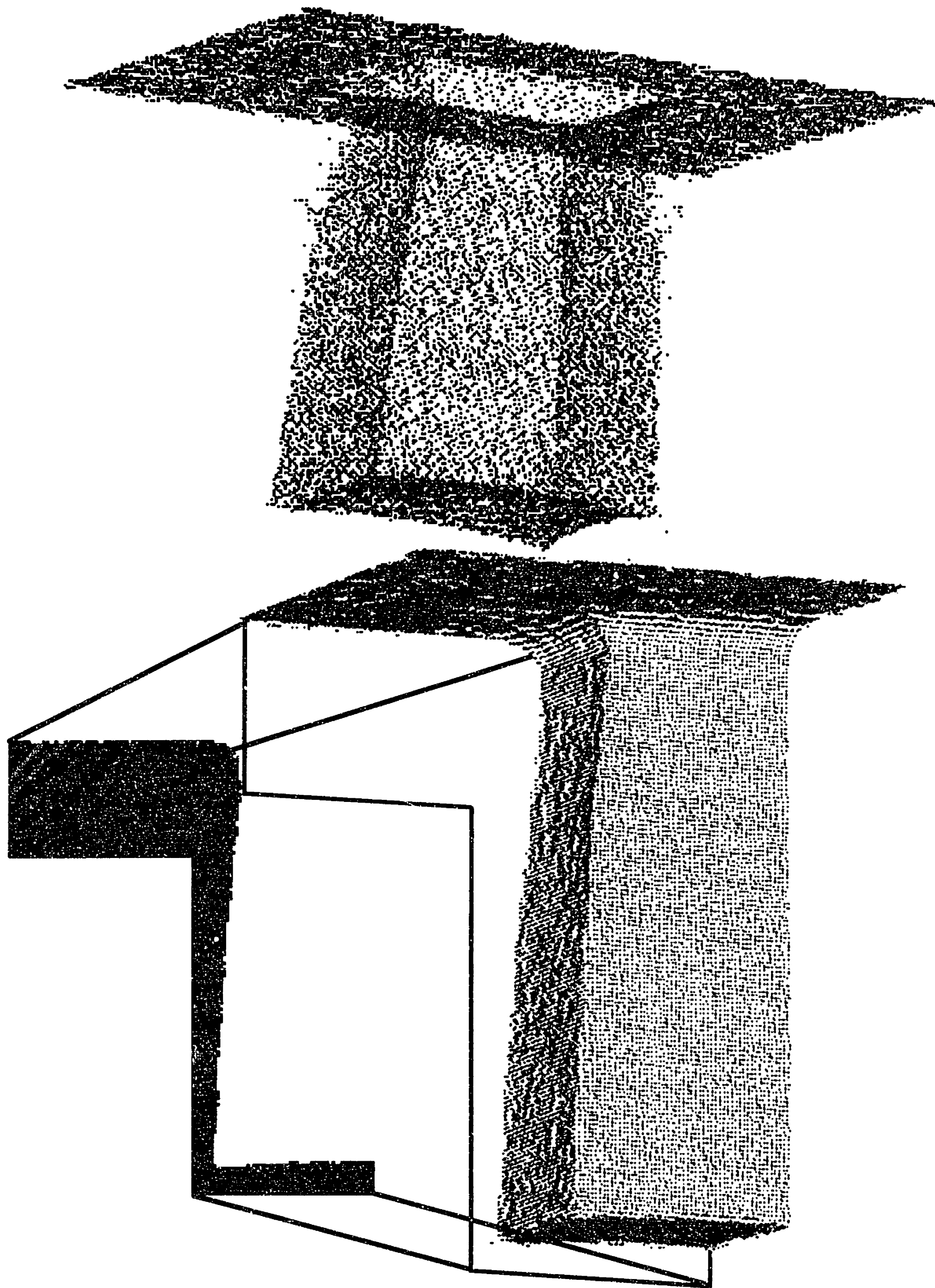

Figure 5-17 : Simulated three-dimensional profile over a square hole structure at Kn = 0.25 and P_{rxn} = 0.3. Also shown is a two-dimensional slice of the profile taken from the central X-Y plane.

rise to significant nonequilibrium transport effects according to their simulations. This section presents the results of a collaborative investigation which couples the reactor scale DSMC sputter deposition results with feature scale profile simulations.

5.4.1 The Siemens sputter deposition reactor

A schematic diagram of the sputter deposition reactor which was modelled by Kersch *et al.* is shown in Figure 5-18. The single wafer axisymmetric reactor chamber includes the target plate located at the top and the substrate at the bottom. The collimator consists of a thin circular quartz disk containing an array of small holes which are utilized to provide a unidirectional flux of atoms to the substrate. The gas inlet and outlet are modelled as annular strips along the perimeter of the top and bottom, respectively. The reactor chamber walls and the substrate are kept at a constant temperature of 323 K.

A titanium target is exclusively considered in this study. The emission of Ti atoms from the target plate is provided by an argon plasma. The erosion profile of the target is taken from experimental measurements. The energy of the emitted Ti atoms is sampled from a Thompson distribution where the ion energy from the plasma (500 eV) and the atom binding energy (5 eV) are specified.

The Ar+ ions are ignored in the simulations and the Ar background gas density and temperature fields are calculated separately from the Ti atom transport using the DSMC method. The Ti atom trajectories are then subsequently calculated in a serial fashion using the test particle Monte Carlo method. This approach enables a more efficient sampling of Ti atoms and is rationalized by the dilute concentration of Ti in the gas phase relative to Ar. The transmission of atoms through the collimator is computed in a stochastic fashion based upon the aspect ratio of the holes (height/diameter = 1.5).

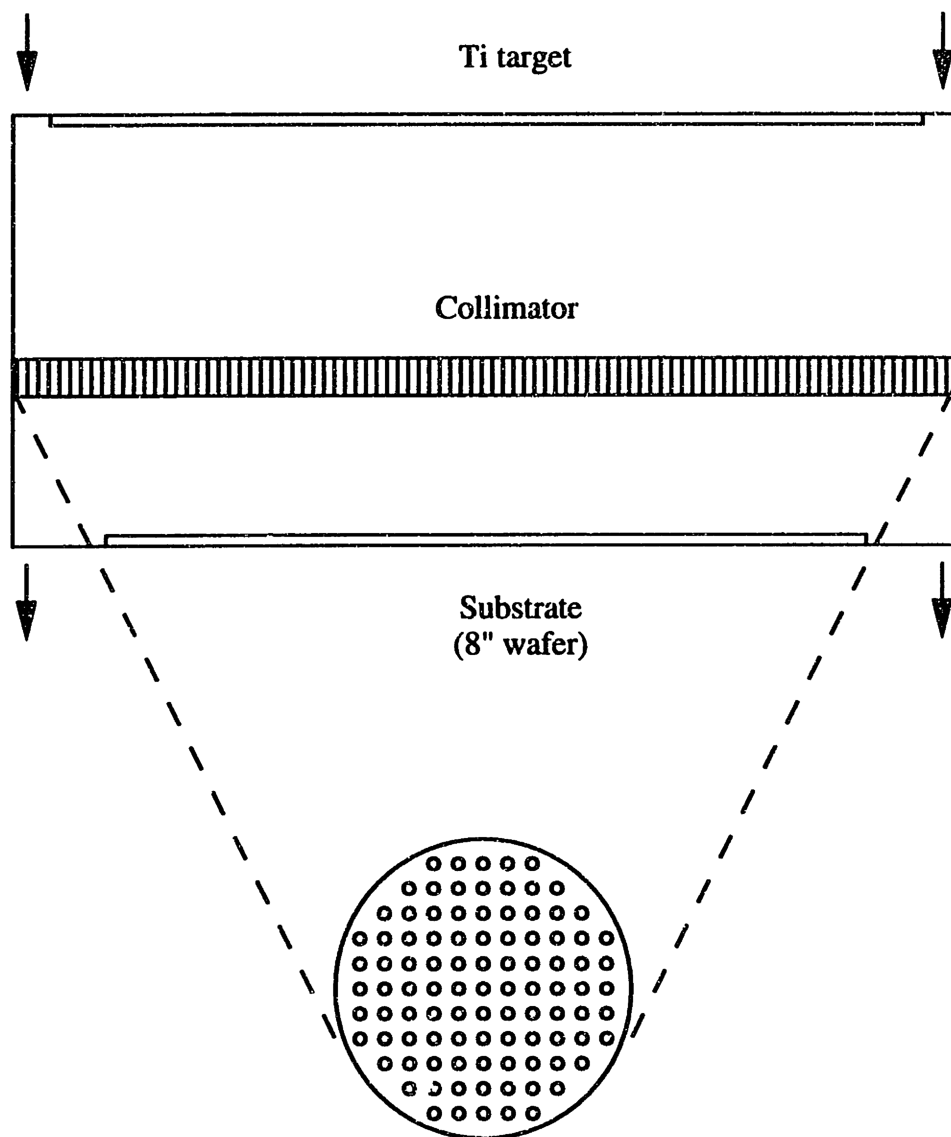

Figure 5-18 : Schematic diagram of Siemens sputter deposition reactor (Kersch *et al.*, 1992).

The background gas density is set to 2.9×10^{13} cm^{-3} (0.13 Pa) at both the inlet and outlet boundaries.

5.4.2 Free molecular profile simulations

The operating pressures utilized in the sputter deposition reactor result in a mean free path on the order of several centimeters. Although intermolecular collisions are still expected to play a role in the reactor scale gas dynamics, the gas flow in a local feature scale simulation may be regarded as completely free molecular. For this reason, the simulation was simplified by removing the gas phase collision routine and generating the trajectories in a serial fashion since each trajectory may now be independently computed. The modified SOS profile evolution routine remains intact as presented in section 5.2.3.

The Ti atoms are assumed to have a sticking coefficient of unity with no surface diffusion [Kersch, 1993]. Each Ti atom is introduced several mean free paths above the two-dimensional trench feature which was considered in all of the simulations to follow. The entrance cone angle of the impinging Ti atom is sampled from the angular distribution provided by the sputter deposition simulations. This distribution is obtained at several radial positions along the substrate by sampling the angles of impingement of a large number of Ti atoms. A schematic diagram of the combined reactor scale and feature scale simulation study is illustrated in Figure 5-19.

The resulting angular flux distributions from the DSMC sputter reactor simulations at three radial positions are shown in Figure 5-20 along with the cosine distribution. The influence of the collimator is reflected in the sputter simulation distributions as the wide angle ends of the distribution are very abbreviated relative to the cosine distribution. The distributions are seen to become more asymmetric away from

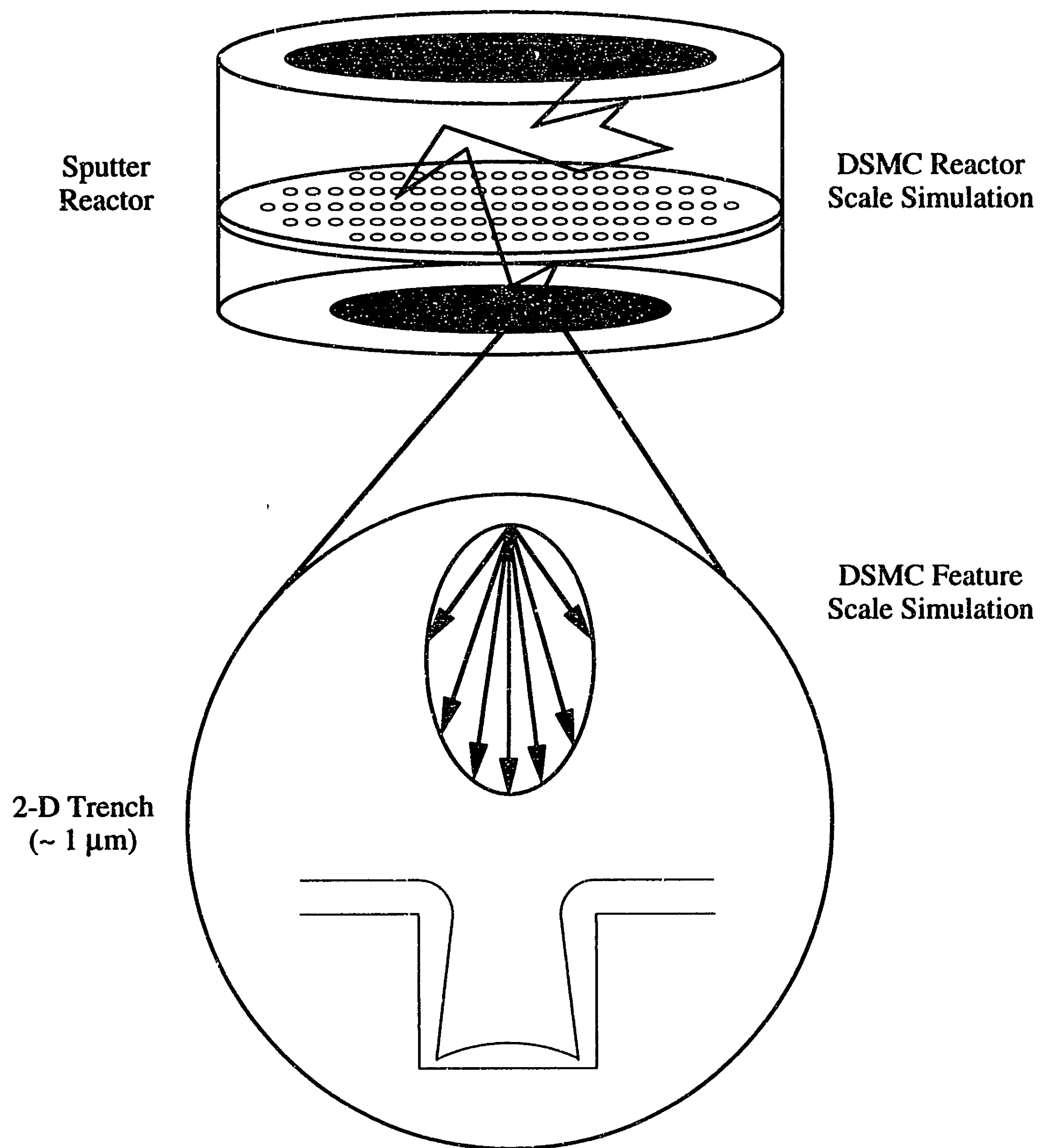

Figure 5-19 : Schematic diagram of combined reactor scale and feature scale DSMC simulation study.

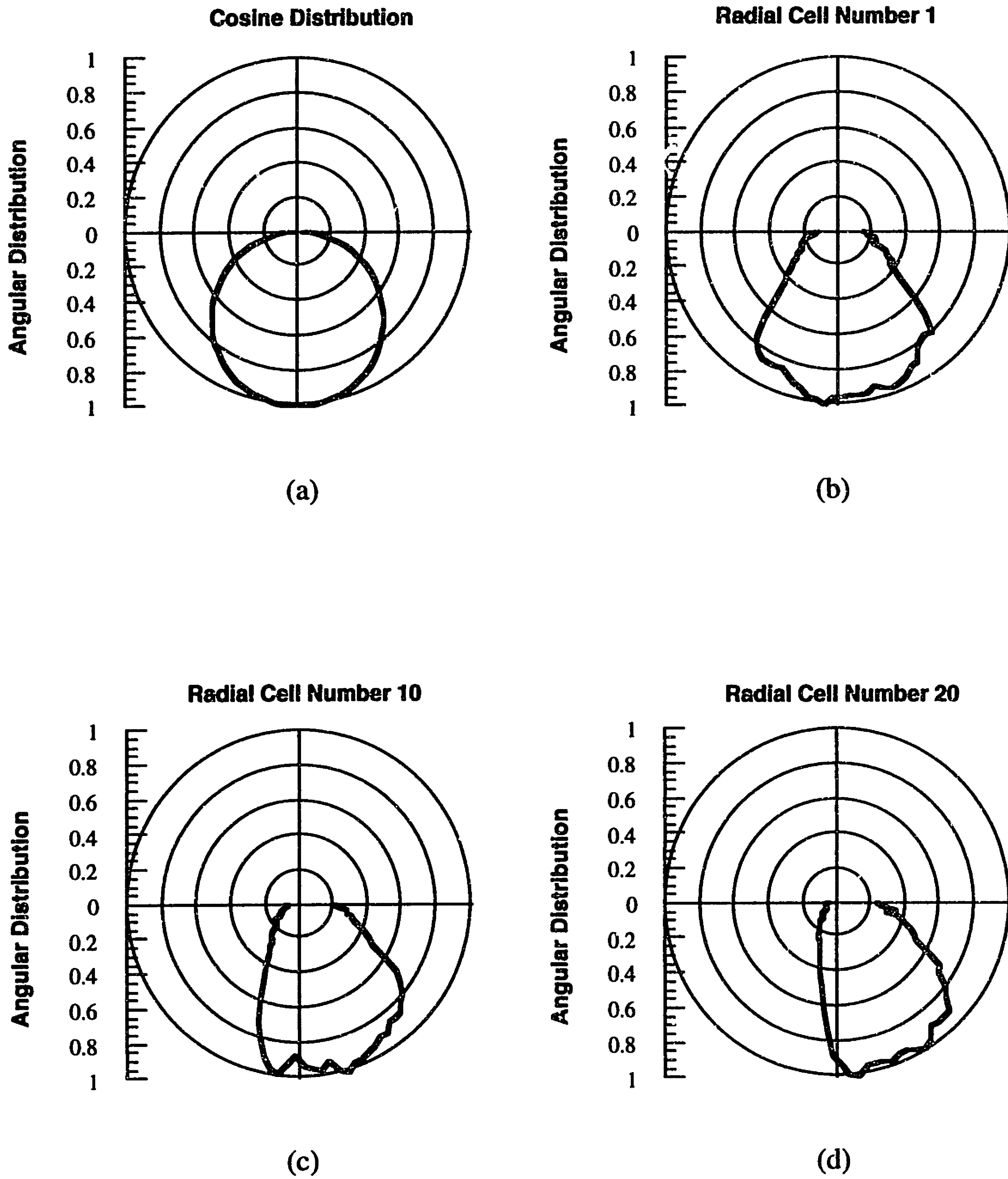

Figure 5-20 : Angular flux distributions corresponding to a (a) cosine distribution and DSMC computed distributions at (b) r = 0, (c) r = 7 cm and (d) r = 10 cm.

the symmetry axis as well. This is probably due to the increasing proximity of the wall. The corresponding simulated profiles for these distributions are given in Figure 5-21. The step coverage of the Ti films is only slightly improved over the cosine distribution when employing the collimator. This modest improvement is more than offset by the effects of the asymmetry in the distributions which lead to asymmetrical film growth. The simulated profiles for these distributions are given for an aspect ratio of 2 in Figures 5-22 and 5-23. The same trends are evident for the deeper trenches with a degradation in the step coverage as was previously shown in Figure 5-15.

Cosine Distribution

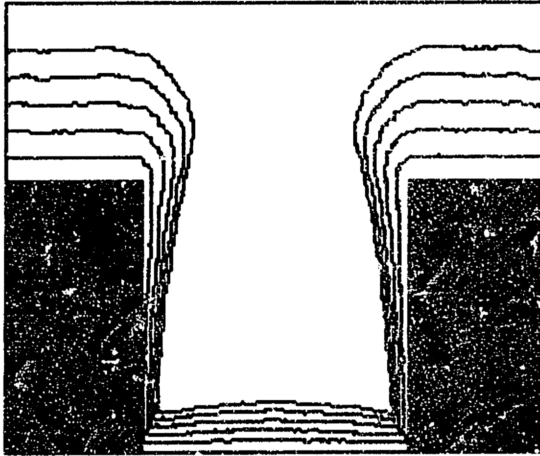

(a)

Radial Cell # 1

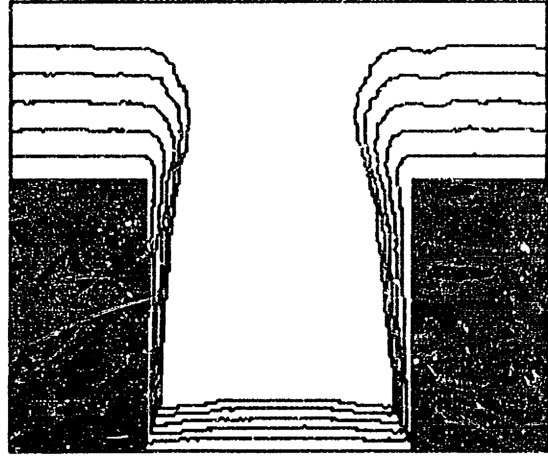

(b)

Radial Cell # 10

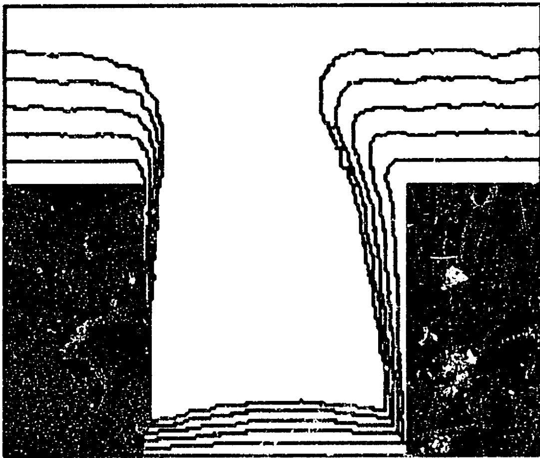

(c)

Radial Cell # 20

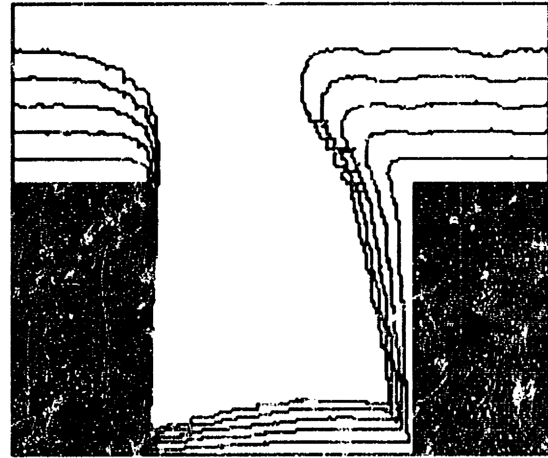

(d)

Figure 5-21 : Profile simulations corresponding to the angular distributions given in Figure 5-20.

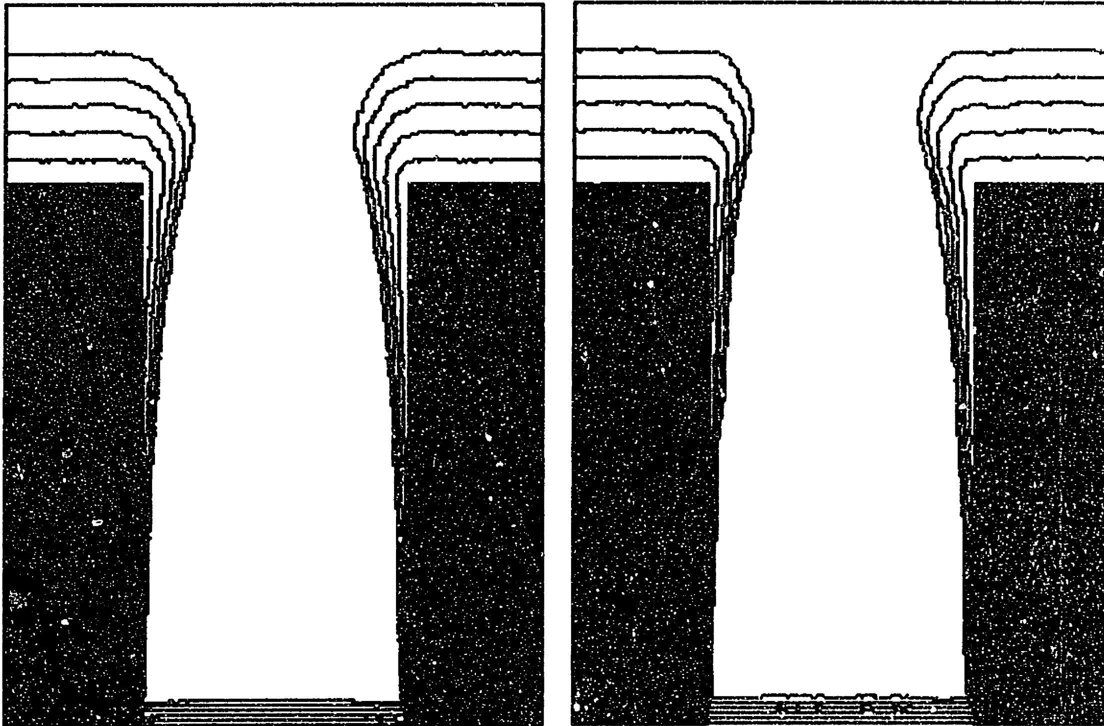

(a) (b)

Figure 5-22 : Profile simulations corresponding to the angular distributions given in (a) Figure 5-20a and (b) Figure 5-20b for an aspect ratio of 2.

Radial Cell # 10   Radial Cell # 20

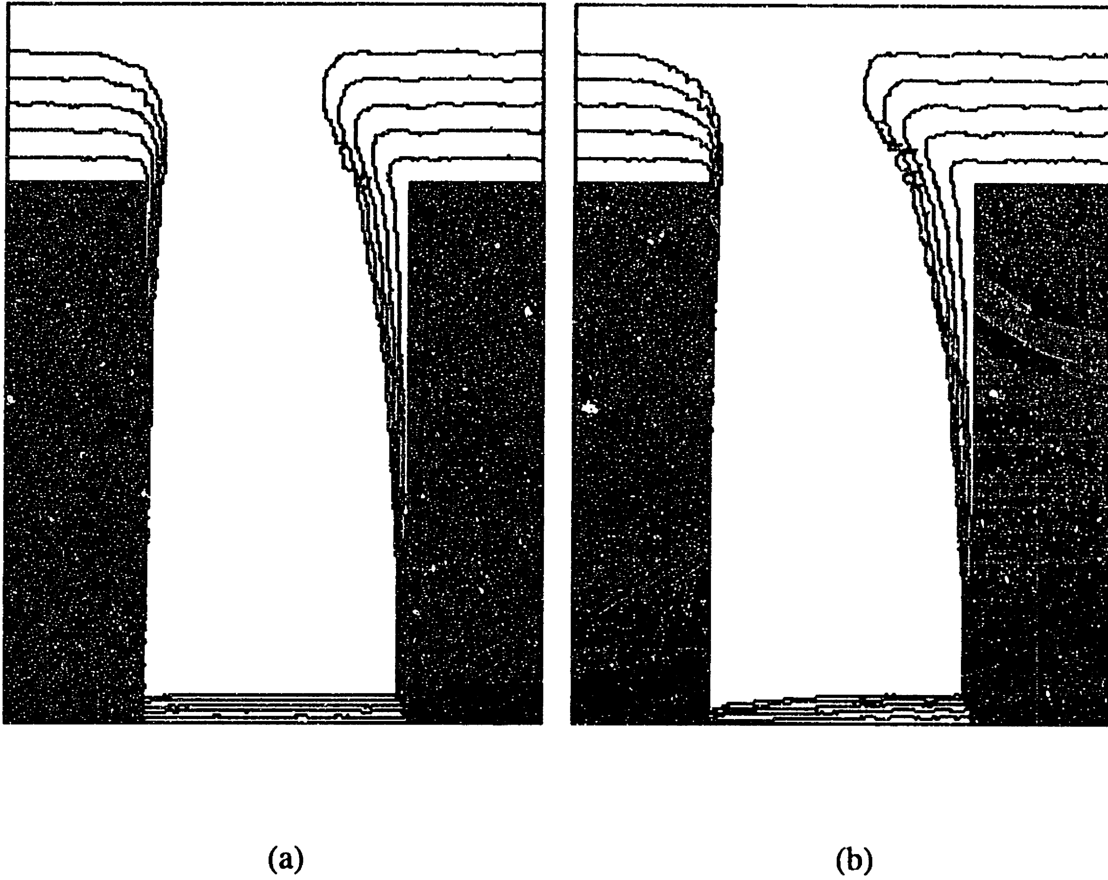

Figure 5-23 : Profile simulations corresponding to the angular distributions given in (a) Figure 5-20c and (b) Figure 5-20d for an aspect ratio of 2.

Chapter 6 : Thesis Summary and Prospects for Future Work

6.1 Rarefied gas flows in the LPCVD reactor

A two-dimensional axisymmetric DSMC program was developed to investigate rarefied gas flows in the multiwafer LPCVD reactor under UHV-CVD conditions. The conventional DSMC algorithm, originally formulated for external flows, was necessarily modified in order to simulate internal flows in the LPCVD reactor. This involved a determination of the downstream boundary condition by a dynamic updating procedure which computed the influx of molecules at the boundary according to the prevailing local conditions, thus avoiding a costly iterative procedure.

The flow of pure H_2 through an isothermal research scale LPCVD reactor was used as a reference base case simulation. A feature common to all of the UHV-CVD flows was the compressibility of the gas, resulting in substantial density and pressure variations throughout the reactor. The largest variations occurred as the gas was throttled through the annular flow region. For the range of operating pressures investigated, which effectively covered the transition and free molecular flow regimes ($\lambda \geq 1$ cm), the outlet gas pressure or density was around 50% of the inlet gas pressure, *i.e.* $\Delta p/p \sim 0.5$. The relative magnitude of the pressure drop was largely influenced by the cross-sectional area of the annular flow region (wafer diameter), the number of wafers, and the outlet diameter.

The rarefaction of the gas gave rise to an increased influence of the gas-surface interactions on the flow. This was confirmed through the visualization of several molecular trajectory plots which dramatically illustrated the deviation of the molecules from the

streamlines suggested by the macroscopic velocity field. The transport of the rarefied gas stream through the LPCVD reactor was thus dictated by the diffusive motion of the individual molecules rather than the macroscopic convective forces. This had an important consequence on the average residence time of the gas in the LPCVD reactor. The diffusive motion or, equivalently, the thermal velocity of a gas is inversely proportional to the square root of the molecular weight. As a result the average residence times, computed directly with the DSMC method, were found to be proportional to the square root of the molecular weight of the species.

Simulations of rarefied gas mixtures in the LPCVD reactor revealed significant species separation effects. This was attributed to pressure diffusion, a phenomenon which acts to drive the heavier species towards regions of higher pressure. This effect is ordinarily negligible for continuum flows but becomes increasingly important as $\Delta p/p$ approaches unity. In gas flows containing equal amounts of N_2 and H_2 in the inlet stream, the heavier N_2 species accumulated in a region immediately upstream of the wafers. This is consistent with the computed pressure fields which indicated a strong pressure gradient across the wafers.

6.2 Heat transfer in the LPCVD reactor

A two-dimensional axisymmetric heat transfer model was developed to investigate the underlying nature of thermal variations in the LPCVD reactor and their resulting influence on the rarefied gas dynamics. The radiative heat transfer between the wafers, the semi-transparent quartz tube, the stainless steel ends of the reactor, and the surrounding furnace was simulated using a Monte Carlo approach. In addition, the axial conductive heat transfer in the quartz tube was computed using finite differences. The simulation

solved for the temperatures of the wafers and the quartz tube given the temperature of the furnace and the water-cooled ends of the reactor. The model made use of no adjustable parameters.

The cooled ends of the reactor resulted in a suppression of the temperature of several wafers at each end of the wafer stack. The pronounced cooling of the two end wafers was primarily due to the direct radiative heat loss to the cooled ends of the reactor. The simulations have shown, however, that the conductive dissipation of the furnace heat through the quartz tube was responsible for the cooling of several more wafers from each end of the wafer stack. The simulated wafer temperatures for a commercial scale LPCVD reactor showed excellent agreement with experimentally measured wafer temperatures.

The computed wafer and quartz tube temperature profiles were also implemented as thermal boundary conditions in DSMC calculations of rarefied gas flows in the LPCVD furnace. The nonisothermal reactor environment was found to give rise to substantial variations in the temperature and density fields of a H_2 gas stream under UHV-CVD conditions. Nonisothermal simulations of N_2/H_2 mixtures also showed evidence of species separation due to thermal diffusion which resulted in localized accumulations of N_2 near the cooled ends of the reactor.

6.3 Microscale gas flows and profile evolution

A simulation model for feature scale rarefied gas transport and film profile evolution was developed. The model rigorously treats the gas transport with the direct simulation Monte Carlo method. A new profile simulation method was developed which is implemented directly in the gas transport calculation and captures the microstructural detail of the growing film in addition to providing dynamic step coverage performance. The

simulation model is applicable from near continuum conditions to free molecular flow and may be used to investigate realistic three-dimensional structures.

A parametric investigation of the influence of various parameters on the step coverage was performed. The results showed that as the reactive sticking coefficient approaches unity shadowing effects become predominant. This resulted in very pronounced reductions in the step coverage at high values of P_{rxn} for structures with large aspect ratios and "two-dimensional" shadowing (*e.g.* contact holes and three-dimensional structures). For low values of P_{rxn} re-emission from the surface was the major influence on the step coverage and the shadowing effects were less severe. The action of intermolecular collisions to dissipate concentration gradients in the gas phase resulted in a slight improvement in the step coverage as the Knudsen number was lowered. The surface mobility of the adsorbed species did not influence the step coverage but had a pronounced effect on the microstructure of the film. As the surface mobility was reduced, the roughness of the films increased and the nonplanar deposits became more prone to cracks forming in the film, especially at the corners of a trench structure. The extension of the simulation model to a three-dimensional calculation was demonstrated for the deposition over a square hole structure.

6.4 Prospects for future work

6.4.1 Reactor scale simulations of rarefied gas flows

There appear to be two primary driving forces motivating a molecular level description of gas flows in CVD reactors. The most obvious of these is the rarefaction of the gas accompanying reduced pressure operation, an increasingly attractive approach to

CVD processing. Here the conventional continuum equations describing the gas flow are no longer valid and the molecular description is the only alternative.

The second motivating factor stems from the level of complexity which may be incorporated into molecular level simulations such as internal energy modes and highly nonequilibrium conditions. An example of the exploitation of these advantages may be found in the recent publication by DeJong and coworkers [DeJong *et al.*, 1992]. The DSMC method was employed to simulate the chemistry in a highly nonequilibrium hypersonic flow in the framework of a continuum flow calculation. Here the molecular level approach does not supplant the continuum description but instead serves in a complementary fashion. This hybrid approach appears to be quite promising for simulating plasma CVD processes.

Other candidate systems exist which may benefit from analysis of the fundamental issues which were explored in this work with respect to UHV-CVD. Sputter deposition reactors typically operate in the transition regime and present a host of unique and interesting issues which may be pursued using a DSMC approach. Initial efforts along these lines have already been reported by researchers at Siemens [Kersch *et al.*, 1992]. Metalorganic chemical vapor deposition (MOCVD) processes may extract the same benefits from low pressure operation as was emphasized in this work for Si CVD. Commercial scale low pressure MOCVD reactors employing several wafers where transport effects impact the growth rate uniformity may be characterized and optimized using DSMC as well.

6.4.2 Monte Carlo calculations of thermal radiation heat transfer

The Monte Carlo approach to performing radiation heat transfer calculations includes advantages which are analogous to those outlined above for molecular flow

descriptions. These include the ability to incorporate spectral, directional, and temperature dependencies into the calculation with a minimal corresponding computational effort. In CVD processes where the slightest thermal variations may render the product useless, this level of detail is required in a model of the process.

This is particularly true for rapid thermal processing (RTP) where precise spatial and temporal control of the temperature is used to obtain extreme uniformity and abruptness across the substrate. The Monte Carlo approach appears well-suited for dealing with the complexities associated with the reactor geometry, the variety of materials participating in the radiation heat transfer, and the time-dependent nature of the calculation. The Monte Carlo calculation of the radiation heat transfer should easily interface with the computations for other coupled physical phenomena (*e.g.* conductive heat transfer, gas flow). The challenge lies in reducing the computational time required to perform the Monte Carlo calculation to be of the same order-of-magitude as the remaining parts of the problem. This may not be such an important issue for employing Monte Carlo to perform steady-state radiation heat transfer calculations for conventional CVD processes.

6.4.3 Feature scale simulations of rarefied gas flows

The rarefied gas transport and profile evolution model developed in this work has extended the capabilities of existing process models in two respects. First, the extension of the model to include three-dimensional structures of arbitrary shape now enables the simulation of film growth over realistic geometries. The example calculation of deposition over a square hole presented in Chapter 5 clearly demonstrated the additional shadowing which occurs upon taking into consideration the third dimension. This creates the opportunity to investigate the deposition over finite trenches of various lengths in order to determine the appropriateness of employing a two-dimensional model.

The other feature developed in the model which offers new possibilities is the modified SOS profile evolution method. Apart from the ability to predict step coverage performance, insight is gained into the process parameters which affect the roughness of the film surface, the formation of voids and cracks, the appearance of columnar growth structures, and the bulk film density. A systematic study of the process conditions which lead to the various film growth regimes would be a valuable extension of the current work.

References

Allen, M., and D. Tildesley, *Computer Simulation of Liquids*, Oxford University Press, New York (1987).

Aris, R., *The Mathematical Theory of Diffusion and Reaction in Permeable Catalysts : Volume I : The Theory of the Steady-State*, Clarendon Press, Oxford (1975).

Badgwell, T., T. Edgar and I. Trachtenberg, "Modeling and Scale-Up of Multiwafer LPCVD Reactors," *AIChE J.*, **38**, pp. 926-938 (1992).

Badgwell, T., T. Edgar, I. Trachtenberg and J. Elliott, "Experimental Verification of a Fundamental Model for Multiwafer Low-Pressure Chemical Vapor Deposition of Polysilicon," *J. Electrochem. Soc.*, **139**, pp. 524-532 (1992).

Bhatnagar, P., E. Gross and M. Crook, "A Model for Collision Processes in Gases," *Phys. Rev.*, **94**, pp. 511-524 (1954).

Bird, G., "Approach to Translational Equilibrium in a Rigid Sphere Gas," *Phys. Fluids*, **6**, pp. 1518-1519 (1963).

Bird, G., *Molecular Gas Dynamics*, Clarendon Press, Oxford (1976).

Bird, G., "Direct Molecular Simulation of a Dissociating Diatomic Gas," *J. Comp. Phys.*, **25**, pp. 353-365 (1977).

Bird, G., "Monte Carlo Simulation of Gas Flows," *Ann. Rev. Fluid Mech.*, **10**, pp. 11-31 (1978).

Bird, G., "Monte Carlo Simulation in an Engineering Context," *Proc. 12th Int. Symp. Rarefied Gas Dyn.*, pp. 239-255 (1980).

Bird, G., "Definition of Mean Free Path for Real Gases," *Phys. Fluids*, **26**, pp. 3222-3223 (1983).

Bird, G., "Shock Wave Structure in Gas Mixtures," *Proc. 14th Int. Symp. Rarefied Gas Dyn.*, pp. 175-182 (1984).

Bird, G., "Low Density Aerothermodynamics," AIAA Paper No. 85-0994 (1985).

Bird, G., "Direct Simulation of Typical AOTV Entry Flows," AIAA Paper No. 86-1310 (1986).

Bird, G., "Thermal and Pressure Diffusion Effects in High Altitude Flows," AIAA Paper No. 88-2732 (1988).

Bird, G., "Direct Simulation of Gas Flows at the Molecular Level," *Comm. Appl. Num. Meth.*, **4**, pp. 165-172 (1988).

Bird, G., "Perception of Numerical Methods in Rarefied Gas Dynamics," *Proc. 16th Int. Symp. Rarefied Gas Dyn.*, pp. 211-226 (1988).

Bird, G., "Application of the Direct Simulation Monte Carlo Method to the Full Shuttle Geometry," AIAA Paper No. 90-1692 (1990).

Bird, G., "Efficiency and Discrepancy in the Direct Simulation Methods," *Proc. 17th Int. Symp. Rarefied Gas Dyn.*, pp. 655-662 (1990).

Bird, G., personal communication (1991).

Bird, R., W. Stewart and E. Lightfoot, *Transport Phenomena*, Wiley, New York (1960).

Borgnakke, C., and P. Larsen, "Statistical Collision Models for Monte Carlo Simulation of Polyatomic Gas Mixture," *J. Comp. Phys.*, **18**, pp. 405-420 (1975).

Box, G., W. Hunter and J. Hunter, *Statistics for Experimenters*, Wiley, New York (1978).

Boyd, I., "Assessment of Chemical Nonequilibrium in Rarefied Hypersonic Flow," AIAA Paper No. 90-0145 (1990).

Boyd, I., "Vectorization of a Monte Carlo Simulation Scheme for Nonequilibrium Gas Dynamics," *J. Comp. Phys.*, **96**, pp. 411-427 (1991).

Broadwell, J., "Study of Rarefied Shear Flow by the Discrete Velocity Method," *J. Fluid Mech.*, **19**, pp. 401-414 (1964).

Buss, R., P. Ho, W. Breiland and M. Coltrin, "Reactive Sticking Coefficients for Silane and Disilane on Polycrystalline Silicon," *J. Appl. Phys.*, **63**, pp. 2808-2819 (1988).

Cale, T., and G. Raupp, "Free Molecular Transport and Deposition in Cylindrical Features," *J. Vac. Sci. Tech. B*, **8**, pp. 649-655 (1990).

Cale, T., and G. Raupp, "A Unified Line-Of-Sight Model of Deposition in Rectangular Trenches," *J. Vac. Sci. Tech. B*, **8**, pp. 1242-1248 (1990).

Cercignani, C., *The Boltzmann Equation and its Applications*, Springer-Verlag, Berlin (1988).

Chapman, S., and T. Cowling, *Mathematical Theory of Non-Uniform Gases*, 3rd ed., Cambridge University Press, London (1970).

Cheng, L., J. McVittie and K. Saraswat, "New Test Structure to Identify Step Coverage Mechanisms in Chemical Vapor Deposition of Silicon Dioxide," *Appl. Phys. Lett.*, **58**, pp. 2147-2149 (1991).

Chung, C., K. DeWitt and P. Penko, "DSMC Analysis of Species Separation in Rarefied Nozzle Flows," AIAA Paper No. 92-2859 (1992).

Coltrin, M., R. Kee and G. Evans, "A Mathematical Model of the Fluid Mechanics and Gas-Phase Chemistry in a Rotating Disk Chemical Vapor Deposition Reactor," *J. Electrochem. Soc.*, **136**, pp. 819-829 (1989).

Cooke, M., and G. Harris, "Monte Carlo Simulation of Thin-Film Deposition in a Rectangular Groove," *J. Vac. Sci. Tech. A*, **7**, pp. 3217-3221 (1989).

DeCroon, M., and L. Giling, "Chemical Boundary Layers in CVD : I. Irreversible Reactions," *J. Electrochem. Soc.*, **137**, pp. 2867-2876 (1990).

DeJong, F., J. Sabnis, R. Buggeln and H. McDonald, "Hybrid Navier-Stokes/Monte Carlo Method for Reacting Flow Calculations," *J. Space. Rockets*, **29**, pp. 312-318 (1992).

Dew, S., T. Smy and M. Brett, "Simulation of the Microstructure of Chemical Vapor Deposited Refractory Thin Films," *J. Vac. Sci. Tech. B*, **10**, pp. 618-624 (1992).

Dongarra, J., "Performance of Various Computers Using Standard Linear Equations Software," U.S. D.O.E./Univ. Tennessee-Knoxville Report (1993).

Eldridge, B., and L. Brown, "The Effect of Cross-Sectional Pore Shape on Knudsen Diffusion in Porous Materials," *AIChE J.*, **22**, pp. 942-944 (1976).

Elliott, J., personal communication (1993).

Erwin, D., E. Muntz and G. Pham-Van-Diep, "A Review of Detailed Comparisons Between Experiments and DSMC Calculations in Nonequilibrium Flows," AIAA Paper No. 89-1883 (1989).

Fotiadis, D., M. Boekholt, K. Jensen and W. Richter, "Flow and Heat Transfer in CVD Reactors : Comparison of Raman Temperature Measurements and Finite Element Model Predictions," *J. Crystal Growth*, **100**, pp. 577-599 (1990).

Furlani, T., and J. Lordi, "Implementation of the Direct Simulation Monte Carlo Method for an Exhaust Plume Flowfield in a Parallel Computing Environment," *Comp. Fluids*, **18**, pp. 212-227 (1990).

Gates, S., C. Greenlief, D. Beach and P. Holbert, "Decomposition of Silane on Si (111)-(7x7) and Si (100)-(2x1) Surfaces Below 500 °C," *J. Chem. Phys.*, **92**, pp. 3144-3153 (1990).

Gates, S., C. Greenlief and D. Beach, "Decomposition Mechanisms of SiH_x Species on Si (100)-(2x1) for x = 2,3, and 4," *J. Chem. Phys.*, **93**, pp. 7493-7503 (1990).

Gates, S., and S. Kulkarni, "Kinetics of Surface Reactions in Very Low-Pressure Chemical Vapor Deposition of Si from SiH_4," *Appl. Phys. Lett.*, **58**, pp. 2963-2965 (1991).

Goodman, F., and H. Wachman, *Dynamics of Gas-Surface Scattering*, Academic Press, New York (1976).

Greve, D., and M. Racanelli, "Construction and Operation of an Ultrahigh Vacuum Chemical Vapor Deposition Epitaxial Reactor for Growth of Ge_xSi_{1-x}," *J. Vac. Sci. Tech. B*, **3**, pp. 511-515 (1990).

Greve, D., and M. Racanelli, "Growth Rate of Doped and Undoped Silicon by Ultra-High Vacuum Chemical Vapor Deposition," *J. Electrochem. Soc.*, **138**, pp. 1744-1748 (1991).

Greve, D., and M. Racanelli, "Incorporation of Boron into UHV/CVD-Grown Germanium-Silicon Epitaxial Layers," *J. Elec. Mat.*, **21**, pp. 593-597 (1992).

Grew, K., and T. Ibbs, *Thermal Diffusion in Gases*, Cambridge University Press, Cambridge (1952).

Haji-Sheikh, A., and E. Sparrow, "Probability Distributions and Error Estimates for Monte Carlo Solutions of Radiation Problems," *Prog. Heat Mass Transfer*, **2**, pp. 1-12 (1969).

Haji-Sheikh, A., "Monte Carlo Methods" in *Handbook of Numerical Heat Transfer*, W. Minkowycz, E. Sparrow, R. Pletcher and G. Schneider, eds., Wiley, New York (1988).

Hasper, A., J. Holleman, J. Middlehoek, C. Kleijn and C. Hoogendoorn, "Modeling and Optimization of the Step Coverage of Tungsten LPCVD in Trenches and Contact Holes," *J. Electrochem. Soc.*, **138**, pp. 1728-1738 (1991).

Hasslacher, B., "Discrete Fluids," *Los Alamos Sci.*, Special Issue, pp. 175-217 (1987).

Haviland, J., in *Methods of Computational Physics*, ed. B. Alder, Academic Press, New York (1965).

Hess, D., and D. Graves, "Plasma-Enhanced Etching and Deposition," in *Microelectronics Processing : Chemical Engineering Aspects*, D. Hess and K. Jensen, eds., Advances in Chemistry Series, **221** (1989).

Hill, C., *An Introduction to Chemical Engineering Kinetics and Reactor Design*, Wiley, New York (1977).

Hiroi, M., and T. Tatsumi, "Selective Epitaxial Growth of Si_xGe_{1-x} by Cold-Wall Ultrahigh Vacuum Chemical Vapor Deposition using Disilane and Germane," *J. Crystal Growth*, **120**, pp. 279-283 (1992).

Hirschfelder, J., C. Curtiss and R. Bird, *Molecular Theory of Gases and Liquids*, Wiley, New York (1954).

Hitchman, E., and K. Jensen, "Chemical Vapor Deposition : An Overview," in *Chemical Vapor Deposition : Principles and Applications*, M. Hitchman and K. Jensen, eds., Academic Press, New York (1993).

Hopfmann, C., C. Werner and J. Ulacia, "Numerical Analysis of Fluid Flow and Nonuniformities in a Polysilicon LPCVD Batch Reactor," *Appl. Surf. Sci.*, **52**, pp. 169-187 (1991).

Houf, W., J. Grcar and W. Breiland, "A Model for Low Pressure Chemical Vapor Deposition in Batch Furnaces," *Proc. 12th Int. Conf. CVD*, K. Jensen and D. Cullen, eds., pp. 85-93 (1993).

Howell, J., "Application of Monte Carlo to Heat Transfer Problems" in *Advances in Heat Transfer*, J. Hartnett and T. Irvine, eds., **5**, Academic Press, New York (1968).

Hsieh, C., and K. Su, "Thermal Radiative Properties of Glass from 0.32 to 206 μm," *Solar Energy*, **22**, pp. 37-43 (1979).

Igarashi, S., K. Nanbu, S. Mitamura and T. Sugawara, "Grwoth Rate of Films in Low-Pressure CVD Reactors," *Proc. 17th Int. Symp. Rarefied Gas Dyn.*, pp. 671-678 (1990).

Ikegawa, M., and J. Kobayashi, "Deposition Profile Simulation Using the Direct Simulation Monte Carlo Method," *J. Electrochem. Soc.*, **136**, pp. 2982-2986 (1989).

Iyer, S., G. Patton, J. Stork, B. Meyerson and D. Harame, "Heterojunction Bipolar Transistors Using Si-Ge Alloys," *IEEE Trans. Elec. Dev.*, **36**, pp. 2043-2064 (1989).

Jain, M., T. Cale and T. Gandy, "Comparison of LPCVD Film Conformalities Predicted by Ballistic Transport-Reaction and Continuum Diffusion-Reaction Models," *J. Electrochem. Soc.*, **140**, pp. 242-247 (1993).

Jasinski, J., B. Meyerson and B. Scott, "Mechanistic Studies of Chemical Vapor Deposition," *Ann. Rev. Phys. Chem.*, **38**, pp. 109-140 (1987).

Jensen, K., and D. Graves, “Modeling and Analysis of Low Pressure CVD Reactors,” *J. Electrochem. Soc.*, **130**, pp. 1950-1957 (1983).

Jensen, K., “Chemical Vapor Deposition,” in *Microelectronics Processing : Chemical Engineering Aspects*, D. Hess and K. Jensen, eds., Advances in Chemistry Series, **221** (1989).

Jensen, K., “Fundamentals of Chemical Vapor Deposition,” in *Chemical Vapor Deposition : Principles and Applications*, M. Hitchman and K. Jensen, eds., Academic Press, New York (1993).

Kato, M., J. Murota and S. Ono, "Control of Composition and Deposition Rate in Si-Ge CVD Epitaxy," *J. Crystal Growth*, **115**, pp. 117-121 (1991).

Kawahara, T., A. Yuuki and Y. Matsui, “A Study on the Behavior of SiO_2 Film Precursors with Trench Deposition Method for SiH_4/O_2 Low Pressure Chemical Vapor Deposition,” *Jap. J. Appl. Phys.*, **30**, pp. 431-436 (1991).

Kennard, E., *Kinetic Theory of Gases*, McGraw-Hill, New York (1938).

Kersch, A., W. Morokoff, C. Werner, D. Restaino and B. Vollmer, "Modeling of a Sputter Reactor Using the Direct Simulation Monte Carlo Method," *Proc. Int. Elec. Dev. Mtg.*, pp. 181-184 (1992).

Kersch, A., personal communication (1993).

Kleijn, C., “Transport Phenomena in Chemical Vapor Deposition Reactors,” Ph.D Thesis, Delft University, The Netherlands (1991).

Kogan, M., "Molecular Gas Dynamics," *Ann. Rev. Fluid. Mech.*, **5**, pp. 383-404 (1973).

Kreyszig, E., *Advanced Engineering Mathematics*, 6th ed., Wiley, New York (1988).

Kuech, T., "Metal-Organic Vapor Phase Epitaxy of Compound Semiconductors," *Mat. Sci. Rep.*, **2**, pp. 1-50 (1987).

Kuiper, A., C. VanDenBrekel, J. DeGroot and G. Veltkamp, "Modeling of Low-Pressure CVD Processes," *J. Electrochem. Soc.*, **129**, pp. 2288-2291 (1982).

Levenspiel, O., *Chemical Reaction Engineering*, 2nd ed., Wiley, New York (1972).

Matsumoto, Y., and J. Matsui, "Numerical Analysis of Gas-Surface Interaction by the Molecular Dynamics Method," *Proc. 17th Int. Symp. Rarefied Gas Dyn.*, pp. 889-896 (1990).

McConica, C., and S. Churchill, in *Tungsten and Other Refractory Metals for VLSI Applications III*, ed. V. Wells, MRS Publications, Pittsburgh (1988).

McQuarrie, D., *Statistical Mechanics*, Harper and Row Publishers, New York (1976).

Meyerson, B., and W. Olbricht, "Phosphorus-Doped Polycrystalline Silicon via LPCVD : I. Process Characterization," *J. Electrochem. Soc.*, **131**, pp. 2361-2365 (1984).

Meyerson, B., and M. Yu, "Phosphorus-Doped Polycrystalline Silicon via LPCVD : II. Surface Interactions of the Silane/Phosphine/Silicon System," *J. Electrochem. Soc.*, **131**, pp. 2366-2368 (1984).

Meyerson, B., "Low-temperature Silicon Epitaxy by Ultrahigh Vacuum Chemical Vapor Deposition," *Appl. Phys. Lett.*, **48**, pp. 797-799 (1986).

Meyerson, B., B. Scott and R. Tsui, "Experimental and Chemical Kinetic Modelling Study of Silicon CVD from Monosilane and Disilane," *Chemtronics*, **1**, pp. 150-155 (1986).

Meyerson, B., E. Ganin, D. Smith and T. Nguyen, "Low Temperature Silicon Epitaxy by Hot Wall Ultrahigh Vacuum/Low Pressure Chemical Vapor Deposition Techniques : Surface Optimization," *J. Electrochem. Soc.*, **133**, pp. 1232-1235 (1986).

Meyerson. B., F. LeGoues, T. Nguyen and D. Harame, "Nonequilibrium Boron Doping Effects in Low-Temperature Epitaxial Silicon Films," *Appl. Phys. Lett.*, **50**, pp. 113-115 (1987).

Meyerson, B., K. Uram and F. LeGoues, "Cooperative Growth Phenomena in Silicon/Germanium Low-Temperature Epitaxy," *Appl. Phys. Lett.*, **25**, pp. 2555-2557 (1988).

Meyerson, B., VLSI Seminar Series, Massachusetts Institute of Technology, March 31 (1992).

Middleman, S., and A. Yeckel, "A Model of the Effects of Diffusion and Convection on the Rate and Uniformity of Deposition in a CVD Reactor," *J. Electrochem. Soc.*, **133**, pp. 1951-1956 (1986).

Mo, G., and F. Rosenberger, "Molecular Dynamics Simulations of Flow in a Two-Dimensional Channel with Atomically Rough Walls," *Phys. Rev. A*, **42**, pp. 4688-4692 (1990).

Moffat, H., and K. Jensen, "Three-dimensional Flow Effects in Silicon CVD in Horizontal Reactors," *J. Electrochem. Soc.*, **135**, pp. 459-471 (1988).

Moffat, H., K. Jensen and R. Carr, "Estimation of the Arrhenius Parameters for $SiH_4 \leftrightarrow SiH_2 + H_2$ and ΔH_f (SiH_2) by a Nonlinear Regression Analysis of the Forward and Reverse Reaction Rate Data," *J. Phys. Chem.*, **95**, pp. 146-154 (1991).

Mott-Smith, H., "The Solution of the Boltzmann Equation for a Shock Wave," *Phys. Rev.*, **82**, pp. 855-892 (1951).

Nanbu, K., and Y. Watanabe, "Analysis of the Internal Structure of Shock Waves by Means of the Exact Direct-Simulation Method," *Proc. 14th Int. Symp. Rarefied Gas Dyn.*, pp. 183-190 (1984).

Nanbu, K., T. Sugawara, S. Mitamura and S. Igarashi, "Molecular Simulation of Flows in Low-Pressure CVD Reactors," *ASME Forum on Micro Fluid Mechanics*, **113**, pp. 59-64 (1991).

Nelson, D., and Y. Doo, "Simulation of Multicomponent Nozzle Flows into a Vacuum," *Proc. 16th Int. Symp. Rarefied Gas Dyn.*, pp. 340-349 (1988).

Neureuther, A., C. Ting and C. Liu, "Application of Line-Edge Profile Simulation to Thin-Film Deposition Processes," *IEEE Trans. Elec. Dev.*, **ed-27**, pp. 1449-1455 (1980).

Nordsieck, A., and B. Hicks, "Monte Carlo Evaluation of the Boltzmann Collision Integral," *Proc. 5th Int. Symp. Rarefied Gas Dyn.*, pp. 695-710 (1967).

O'Hanlon, J., *A User's Guide to Vacuum Technology*, 2nd ed., Wiley, New York (1989).

Perry, R., and D. Green, eds., *Perry's Chemical Engineers' Handbook*, 6th ed., McGraw-Hill, New York (1984).

Pollard, W., and R. Present, "On Gaseous Self-Diffusion in Long Capillary Tubes," *Phys. Rev.*, **73**, pp. 762-774 (1948).

Press, W., S. Teukolsky, W. Vetterling and B. Flannery, *Numerical Recipes in Fortran : The Art of Scientific Computing*, 2nd ed., Cambridge University Press, New York (1992).

Prisco, G., "Optimization of Direct Simulation Monte Carlo (DSMC) Codes for Vector Processing," *J. Comp. Phys.*, **94**, pp. 454-466 (1991).

Raupp, G., and T. Cale, "Step Coverage Prediction in Low-Pressure Chemical Vapor Deposition," *Chem. Mat.*, **1**, pp. 207-214 (1989).

Rendulic, K., "Sticking and Desorption : A Review," *Surf. Sci.*, **272**, pp. 34-44 (1992).

Roenigk, K., "Analysis of Low Pressure Chemical Vapor Deposition Processes," Ph.D. Thesis, University of Minnesota (1987).

Roenigk, K., and K. Jensen, "Low Pressure CVD of Silicon Nitride," *J. Electrochem. Soc.*, **134**, pp. 1778-1785 (1987).

Sala, A., *Radiant Properties of Materials*, Elsevier, New York (1986).

Scott, B., and R. Estes, "Role of Gas Phase Reactions in Silicon Chemical Vapor Deposition from Monosilane," *Appl. Phys. Lett.*, **55**, pp. 1005-1007 (1989).

Siegel, R., and J. Howell, *Thermal Radiation Heat Transfer*, 3rd ed., McGraw-Hill, New York (1992).

Tait, R., T. Smy and M. Brett, "A Ballistic Deposition Model for Films Evaporated Over Topography," *Thin Solid Films*, **187**, pp. 375-384 (1990).

Tsai, C., J. Knights, G. Chang and B. Wacker, "Film Formation Mechanisms in the Plasma Deposition of Hydrogenated Amorphous Silicon," *J. Appl. Phys.*, **59**, pp. 2998-3001 (1986).

Tsien, H., "Superaerodynamics, Mechanics of Rarefied Gas Dynamics," *J. Aeronaut. Sci.*, **13**, pp. 653-664 (1946).

Wachman, H., personal communication (1991).

Watanabe, K., and H. Komiyama, "Micro/Macrocavity Method Applied to the Study of the Step Coverage Formation Mechanism of SiO_2 Films by LPCVD," *J. Electrochem. Soc.*, **137**, pp. 1222-1227 (1990).

Weeks, J., and G. Gilmer, in *Advances in Chemical Physics*, Vol. XL, I. Progogine and S. Rice, eds., Wiley, New York (1978).

Weston, R., and H. Schwarz, *Chemical Kinetics*, Prentice-Hall, New Jersey (1972).

Wilmoth, R., "Direct Simulation Monte Carlo Analysis of Rarefied Flows on Parallel Processors," *J. Therm. Heat Transfer*, **5**, pp. 292-300 (1991).

Wulu, H., K. Saraswat and J. McVittie, "Simulation of Mass Transport for Deposition in Via Holes and Trenches," *J. Electrochem. Soc.*, **138**, pp. 1831-1840 (1991).

Yeckel, A., and S. Middleman, "A Model of Growth Rate Nonuniformity in the Simultaneous Deposition and Doping of a Polycrystalline Silicon Film by LPCVD," *J. Electrochem. Soc.*, **134**, pp. 1275-1281 (1987).

Yeckel, A., S. Middleman and A. Hochberg, "The Origin of Nonuniform Growth of LPCVD Films from Silane Gas Mixtures," *J. Electrochem. Soc.*, **136**, pp. 2038-2050 (1989).

Yuuki, A., Y. Matsui and K. Tachibana, "A Study on Radical Fluxes in Silane Plasma CVD from Trench Coverage Analysis," *Jap. J. Appl. Phys.*, **28**, pp. 212-218 (1989).

List of Publications

The following is a list of publications regarding various aspects of the research which have been presented in this dissertation.

Coronell, D.G. and K.F. Jensen, "Analysis of MOCVD of GaAs on Patterned Substrates," *J. Crystal Growth*, **114**, pp. 581-592 (1991).

Coronell, D.G. and K.F. Jensen, "Analysis of Transition Regime Flows in Low Pressure CVD Reactors using the Direct Simulation Monte Carlo Method," *J. Electrochem. Soc.*, **139**, pp. 2264-2273 (1992).

Coronell, D.G. and K.F. Jensen, "Modelling of Transport and Film Growth Over Patterned Substrates," OE/Fibers '92, Boston, *SPIE Proc.*, **1788** (1992).

Coronell, D.G. and K.F. Jensen, "Monte Carlo Simulations of Film Profile Evolution during Nonplanar CVD Processes," in Evolution of Surface and *Thin Film Microstructure*, H. Atwater, E. Chason, M. Grabow and M. Lagally, eds., *MRS Proc.*, **280** (1993).

Coronell, D.G. and K.F. Jensen, "Models of Rarefied CVD Processes at Reduced Pressures and Reduced Dimensions," *Proc. 12th Int. Conf. CVD*, K.F. Jensen and G.W. Cullen, eds., *The Electrochemical Society*, Pennington, NJ, pp. 57-63 (1993).

Coronell, D.G. and K.F. Jensen, "Simulation of Rarefied Gas Transport and Profile Evolution in Nonplanar Substrate CVD," submitted to the *J. Electrochem. Soc.* (1993).

Coronell, D.G. and K.F. Jensen, "A Monte Carlo Simulation Study of Radiation Heat Transfer in the Multiwafer LPCVD Reactor," submitted to the *J. Electrochem. Soc.* (1993).